

ACOUSTIC WAVES AND ELECTRON WAKES IN A
POSITIVE COLUMN PLASMA

An experimental study of periodic spatial variations in
the wake of an obstacle and externally excited waves of plasma
density in a positive column with a longitudinal magnetic field.

Thesis
submitted by
Peter John Barrett
for the degree of
Doctor of Philosophy
in the University of London

Imperial College of Science and Technology

1966

ABSTRACT

Part A. Measurements with a plane Langmuir probe near an obstacle in a positive column with a longitudinal magnetic field reveal periodic spatial variations in the number of high energy electrons reaching the probe, and in the local plasma parameters (density, potential, electron temperature). The variations are due to the helical motion of electrons along the wake after partial selection of the phase of their motion by the obstacle. The distribution of high energy electrons in the region downstream from the obstacle is similar to that calculated by Al'pert et al for the ions behind a satellite moving through the ionosphere, parallel to a magnetic field. There is strong evidence that the spatial variations of plasma parameters, as seen in the frame of reference moving with the average velocity of the anode-directed electrons, constitute an electron cyclotron wave.

Part B. Externally excited waves of small amplitude in low pressure mercury, argon, neon and hydrogen positive columns have been observed at frequencies mainly below 100 kc/s. A weak longitudinal magnetic field is usually employed to facilitate propagation. Phase sensitive detection is used to distinguish the weak wave signal from the strong background of noise. The experimental dispersion curves of frequency against wave number fall into two groups, those having positive slope (forward waves) and those having negative slope (backward waves). The phase velocities of the former are, on the whole, somewhat less than the electro-acoustic velocity $(KT_e/m_i)^{1/2}$ predicted by Tonks & Langmuir. With the aid of L.C. Woods' theory of electro-acoustic waves in a low pressure positive column, the forward waves are identified with one or other of the two lowest radial modes. Fair agreement is found between the dispersion curves for the backward waves and the dispersion equation derived by Pekárek & Krejčí for ionization waves. The backward waves are consequently identified as ionization waves.

CONTENTS

	<u>Page</u>
GENERAL INTRODUCTION	5
<u>PART A ELECTRON WAKES</u>	7
<u>CHAPTER I INTRODUCTION</u>	
(1) Dark and bright regions	8
(2) The term "electron wake"	10
(3) Other studies of wakes in plasmas	11
(4) Lay-out of Part A	13
<u>CHAPTER II APPARATUS</u>	
(5)	14
<u>CHAPTER III EXPERIMENTAL RESULTS</u>	
III A. SPATIAL VARIATION OF FLOATING POTENTIAL V_f OF PROBE	
(6) Radial variation	16
(7) Variation with z on each side of obstacle	16
(8) Ranges of discharge conditions	19
(9) Spatial period Λ_z	19
(10) Amplitude	21
(11) Damping	25
(12) Phase	25
(13) Shape	27
PERIODIC SPATIAL VARIATIONS OF PROBE POTENTIAL V_a	
(14)	27
III.B PERIODIC SPATIAL VARIATIONS OF PLASMA PARAMETERS	
(15)	29
(16) Concepts underlying the probe current-voltage curves	30
(17) First series of probe current-voltage curves	32
(18) Second series of probe current-voltage curves	34
(19) Radial variation of plasma potential	37
<u>CHAPTER IV DISCUSSION AND INTERPRETATION OF RESULTS</u>	
IV A. PERIODIC SPATIAL VARIATIONS OF PROBE POTENTIAL	
(20)	38
(21) Response of floating probe to electron density variations	38
(22) Shape	39
(23) Spatial period	39
(24) Amplitude, dependence on ρ/R	39
(25) Amplitude, dependence on r	41

	<u>Page</u>
(26) Damping	42
(27) Phase	44
(28) Positive column instability	44

V_a VARIATIONS

(29) Comparison with V_f variations	45
(30) Relationship between V_a and the density $n_e(\Delta V)$	46
(31) Spatial period	46

COMPARISON OF PRESENT EXPERIMENTAL WAKES AND SATELLITE WAKES DESCRIBED BY AL'PERT, GUREVICH AND PITAEVSKII

(32) Ion density in satellite wake according to Al'pert et al.	47
(33) Comparison of physical conditions	49
(34) Comparison of V_f and V_a curves with results of Al'pert et al	50

INCREASE OF PERPENDICULAR VELOCITY v_{\perp}

(35)	50
------	----

IV B. PERIODIC SPATIAL VARIATIONS OF PLASMA PARAMETERS

(36)	52
(37) Curves of V_p , n_e and T_S versus z	52
(38) Relationship between n_e and n_i	53
(39) Excess group of faster electrons	54

PLASMA WAVE

(40)	56
(41) Identification of the wave	56
(42) Magnitude of the wave vector	57

CHAPTER V CONCLUSIONS

(43) Summary	60
(44) Significance of results	61

Published paper: "Electron wakes in a plasma".

PART B WAVES OF PLASMA DENSITY 62

CHAPTER I INTRODUCTION

(1) The two types of low frequency density wave in a positive column	63
(2) Spontaneously occurring density waves	64

ELECTRO-ACOUSTIC WAVES

(3)	64
(4) Basic dispersion equation	65

	<u>Page</u>
(5) Effect of ion-neutral collisions and finite radius	66
(6) Effect of ion and electron longitudinal drift velocities	69
(7) Electro-acoustic waves in collision-dominated positive column	70
(8) Electro-acoustic waves in low pressure, bounded plasma	70
(9) Damping: discrepancy between theory and experiment	74
(10) The adiabatic compression coefficient γ_e for the electron gas	75
(11) History of experimental studies of electro-acoustic waves	76

IONIZATION WAVES

(12) Recent history	80
(13) The mechanism of ionization waves	83

CHAPTER II APPARATUS

(14) Discharge apparatus	88
(15) The non-mercury plasma columns	90
(16) Magnetic fields	91
(17) Diagnostic apparatus	91

CHAPTER III EXPERIMENTAL RESULTS

(18)	96
(19) The two groups of dispersion curves	97
(20) Waves in mercury vapour	100
(21) Waves in neon	113
(22) Waves in argon	117
(23) Waves in hydrogen	121
(24) Radial variation of amplitude and phase of forward waves	126

CHAPTER IV DISCUSSION

(25) Excitation of the waves	127
------------------------------	-----

FORWARD WAVES

(26) Waves in the (0,1) mode	129
(27) The dispersion curves $\omega/k = ac_s$	129
(28) Mode of the waves corresponding to $\omega/k = ac_s$	133
(29) Comments by Bertotti et al. concerning the effect of the electron drift velocity on the principal mode	133
(30) Absence of forward waves in the argon discharge	134

BACKWARD WAVES

(31) Dispersion equation according to Pekárek & Krejčí	135
(32) Dispersion equation in the ion drift frame of reference	137
(33) Determination of Z'	138
(34) Accuracy of calculated values of Z'	142
(35) Experimental and theoretical values of ωk	145

	<u>Page</u>
(36) Minimum value of the wave number	146
(37) Long wavelength branch of the dispersion curve in the argon discharge	147
(38) The two dispersion curves in hydrogen	148
(39) Damping of the backward waves	150
(40) Effect of magnetic field on wave propagation	151

CHAPTER V CONCLUSIONS

(41) Summary	153
(42) Significance of results	153
(43) Suggestions for further investigation of forward and backward waves	154

Published paper: "Externally excited waves in low-pressure plasma columns" (by P.J. Barrett & P.F. Little).

APPENDICES FOR PART A

APPENDIX A Relationships between $\frac{\partial v_p}{\partial z}$, $\frac{\partial n_e}{\partial z}$ and $\frac{\partial T_s}{\partial z}$	155
APPENDIX B Electron cyclotron wave	159

APPENDICES FOR PART B

APPENDIX C Basic dispersion equation for electro-acoustic waves	163
APPENDIX D Dispersion equation for electro-acoustic waves in a plasma column with ion collisions	165
APPENDIX E Three types of anode-approaching striation	167
APPENDIX F Failure of cold trap	169
APPENDIX G Mechanism of wave excitation	170
REFERENCES	175
ACKNOWLEDGEMENTS	180

GENERAL INTRODUCTION

This thesis is concerned with two widely different types of periodic variation that can be produced in the positive column of an arc discharge. They are treated separately in Parts A and B. Part A deals with the periodic spatial variation of various quantities in the perturbed region, or wake, near an obstacle placed in a column when a longitudinal magnetic field is present. Part B is an account of electro-acoustic and ionization waves, excited by means of a weak, localised, alternating magnetic field and propagated along the column on the anode side of the exciter.

The experiments were carried out with the apparatus previously used by Little and Jones for studying the propagation of electro-acoustic (often called ion acoustic) waves in a mercury positive column⁽¹⁾. One of the questions posed by their use of a probe such as that shown on p. 92 for some of their measurements, was that of the perturbation of these measurements by the radial portion of the probe. The probe was therefore moved about on the anode side of a thin rod inserted radially into the discharge and it was observed that in the shadow cast by the rod the floating potential of the probe varied periodically with distance in the axial direction. The experiments of Part A were carried out to investigate this phenomenon.

In the experiments of Part B the author's intention was to investigate electro-acoustic wave propagation under more varied conditions than those of Little and Jones. These authors had obtained dispersion curves of ω versus k for electro-acoustic waves in mercury vapour and hydrogen⁽²⁾ discharges, which exhibited different behaviour at low frequencies: the mercury curve approached a cut-off on the ω -axis and the hydrogen curve a cut-off on the k -axis. The immediate aim in the present experiments was to investigate this difference in behaviour by obtaining dispersion curves from (a) positive columns in gases of intermediate atomic mass, such as neon and argon, and (b) a mercury vapour column of smaller diameter. With the observation of dispersion curves not only of positive slope (including

some which were straight lines through the origin) but also of negative slope, the identification of the different types of curve became the main objective in the analysis of the experiments of Part B.

PART A

ELECTRON WAKES

CHAPTER I

INTRODUCTION

(1) Dark and bright regions

When an obstacle is placed in a low pressure positive column with a longitudinal magnetic field B_z a dark region is observed on the anode side of the obstacle and a bright region on the cathode side. These are labelled D and E in fig. 1(a). They are regions of diminished and increased density of electrons and, therefore, of excited atoms. They occur because of the electron drift towards the anode. Their length is of the order of an electron mean free path which, in these experiments, is much greater than the obstacle dimensions. They appear most distinct when the electron Larmor radius is much smaller than the obstacle dimensions.

Typical values of parameters in these experiments are as follows: column diameter 5 cm, obstacle diameter 1 cm, electron Larmor radius 1 mm, electron mean free path 15 cm.

When B is very large, the lateral dimensions of the dark and bright regions are exactly those of the obstacle: the regions coincide with the geometrical shadow on either side of the obstacle. The edge of each of these regions is in fact blurred over a radial distance equal to the mean Larmor diameter of the electrons, but the terms "bright region" and "dark region" will nevertheless be used here to denote the geometrical shadow on either side of the obstacle.

The increased density in E is assumed to be the result of the reflection of anode-directed electrons by an electron sheath at the cathode-facing surface of the obstacle. It is also assumed that there is a corresponding ion sheath at the anode-facing surface. These assumptions are consistent with the observation that the floating potential of a Langmuir probe goes more negative when it moves close to the cathode-facing surface, and more positive near the anode-facing surface.

It is clear that dark and bright regions will occur whenever an

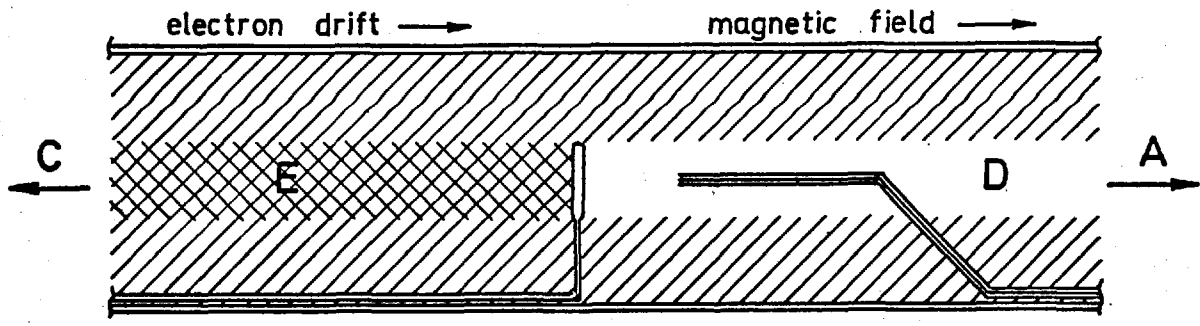


FIG 1(a) Obstacle and probe in positive column.

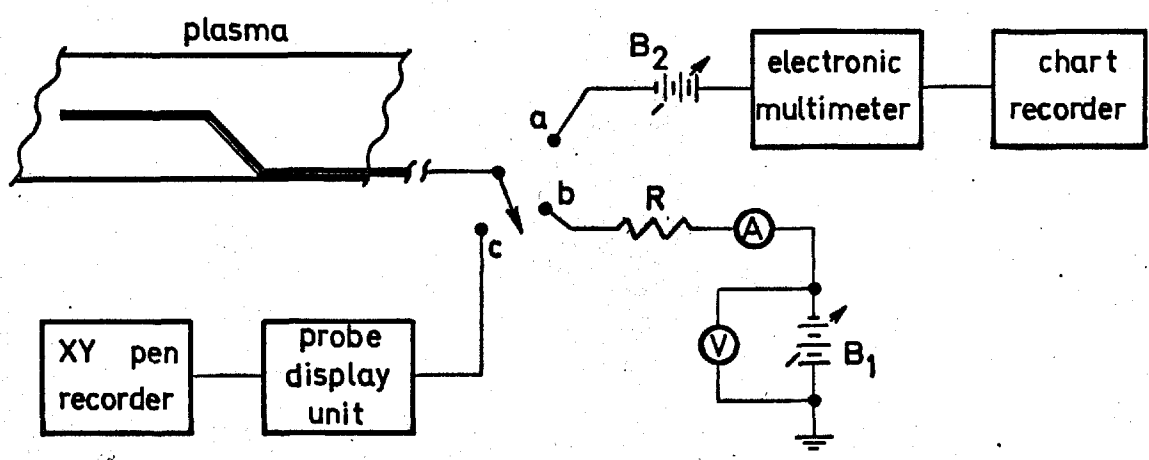


FIG 1(b) Probe connections for (a) measurement of V_f or V_a , and (b), (c) obtaining current-voltage curve.

object is immersed in a partially ionized gas carrying a current of electrons, provided that the perpendicular velocity of the electrons is comparatively small or is constrained by a magnetic field, and that the mean free path of the electrons is not unduly short. These regions were observed for example by K. Nobata⁽³⁾ in his studies of Langmuir probe characteristics in a strong magnetic field. He states that there was a decrease of plasma potential near the surface of a cathode-facing probe, compared to the potential near a radial probe, and he assumes that this was responsible for the slightly low value (by 10%) of the ratio of the saturation electron current and saturation ion current to the probe. Probe shadows in a stable toroidal plasma with a strong axial magnetic field were studied briefly by R.J. Bickerton (private communication) at A.E.R.E., Harwell. In this case a comparatively weak azimuthal field was produced by the axial current and the net magnetic field in the torous was therefore slightly helical. Streak photographs provided evidence that the shadow cast by a probe extended more than once round the torous, following the twist of the field lines. They gave some indication of (i) the ratio of azimuthal and axial fields, and (ii) the rate of diffusion of the plasma across the field.

(2) The term "electron wake"

The term "electron wake" is used here to signify the perturbed region on either side of the obstacle. Such a region extends radially outside the geometrical shadow by a distance equal to the Larmor diameter of electrons with the highest perpendicular velocities. Regions D and E thus lie within the two wakes. A wake is produced on the cathode side of the obstacle, as well as on the anode side, because an appreciable number of electrons at any instant are moving towards the cathode, owing to the fact that the electron thermal velocity is several times greater than the drift velocity.

The word "wake" is usually used in the context of fluid flow in one direction only, in which case there is a small perturbed region upstream from the obstacle as well as a longer perturbed region downstream. In

the present case of a positive column, in which electrons travel in both directions along the magnetic field, it will be convenient to limit the term "wake" to the downstream region. The obstacle then produces a wake on the anode side in the flow of anode-directed electrons and, similarly, a wake on the cathode side in the flow of cathode-directed electrons.

A further distinction may be drawn between the two wakes and the dark and bright regions. The wake pertaining to either the anode-directed or cathode-directed electrons is a region of diminished density of that particular group. On the anode side the wake and the dark region seem to be approximately the same entity, but on the cathode side, the wake coincides with the region of increased electron density. The latter region contains both anode-directed and reflected electrons, but few of the cathode-directed electrons which have travelled past the obstacle. The dark and bright regions arise from the electron drift motion alone, whereas each wake results from the total electron motion in the appropriate axial direction.

Some of the spatial variations observed, such as those of the floating potential V_f of the probe, represent the motion of the high energy electrons only, whereas other spatial variations are related to the electrons of the entire energy range. The disturbance in the flow of high energy electrons may be distinguished from the wake produced in the total flow of electrons; the former is part of the latter but will be treated separately.

(3) Other studies of wakes in plasmas

The type of wake described above is to some extent similar to the wake produced when there is relative motion between a body and a plasma at a velocity intermediate between the ion and electron thermal speeds. A noteworthy example of the latter is the wake due to an artificial earth satellite travelling through the ionosphere. The similarities between this and the wake observed in these experiments, are discussed in section (33).

A theoretical account of wakes in plasmas, with special reference to

satellite wakes, has been given by several authors,⁽⁴⁾⁻⁽⁷⁾ notably Al'pert, Gurevich and Pitaevskii⁽⁶⁾ who include a bibliography of the theoretical work done before 1963. A more recent bibliography appears in the Ph.D. thesis by J.C. Taylor.⁽⁸⁾ As these particular authors point out, an understanding of satellite wakes is important for two main reasons: firstly, the perturbation of ion and electron densities in the immediate vicinity of a satellite, or other type of spacecraft, affects the measurement of these quantities by probes attached to the spacecraft; and secondly, the periodic spatial variation of the plasma density along the length of the wake, due to the presence of the earth's magnetic field, can lead to considerable scattering in certain directions of an incident beam of electromagnetic waves if the wavelength of the latter is comparable with the spatial period.

Experiments connected with satellite wakes may be placed in either of two categories: (i) those in which measurements are made with probes carried by a satellite, where only the region close to the satellite may be investigated, and (ii) laboratory experiments which simulate the plasma-satellite interaction, where the entire wake is observable.

An example of the first type of experiment is reported by Samir and Willmore⁽⁹⁾ who have analyzed data obtained from the satellite Ariel I and from a Black Knight rocket. It was found that immediately behind either spacecraft the plasma density is considerably depleted, but is much higher than expected. The authors claim that this and other evidence point to the existence of ion plasma oscillations in the wake.

Several simulation experiments on satellite wakes have been published⁽¹⁰⁾⁽¹¹⁾⁽¹²⁾, in which a small body is situated in the path of a continuous plasma jet or of a plasmoid from a plasma gun. These all illustrate the expected depletion of plasma downstream from the body. In the experiment by N. Kawashima⁽¹²⁾ a magnetic field ($B \leq 1000$ gauss) is employed, both parallel and perpendicular to the plasma velocity. An extra feature of this experiment is the appearance of an upstream disturbance when the plasma flow velocity is less than the Alfvén velocity (the flow velocity is supersonic). The probe measurements

reported by Kawashima were not made over a sufficiently large distance from the body to reveal any periodic spatial variations in the plasma density, neither did such variations appear in photographs of the wake; it is possible that the ion collision frequency was too high for the phenomenon to occur ($n_e \sim 10^{12} - 10^{15} \text{ cm}^{-3}$). It appears that no simulation experiments illustrating such spatial variations in a magnetic field have been published.

Two wakes that occur in the plasma of interplanetary space may be noted: the wake produced by the moon (Ness et. al., quoted in ref. 12)* and the wake produced in the solar wind by the dipole magnetic field of the earth. The latter is the subject of several simulation experiments, references to which are given in refs. 12 and 13.

(4) Lay-out of Part A

We are concerned in Part A with plane Langmuir probe measurements in the wake on either side of an obstacle. These have been published in brief form⁽¹⁴⁾ and a copy of the article is inserted at the end of Part A.

A short description of the apparatus is given in Chapter II; a more detailed account of the discharge and probes appears in Part B. Chapter IIIA contains a description of the periodic variation of probe potential with distance along the axial direction (which will also be called the z direction). This includes variations of probe potential V_f when the probe is floating, and variations of the probe potential V_a when the probe is drawing a small negative or positive current from the plasma; V_f is a particular value of V_a , and $V_a \leq V_f$. In both the V_f and V_a measurements the probe receives only those electrons in the high energy tail of the electron energy distribution. Chapter IIIB deals with the periodic spatial variation of the total electron density, plasma potential and electron temperature in the dark region. Discussion and explanation of the results are presented in Chapter IVA and IVB, and a brief summary and conclusions are given in Chapter V.

* J. Geophys. Res., 69, 3531 (1964)

CHAPTER II

APPARATUS

(5) The wake experiments were carried out with the discharge apparatus described in Part B. A mercury positive column was used for most of the experiments and a few measurements were also made in neon.

The obstacle was situated at a distance of 60 cm from the right angle bend of the plasma column. It was either a rod inserted through the side tube ST or a quartz disc supported on a thin quartz stem at the end of a 1 mm diameter quartz rod, inserted at the cathode end of the main tube (as in fig. 1(a)). Discs of diameter 6, 12 and 30 mm were used. The 6 and 12 mm discs were somewhat oval in cross-section when viewed along a diameter, with a maximum thickness of 2 mm. Non-conducting rods of diameter 0.5, 1 and 5 mm were used, and also a 5 mm steel rod held at three different potentials.

Most of the measurements were carried out with the cathode-facing probe CP, shown in fig. 1(a) and described in detail in Part B. Some were also made with an anode-facing probe AP, which was identical to CP except that the end segment was only 7 mm long and was bent back so that the tip faced the anode. Each probe presented to the plasma a plane tip, of diameter 0.25 mm, which was supported in a ceramic tube of external diameter 0.5mm.

The various measurements required different probe connections a, b and c, which are shown in fig. 1(b). The probe was connected to a for the measurement of V_f or V_a variations. Its position was continuously varied by means of a synchronous motor, and V_f or V_a was simultaneously recorded on a chart recorder. In the V_f measurements it was essential that the meter to which the probe was connected should draw negligible current from the probe. An Emouzy Precision Electronic Multimeter with an input impedance $> 10^{12}$ ohms was used, and the signal to the chart recorder was taken from an output terminal of the meter. When variations of V_a were to be observed, probe current was drawn through the 1 megohm resistor R and battery B, and the variations registered as before on the chart recorder.

In the measurements of plasma parameter variations, R was reduced to a few hundred ohms and current-voltage characteristics were obtained at a number of different positions of the probe. Current and voltage were measured either with the Avometers A and V (connection b in fig. 1(b)), or were plotted directly on an X-Y pen recorder with the aid of a "Langmuir Probe Display Unit" (connection c).

The probe display unit converted the probe current I into a $\log I$ signal, to which could be added a component to make the probe characteristic, as displayed on an oscilloscope, as closely linear as possible. With a Maxwellian velocity distribution of electrons this would be equivalent to displaying $\log I_e$ against V , where I_e = electron current. A sawtooth voltage of amplitude 50 volts and frequency less than 1 c/s was supplied from the time base of the oscilloscope to the probe and X-Y recorder.

Accurate information on the variation of plasma parameters along one line in the dark region of the 6 mm disc was obtained from the Avometer readings, whilst the probe display unit produced less accurate curves which indicated how the plasma potential varied throughout the dark region of the 12 mm disc.

CHAPTER III

EXPERIMENTAL RESULTS

IIIA SPATIAL VARIATION OF FLOATING POTENTIAL V_f OF PROBE

(6) Radial variation

When the cathode-facing probe CP was moved radially through the dark region, the floating potential V_f changed to a less negative value as the probe entered the region, and reverted to its undisturbed value as it left the region. When the probe was situated close to the obstacle, most of the change took place over a distance of about 2ρ where ρ is the electron Larmor radius. A few centimetres further from the obstacle, the change of V_f was smaller and occurred over a larger radial distance, as expected from the increased blurring of the edge of the dark region.

(7) Variation with z in wake on each side of obstacle

As CP was moved along the z (axial) direction in the wake on the anode side, periodic spatial variations in V_f were observed, with a spatial period Λ_z which was found to be inversely proportional to the magnetic field B_z . These are associated with the helical motion of electrons, as explained in section (20). Examples of such variations in the dark region are given in figs. 2 and 3.

When CP was moved axially just outside the bright region, or inside the bright region as near to the obstacle as its end segment allowed, no periodic variations in V_f were observed. Corresponding results were obtained with the anode-facing probe AP: periodic variations in V_f were observed in the bright region but were not detected in the dark region.

Only a few measurements were made with AP, sufficient to establish the symmetry in the variations of V_f on either side of the obstacle. The product $\Lambda_z B_z$ and the qualitative features of the variations were the same on both sides, under given discharge conditions. No further reference is made, therefore, to the variations of V_f on the cathode side.

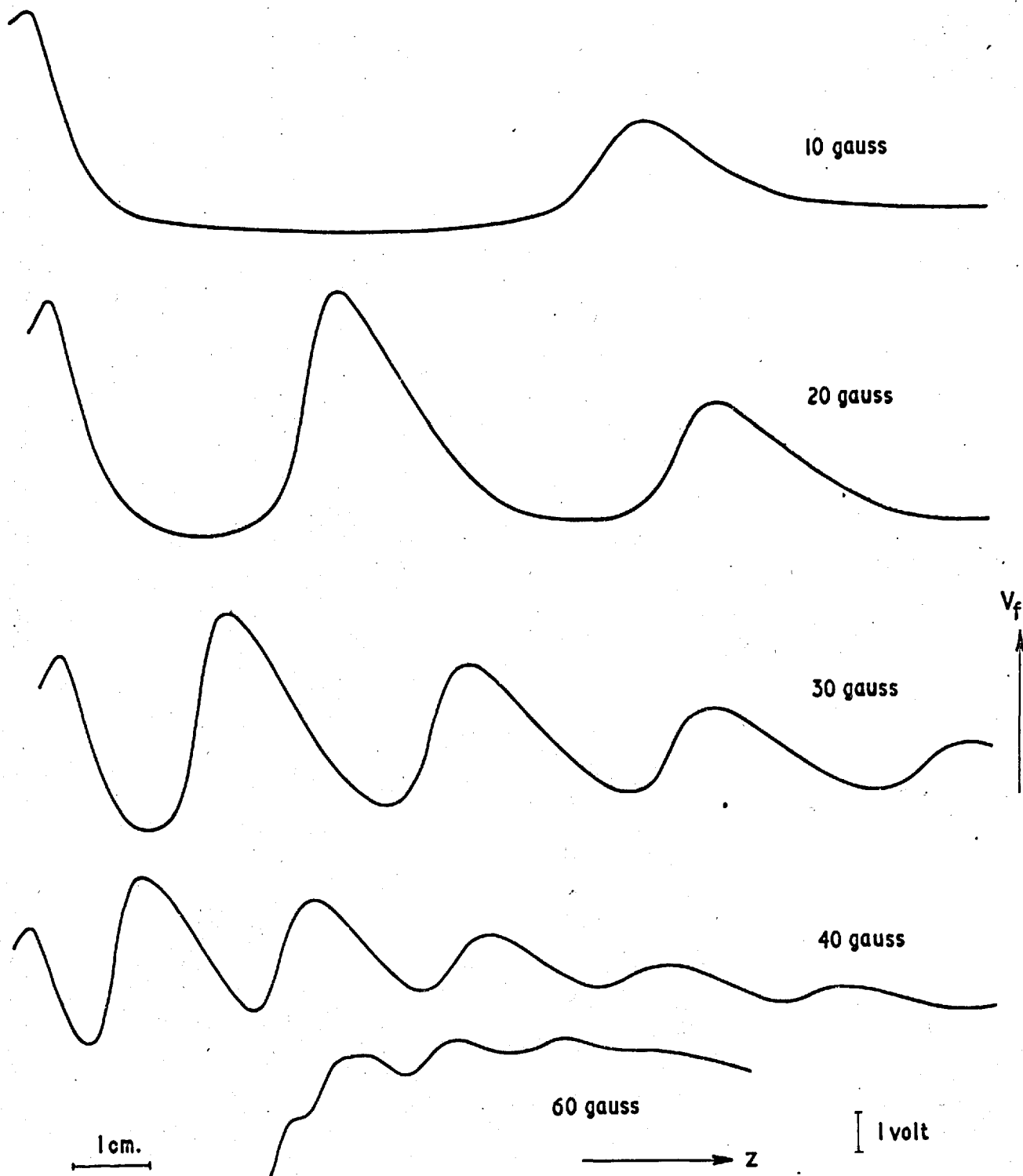


FIG 2 Variation of V_f along wake of 12 mm disc. $I_D = 3A$, $p = 0.2$ mtorr.

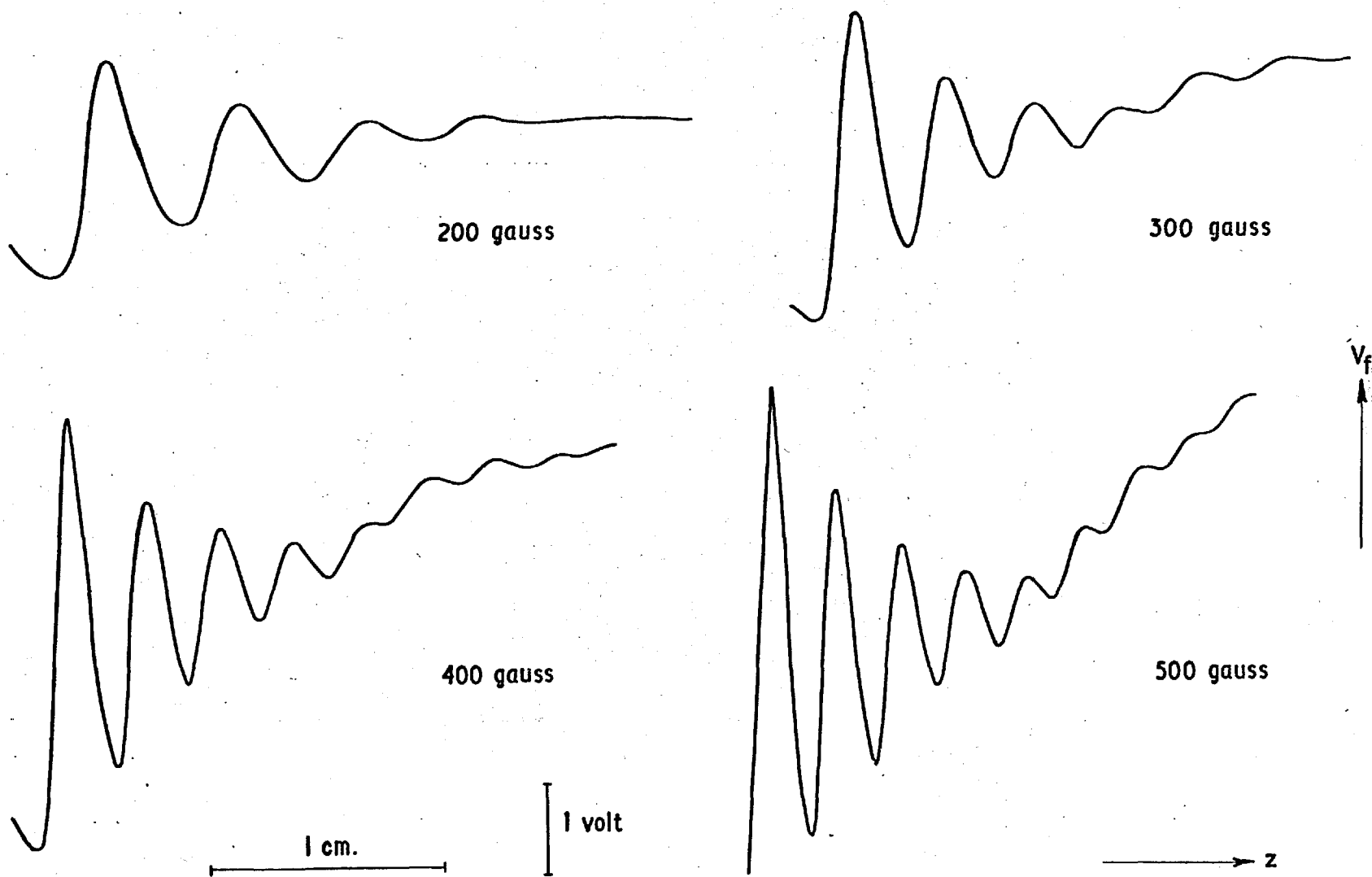


FIG 3 Variation of V_f along wake of 0.5 mm rod. $I_D = 3A$, $p = 0.2$ mtorr.

(8) Ranges of discharge conditions

The V_f variations, as observed on the anode side of the obstacle, depended in various ways on the plasma conditions, the size of the obstacle and the radial distance r from the centre of the wake. They were investigated in the following ranges of discharge conditions: pressure 0.1 - 5 millitorr (microns of mercury); magnetic field 10-600 gauss; discharge current 0.002-9A; positive column media, mercury and neon.

(9) Spatial period Λ_z

The spatial period is taken to be the average value of the period in a train of V_f or V_a variations, omitting the first period, which is always shorter than the spacing of the succeeding peaks. In the case of the V_f variations, measurements were made to determine the dependence of Λ_z on the following parameters: (a) magnetic field B_z ; (b) pressure p ; (c) ion mass m_i ; (d) discharge current I_D ; (e) shape, size, potential and radial position of the obstacle, and (f) the radial position r within the wake.

(a) The dependence on B_z is illustrated in fig. 4. At values of B_z less than 100 gauss, the spatial "wave number" $K_z (= 2\pi/\Lambda_z)$ is proportional to B_z . Immediately above this transition value the curves take on a new slope at which the proportionality is maintained. The mercury curves also have a second kink at about 160 gauss. The error bars in the neon curve represent typical values of the errors in the three curves at the left in fig. 4. The middle of these curves is repeated on a smaller scale at the right in order to show the entire range of experimental points. In the latter curve the increasing error bars reflect simply the inaccuracy in the measurement of very short distances on the chart recorder traces; the chart recorder was operating at its slowest speed in this particular case.

(b) The effect of pressure on Λ_z was comparatively slight. We see in fig. 4 that a decrease of pressure in the mercury discharge by a factor of 50 produced an increase of only 50% in the slope K_z/B_z . It is noted from an extrapolation of curves obtained by Allen and

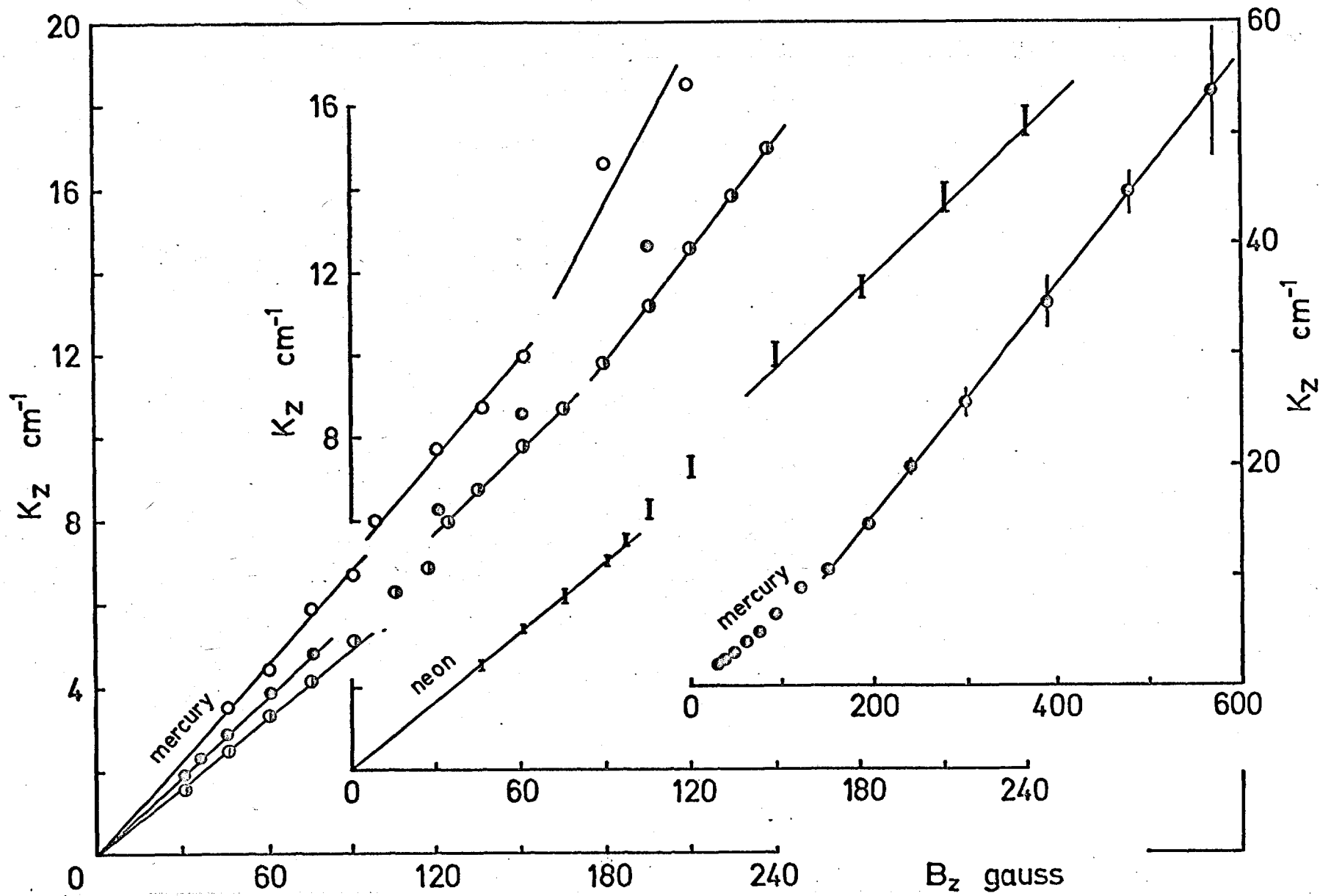


FIG 4 Wave number of V_f variations versus magnetic field using different gases, pressures and obstacles. \circ 5 mtorr, 12 mm disc; \bullet 0.2 mtorr, 0.5 mm rod; \odot 0.1 mtorr, 12 mm disc; I 5 mtorr, 1mm rod.

Magistrelli⁽¹⁵⁾, that the electron drift velocity v_d also increases by roughly 50% over this pressure range. It is evident from the interpretation in Chapter IVA, however, that there is only an indirect connection between K_z/B_z and v_d ; K_z is determined by the helical pitch of electrons in the tail of the electron energy distribution.

(c) The value of K_z/B_z in neon is 0.75 of that in mercury at the same pressure and at $B_z < 100$ gauss. The difference in slope is in accordance with the fact that the electron thermal and drift velocities are somewhat higher in neon than in mercury (the ratio of electron temperatures is roughly 3 to 1). No further explanation of the difference in slope seems to be required and so it appears that the effect of the ion mass on the values of Λ_z is not significant.

(d) No dependence of Λ_z on discharge current was noticeable in the range 0.7 to 9A.

(e) The obstacle itself played a negligible role in determining the value of Λ_z . The two curves marked \bullet and \circ in fig. 4 were obtained with obstacles of different shape and size, and the 10% difference in their slopes is attributed mainly to the pressure difference. In the case of a 5 mm diameter stainless steel rod inserted radially as the obstacle, Λ_z was measured when the rod was held at +11, 0 and -23 volts with respect to its floating potential; no change of Λ_z was observed. When Λ_z was measured in the wake produced by a 0.5 mm rod, first at the axis of the tube and then when the rod was moved 1.5 cm off the axis, there was again no difference in Λ_z .

(f) The radial position r within the wake affected Λ_z slightly. Λ_z was a few per cent larger outside the dark region than inside and, in the dark region of the 3 cm disc, the value at the centre was appreciably less than the value near the edge. This effect is shown in Fig. 5(a) in the case of a particularly small value of ρ/R (i.e. 0.1) where R = radius of the disc and ρ is calculated from the expression $(m/eB)(2T_e/m)^{1/2}$.

(10) Amplitude

The amplitude of the V_f variations inside the dark region is

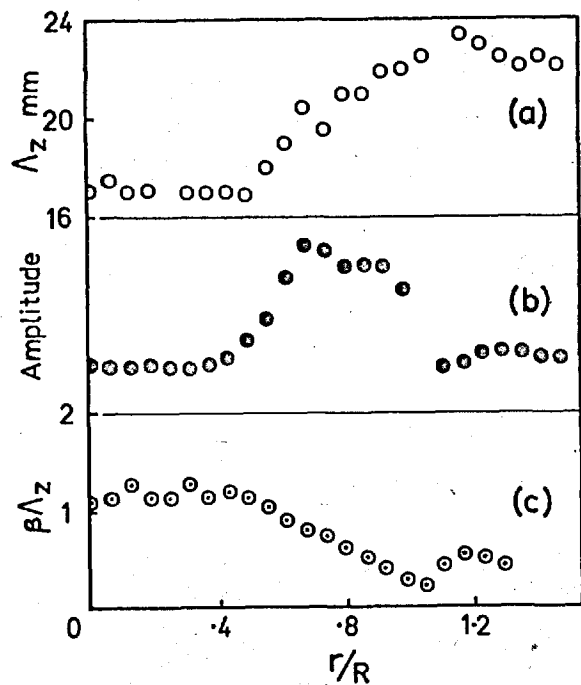


FIG 5 (a) Spatial period, (b) amplitude (arbitrary units) and (c) damping term $\beta\Lambda_z$, versus r in wake of 30 mm disc. $B_z = 28$ gauss, $\rho/R = 0.1$.

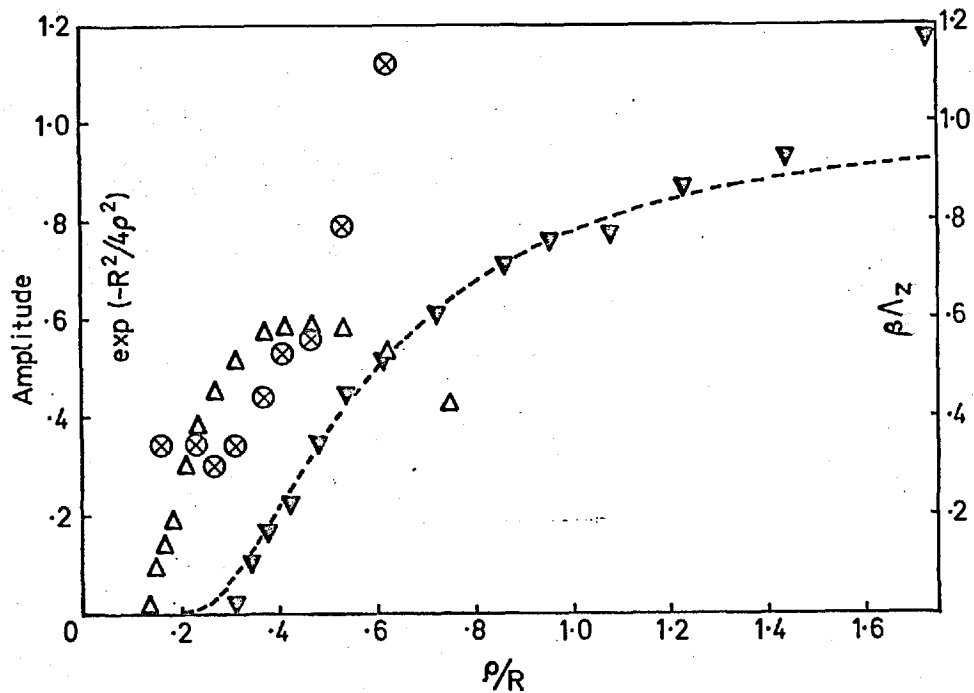


FIG 6 Amplitude (arbitrary units) and $\beta\Lambda_z$ versus ρ/R for 12 mm disc. Δ observed amplitude, ∇ corrected amplitude, ---- $\exp(-R^2/4\rho^2)$, \otimes $\beta\Lambda_z$. $I_D = 5$ A, $p = 0.5$ mtorr.

taken to be the change of potential from the first downward (more negative) peak to the succeeding upward peak. Outside the dark region it is measured from the first upward to the next downward peak. Due allowance is made for any slope of the median line of the "wave train". Inside the dark region the largest amplitudes recorded were almost $2T_e$ volts, where T_e is the electron temperature in eV, and they were less by an order of magnitude just outside this region.

The amplitude was investigated in two ways: (a) with a given obstacle and magnetic field (i.e. with ρ/R fixed), the amplitude was measured at various values of r in the wake, and (b) it was measured at the centre of the wake at various values of ρ/R . It was also observed as a function of (c) pressure and (d) discharge current. The description of amplitude variation will be confined to disc obstacles; similar behaviour would be expected with rod obstacles.

(a) The dependence of the amplitude on r was affected by the value of ρ/R . If the latter was about 0.3 or larger, the amplitude decreased by nearly an order of magnitude when r increased from 0 to R , and then decreased more gradually in the outer part of the wake. If ρ/R was somewhat less than 0.3, the amplitude increased from a lower value at the centre to a maximum at a distance of about 3ρ inwards from the edge of the dark region, and then decreased rapidly towards the edge of the dark region. Further outwards the decrease was gradual or, as in the case of the 3 cm disc, the amplitude reached a minimum at a distance ρ outside the dark region before rising again to a slight maximum at 2ρ from the dark region (see Fig. 5(b)). A noteworthy feature of the wake produced by the 3 cm disc was the appearance, at $B_2 = 28$ gauss, of small V_p variations at the axis of the wake, a distance 10ρ from the edge of the dark region.

(b) The variation of the amplitude at the axis of the wake with ρ/R is illustrated in fig. 6. It is also illustrated to some extent in fig. 2, but not in fig. 3 because the probe tip in this case almost spans the dark region. As stated above, the values of ρ were determined from the expression $(m/eB_2)(2T_e/m)^{1/2}$, where T_e was measured at only one value of ρ/R , viz. 0.37. The variation of T_e over the

range of B_z represented in fig. 6 has been shown by Little⁽¹⁶⁾ to be only about 10%, and its effect on the calculation of ρ is therefore assumed to be negligible.

The uncorrected amplitude points in fig. 6 lie mainly to the left of the theoretical curve, $\exp(-R^2/4\rho^2)$, and fail to increase with ρ/R at the larger values. They have been corrected in two stages, in order to produce the best fit with the theoretical curve. Firstly, allowance has been made for the damping (represented in fig. 6 by the term $\beta\Lambda_z$, described in the next sub-section) which, over half a period, makes a noticeable difference to the amplitude, especially at the large values of ρ/R . The corrected values then represent the amplitude within the first half period from the obstacle. Secondly, the points have been shifted to the right by multiplying the values of ρ/R by 2.3. The corrected value of the Larmor radius will be written as ρ_c .

In the range of ρ_c/R from 0.34 to 1.3 there is good agreement between the corrected V_f amplitude and the expression $\exp(-R^2/4\rho^2)$. This term represents the fraction of electrons in a Maxwellian distribution which have Larmor radii greater than $\frac{1}{2}R$ and which are therefore able to reach the axis of the wake after passing close to the obstacle. At the highest values of ρ/R the heavy damping makes the values of the corrected amplitude unreliable; in any case, agreement is not expected in this region because of the non-linearity between changes in V_f and changes in the electron density. The small value of the corrected amplitude at $\rho_c/R = 0.31$ probably represents a shortage of electrons which fulfil the dual requirement of fairly high perpendicular velocity ($\frac{1}{2}mv_1^2 > 8 \text{ eV}$) and high axial velocity ($\frac{1}{2}mv_z^2 \gtrsim 16 \text{ eV}$).

(c) The amplitude was fairly dependent on pressure. It decreased by a factor of 2 or 3 when the pressure was increased by an order of magnitude. It would be expected to approach zero as the electron mean free path becomes comparable with Λ_z .

(d) The amplitude depended only slightly on the discharge current. It increased by 10% as the current was reduced from 9 to

0.7A. A few measurements were also made in a hot cathode discharge of a few mA, with the cathode situated in the main horizontal tube. A periodic spatial variation of V_f was clearly observed at 10 mA but its existence at 2 mA was questionable. No attempt was made to compare the measurements of Λ_z at these very low discharge currents with those in the pool cathode discharge.

(11) Damping

The word "damping" is not used here entirely in the usual sense of energy dissipation; to a large extent it describes simply the averaging of the phase of helical motion of the electrons, owing to the spread in their velocities. It may be represented approximately by the expression $\exp(-\beta\Lambda_z)$.[⊕] Since $\beta\Lambda_z$ changes appreciably with z it has been measured only in the range $0.5\Lambda_z < z < 1.5\Lambda_z$. Many of the V_f curves obtained had $\beta\Lambda_z$ lying in the range 0.3 to 0.6.

The quantity $\beta\Lambda_z$ was investigated briefly as a function of r at constant B_z , and as a function of B_z when $r = 0$. No clear pattern emerged at constant B_z except that the lowest value of $\beta\Lambda_z$ occurred just inside or just outside the dark region. In the case of the 3 cm disc with $\rho/R = 0.1$, the damping was large at radial distances into the wake greater than 3ρ , as shown in fig. 5(c).

The damping at the axis of the wake varied with ρ/R as shown in fig. 6. It was fairly constant at low values of ρ/R and V_f amplitude, and increased rapidly at $\rho/R > 0.35$, where the V_f amplitude lay in the range $1.6 T_e$ to $2T_e$ and where an increasing proportion of electrons from well outside the dark region were able to reach the axis.

(12) Phase

When the probe tip was moved axially from $z = 0$, well inside the dark region, an upward (more positive) peak was the first to appear, at a distance $z \ll \Lambda_z$. This effect is shown in fig. 2. The curves of fig. 3 appear to contradict this observation, but this is due to the starting of the probe run at $z = 2$ or 3 mm, which is an appreciable fraction of Λ_z .

The behaviour of V_f at $z \ll \Lambda_z$ outside the dark region was not

[⊕] β is the reciprocal of the damping length.

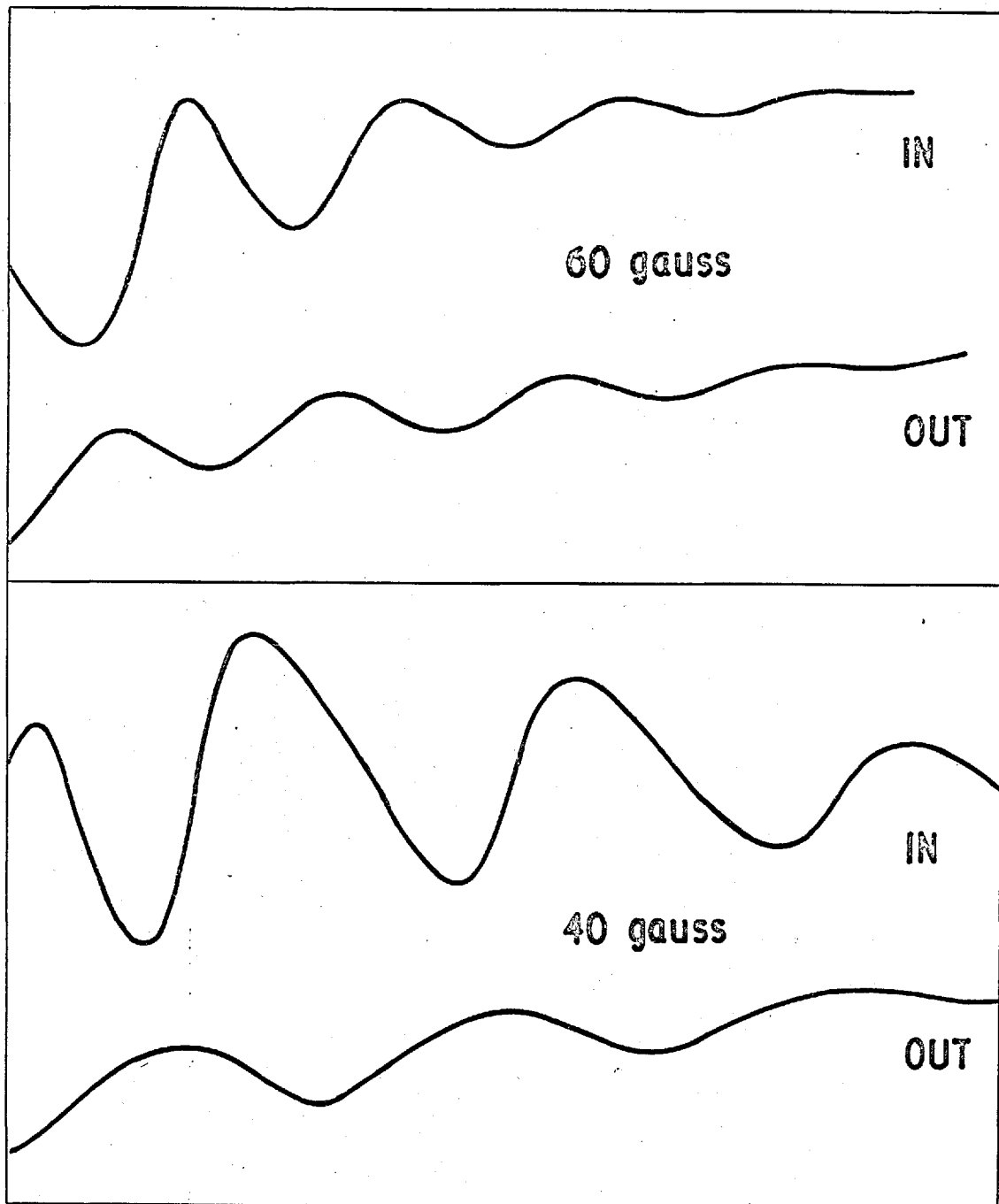


FIG 7 V_f versus z inside and outside dark region.

as consistent as that inside, but at larger values of z the variations were approximately out of phase with those inside. This is illustrated in fig. 7 in which the "in" and "out" curves alternately approach and recede from one another. Where they approach one another, the peaks do not coincide exactly but are displaced by a small fraction of a period; this displacement persists throughout each pair of "wave trains". Where they recede from one another, the peaks are displaced to a greater extent because of the large asymmetry of the peaks inside the dark region.

(13) Shape

Two points are noted in connection with the shape of the V_f variations. Firstly, the upward peaks inside the dark region have smaller widths than the downward peaks at low values of B (less than about 30 gauss according to fig. 2). Secondly, the upward peaks inside the dark region have a larger slope on the side nearer the obstacle. The same usually applies to the downward peaks of curves outside the dark region, but their asymmetry is less.

PERIODIC SPATIAL VARIATIONS OF PROBE POTENTIAL V_a .

(14) In the observations of the probe potential V_a ($\neq V_f$), the probe was connected via a 1 megohm resistor and battery to earth. It was made to draw a negative or positive current of a few microamperes from the plasma. Periodic spatial variations were observed in the probe potential V_a which represented variations in the current drawn by the probe. Curves obtained at $V_a \sim V_f - 8$ volts, where the absolute values of V_a and V_f were measured close to the obstacle, are given in fig. 8.

When the probe was biased several volts more negative than V_f , the variations in V_a were of much smaller amplitude and were less damped than those in V_f . This is clear from a comparison of the curves in figs. 2 and 8 at $B_z \approx 40$ gauss. The amplitudes of these V_f and V_a curves were 4 and 0.2 volts, and the average values of

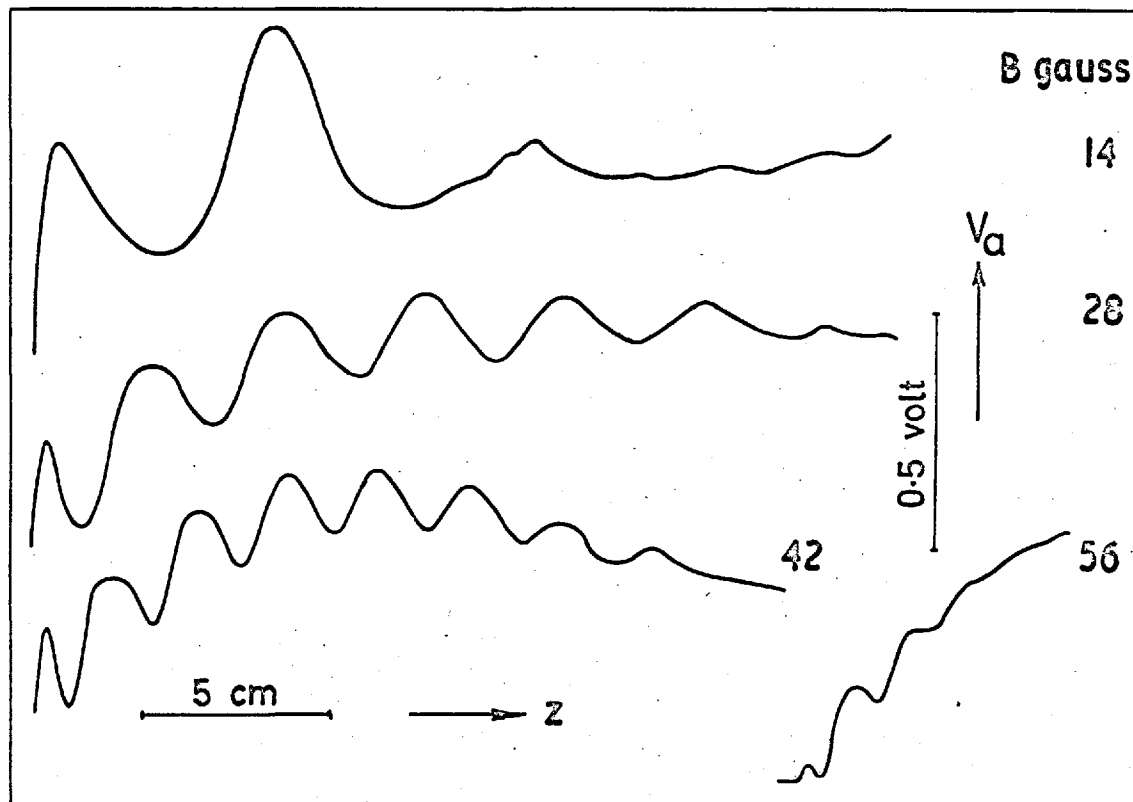


FIG 8 Variation of probe potential V_a along axis of wake due to 12 mm disc. $V_a = V_f - 8$ volts, $I_D = 5$ A, $p = 0.4$ mtorr.

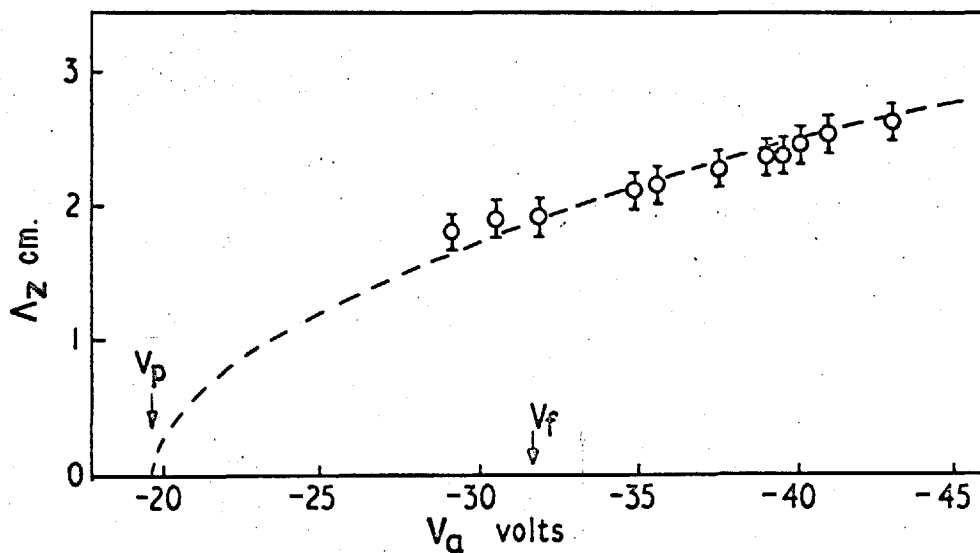


FIG 9 Spatial period Λ_z versus probe potential V_a . 12 mm disc, $B_z = 42$ gauss, $I_D = 5$ A, $p = 0.2$ mtorr. Potential measured with respect to anode.

$\beta\Lambda_z$ over the entire "wave train" were 0.55 and 0.2 respectively.

A significant feature of the V_a variations is the change in shape of the peaks as B_z is increased, especially the first two or three peaks in each train. At the lowest value of B_z the peaks are sharper upwards than downwards (as in V_p), and vice versa for the larger values of B_z . At $B_z = 28$ gauss, where $\rho/R = 0.37$, the upward and downward peaks have approximately the same width.

Fig. 9 shows the variation of Λ_z with V_a , where V_a is measured close to the obstacle, at a magnetic field of 42 gauss. Λ_z increased as V_a became more negative, i.e. as the axial velocity required by the electrons in order to reach the probe increased. At $V_a < V_f - 11$ volts, where the probe current consisted almost entirely of ion current, no periodic spatial variations were observable in the wake. The dashed parabolic line in fig. 9 represents the variation of the helical pitch of electrons which have an axial velocity given by the relation $\frac{1}{2}mv_z^2 = e(V_p - V_a)$.

IIIB. PERIODIC SPATIAL VARIATIONS OF PLASMA PARAMETERS

(15) The variation of plasma parameters (density, potential, electron temperature) in the wake was investigated by means of two series of probe current-voltage curves, using the probe CP on the anode side of the obstacle. The curves of one series were plotted from Avometer readings of current and voltage when the probe was placed at successive positions along the z direction, 1 mm off the axis of the 6 mm disc. In the other series, both the radial and the axial positions of the probe were varied in the dark region produced by the 12 mm disc, and values of $\log I$ and V were plotted directly on the X-Y pen recorder with the aid of the probe display unit. Both series of current-voltage curves were obtained with $B_z = 42$ gauss and $p \approx 0.4$ millitorr. Throughout both series the discharge current, pressure and magnetic field showed little tendency to wander; the discharge was particularly stable.

(16) Concepts underlying the probe current-voltage curves

In the first series of current-voltage curves the voltage V was varied from values sufficiently negative to prohibit the collection of electron current by the probe, as for example at $V < V_p - 15$ volts in fig. 10, to values more positive than the local plasma potential V_p , as in fig. 11. The value of the electron current I_e to the probe at any particular voltage was obtained by adding to the net probe current the corresponding value of the ion current. The latter was obtained from curves such as those in fig. 10 by extrapolating the linear portion to more positive potentials.

The ion current in fig. 10 does not reach a saturation value when the probe potential goes increasingly negative, but rises because of the growth in thickness of the ion sheath between probe tip and plasma, and therefore of the effective collecting area of the probe as far as the ions are concerned. The sheath thickness x may be calculated from the formula:

$$x^2 = \frac{(V_p - V)^{3/2}}{9\pi j_+ (m_i/2e)^{1/2}} \quad (\text{from ref. (17)}) \quad (1)$$

where $V_p - V$ and the random ion current density j_+ are in electrostatic units. Under the conditions of the present experiments, a voltage difference of 20 volts produces an ion sheath with a thickness of the same order of magnitude as the diameter of the probe tip.

All the ions impinging on the sheath are collected by the probe, but, as far as the electrons are concerned, those which reach the probe must fulfil the condition that their total kinetic energy is $\geq e(V_p - V)$. A fairly large fraction of these electrons enter the sheath either parallel to, or at a small angle to, the z direction and therefore fulfil the condition $\frac{1}{2} m v_z^2 \geq e(V_p - V)$. In order to simplify the discussion in section IVA, this condition will be assumed

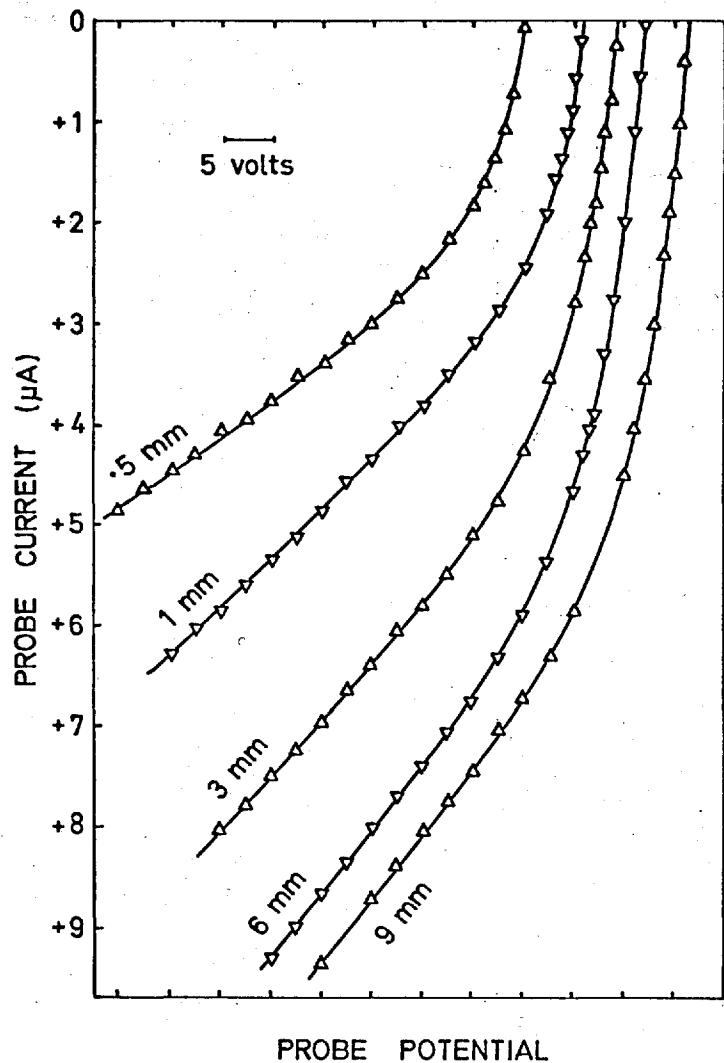


FIG 10 Positive current to probe in wake of 6 mm disc at different axial distances. $B_z = 25$ gauss, $I_D = 6$ A, $p = 0.4$ mtorr. The curves are successively displaced by 5V.

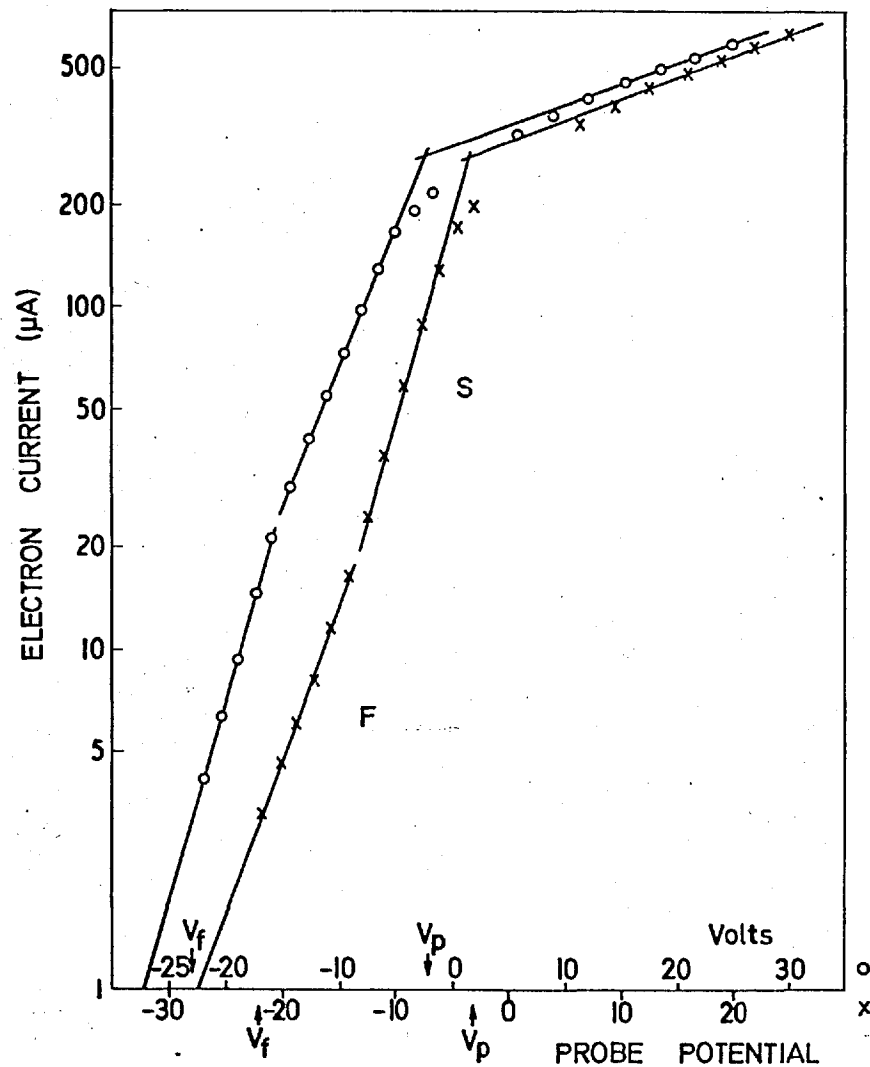


FIG 11 Electron current to probe in wake of 6 mm disc. $B_z = 42$ gauss, $I_D = 9$ A, $p = 0.4$ mtorr. Curve o : $z = 8$ mm, $T_S = 5.2$ eV, $T_F = 3.8$ eV. Curve x : $z = 12$ mm, $T_S = 3.5$ eV, $T_F = 5.3$ eV.

to apply to all the received electrons. When V goes more positive than V_p , an electron sheath is formed which leads to the non-saturation of electron current, as in fig. 11.

If the velocity distribution of the electrons were Maxwellian the density of electron current to the probe, at voltages $V < V_p$, would be given by the expression

$$j_e = j_s \exp [-e(V_p - V)/kT_e] \quad (2)$$

where

$$j_s = n_e e \bar{v} / 4 = n_e e (kT_e / 2\pi m_e)^{1/2}$$

The relationship between I_e and probe potential V would then be of the form $\log I_e = \text{constant} + eV/kT_e$, and T_e would be obtained from the slope of the $\log I_e$ versus V curve. The examples in fig. 11, selected from the first series of current-voltage curves, illustrate comparatively large deviations from the Maxwellian condition in the lower decade of current. Similar but smaller changes of slope occurred in most of this series of curves. The "temperatures" corresponding to the slopes in the upper and lower decades are labelled T_S and T_F , and the values in electron-volts are given below the figure. The suffix S refers to the main body of slower electrons and F to the top few per cent of faster electrons. Because of the comparatively large electron drift velocity, T_S exceeds $\frac{1}{2} \bar{v}^2$, where \bar{v}^2 is the mean square random velocity of the electrons, as shown by Allen and Magistrelli⁽¹⁵⁾. T_S will therefore be called the "apparent electron temperature".

The upper intersection point on each current-voltage curve is assumed to mark the plasma potential V_p . The electron number density n_e may be obtained approximately from the electron current I_s at this point and the temperature T_S , using the expression given above for j_s .

(17) First series of probe current-voltage curves

The analysis of the first series of current-voltage curves

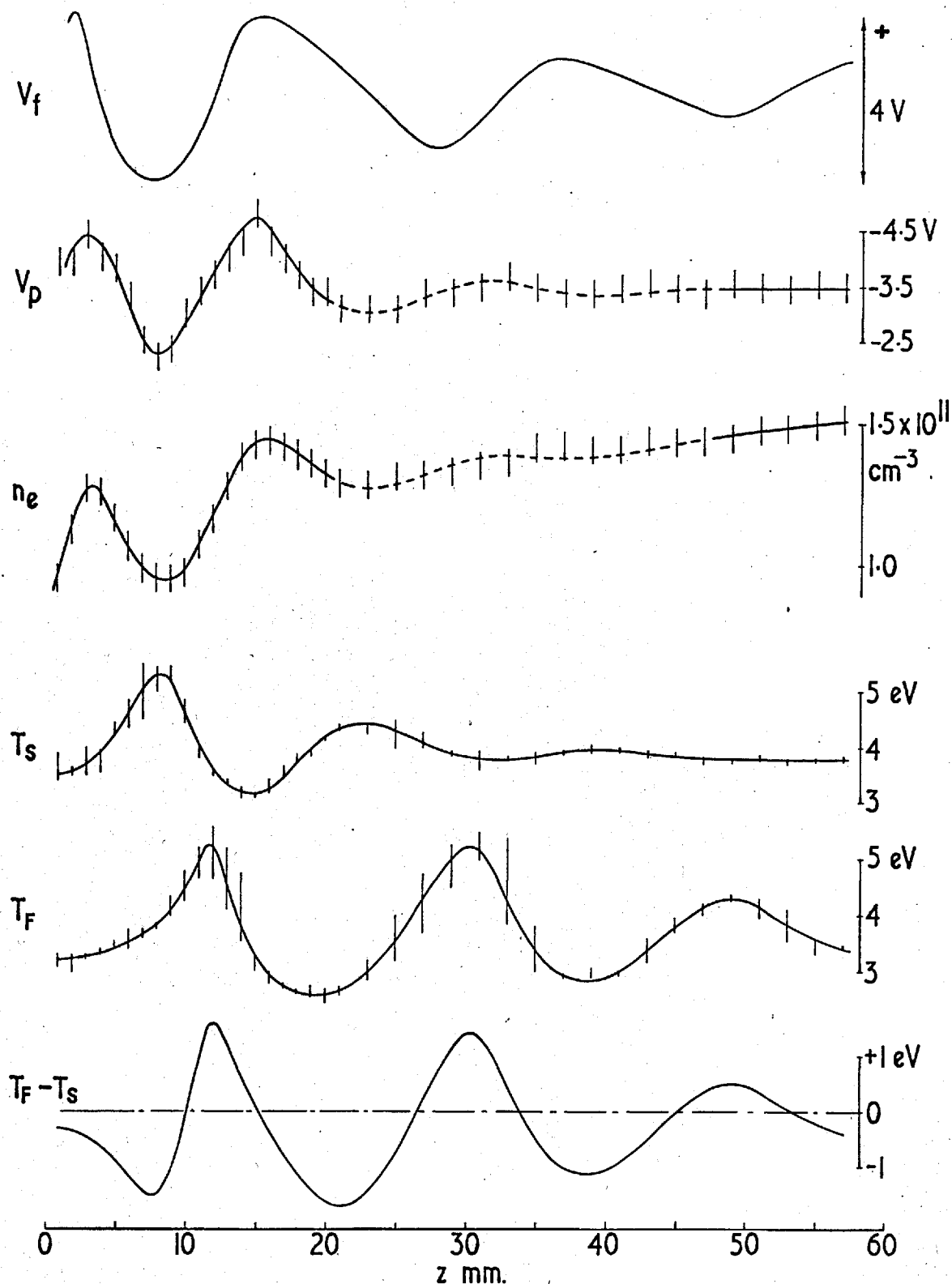


FIG 12 Variation of plasma parameters along wake of 6 mm disc, 1 mm off axis. $B_z = 42$ gauss, $I_D = 9$ A, $p = 0.2$ mtorr. Vertical lines represent errors in the computation of the parameters from the probe characteristics.

revealed periodic spatial variations in the parameters V_p , n_e , T_S and T_F . These are shown in fig. 12 together with the variations of V_f along the same line in the wake. The vertical lines represent errors in measuring and computing the parameters from the experimental curves. Any systematic errors due to electron drift or other factors are not important because it is only the variation in these quantities that is of interest.

The three parameters V_p , n_e and T_S are closely linked in their variations. Despite the uncertainty in the curves of V_p and n_e at values of z exceeding 25 mm, it appears that the peaks of the three parameters approximately coincide. The distance z was measured from the surface of the disc; $(z + 1)$ mm represents the distance from the maximum cross-section of the disc. The first minimum in V_p occurs at 4 mm from this cross-section and the distances between the succeeding maxima and minima are approximately 5, 7, 8 and (perhaps) 9 mm respectively. The spatial period λ_z thus increases with z from an initial value of about 9 mm to a final value, hardly discernible, of about 17 mm.

Several other features are noted in fig. 12: the heavy damping of the V_p , n_e and T_S curves ($\beta\lambda_z = 1.8 \pm 0.5$ in the latter curve); the approximate coincidence of the first three peaks in V_f with those in V_p ; the value of Λ_z in the V_f variations (21 mm); the sharpness of the maxima in the T_F and $T_F - T_S$ curves and the spatial period of these curves (18.5 mm).

(18) Second series of probe current-voltage curves

In the second series of probe current-voltage curves, examples of which are given in fig. 13, the conversion of I to $\log I$ by the probe display unit was not sufficiently accurate to warrant as detailed an analysis as in the first series. Despite the non-linearity of such a large portion of each curve and the instability in the probe current over certain regions of potential, regular variations of V_p were detectable with maximum amplitudes of ~ 3 volts. These are given in fig. 14(a). The large downward slope of the median line in the

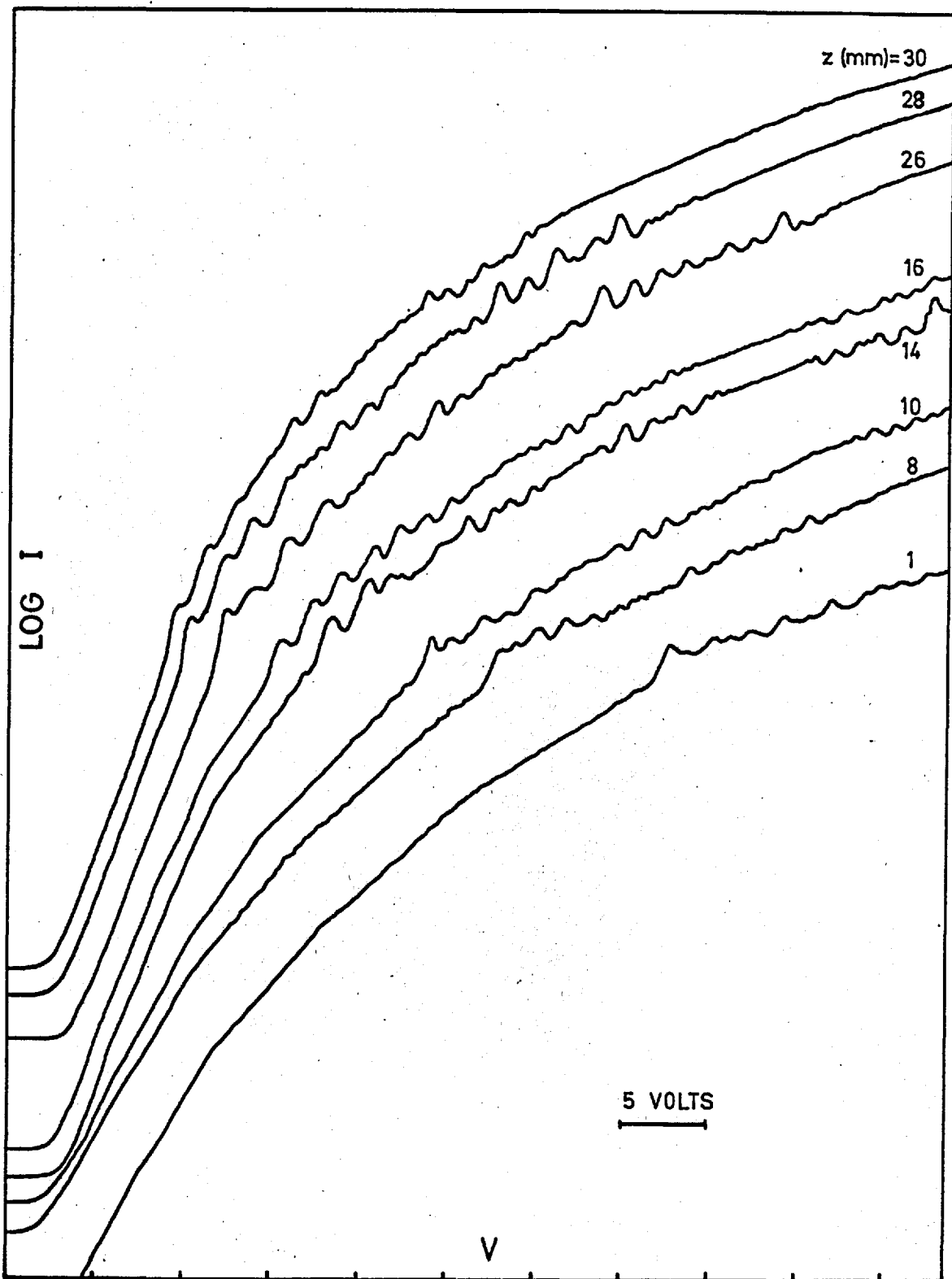


FIG 13 Current-voltage characteristics at $r = 2$ mm and different values of z , obtained by means of Probe Display Unit. The curves start at the left from different "zero" lines.

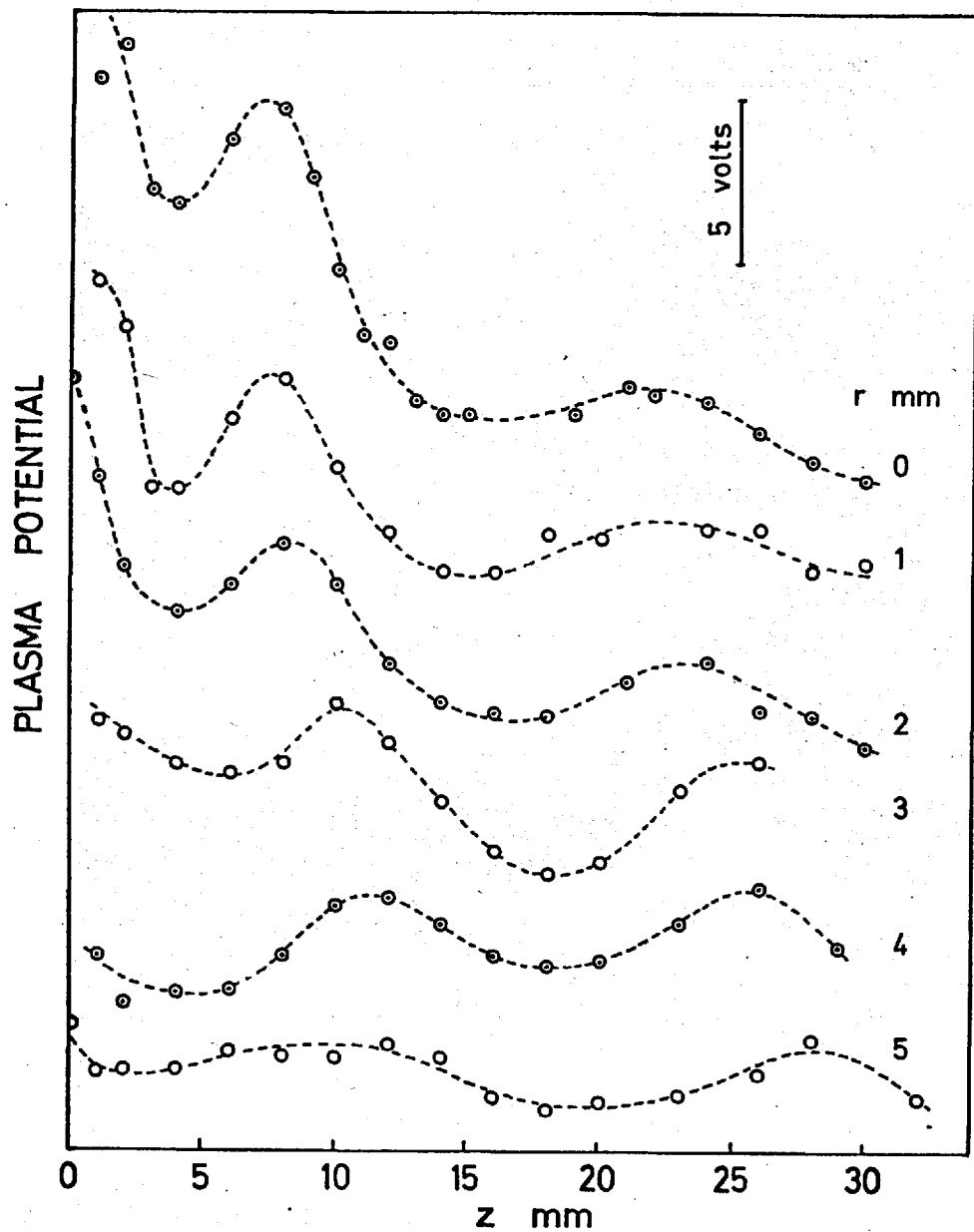


FIG 14(a) Variation of plasma potential V_p along wake of 12 mm disc at different distances from axis. $B_z = 42$ gauss, $I_D = 3$ A, $p = 0.3$ mtorr.

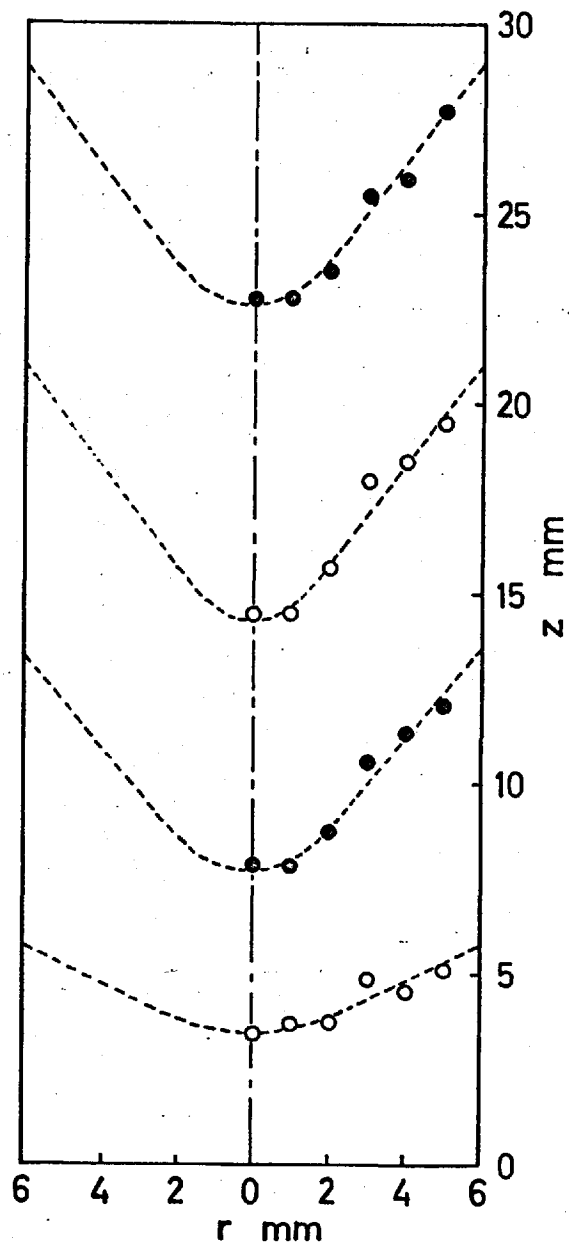


FIG 14(b) Positions of the maxima (●) and minima (○) in the curves of V_p versus z .

upper four curves is thought to be introduced by the probe display unit. These V_p curves are shown inverted relative to the V_p curve in fig. 12. The positions of the V_p maxima and minima at $r = 0, 1, 2$ mm are in good agreement with those in fig. 12.

Fig. 14(b) shows the positions (z, r) of the maxima and minima in V_p . These form a series of "wave fronts". The wave fronts at $z > 6$ mm define an axial spatial period $\lambda_z = 15$ mm and a radial spatial period λ_r which is approximately equal to the diameter of the dark region. The normal to these wave fronts makes an angle of about 50° with the negative z direction.

(19) Radial variation of plasma potential

A number of current-voltage curves were also obtained at various distances from the axis of the 12 mm disc, 2 mm from the disc, at a field of 42 gauss and a discharge current of 5A. These showed that the plasma potential at this value of z was about 3 volts more positive inside the dark region than outside. The change of potential occurred mainly at the edge of the dark region over a distance of about 2ρ .

CHAPTER IV

DISCUSSION AND INTERPRETATION OF RESULTS

IV A. PERIODIC SPATIAL VARIATIONS OF PROBE POTENTIAL

(20) The periodic spatial variations of V_f and V_a are associated with the helical motion of the electrons. If the helix described by an electron lies partly inside and partly outside the geometrical shadow as the electron approaches the obstacle, the electron will pass beyond the obstacle provided that its motion is of suitable phase. It is this phase selection by the obstacle which is responsible for the various periodic spatial variations in the wake.

In developing a model of the V_f and V_a variations it is convenient to allocate the symbol $n_e(\Delta V)$, where $\Delta V = V_p - V_f$ or $V_p - V_a$, to the density of those electrons at any point in the wake which would reach a probe (whose potential was V_f or V_a) situated at that point. It is assumed that these electrons have velocities v_z such that $\frac{1}{2} m v_z^2 \geq e \Delta V$ and constitute a flux in the z direction which will be written as $i_{ez}(\Delta V)$; because of the comparatively large thickness of the ion sheath at the probe, this limitation on v_z is only approximately valid. The electron current received by the probe will be written as $I_e(\Delta V)$ and the ion current as $I_+(\Delta V)$.

Let us consider the dependence of $I_e(\Delta V)$ on z in the case of a floating probe where $\Delta V = V_p - V_f$ and $I_e(\Delta V) = I_+(\Delta V)$. It is evident from the curves of positive current versus probe potential that at the larger values of z the ion current corresponding to the floating potential is roughly constant. A variation of 3 volts in V_f corresponds to a change of less than 10 % in $I_+(\Delta V)$. In the following qualitative explanation of the V_f variations we shall assume $I_+(\Delta V)$, and therefore $I_e(\Delta V)$, to be independent of z .

V_f VARIATIONS

(21) Response of floating probe to electron density variations

We shall consider first how the electron flux $i_{ez}(\Delta V)$ varies with z at a constant value of ΔV . The variation with z of the

number density and current density of electrons lying in a small range of axial velocities, v_z to $v_z + dv_z$, is to a first approximation sinusoidal (see fig. 17), with a spatial period equal to the helical pitch of these electrons, $2\pi v_z / \omega_{ce}$ (where ω_{ce} is the electron cyclotron frequency). The superposition of the motions of all the electrons with $\frac{1}{2}mv_z^2 \geq e\Delta V$ would then lead to a damped sinusoidal waveform for both the density $n_e(\Delta V)$ and flux $i_{ez}(\Delta V)$ of these electrons. Such waveforms are drawn qualitatively in fig. 15 for several values of $\Delta V/T_S$. As the probe reaches any position z the floating potential assumes the value at which $I_e(\Delta V)$, or $i_{ez}(\Delta V)$, remains equal to a particular constant value. The corresponding points a to e on the $i_{ez}(\Delta V)$ and $\Delta V/T_S$ curves illustrate this behaviour.

(22) Shape

It is clear in fig. 15 that the positions of the lower peaks in $\Delta V/T_S$ are further to the right than the mid points between the upper peaks, owing to the increase of the spatial period of $i_{ez}(\Delta V)$ with ΔV . This is the main reason for the asymmetry in the observed V_f peaks.

(23) Spatial period

It is also noted in fig. 15 that the spatial period Λ_z of the $\Delta V/T_S$ curves lies between that of the top and that of the bottom $i_{ez}(\Delta V)$ curve. It is approximately equal to the spatial period of the $i_{ez}(\bar{\Delta V})$ curve where $\bar{\Delta V}$ is the average value of ΔV in the $\Delta V/T_S$ curve. Λ_z may be calculated from the value of $\bar{\Delta V}$ in any of the V_f curves and compared with the observed value. In the top curve of fig. 12 for example, $\bar{\Delta V} = 17 \pm 1$ volts ($= 4.5 T_S$) and $B_z = 42 \pm 2$ gauss. In this case the average axial velocity \bar{v}_z of the electrons is given by the expression $1.07(2e\bar{\Delta V}/m)^{1/2}$, which leads to a value for the spatial period, $2\pi\bar{v}_z/\omega_{ce} = 2.1 \pm 0.2$ cm. This is in agreement with the observed value of Λ_z which is also 2.1 ± 0.2 cm.

(24) Amplitude, dependence on ρ/R

The V_f amplitude at the axis of the wake was compared in fig. 6 with

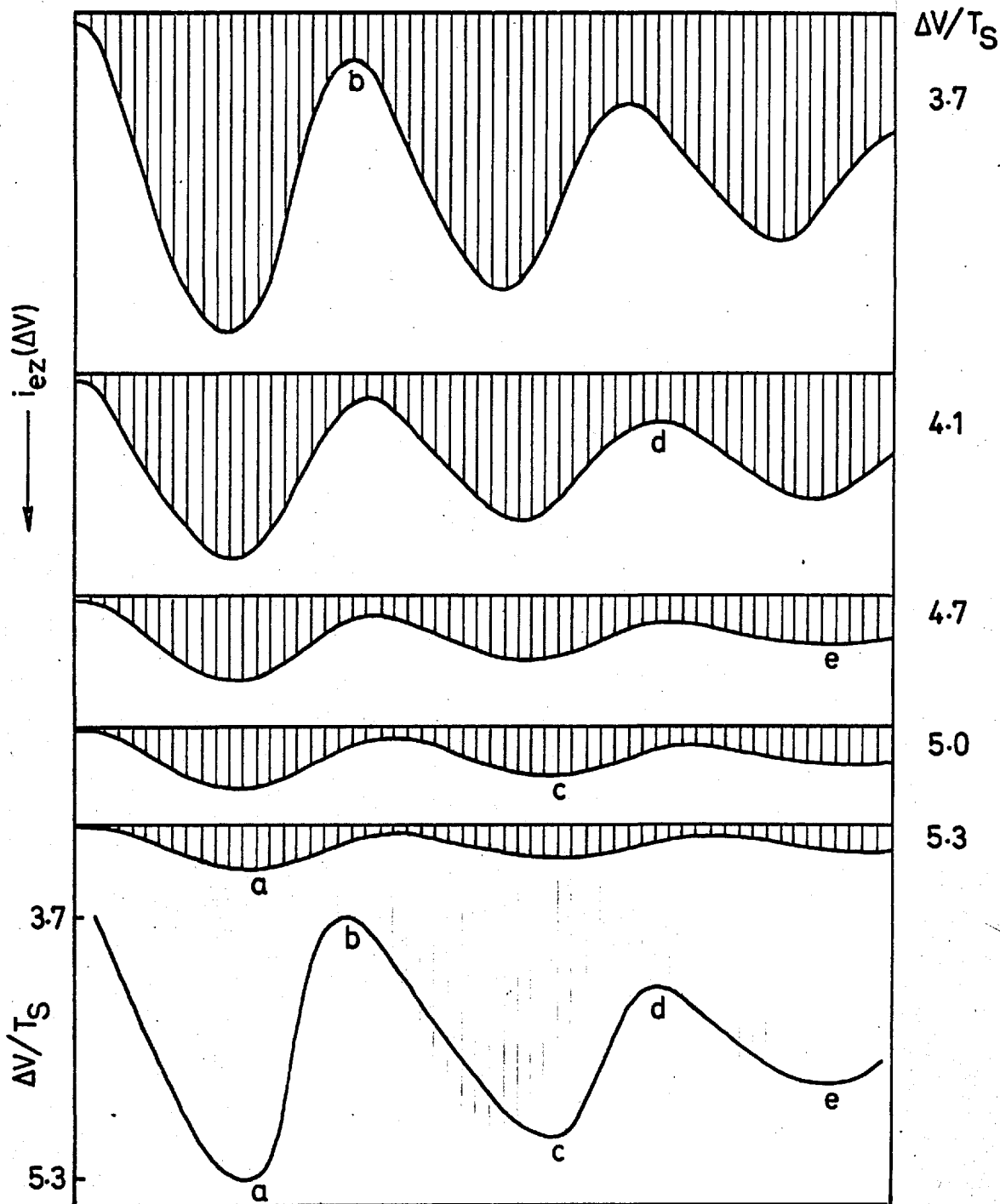


FIG 15. Curves showing relation between spatial variations of $i_{ez}(\Delta V)$ and $\Delta V/T_S$ (not drawn to scale). The $\Delta V/T_S$ curve is inverted to correspond to observed V_f curves and the values of $\Delta V/T_S$ have been chosen arbitrarily. Points a, b, c, d, e represent the same value of $i_{ez}(\Delta V)$.

the term $\exp(-R^2/4\rho^2)$, where ρ is the mean Larmor radius and R is the obstacle radius. It was measured as the difference between the first maximum V_{f1} and the first minimum V_{f2} . After allowance is made for damping and increase of effective Larmor radius (see p. 24) $V_{f1} - V_{f2}$ is proportional to $\exp(-R^2/4\rho^2)$ over the range of ρ/R from 0.35 to 1.3.

Applying equation (6) (p. 49) to the present wakes we see that the maximum number density, along the axis, of electrons with a particular value of v_z and a Maxwellian distribution of v_1 is $\sim n_0 \exp(-R^2/4\rho^2)$, where n_0 is the density of such electrons in the undisturbed plasma. It follows that the maximum density n_m , along the axis, of all electrons with $\frac{1}{2}m v_z^2 \geq e\Delta V$ is proportional to this exponential term. Thus it appears that over the range of ρ/R mentioned above, the corrected value of $V_{f1} - V_{f2}$ is proportional to n_m .

The quantities $V_{f1} - V_{f2}$ and n_m must clearly go to zero at the same value of ρ/R . This condition lends support to the assumption that the effective values of the Larmor radius in the wake (near the obstacle) are larger than those calculated from the value of T_e in the undisturbed plasma. Although some measure of qualitative agreement between n_m and the corrected values of $V_{f1} - V_{f2}$ is to be expected it is not clear why the two quantities should be proportional to one another over such a wide range of ρ/R .

(25) Amplitude, dependence on r

Two features are prominent in the dependence of the V_f amplitude on radial position in the wake: (i) the low value of the amplitude outside the dark region compared with that inside, and (ii) the occurrence of a maximum in amplitude at a distance of two or three times ρ from the edge of the dark region, both inside and outside. The first feature is due simply to the difference in density of the background plasma (in which the phase of electron helical motion is random) inside and outside the dark region. Of the electrons reaching the probe when the latter is situated outside this region, the fraction that has undergone phase selection by the obstacle is small. The second feature is connected with the degree of phase alignment of the electron helical motion effected by the obstacle on (a) those electrons whose helical paths lie almost entirely inside the geometrical shadow, and (b) those whose paths lie almost entirely outside this region. The electrons in (a) have a high degree of

phase alignment on entering the wake and produce the maximum amplitude in $n_e(\Delta V)$, and therefore in V_f , at a distance into the dark region equal to the most probable value of their Larmor diameter ($\sim 2\rho$). The observed distance (3ρ) is larger than this because of the increase in effective Larmor radius suggested by fig. 6. The electrons in (b) have random phase except for a sharply defined gap in the range of phase, left by those which strike the obstacle. The effect of the "helical motion" of this "gap" (cf. concept of "holes" in semi-conductors), together with the complementary effect of partially aligned electrons whose paths lie further into the geometrical shadow, would be expected to reach a maximum at some distance outside the geometrical shadow. The "gap" would have its greatest effect on V_f at a distance $\sim 2\rho$.

(26) Damping

The damping term $\beta\Lambda_z$ of the V_f variations along the wake axis is shown in fig. 6 to increase rapidly with Λ_z (or ρ/R) at values of ρ/R exceeding 0.35. It appears from the large rate of increase that $\beta\Lambda_z$ may be divided into three parts: (i) a component which is approximately independent of Λ_z due to the spread in velocity of the received electrons and consequent averaging of phase of their helical motion; this produces a damping of the variations in $n_e(\Delta V)$ and therefore, to zero order, of the V_f variations; (ii) terms containing ρ/R (or Λ_z) to first order and higher orders, due to the increasing non-linearity between V_f and $n_e(\Delta V)$ as ρ/R increases, and (iii) a component which is proportional to Λ_z , due to electron-neutral collisions ($\Lambda_z \approx 0.5 \times$ electron mean free path at $\rho/R = 0.63$ and $p = 0.5$ millitorr).

The damping of $n_e(\Delta V)$ due to the averaging effect alone is illustrated, for the condition $\rho/R = 1$, by the theoretical curve in fig. 16. This curve represents the variation with z of the quantity

$$\frac{n_e(z)}{n_{e0}} = \int_{v_1}^{v_2} f(v_z) \exp \left\{ - \frac{R^2}{4\rho^2 \sin^2 \left\{ \frac{\omega c z}{2v_z} \right\}} \right\} dv_z \quad (3)$$

in which the limits of integration are given by $\frac{1}{2}mv_1^2 = 4T_S$ and $\frac{1}{2}mv_2^2 = 6.8T$ and $f(v_z)$ is assumed to ^{represent} have a Maxwellian distribution. (cf. equation (6)). These two limits have been chosen arbitrarily.

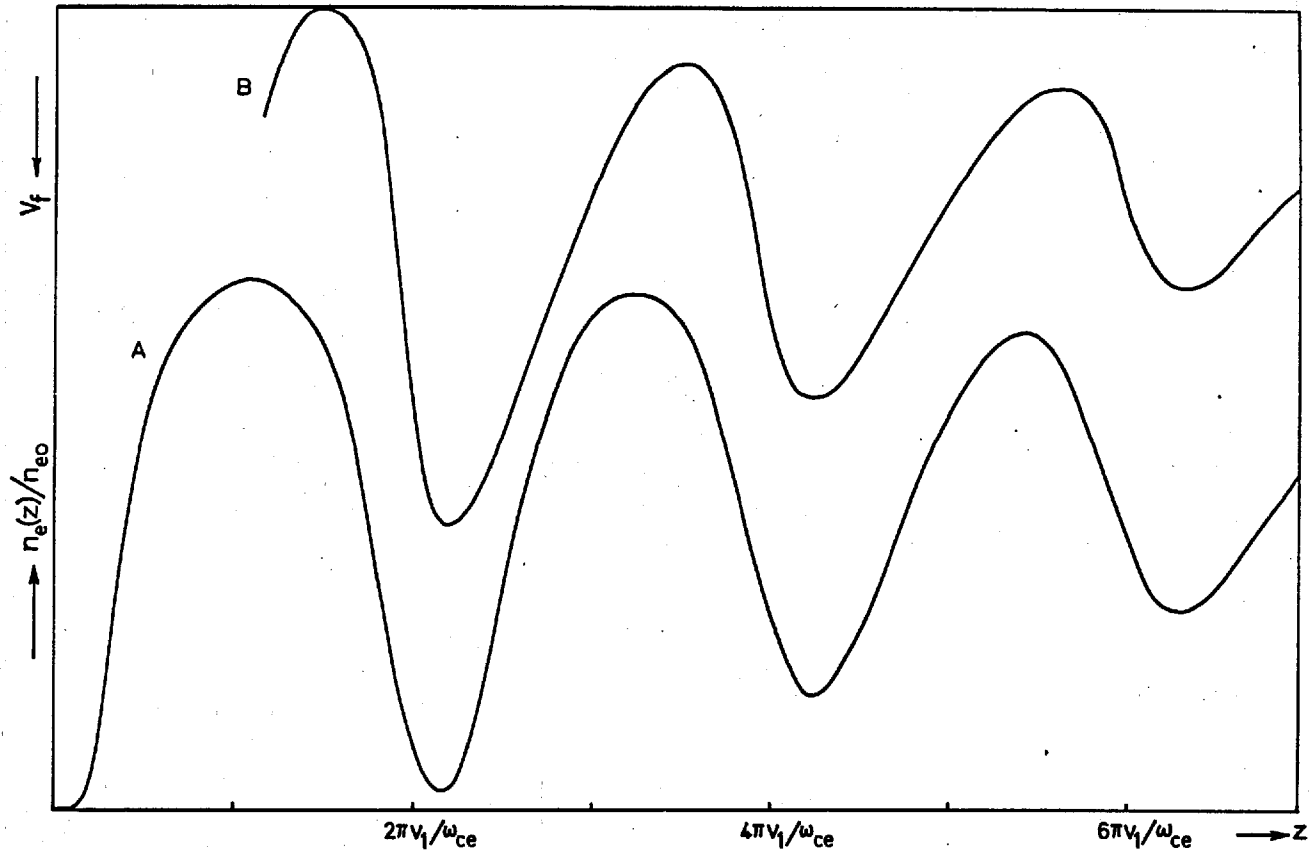


FIG 16 Curve A: $n_e(z)/n_{e0}$ versus z (theoretical). Curve B: V_f versus z (third curve of fig. 2, page 17, drawn on a larger scale).

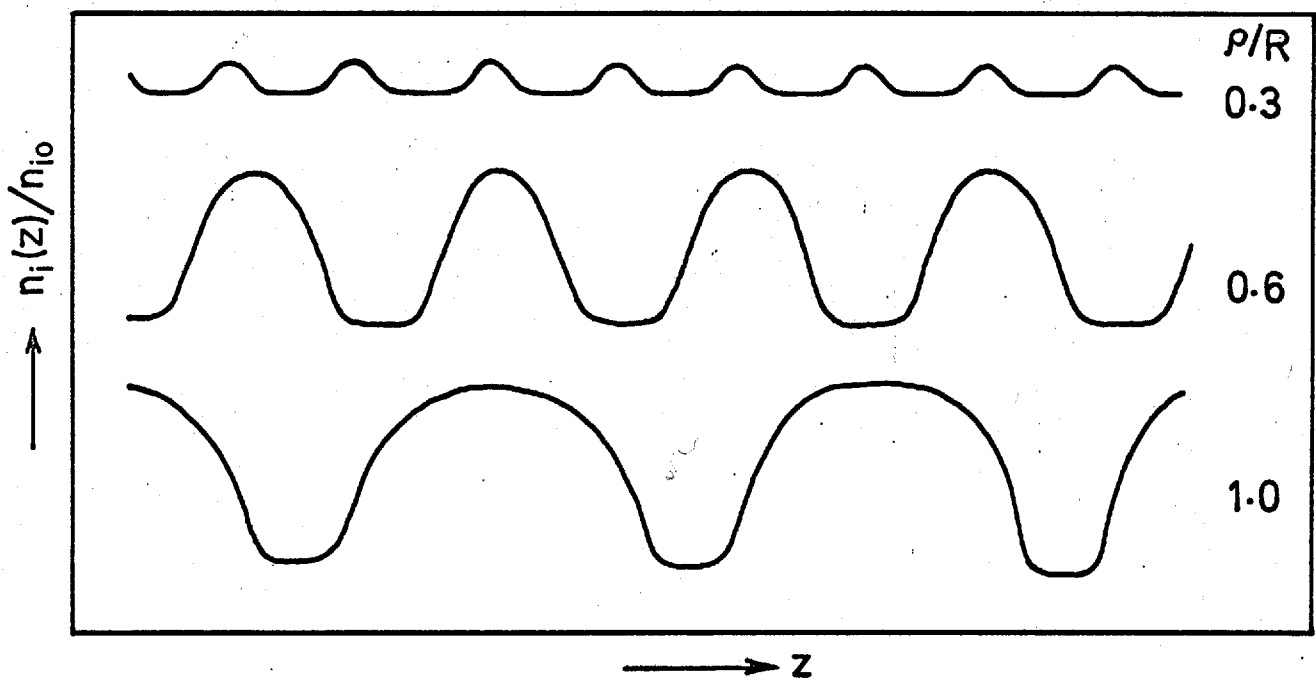


FIG 17 Variation of ion density (from equation 7) along axis of satellite wake at different values of ion Larmor radius.

The exponential expression is obtained from ref. 6 and is described in section (32). It is drawn in fig. 17 as a function of z for three values of ρ/R . The value of $\beta\Delta_z$ in the theoretical $n_e(\Delta V)$ curve is 0.25 which is somewhat less than the lowest values of $\beta\Delta_z$ in the V_f curves (fig. 6). The third curve of fig. 2 is included in fig. 16 for a comparison of damping and asymmetry of peaks.

(27) Phase

It was shown in fig. 7 that the V_f curves outside the dark region are approximately out of phase with those inside. At any position z where there is a maximum density of electrons of given velocity v_z inside the dark region, there is a corresponding "gap" in the density of such electrons outside the dark region; these produce opposite changes in V_f . Any electrons travelling partly inside and partly outside this region will obviously reinforce this effect.

It was noted in fig. 7 that where the "in" and "out" curves approach one another there is a small relative displacement of the peaks. This is connected with the fact that the two curves involve two different sets of electrons, those travelling mainly inside and those mainly outside the dark region. These would be differently affected by the radial and axial space charge fields near the obstacle, but the exact mechanism is not clear.

(28) Positive column instability

The V_f curves exhibit two other features which are probably due to an instability of the positive column. These are the kinks in the $K_z - B_z$ curves of fig. 4, and the increasing slope of the median lines of the curves in fig. 3 as B_z increases.

Little and Jones have observed a convective instability of the low pressure mercury column when B_z exceeds 100 gauss (private communication). At such fields they found that two photomultipliers, at the same axial position but situated to receive light from above and below the axis of the column respectively, transmitted out-of-phase components of a certain resonant frequency. Also the noise in the photomultiplier signals was greater by an order of magnitude than that at the lower values of B_z .

We may add to this the evidence of H.S. Robertson who measured the change of axial electric field E_z , as B_z increased, in a cesium positive column at a pressure of about 70 millitorr. There was a sharp rise in E_z at about 100 gauss which marked the onset of a helical instability. After a slight decrease there was a further sharp rise in E_z at about 200 gauss, accompanied by several changes of multiplicity and pitch of the helix, and E_z then continued to rise fairly steeply as B_z increased to 500 gauss.

An instability of the plasma column, with its associated plasma noise and turbulence, would be expected to cause a general decrease of electron velocities and a consequent increase of K_z . The second kink in the mercury curves of fig. 4, at about 160 gauss, may be associated with the second increase of E_z observed by Robertson. The upward slope of the V_f curves in fig. 3 at $z > 1$ cm correspond to values of E_z which are in excess of the value at low B_z approximately 0.1 V/cm, and which increase as B changes from 200 to 500 gauss.

V_a VARIATIONS

(29) Comparison with V_f variations

Only the curves at very negative values of V_a will be discussed, such as those in fig. 9. It is evident that these are of much smaller amplitude and are in general less damped than the V_f curves. They have the advantage over the V_f curves that they are associated with a portion of the tail of the electron velocity distribution which is far less variable and contains a smaller range of velocities. There were two reasons why the V_a curves were investigated only briefly: firstly, most of the V_f curves were obtained before the V_a curves were studied and their merits understood, and secondly it was considered that a sufficiently clear picture of the distribution of fast electrons in the wake could be formed from the V_f variations already observed.

We consider first the contrast between the V_a and V_f curves as far as the velocity distribution is concerned. No V_a variations are observed at $V_a < V_f - 11$ volts, which sets an upper limit of $(V_p - V_f + 11)$ or $7.3T_S$ on the value of $\frac{1}{2}mv_z^2$. In the V_a curves of fig. 8, the magnitude

and variation of $\Delta V (= V_p - V_a)$ are respectively $6.3T_S$ and $0.1T_S$ (the latter quantity is applicable when $z > 1.5\Lambda_z$). In the V_f curves on the other hand, the average value of ΔV in a "wave train" is about $4.5T_S$ and the variation of ΔV at $z > 1.5\Lambda_z$ is of the order of T_S .

(30) Relationship between V_a and the density $n_e(\Delta V)$

The very negative V_a curves in the region $z > 1.5\Lambda_z$, where changes of ΔV are small, represent the variations in the flux of electrons $i_{ez}(\Delta V)$ and in the corresponding density $n_e(\Delta V)$. In the V_a curves of fig. 8 the electrons received by the probe have values of $\frac{1}{2}mv_z^2$ lying between $6.3T_S$ and $7.3T_S$, assuming always that comparatively few electrons reach the probe at large angles to the axis. Corresponding changes in V_a and $n_e(\Delta V)$ are then related by the equation

$$\delta V_a \approx RAe (12.6eT_S/m)^{\frac{1}{2}} \delta n_e(\Delta V) \approx \text{constant} \times \delta n_e(\Delta V) \quad (4)$$

where R is the resistance in the probe circuit and A is the probe area.

(31) Spatial period

The spatial period has been evaluated for the third V_a curve in fig. 8. The mean axial velocity of the received electrons is $\bar{v}_z = 1.04 (12.6eT_S/m)^{\frac{1}{2}}$ and the mean helical pitch is $2\pi\bar{v}_z/\omega_{ce} = 2.4 \pm 0.2$ cm. The observed value of Λ_z is also 2.4 ± 0.2 cm.

Damping

The damping term $\beta\Lambda_z$ depends to a large extent on the range of velocities of the electrons received by the probe, as discussed in section (26). The V_a and V_f curves at $\rho/R = 0.25$, for example, have $\beta\Lambda_z$ equal to 0.15 and 0.34 respectively. This difference must be due almost entirely to the difference in the velocity ranges concerned.

Shape

The remaining feature of note in the V_a curves of fig. 8 is the change in shape of the peaks as B_z increases. It is noted that the upward and downward peaks of the second curve ($B_z = 28$ gauss) have approximately equal widths, measured between the half-amplitude points.

The change of shape may be explained by means of detailed calculations concerning the spatial distribution of electrons with a given value of v_z . Such calculations have been made by Al'pert et. al. ⁽⁶⁾ for the ion distribution in a satellite wake in the ionosphere, and the results that are relevant to these experiments are described below.

COMPARISON OF PRESENT EXPERIMENTAL WAKES AND SATELLITE WAKES DESCRIBED BY AL'PERT, GUREVICH AND PITAEVSKII.

(32) Ion density in satellite wake according to Al'pert et. al.

These authors have treated various aspects of the wake produced by a spherical body moving rapidly through a plasma, both in the absence and in the presence of a magnetic field. The physical conditions assumed in their theory are described in the next section and are applicable to satellite wakes in the ionosphere. They show that in the presence of a magnetic field the wake contains periodic non-sinusoidal spatial variations of ion density along its length. When the field is perpendicular to the satellite velocity, the amplitude of the variations diminishes rapidly with increasing distance from the satellite. When the field and velocity are parallel (in the z direction), the amplitude is constant along the wake in the limit of zero spread in the ion velocity v_z and zero collision frequency.

When field B and satellite velocity v_0 are parallel, which is the condition relevant to the present experiments, the ion density at any distance r from the axis of the wake is given by the equation

$$\frac{n_i(r,z)}{2n_{i0}} = \exp \left[-\frac{r^2}{4\rho^2 \sin^2 \frac{\omega_{ci} z}{2v_0}} \right] \times \int_{u_1}^{\infty} u e^{-u^2} I_0 \left\{ \frac{ru}{\rho \left| \sin \frac{\omega_{ci} z}{2v_0} \right|} \right\} du \quad (5)$$

where n_{i0} is the unperturbed value of the ion density, ρ the Larmor radius, ω_{ci} the ion cyclotron frequency, $u_1 = (R/2\rho) \left| \sin(\omega_{ci} z/2v_0) \right|$ and I_0 is a zero order Bessel function of imaginary argument. This expression for $n_i(r,z)$ is represented qualitatively by the curves of

SURFACES OF CONSTANT ION DENSITY IN SATELLITE WAKE
(Not drawn to scale)

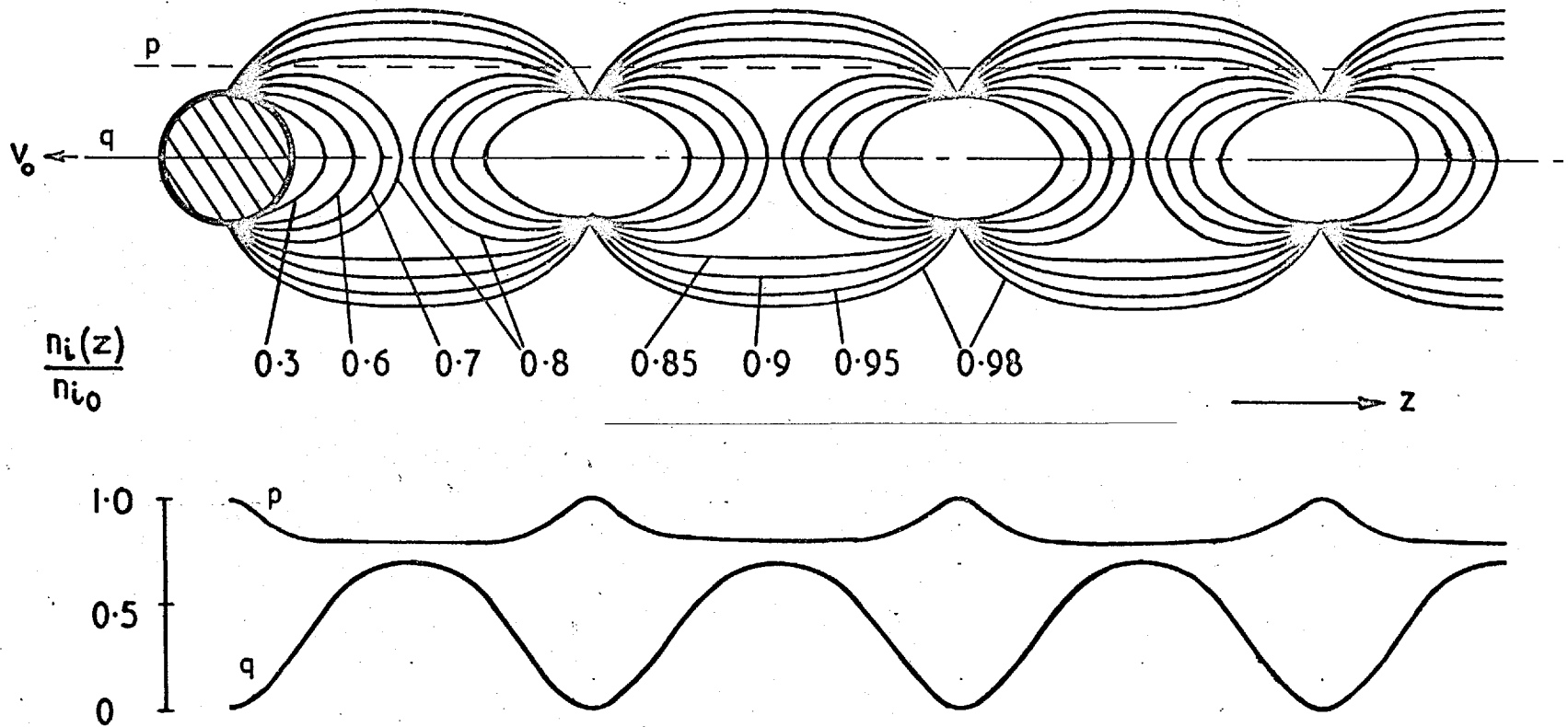


FIG 18 Variation of ion density in satellite wake (from ref. 6a). The two lower curves represent the variation along the lines p and q in the wake.

constant $n_i(r, z)$ shown in fig. 18. These are not drawn to scale in either the r or z direction. The two $n_i(z)/n_{i0}$ curves drawn below in this figure represent the variation outside and inside the geometrical shadow.

The expression for $n_i(r, z)$ assumes the following form at the axis

$$\frac{n_i(z)}{n_{i0}} = \exp \left[- \frac{R^2}{4\rho^2 \sin^2 \frac{\omega_{ci} z}{2v_0}} \right] \quad (6)$$

where R is the radius of the satellite. This is a periodic function of z which has a spatial period $2\pi v_0 / \omega_{ci}$ and which varies between zero and $\exp(-R^2/4\rho^2)$. The amplitude is thus $\exp(-R^2/4\rho^2)$, which varies with ρ/R as shown in fig. 6. The function is drawn in fig. 17 for three values of ρ/R . The upward and downward peaks have the same width when $\rho/R = 0.6$.

(33) Comparison of physical conditions

The conditions governing the ion distribution in the satellite wake are similar to those which determine the distribution of fast electrons in the present experimental wakes. In both situations the mean free path of the relevant particles is much greater than, and the Debye length much smaller than, the dimensions of the body; also, the Larmor radius is roughly of the same order of magnitude as the dimensions of the body.

In the case of a satellite moving with speed v_0 at altitudes of a few thousand kilometres or less, the ion energy $\frac{1}{2} m_i v_0^2$ associated with the relative motion of satellite and plasma is much greater than both the thermal energy kT and the electrostatic energy $e\delta V_p$ due to space charge fields in the wake. Al'pert et. al. were therefore able to make the simplifying assumptions that the ions all have the same velocity v_0 relative to the satellite and are unaffected by space charges. When the velocity v_0 is parallel to the magnetic field B , the problem is reduced to the superposition of helical paths of the same spatial period but of radii which vary in accordance with the Maxwellian

spread in the velocities perpendicular to B.

As far as the V_a , and to a lesser extent the V_f , variations are concerned, the received electrons have a mean kinetic energy $\frac{1}{2} m v_z^2$ which is many times greater than the mean deviation of $\frac{1}{2} m v_z^2$ from this value; this is equivalent to the satellite wake condition $\frac{1}{2} m_i v_o^2 \gg kT$. The mean kinetic energy is also several times greater than the electrostatic energy $e\delta V_p$, where δV_p is the change of plasma potential in the wake and has a maximum value of the order of T_S . The electrostatic energy may be assumed to be negligible in comparison with $\frac{1}{2} m v_z^2$ at $z > \Lambda_z$; this is the same as the satellite wake condition $\frac{1}{2} m_i v_o^2 \gg e\delta V_p$.

Since the V_a variations are proportional to variations of $n_e(\Delta V)$, as explained in (30) above, and involve a narrow spectrum of axial velocities, they should be in fairly good agreement with the theoretical variations of ion density in the satellite wake.

(34) Comparison of V_f and V_a curves with results of Al'pert et. al.

The theoretical distribution of ion density in the satellite wake contains the following features in common with the V_f and/or V_a variations: (i) the exponential term representing the amplitude; (ii) the equality between the spatial period and the helical pitch of the particles concerned; (iii) the difference in amplitude and phase between the variations inside the geometrical shadow and those outside (figs. 7 and 17), and (iv) the change of shape of the peaks as ρ/R increases (figs. 8 and 18).

INCREASE OF PERPENDICULAR VELOCITY v_{\perp}

(35) There are two pieces of evidence which point to an increase in the perpendicular component of electron velocity v_{\perp} , and therefore in the effective Larmor radius, as the electrons enter the dark region.

(a) The dependence of the V_f amplitude on ρ/R (fig. 6) and the appearance of V_f variations at the wake axis when ρ/R has an apparent value as low as 0.1 (in the case of the 30 mm disc), suggest that ρ/R increases by a factor of at least 2. (b) The shape of the V_a curves

(fig. 8) varies with ρ/R in the same way as the shape of the theoretical $n_{\perp}(z)$ curves (fig. 18), but at correspondingly lower values of ρ/R ; the values of ρ/R for the V_a curves need to be multiplied by about 1.6 in order to remove this discrepancy.

There are three ways by which the mean Larmor radius could be increased in the wake beyond its value in the undisturbed plasma.

- (i) The measurements described in section (19) show that there is an outward radial electric field close to the obstacle. In the case of the 12 mm disc, at $B = 42$ gauss and $z = 0.1A_z$, the plasma potential changes by about 3 volts near the edge of the dark region. The electrons therefore receive an initial acceleration into this region. (ii) The transverse electron velocities could be increased by electron plasma oscillations in the wake. Ion plasma oscillations are suggested by Samir and Willmore⁽⁹⁾ to be the cause of the unexpectedly large values of ion and electron density measured immediately behind the satellite Ariel I and a Black Knight rocket during their passage through the ionosphere. (iii) In the case of the 30 mm disc, where the annular gap between disc and tube wall is only 1 cm wide, the electron temperature and collision frequency just outside the obstacle are probably slightly higher than the values in the undisturbed plasma; this would account for a slight increase of Larmor radius.

Notwithstanding the existence of any of these mechanisms, it is possible that the Larmor radius inferred from the observations mentioned in (a) and (b) above is exaggerated by the presence of a small excess group of faster electrons in the distribution of v_{\perp} . It is shown in the next section that there is such an excess group in the distribution of axial velocities. This is a common feature of positive columns⁽¹⁹⁾⁽²⁰⁾. Twiddy⁽¹⁹⁾ finds that in a 1 millitorr, 120 mA mercury column there is generally a slight broad bulge on the electron energy distribution function which arises from the presence of electrons from the cathode which have made no inelastic collisions. Some of the gain in energy of axial motion would be transferred into energy of perpendicular motion through elastic collisions with neutral atoms,

thereby populating the higher values of v_{\perp} in excess of the Maxwellian distribution. Since the electrons which reach the axis of the wake are those with the higher values of v_{\perp} , any such excess population would have the same effect on the V_f and V_a measurements as a larger value of ρ .

It is improbable that ρ increases by a factor as large as 2, as suggested by the observations in (a). This would imply a four-fold increase in $\frac{1}{2}mv^2$ and there is no obvious source to provide this amount of energy; the radial electrostatic field would produce less than a two-fold increase in $\frac{1}{2}mv^2$. It seems necessary therefore to invoke the supposed excess population of higher v_{\perp} , and perhaps the plasma oscillations as well, to account for this large value of the correction factor.

IVB. PERIODIC SPATIAL VARIATIONS OF PLASMA PARAMETERS

(36) A complete description of the plasma in the wake could in principle be obtained from the Boltzmann-Vlasov equations for electrons and ions and the Poisson equation, with the appropriate boundary conditions. This would be an extremely difficult procedure despite the fact that the time-varying terms of the former two equations would be zero. A numerical integration method would be more practicable, as used by some authors ^{(7), (8)} for the problem of a wake in a plasma without a magnetic field. The present observed spatial variations of the plasma may however be explained to some extent by assuming that they constitute a plasma wave; it may then be shown that the wave fits onto one of the branches of the dispersion curves derived from the two fluid plasma equations. Before this is done, the inter-relationships of the various plasma parameter curves shown in fig. 12 will be discussed.

(37) Curves of V_p , n_e and T_s versus z

The parameters V_p , n_e and T_s are associated with the main body of electrons and the coincidence of their peaks in fig. 12 suggests that the three are closely linked. Brief qualitative explanations of these

inter-relationships are given below and more formal explanations are presented in Appendix A.

We consider first the relationship between V_p and n_e . It is observed that V_p goes more positive or more negative as n_e decreases or increases, and this is explained as follows. The plasma density in the wake is determined primarily by the helical motion of the electrons past the obstacle and the ion density follows the variations in the electron density to the extent that quasi-neutrality of the plasma is maintained; the neutrality is not complete, but sufficient simply to make the changes of V_p less than the value of T_S . This requirement follows from the Boltzmann equation

$$n_e = n_o \exp(-V_p/T_e) \quad \text{or} \quad \left| \frac{\delta n_e}{n_e} \right| = \left| \frac{\delta V_p}{T_e} \right|. \quad (7)$$

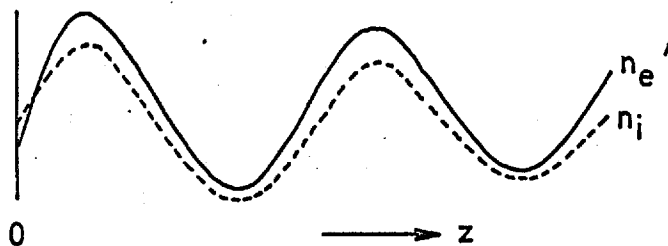
The magnitude of δn_i is therefore permitted to be less than that of δn_e , i.e. $|\partial n_i / \partial z| < |\partial n_e / \partial z|$. It then follows from the Poisson equation, $\nabla^2 V_p = -k^2 V_p = 4\pi e(n_e - n_i)$, that δV_p and δn_e have opposite signs.

The changes in T_S are also opposite in sign to those in n_e . The parameter T_S is related to the electrons of the upper decade of probe current (fig. 11), which constitute over 90% of the total electron density. Within this decade the slow electrons are more numerous than the faster electrons. This means that a region of maximum n_e contains an exceptionally large number of slow electrons and, because of the spatial dispersion of electrons with different axial velocities, a shortage of faster electrons. The current-voltage characteristic in this region is consequently steep and T_S is low. The converse applies to a position of minimum n_e .

(38) Relationship between n_e and n_i

The relationship between n_e and n_i as a function of z may be deduced as follows. The predominant motion of the ions in a low pressure positive column is towards the tube walls from the positions at which they are produced⁽²¹⁾. This applies to the present mercury column even though $B_z \neq 0$, since ρ_i is greater than the tube radius.

It is assumed that the motion of the ions into the dark region, situated near the axis of the tube, is then due primarily to the space charge field of the electrons in that region. As in (37) the number of ions drawn in is only that which is sufficient to keep any change of plasma potential less than T_S . We should therefore expect that n_e is slightly greater than n_i in the dark region, except near the obstacle where there is an ion sheath. It is then assumed from the Poisson equation and from the observed relationship between $\partial n_e / \partial z$ and $\partial V_P / \partial z$ that the relationship between the n_e and n_i variations is of the form drawn below.



(39) Excess group of faster electrons

The quantity $T_F - T_S$ is shown at the bottom of fig. 12 to go alternately negative and positive as z is increased. This corresponds to the alternate absence and presence of a group of faster electrons which lie in the energy range of the lower decade of electron current to the probe, in the region of about $4T_S$ electron-volts. The number density and mean energy of this group are written as n_F and eV_F and may be estimated roughly from the current-voltage curves. A more accurate value of eV_F , 14.5 volts, is obtained from the spatial period of the $T_F - T_S$ curve.

If the straight line through the upper decade of experimental points on a current-voltage curve is extended downwards, the maximum current difference ΔI_e between this line and that through the lower decade of experimental points is a measure of n_F . The ratio of n_F to the total electron density n_e is obtained from the equations

$\Delta I_e = An_F e(2e\Delta V_F/m)^{1/2}$ and $I_s = 0.5An_e e(2eT_S/m)^{1/2}$, where I_s is the "saturation" value of the total electron current to the probe, A is the probe area:

$$(n_F/n_e) = 0.5 (\Delta I_e/I_s)(T_S/eV_F)^{1/2}.$$

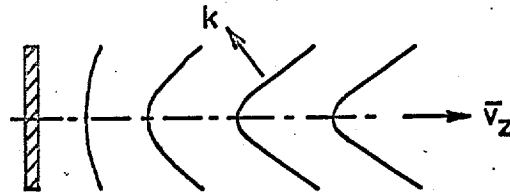
The possible error in the absolute value of n_F/n_e is comparatively large but the relative values of n_F/n_e at different values of z may be determined to within say 30%. If the successive minima and maxima of $T_F - T_S$, at $z = 8, 12, 21, 31, 39$ and 49 mm, are labelled a, b, c, d, e and f respectively, the corresponding values of n_F/n_e are as follows:

$(T_F - T_S)$ maxima	b, 0.002	d, 0.001	f, 0.0003
$(T_F - T_S)$ minima	a, 0.004	c, 0.003	e, 0.001

This set of values of n_F/n_e illustrates two effects. Firstly, there is a decrease in the density of the excess group as z increases, due to the spread of velocities in the group and to collisions. Secondly, the values of n_F/n_e at the $T_F - T_S$ maxima, where the extra electrons are present, are in general less than those at the $T_F - T_S$ minima where these electrons are absent. It is inferred from the latter effect that this group of faster electrons has a smaller mean perpendicular velocity than that of the other electrons. This would be a reasonable property of the excess group which presumably owes its existence to the fact that some electrons will have travelled the distance of five or six mean free paths from the cathode without making any strong collisions, apart from negotiating the right angle bend of the discharge.

PLASMA WAVE

(40) It was shown in sections (17) and (18) that the plasma parameter curves have a spatial period λ_z which increases with z to about 16 mm. In the case of the 12 mm disc, the variations of V_p form wavefronts as shown in fig. 14(b); at $z > 6$ mm the wave normal makes an angle of about 50° with the negative z direction. In the case of the 6 mm disc the parameters were measured along only one line in the wake, but it is likely from the interpretation given below that the parameter variations also form wavefronts whose normal lies at a large angle to the axis.

(41) Identification of the wave

The variations of the plasma parameters are at rest in the laboratory frame of reference, but in another frame they would be observed as some form of plasma wave. The dispersion relations for plasma waves usually apply to situations where the plasma as a whole is at rest with respect to the observer. It is sufficient in the present case to choose a frame of reference which moves with the macroscopic velocity of the electrons; the ion motion is not relevant at the frequencies with which we shall be concerned.

It appears at first sight that these spatial variations should be considered in the frame of reference which moves with the electron drift velocity v_d , the "drift frame". It seems likely, however, that it is only those electrons which move past the obstacle into the dark region that form the variations of V_p , n_e and T_S . Any electrons which move along the dark region in the opposite direction have random phases and their net interaction with the variations is probably small. In this circumstance the variations should be considered in the frame

of reference which moves at the average velocity \bar{v}_z of the anode-directed electrons; this frame will be referred to as the "average frame". The value of \bar{v}_z is taken to be $v_d + \bar{v}_1 \approx (1.0 \pm 0.2) \times 10^8$ cm/sec where \bar{v}_1 is the mean velocity in any particular direction perpendicular to the axis.

In the "average frame" the variations constitute a wave with a velocity component \bar{v}_z in the negative z direction and a component of wave number $k_z = 2\pi/\lambda_z = 4.2 \text{ cm}^{-1}$ (fig. 14). The product $k_z \bar{v}_z$ defines the wave frequency ω in the "average frame":

$$\omega = k_z \bar{v}_z = 4.2 \times 10^8 \text{ rad/sec} = 0.56 \omega_{ce}$$

where ω_{ce} is the electron cyclotron frequency.

The dispersion curves for hydromagnetic waves in a uniform unbounded plasma are examined in the hope of finding a wave in the frequency region just below ω_{ce} and in the velocity region one or two orders of magnitude higher than the Alfvén speed, $c_A \approx 2 \times 10^6$ cm/sec. Such dispersion curves have been derived by T.E. Stringer, (22) for example, who presents curves for several sets of plasma conditions and for propagation at an angle θ to the magnetic field. The upper curve of Stringer's first diagram has been drawn in a modified form in fig. 19 so that it corresponds to $\cos \theta = 0.56$ and to the parameter relationships pertaining to fig. 12: $c_A/c_s = 12$, $c/c_A = 1.6 \times 10^4$, $\omega_{pe}/\omega_{ce} = 28$ and $m_i/m_e = 3.9 \times 10^5$, where c is the speed of light and ω_{pe} the electron plasma frequency. It is evident that the branch which lies in the required frequency and velocity regions is the electron cyclotron branch, along which the frequency has the constant value $\omega_{ce} \cos \theta$. A derivation of the dispersion relation and a physical description of this type of plasma wave are presented in Appendix B.

(42) Magnitude of the wave vector

If the phase velocity of the wave in the direction of the axis is equal to \bar{v}_z , its value in the direction of the wave vector \underline{k} is $\bar{v}_z \cos \theta$. The theoretical value of the wave number is then

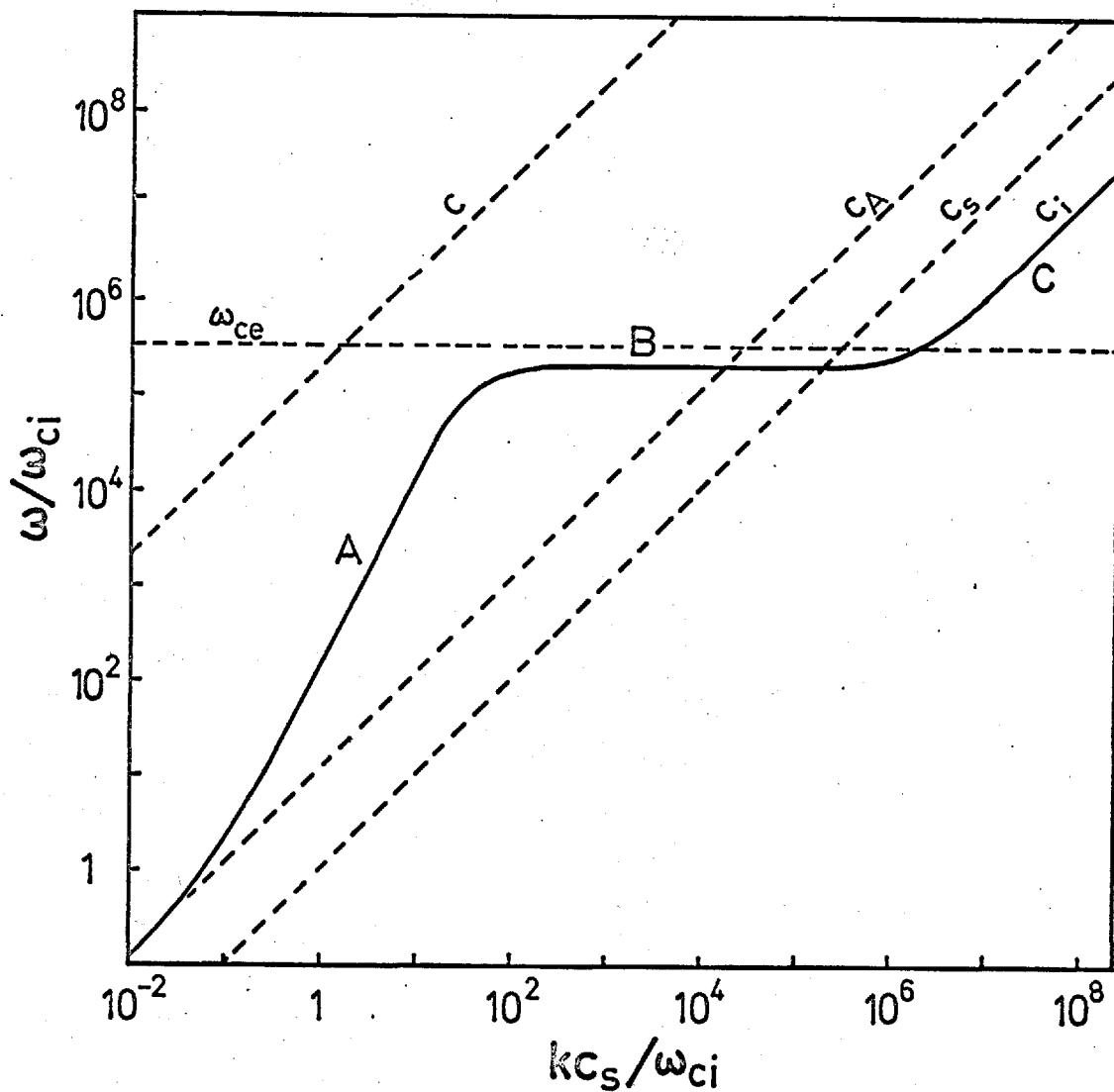


FIG 19 Upper branch of dispersion curves for hydromagnetic waves in an unbounded plasma (ref. 22), showing whistler mode (A), electron cyclotron mode (B) and ion acoustic mode (C). The lines at 45° represent the velocities of light, Alfvén, electro-acoustic and ion acoustic waves.

$$k = \frac{\omega_{ce} \cos \theta}{v_z \cos \theta} = \frac{\omega_{ce}}{v_z} = 7.5 \text{ cm}^{-1}.$$

This compares favourably with the experimentally observed value of 6.7 cm^{-1} obtained from fig. 14 at the larger values of z . The relation $\omega = \omega_{ce} \cos \theta$ is obtained from linearized equations and should not therefore be expected to apply accurately in the region of large variations of n_e and V_p (at $z < 15 \text{ mm}$); nevertheless, the magnitude of k in this region, near the axis, is still close to 7.5 cm^{-1} .

The above interpretation of the spatial variations of the macroscopic properties of the plasma is based on measurements at two similar sets of discharge conditions. The measurements are insufficient to determine whether or not the variations depend on the obstacle dimension. Further measurements of the variations at different values of the magnetic field, electron temperature and obstacle radius are necessary to establish the validity of the electron cyclotron wave model. It appears from the present measurements, however, that this interpretation of the phenomenon is correct.

CHAPTER V

CONCLUSIONS

(43) Summary

Periodic spatial variations in the properties of a particular type of wake in a plasma (a wake produced in the flow of electrons along magnetic field lines with a background of cold ions) have been measured by means of a plane Langmuir probe. Two distinct types of measurement have been made, concerning the variation of (a) the flux of the electrons in the tail of the axial velocity distribution and (b) the macroscopic properties of the plasma.

The behaviour of the fast electrons has been studied over a wide range of conditions and explained in terms of a single particle theory (in which the total density or flux of electrons at a point in the wake represents simply the superposition of the individual particle orbits). The type of wake in these experiments has been compared with the wake of a satellite in the ionosphere and it has been shown that some features of the spatial variations of the fastest electrons, i.e. those with energy \gg the electron temperature, are in good agreement with those predicted for the ion distribution in a satellite wake. It has also been shown that the fraction of electrons able to reach the axis of the wake is somewhat larger than that calculated from the value of the electron temperature in the undisturbed plasma.

Measurements of the spatial variations of plasma parameters along the dark region show that the variations form wave fronts, the normal to which makes a large angle with the magnetic field at the larger values of z . This phenomenon is identified as an electron cyclotron wave, as seen in a frame of reference moving at the average axial velocity \bar{v}_{ez} of the anode-directed electrons. The observed magnitude of the wave vector k is in fair agreement with the theoretical value ω_{ce}/\bar{v}_{ez} . The other features of the wave are explained in qualitative terms.

(44) Significance of results

This appears to be the first report of periodic spatial variations produced by an obstacle in a laboratory plasma.

As probes and other obstacles (e.g. the aperture limiters used in the Stellerator experiments at Princeton) are often inserted into current-carrying plasmas in the presence of magnetic fields, it is of interest to understand how they affect the plasma. The present experiments illustrate some of the features of the plasma perturbation in the particular case of a steady state, low density plasma at low magnetic fields.

A link has also been established between wakes in positive columns and satellite wakes (or their laboratory models). Although the physical conditions are to a large extent different in the two types of wake, it is possible that the spatial periodicity in the positive column wake could find some application in a satellite simulation experiment, e.g. in the investigation of the scattering of electromagnetic waves by a satellite wake.

ELECTRON WAKES IN A PLASMA

P. J. Barrett*

Culham Laboratory, Abingdon, Berkshire, England

(Received 9 November 1964)

Measurements have been made with a Langmuir probe of the floating potential (V_f) and plasma potential (V_p) near a quartz obstacle placed in the positive column of a low-pressure mercury-arc discharge in a longitudinal magnetic field ($p = 0.1\text{--}5$ mTorr, $B = 10\text{--}600$ gauss, $n_e \sim 10^{11}$ cm $^{-3}$, column diameter = 5 cm). Since electrons spiraled past the obstacle in both axial directions (thermal speed $\sim 3 \times$ drift speed), a wake was produced on either side of the obstacle, extending over a distance several times greater than the obstacle diameter. The inner region of the wake on the anode side appeared as a dark shadow and that on the cathode side appeared bright.

The probe presented to the plasma a plane 0.25-mm wire tip which faced either the anode or the cathode end of the column. Measurements with a cathode-facing probe revealed periodic spatial variations of V_f along the z (axial) direction only on the anode side of the obstacle (see top curve in Fig. 1). With an anode-facing probe, similar V_f variations, of smaller amplitude, were observed only on the cathode side. The roughly linear dependence of the reciprocal of the spatial period Λ_z on B is shown in Fig. 2(a). A numerical check shows that Λ_z is equal to the average helical pitch of those electrons of axial speed sufficient to reach the floating probe. A similar Λ_z curve was obtained in the case of a neon positive column (using a mercury-pool cathode and cold trap¹), which indicates that the ion mass is relatively unimportant in the V_f variations. It was also noted that the curves of V_f versus z just outside the shadow were roughly opposite in phase to those inside.

Measurements of the plasma potential, electron density, and electron temperature have been derived in the usual way from probe current-voltage curves obtained at various values of z ; see Fig. 1. These were obtained in the shadow with a cathode-facing probe under only one set of discharge conditions. The current-voltage curves [e.g. Fig. 2(b)] possess, in general, two different slopes between V_p and V_f , indicating the existence of a small excess group of faster electrons with a "temperature" T_F

different from the "temperature" T_S of the main body of slower electrons. Such a group is a common feature of low-pressure positive columns.² $T_F - T_S$ was alternately positive and negative as z increased, representing the alternate presence and absence of this group.

The following interpretation is offered for these results. At floating potential the probe receives all incident ions, but only those electrons of energy $\geq e(V_p - V_f)$. In the wake V_f is determined by the number of such energetic electrons available at the probe tip after passing close to the obstacle edge. Only those whose helical motion is of suitable phase at the obstacle are permitted to move into the wake. This phase selection causes space modulation of the density of these electrons, or of any other

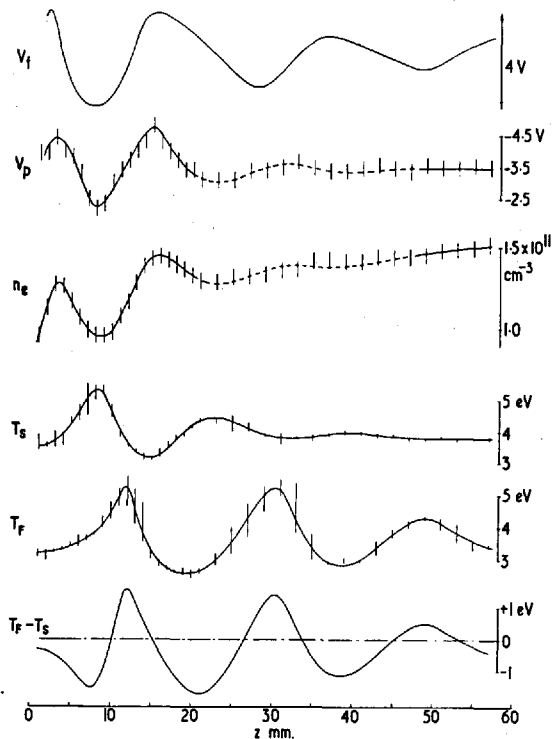


FIG. 1. Variations of plasma parameters in the shadow of a 6-mm disc obstacle, 1 mm off axis. $B = 42$ gauss, $p = 0.2$ millitorr, discharge current = 9 A. Vertical lines represent errors in the computation from the probe current-voltage curves.

PART B

WAVES OF PLASMA DENSITY

(ELECTRO-ACOUSTIC AND IONIZATION WAVES)

CHAPTER I

INTRODUCTION

(1) The two types of low frequency density wave in a positive column

This part of the thesis is concerned with two types of plasma density wave that may be excited artificially in the positive column of an arc discharge and observed on the anode side of the exciter. These are (i) the electro-acoustic type of wave predicted by Tonks & Langmuir⁽¹⁾ which travels from the exciter towards the anode (the observation of heavily damped electro-acoustic waves travelling from the exciter towards the cathode has also been reported by Little⁽²⁾ and Hatta & Sato⁽³⁾), and (ii) the ionization type which, in the case of some monatomic media such as the inert gases or mercury vapour, travels towards the exciter (these do not exist on the cathode side of the exciter⁽⁴⁾). The latter type is often observed in the form of large amplitude, spontaneously occurring waves which have usually been called "moving striations"; in the last two years, these have also acquired the name "ionization waves" (first used by L. Pekarek⁽⁵⁾). Since the energy of a wave travels away from its source, the former type is a forward wave and the latter a backward wave.

The two types of wave represent perturbations in the density of both ions and electrons, and are observed mainly at frequencies less than 100 kc/s in these experiments. They do not necessarily occur simultaneously at the same discharge conditions: in general the forward waves are more easily propagated at the lowest pressures and the ionization waves at the higher pressures. The pressures used are all less than or roughly equal to 30 millitor and the discharge currents lie in the range 2.5 - 8A. Under these conditions, no spontaneously occurring propagating waves of either type are observed. Both types of wave are more readily excited in the presence of a weak, longitudinal magnetic field than without a field; in either case it is necessary to extract the weak wave signal from the background of plasma noise by means of a phase sensitive detector. We are thus concerned with small amplitude, low frequency waves, both forward and backward, in low pressure positive columns.

(2) Spontaneously occurring density waves

Electro-acoustic and ionization waves may each occur spontaneously in the positive column at appropriate operating conditions of the discharge. Such electro-acoustic waves are observed mainly at low pressures and may take the form of propagating or stationary waves at discrete frequencies, or of propagating low frequency components of the plasma noise. Spontaneous ionization waves occur within certain unstable regimes of the discharge, mainly in the 10^{-2} - 10^2 torr range of pressure and at discharge currents less than 1 A. These are large amplitude, non-linear disturbances; they can modulate the light emitted by a discharge to a depth of almost 100% and are accompanied by fluctuations of several volts in the discharge voltage⁽⁶⁾. At a given pressure there is a critical discharge current, called the "Pupp limit", above which spontaneous striations do not occur⁽⁸⁾. Just above the Pupp limit the discharge is in a quasi-stable regime in which large amplitude ionization waves may be excited artificially⁽⁹⁾⁽¹⁰⁾.

Two review articles on oscillations in low pressure discharges⁽⁷⁾⁽³¹⁾ and a comprehensive "Bibliography on Moving Striations"^(7a) have been produced recently.

ELECTRO-ACOUSTIC WAVES

(3) Tonks & Langmuir⁽¹⁾ predicted the existence of longitudinal plasma waves in which the inertia is predominantly that of the ions and the restoring force is provided mainly by the pressure gradient in the electron gas; the ion and electron density perturbations are everywhere maintained approximately equal by the electrostatic space charge field. From the analogy of ordinary sound waves in a gas, it is clear that such waves would travel at the characteristic speed $c_s = (\gamma_e K T_e / m_i)^{1/2}$ where γ_e is the adiabatic compression coefficient of the electron gas and K is the Boltzmann constant (boundary conditions and damping effects are ignored here). The assumption is made in this prediction that the electron temperature T_e is much greater than the ion temperature T_i , otherwise the pressure gradient in the ion gas should be added to that of the electron gas in calculating c_s .

Nomenclature. These waves were called electric sound waves by Tonks & Langmuir and since then have been variously known as ion(ic) waves, ion(ic) sound waves, ion acoustic waves, electrostatic sound waves and electro-acoustic waves. The last of these names has been used by Little⁽¹⁾, Stringer⁽¹¹⁾ and Vasil'eva et. al.⁽¹²⁾, and is perhaps more appropriate than any of the first three names as it emphasises the electrostatic link between the ions and electrons, which is a singular feature of these waves. The adjective "ion" or "ionic" is slightly misleading inasmuch as the wave is comprised of density variations of ions and electrons together, both of which are essential ingredients of the wave. Stringer reserves the description "ion acoustic" for waves of ion density, which have the speed $c_i = (\gamma_i KT_i/m_i)^{1/2}$. As shown in the next section, these should occur at wave lengths much less than the electron Debye length where the perturbations of the ions are uncoupled from those of the electrons. Such waves would admittedly be difficult to observe because of heavy Landau damping, unless this was counterbalanced by the amplification produced, for example, by an electron current along the wave direction.

(4) Basic dispersion equation

The basic dispersion equation describing low frequency oscillations in a plasma was derived by Tonks & Langmuir⁽¹⁾ in 1929 for an unbounded plasma in which collisions are ignored. A more general derivation from the fluid equations for continuity and conservation of momentum and the Poisson equation is given by Spitzer⁽¹³⁾ and other authors. The equation is derived in Appendix C where it is written in the form

$$\left(\frac{\omega}{k}\right)^2 = \frac{(c_e^2 m_e/m_i) + c_i^2 (1 + c_e^2 k^2/\omega_{pe}^2)}{1 + c_e^2 k^2/\omega_{pe}^2} \quad (1)$$

where $c_e = (\gamma_e KT_e/m_e)^{1/2}$, $c_i = (\gamma_i KT_i/m_i)^{1/2}$ and $\omega_{pe} = (4\pi n_0 e^2/m_e)^{1/2}$.

At frequencies sufficiently high to make $k^2 \gg \omega_{pe}^2/c_e^2$ (which is the same condition as $\lambda^2 \ll (2\pi\lambda_D)^2$ where λ_D , the electron Debye length, is about 10^{-2} cm in the present experiments), equation (1)

assumes the form

$$\omega^2 = \omega_{pi}^2 + c_i^2 k^2 \quad (2)$$

where ω_{pi} is the ion plasma frequency $(4\pi n_o e^2/m_i)^{1/2}$. At frequencies such that $\omega_{pi}^2 \ll \omega^2 \ll \omega_{pe}^2$, equation (2) represents the "ion acoustic" waves described by Stringer (mentioned above), with the phase velocity c_i . At the lower frequencies, where $\lambda^2 \gg (2\pi\lambda_D)^2$, equation (1) becomes

$$\frac{\omega}{k} = \left(\frac{\gamma_e K T_e + \gamma_i K T_i}{m_i} \right)^{1/2}$$

and when $T_i \ll T_e$ the equation is further simplified to

$$\frac{\omega}{k} = \left(\frac{\gamma_e K T_e}{m_i} \right)^{1/2} = c_s \quad (3)$$

(5) Effect of ion-neutral collisions and finite radius

Equation (3) is only applicable as it stands if the plasma is uniform and unbounded and if the collision frequency of the ions is much smaller than ω .

In a weakly ionized gas, such as that in a positive column, the ions collide mainly with neutral atoms or, at very low pressures, with the tube wall. The ion-neutral collision frequency ν_{in} in the neon and hydrogen columns of the present experiments is estimated to be 3×10^5 c/s and 3×10^6 c/s respectively. In the 5 cm diameter mercury column, at a pressure of about 1 millitorr or less, the ion-wall collision frequency ν_{iw} is of the order of 6×10^4 c/s (as calculated from the radial distribution of ion density given by J.V. Parker⁽¹⁴⁾). These collision frequencies are of the order of or greater than the wave frequencies.

The effect of the ion-neutral collisions is included in the theory by inserting the term $g m_i v_i n_o \nu_{in}$ in the equation of motion for the ions (equation (5), Appendix C), where g is the average fraction of wave momentum which is lost by an ion on collision (g is assumed to be of the order of unity⁽¹⁵⁾ and is therefore omitted in the equation). This leads to the dispersion relation for collision-modified electro-

acoustic waves in an unbounded plasma ⁽¹⁵⁾;

$$\omega(\omega + i\nu_{in}) = c_s^2 k^2 \quad (4)$$

If ω is real and $k = k_R + ik_I$, the phase velocity is given by the relation

$$\frac{\omega}{k_R} = \frac{c_s}{\left[\frac{1}{2} + \frac{1}{2} \sqrt{1 + (\nu_{in}^2 / \omega^2)} \right]^{\frac{1}{2}}} \quad (5)$$

and the damping by the relation

$$k_I = \frac{\nu_{in}}{2c_s \left[\frac{1}{2} + \frac{1}{2} \sqrt{1 + (\nu_{in}^2 / \omega^2)} \right]^{\frac{1}{2}}} \quad (6)$$

It is clear that as the gas pressure (and therefore ν_{in}) is raised, the damping increases and the phase velocity decreases. The latter effect is due to the increase in the number of neutral atoms entrained in the wave motion, thereby increasing the inertia without proportionately increasing the restoring force.

The dispersion equation is further modified by the finite extent of the column in the radial direction. If the amplitude of the density perturbation is a function of longitudinal and radial distance only ($m = 0$ being the only azimuthal mode generated by an exciter coil situated coaxially with the column), it may arbitrarily be assumed proportional to the zero order Bessel function $J_0(k_c r)$. A series of values for k_c is obtained from the assumed value of the amplitude at the edge of the column. These represent a series of radial modes of the wave, the lowest of which has $k_c = 0$ (i.e. $J_0(k_c r) = \text{constant}$) and is called the first or principal mode. As shown in Appendix D, the dispersion relation becomes

$$\omega^2 + i\omega\nu_{in} = c_s^2 (k^2 + k_c^2) \quad (7)$$

for a plasma column in which there is no creation and loss of particles, and no particle drifts.

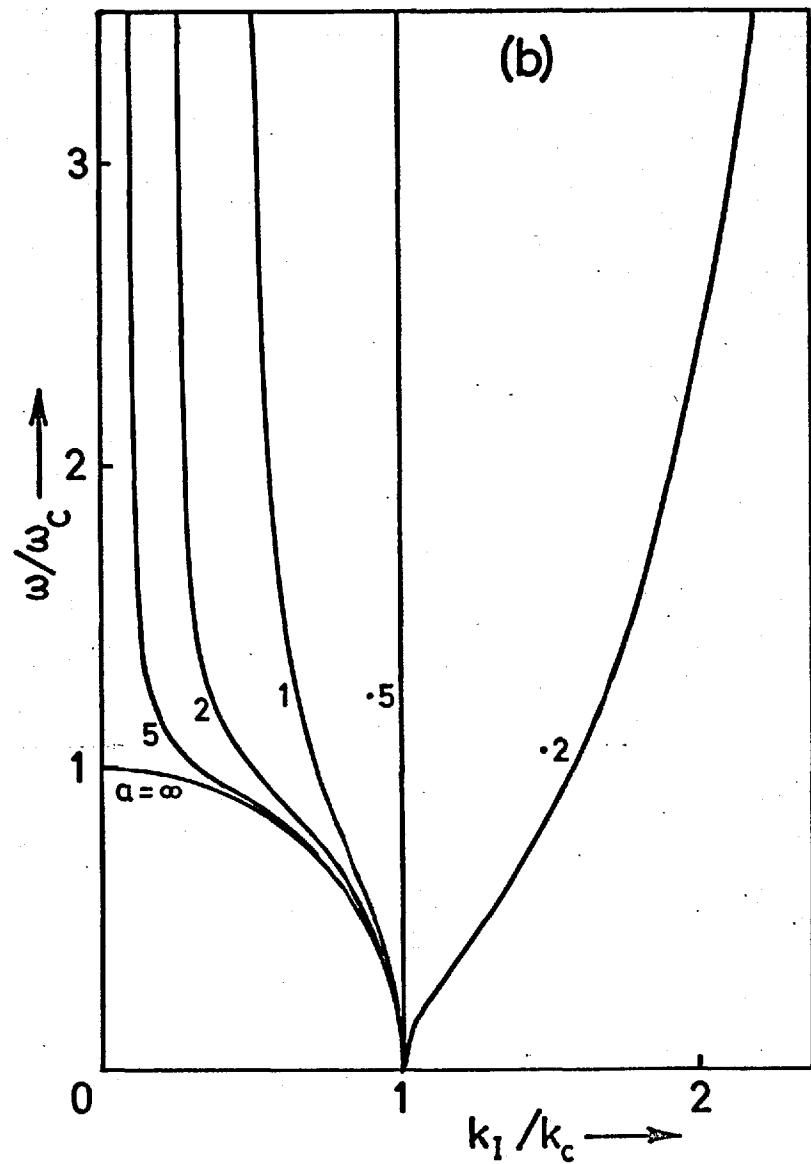
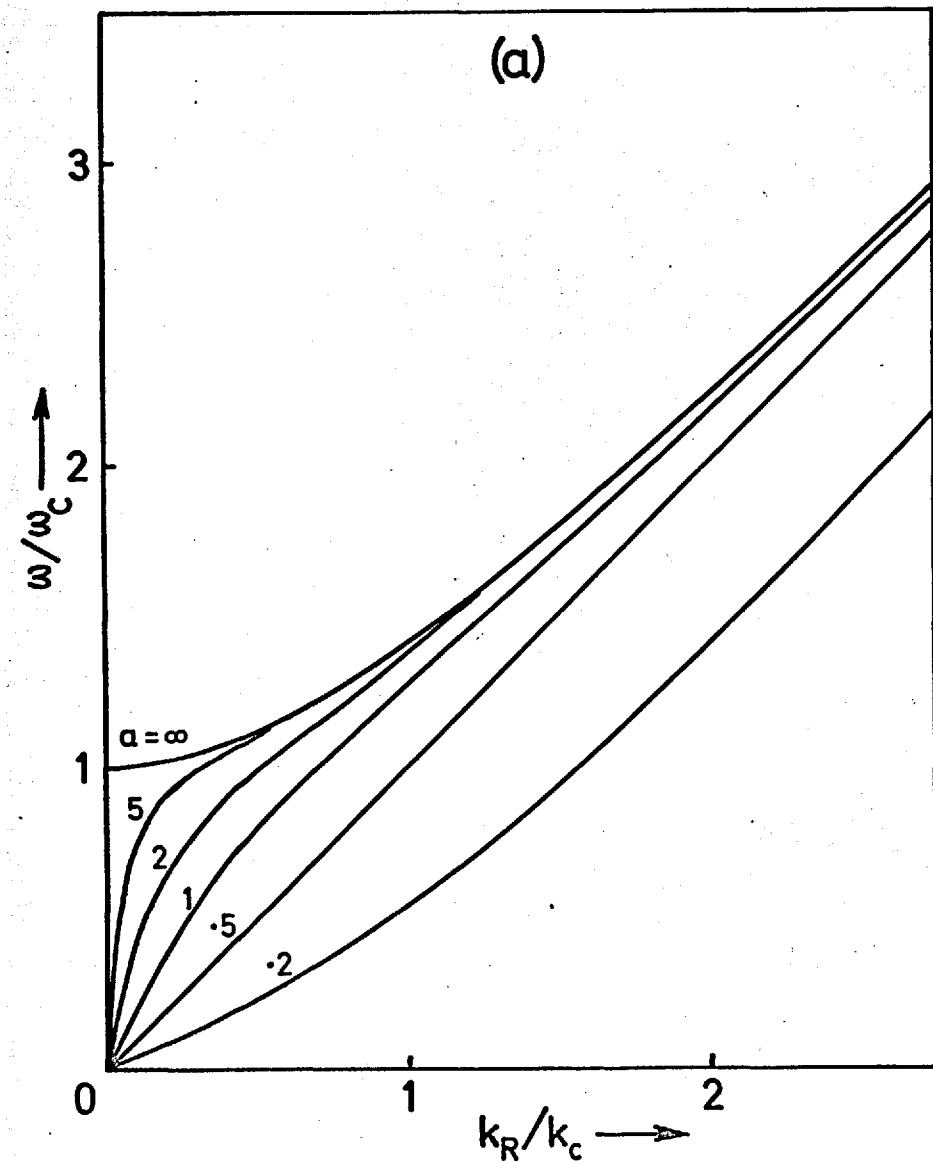


FIG 1 Curves from equation (7) showing dependence of ω on k_R and k_I at different values of the parameter $a = \omega_c/v_{in}$ where $\omega_c = k_c c_s$.

The variation of $\omega/c_s k_c$ with k_R/k_c and k_I/k_c , obtained from this equation, is given in fig. 1 (a) and (b) for several values of the parameter $a = (v_{in}/k_c c_s)^{-1}$. (k_R and k_I are again the real and imaginary parts of the wave number. It should be noted that except on pages 73 and 74, k_R will hereafter be written simply as k).

It is noted in fig. 1(a) that the effect of collisions is to eliminate the cut-off in frequency at $\omega = k_c c_s$. At values of a greater than 0.5 the waves become more heavily damped as ω falls below this value (cf. experimental points on p. 102 where $k_c c_s = 1.3 \times 10^5$).

(6) Effect of ion and electron longitudinal drift velocities

In the equations given above, no account is taken of the drift velocities of ions and electrons in the z direction. Such drifts have been included, together with ion-neutral and electron-neutral collisions, in the one-dimensional treatment of electro-acoustic waves by Liperovski⁽¹⁶⁾. This author was able to account fairly accurately for the speed of anode-approaching striations observed by Vasil'eva et. al.⁽¹²⁾ (although his assumption that $\gamma_e = 3$ is of doubtful validity when applied to the low pressure discharge of Vasil'eva et. al.; see section (10)). He also showed that the drifts produced a growth effect on anode-approaching electro-acoustic waves and a stronger damping effect on such waves travelling towards the cathode.

A simplified form of Liperovski's dispersion equation is readily obtained by ignoring the collision terms in the fluid equations (as in Appendix C). The drift velocity terms, $v_d \frac{\partial n}{\partial z}$ and $n_0 m v_d \frac{\partial v_z}{\partial z}$, are included in the equations of continuity and the equations of motion respectively, and the following equation is obtained:

$$\frac{\omega}{k} = \pm \left(c_s - \frac{m_e}{2m_i} \frac{v_d^2}{c_s} \right) - v_{di} \quad (8)$$

where the + sign applies to anode-approaching waves and the - sign to cathode-approaching waves.

As far as the growth and damping effects of the drifts are concerned, Liperovski's one-dimensional treatment illustrates the anisotropy about the two longitudinal directions but does not account for the experimentally observed values of k_I .

(7) Electro-acoustic waves in collision-dominated positive column

By applying perturbation theory to a steady state hydrodynamic model of the collision-dominated positive column, D.R. Davies⁽¹⁷⁾ has obtained a dispersion relation of the form

$$\omega^2 + i\omega\nu = c_s^2 (k^2 - k_c^2) \quad (9)$$

where $\nu = (m_e \nu_{en} + m_i \nu_{in}) / (m_e + m_i)$, $k_c^2 = (\nu + \xi)\xi / c_s^2$ and ξ is the ionization frequency. The steady state theory leads to the result

$$[\xi(\nu + \xi) / c_s^2]^{1/2} R = 2.405$$

from which k_c may be calculated (2.405 is the first zero of the Bessel function J_0 and R is the column radius).

Equation (9) represents the 2nd radial mode, in which the modulus of the density perturbation is constant across the column and the phase at the wall lags on that at the axis by $[\omega / (\nu + \xi)] \log(\phi_{r=R} / \phi_{r=0})$ radians (ϕ represents the plasma potential). This mode exhibits a cut-off wave number k_c at $\omega = 0$. Somewhat similar behaviour occurs in the curves for large ν_{in} in fig. 1(a), which approach a cut-off on the k -axis before going to the origin.

Davies also finds that the dispersion equation for the principal radial mode, where ν_{iz} is constant across the column, simplifies to equation (4).

(8) Electro-acoustic waves in low pressure, bounded plasma

This problem has been treated by L.C. Woods⁽¹⁸⁾ and by Bertotti, Cavaliere, and Giupponi^{(19a)(19b)}. Furthermore, the computation of Woods' dispersion curves has been repeated and extended to higher pressure regimes by D.R. Davies⁽¹⁷⁾. Woods deals with the problem of low frequency waves in a cylindrical plasma column in which $T_i = 0$ and the only drift of particles is the radial drift of ions to the wall. Bertotti et. al. consider the two-dimensional problem of low frequency waves in a plasma under the same conditions of T_i and particle drift. The effect of the

longitudinal electron drift is discussed qualitatively in both papers. Woods discusses the effect of this drift on the wave damping. Bertotti et. al. state that their theoretical model is "suited for describing completely ion waves in a R.F. discharge, not in an arc where the electron drift is of major importance"; they suggest that one effect of the electron drift would be the elimination of the lowest wave mode (19a). The two papers contain similar dispersion curves for the two lowest modes. Those obtained by Woods are shown in fig. 2(a) and (b).

We shall consider Woods' theory in some detail. At pressures sufficiently low for the mean free paths of electrons and ions to be much larger than the tube radius, the steady state condition of the positive column may be described by an integral equation derived by Tonks & Langmuir (20). Woods applies perturbation theory to a simpler version of the Tonks-Langmuir equation and obtains a second order differential equation in $w (= v_{iz}/c_s)$:

$$(1-u^2) \frac{d^2 w}{dx^2} + \frac{1}{x} \left[1 - 2xu \left(\frac{du}{dx} + \alpha - i\sigma \right) \right] \frac{dw}{dx} - \left(k^2 R^2 + \frac{m^2}{x^2} - \sigma^2 - i\sigma\alpha \right) w = 0 \quad (10)$$

where $uc_s = \bar{v}_{ir}$ (the radial ion drift velocity), $x = r/R$, $\sigma = \omega R/c_s$, $m =$ azimuthal mode number and $\alpha = 1.109$ (eigenvalue obtained from the steady state boundary condition that the radial electric field $E_r = \infty$ at $r = R$). The boundary conditions imposed on v_{iz} are:

$$\left. \begin{aligned} v_{iz} &= 0 && \text{if } m \neq 0 \\ \frac{dv_{iz}}{dr} &= 0 && \text{if } m = 0 \end{aligned} \right\} \text{at } r = 0 \quad (11)$$

$$\frac{dv_{iz}}{dr} = 0 \quad \text{at } r = R$$

L. C. Woods

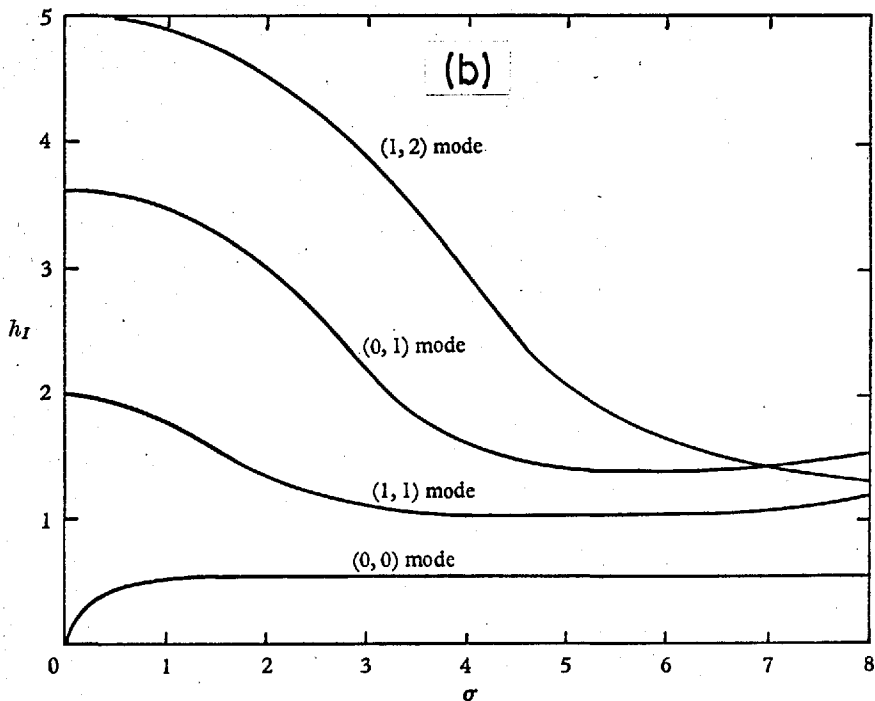
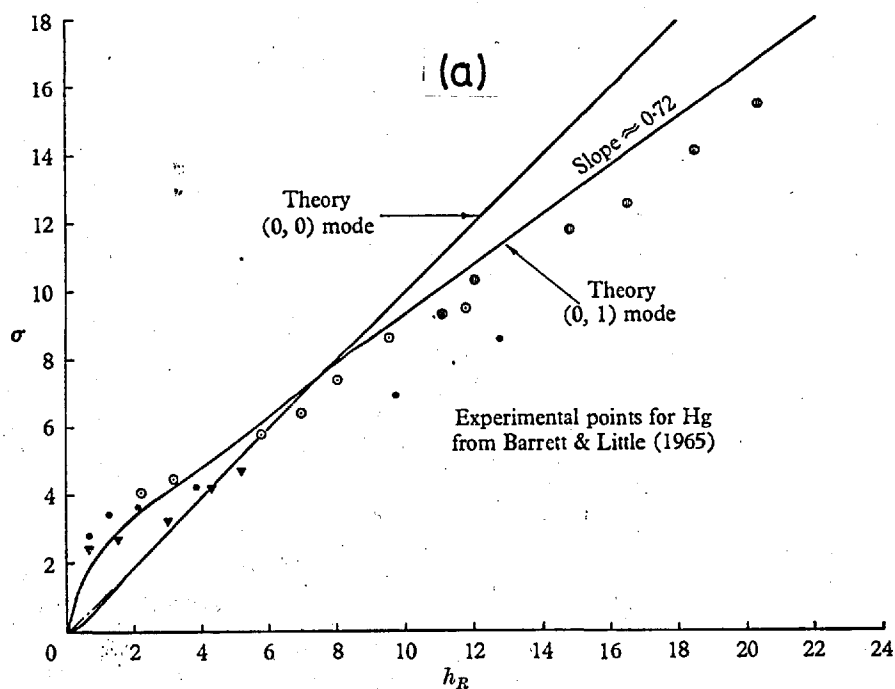


FIG 2 (a) Dispersion and (b) damping of electro-acoustic waves in a low pressure positive column. From paper by L.C.Woods (ref. 18). $\sigma = \omega R/c_s$, $h_R = k_R R$, $h_I = k_I R$.

(Bertotti et al show that the perturbation of the ion radial velocity is zero at the edge of the plasma^(19b)). Equation (10) may be solved for a given value of the frequency ω , subject to the boundary conditions, only for a particular value of the wave number k . Corresponding values of ω and k are computed for the first and second radial modes, for $m = 0$ and $m = 1$.

We shall be concerned only with the first and second radial modes for which $m = 0$; these may be written as the (0,0) and (0,1) modes. The (0,0) mode is that in which v_{iz} is independent of r . Under this condition, (11) is satisfied and equation (10) becomes

$$(k^2 R^2 - \sigma^2 - i\sigma a) v_{iz} = 0 \quad (12)$$

or

$$k_R = \frac{\omega}{c_s} \left[\frac{1}{2} + \frac{1}{2} \left(1 + \left(\frac{1.109 c_s}{\omega R} \right)^2 \right)^{\frac{1}{2}} \right]^{\frac{1}{2}}$$

and

$$k_I = \frac{1.109 \omega}{2R c_s k_R}$$

When $\omega R/c_s \gg 1.109$, $k_R = \omega/c_s$ and $k_I = 1.109/2R$.

No such simple description of the (0,1) mode may be given. In this mode the radial distribution of the density perturbation amplitude $|n_1(r)|$ and of the phase of the perturbation relative to the phase at the axis, varies with frequency. At low frequencies, the amplitude falls from a maximum at $r = 0$ to almost zero at $r \approx 0.5R$, and rises to a subsidiary maximum near the wall; at higher frequencies the amplitude rises from a minimum at $r = 0$ to a maximum near the wall. At $\omega < 10c_s/R$ as in the present measurements on mercury columns, the phase of the wave near the wall lags behind the phase at the axis: the lag at $\omega = 4c_s/R$ for example is about 120° , as in fig. 26(c).

The ω versus k_R curve for the (0,1) mode is repeated in fig. (9) where it may be compared with the experimental points. This curve is similar to those obtained from eqn. (7) for $v_{in} \lesssim k_0 c_s$; as $k \rightarrow 0$, the curve approaches a cut-off frequency $\sigma_0 \approx 2.5$ (or $\omega_0 = 2.5 c_s/R$) before steepening in slope and approaching the origin. Almost the same

cut-off frequency is obtained from equ. (7) if $k_c R$ is set equal to the first zero of $J_0(k_c R)$. At the higher frequencies the (0,1) curve lies well below the $\omega = kc_s$ line.

(9) Damping: discrepancy between theory and experiment

The damping at high pressures in a weakly ionized gas (i.e. where ion mean free path $\ll R$) is due mainly to ion-neutral collisions. In the low pressure regime of the positive column, damping occurs mainly through the loss of ions (and therefore of wave momentum) to the tube wall. The shorter the life-time of an ion in comparison with the wave period, the greater the damping we should expect. The average transit time of an ion between its point of formation and the wall is of the order of R/c_s , i.e. 1.6×10^{-5} and 0.5×10^{-5} sec in the mercury and neon columns respectively. The period of the waves observed in these columns lies in the range 10^{-5} to 10^{-4} sec, mainly longer than the ion transit time.

The damping obtained from any of the dispersion equations given above is much heavier than that observed experimentally. The same discrepancy is found by Alexeff & Jones⁽¹⁵⁾ when they compare the damping of their anode-approaching and cathode approaching waves with equation (6).

We may note that as the electron velocity distribution is displaced through v_{de} to higher velocities in the case of anode-directed electrons, the velocity distribution curve has a positive slope $\frac{\partial f}{\partial v_z}$ at the speed c_s and therefore exerts a growth effect on the waves moving towards the anode. L.C.Woods suggests that the electron drift would account for the difference between the observed and calculated values of k_I . He refers to the growth rates computed by T.E. Stringer⁽²¹⁾ for electrostatic instabilities in a current-carrying plasma. Under the conditions that kv_{de}/ω_{pe} is small and $T_i \ll T_e$ (where v_{de} is the electron drift velocity), Stringer shows that the instabilities are electro-acoustic and have a growth rate $\gamma = 0.62 k_R v_{de} (m_e/m_i)^{1/2} \text{ sec}^{-1}$. The growth coefficient $\gamma k_R/\omega$ is subtracted from the calculated damping coefficient k_I to obtain the net damping coefficient $k_I^* = k_I - \gamma k_R/\omega$. A critical value of ω may then be obtained at which the net damping is zero; at higher frequencies, growth of the wave is predicted.

(10) The adiabatic compression coefficient, γ_e , for the electron gas

There has been some uncertainty about the value of γ_e in electro-acoustic wave experiments.⁽²²⁾⁻⁽²⁵⁾ This quantity was omitted in the Tonks-Langmuir theory and was thus effectively set equal to 1. Since then the values 1, $5/3$ and 3 have each been suggested, under different plasma conditions.

The conditions under which each of the values of γ_e is applicable, are as follows. (a) Isothermal compressions; $\gamma_e = 1$: the compressions are isothermal if the thermal perturbation energy given to a volume element of the electron gas is either transported from the element or converted into some other form of energy (e.g. used to ionize or excite atoms) in a time which is much shorter than the wave period. (b) Adiabatic compressions, $\gamma_e = 5/3$ or 3: if the thermal perturbation energy is to a large extent not permitted to escape from the volume element but is distributed amongst the n degrees of freedom in the electron gas, in a time much shorter than the wave period, the perturbation is adiabatic and γ_e assumes the value $(n+2)/n$. The number n is usually equal to 3, although it has been argued that in the presence of a strong magnetic field parallel to the wave vector, n should be taken as 1.⁽²⁶⁾ If some of the thermal energy is converted or lost during a wave period, γ_e should lie between 1 and $(n+2)/n$, and the waves would then be heavily damped⁽²³⁾.

Little & Jones⁽²⁵⁾ put $\gamma_e = 1$ for waves in a low pressure (0.4 millitorr) mercury discharge. They give two reasons: (i) because of the long electron mean free path (~ 10 cm) any local perturbation of the electron thermal energy is rapidly dispersed through distances much greater than the wave length, and (ii) the neutral atoms act as a stabilizing influence on the electron temperature; the excitation probability is a very rapidly rising function of T_e , so that compressions will tend to be isothermal for this reason alone. To these reasons may be added the fact that the electron drift motion would rapidly remove the local increase of thermal energy still retained by the electrons after collisions with neutrals.

In the non-mercury plasma columns of the present experiments ($p \leq 30$ millitorr), where the electron mean free path is somewhat shorter than most of the wavelengths observed, the arguments given above are on the whole still in favour of the value $\gamma_e = 1$. This is supported by the fact that $\gamma_e = 1$ was obtained experimentally by Alexeff & Jones⁽²⁷⁾ from the time-of-flight measurement of an electro-acoustic pulse across a freely-drifting quiescent plasma at pressures 1-20 millitorr.

(11) History of experimental studies of electro-acoustic waves

Early studies. Two years after the Tonks-Langmuir prediction of electro-acoustic waves in 1929, partial evidence for their existence was found by T.C. Chow⁽²⁸⁾. This author measured the frequency of moving striations and the electron temperature at several pressures (between 70 and 700 millitorr) in a 2A argon discharge and observed that the length obtained by dividing the striation frequency into the velocity $(KT_e/m_i)^{1/2}$ was an integral or half-integral multiple of the tube length. As shown by Alexeff & Jones⁽¹⁵⁾, the striation phase velocities measured by Chow are in good agreement with those calculated from equation (5).

Further evidence was obtained by R.W. Revans⁽²⁹⁾ in 1933 from measurements on low pressure (~ 1 millitorr) mercury discharges, both spherical and cylindrical. Resonances were observed in the low frequency noise spectra, at frequencies related to $(KT_e/m_i)^{1/2}$ and the dimensions of the plasma; the author thought that these represented standing electro-acoustic waves.

During the 26 years after Revans' experiment, little further work on electro-acoustic waves was reported, although an unsuccessful attempt to observe them was made by Armstrong, Emeleus & Neill⁽³⁰⁾ in 1951. They injected 50 volt pulses onto an electrode situated near the cathode of a 10 mA, 1 millitorr mercury discharge and observed the responses of three probes situated at different distances along the column. Instead of observing a phase shift of the pulse, an apparently instantaneous response was observed at all the observation points, a result which was later confirmed in unpublished work by Kino & Woods (mentioned by Crawford & Kino⁽³¹⁾). In spite of the earlier experimental evidence, Armstrong et al arrived at a pessimistic assessment of the possibility

of finding small amplitude electro-acoustic waves, i.e. of amplitude sufficiently small for the potential fluctuations in the wave to be much less than T_e and for linearised theory to be applicable. They observed that no evidence of propagating waves of the type described by the Tonks-Langmuir relation (equ. (1)) had yet been reported and, because such factors as noise, density gradients and collisions had not been included in the Tonks-Langmuir theory, they believed it to be "uncertain if plasma-ion oscillations of small amplitude have ever been observed". (The word "oscillations" in this quotation presumably refers to propagating waves).

Anode-approaching striations. Experiments on artificially-excited moving striations were carried out from about 1951 by A.A. Zaitsev and his co-workers, and in 1959 the measurements on some of the inert gases were extended to lower pressures, by Vasil'eva, Zaitsev & Zndryukhina⁽¹²⁾. The striations were excited by means of an alternating voltage applied to a wire situated close to the cathode. It was found that at pressures of several tens of millitorr (or more) in helium, the striations travelled towards the exciter, but at $p \leq 10$ millitorr they travelled away from the exciter towards the anode. The same reversal was found in argon and xenon at about 4 millitorr. The observed velocity of the anode-approaching striations was about $1.7 (KT_e/m_i)^{1/2}$ in the helium discharge, and $1.1 (KT_e/m_i)^{1/2}$ in the argon discharge of slightly larger diameter and lower pressure. The helium result was shown by Liperovski⁽¹⁶⁾ to be in good agreement with the theoretical phase velocity of electro-acoustic waves in an unbounded plasma containing electron and ion drifts and collisions with neutral particles.

The reversal of direction of striations as the pressure is decreased was also observed by Alexeff & Jones⁽¹⁵⁾ in the case of spontaneously occurring striations. These authors measured the velocity of such striations in all the inert gases over a wide range of pressure. There was good agreement with the velocities calculated from equation (5) and the authors discuss briefly the possibility that moving striations are manifestations of electro-acoustic waves. In this connection they do not

distinguish between the anode-approaching and cathode-approaching waves, and it appears that the transition between the two types has not yet been explained.

Standing waves. Further observations of low frequency resonances in low pressure discharges have been carried out in the last five years by F.W. Crawford⁽³²⁾, Alexeff & Neidigh⁽²³⁾, Geller & Lucerain⁽³³⁾ and J.A. Decker⁽³⁴⁾. These results showed, as in the earlier experiment by Revans, that the resonant frequencies are related to c_s and the plasma dimensions. They raised the problem of the possible modes of the standing waves. In the case of radially directed standing waves of cylindrical discharges and those in spherical discharges, it was important to establish whether a pressure node or anti-node occurred at the containing wall. This problem was not solved, mainly because of the uncertainty in the value of γ_e .

Propagating Waves. The next observations of propagating electro-acoustic waves in positive columns, after those of Vasil'eva et. al., were carried out by P.F. Little⁽²⁾, Hatta & Sato⁽³⁾ and Alexeff & Jones⁽²⁴⁾. A different method of defeating the poor signal-to-noise ratio was used in each of these experiments. In an arc discharge of several amperes in mercury, with a localised alternating magnetic field as the exciter, Little used the phase sensitive detection technique described in section (17) to select the wave signal from the total detected signal, and recorded the phase and amplitude variation along the plasma column. Hatta & Sato resorted to a discharge of low current (~ 10 mA) and therefore of low noise. They excited a rapidly damped electro-acoustic wave by means of an alternating voltage applied to a plane grid near the anode; the wave propagated towards the cathode and was measured only over a distance of less than one wave length from the grid. Alexeff & Jones used a time-of-flight technique: a sharp voltage pulse applied between anode (earthed) and cathode of a glow discharge resulted in the detection of a pulse τ seconds later by a probe situated anywhere in the discharge. This was explained as follows: the initial pulse produces a plasma density pulse at the anode which, as they deduced from measurements with a special probe, travelled towards the cathode and, by partially neutralising

the electron space charge there, caused a drastic increase in the cathode emission. This was then detected almost instantaneously by the probe.

In the experiments of Little and Hatta & Sato, dispersion curves were obtained in 0.4 millitorr mercury and 40 millitorr argon discharges respectively, both of which agreed reasonably well with the theoretical curves presented. Little found that the curve approached a cut-off frequency $k_c c_s$ (where $k_c \approx 2.4/R$) at the longest wavelengths. The experimental curve obtained by Hatta & Sato is included in fig. 8(b). Despite the fairly good agreement with their theory it is not clear why the curve has two distinct slopes ($1.4 c_s$ and $0.85 c_s$); no mention is made of this fact in their report. The velocities of the electro-acoustic pulses in inert gases, measured by Alexeff & Jones, were fairly widely spread but were found to be proportional to $T_e^{1/2}$ and $m_i^{-1/2}$ and led to an average value $\gamma_e \approx 2$. It should be noted, however, that the velocity of an electro-acoustic wave travelling towards the cathode (if such a wave can survive the heavy damping predicted), could be increased by about 30% by the presence of the ion drift (see section 6). The value $\gamma_e = 1$ would then almost account for the values of wave velocity obtained by these authors. These authors later measured the time of flight of a pulse between two electrodes, across a freely drifting quiescent plasma, (mentioned in section (10)) and obtained $\gamma_e = 1$.

In a more recent experiment, Little & Jones⁽²⁵⁾ used the same phase sensitive detection technique to investigate the propagation of narrow-frequency-band components of the self-generated noise of the plasma, between a fixed and a movable probe or photomultiplier. The dispersion curve for these noise components was similar to that of the artificially excited waves except at the highest frequencies where the velocity of the noise components falls well below c_s . The curve approached a cut-off frequency at the longest wavelengths. The measurements on the noise components and those on excited waves without the steady B_z field⁽³⁵⁾ are reasonably well accounted for by the theory of L.C. Woods described in section (8).

Other plasmas. In the last four years, electro-acoustic waves⁽³⁶⁾-(38) have been observed in plasmas of other than the positive column type.

In an important experiment, Wong, D'Angelo & Motley⁽³⁶⁾ excited and detected such waves in low density caesium and potassium plasmas. These are steady state, highly ionized plasmas, produced by surface ionization of atoms on a hot tungsten plate and confined by a straight uniform magnetic field; the ion and electrons temperatures are equal ($\sim 2000^\circ\text{K}$). The main feature of the waves is the fact that the wave speed $\sim [(KT_e + KT_i)/m_i]^{1/2}$, lies within the spectrum of the ion velocity distribution; the waves are consequently subjected to heavy Landau damping (i.e. collisionless damping due to interchange of energy between the ions travelling at about the wave speed and the electric field of the wave). This was the first direct experimental evidence of such damping.

IONIZATION WAVES

(12) Recent history

Oscillations of the voltage and current of a d.c. discharge were investigated as long ago as 1923 by Appleton & West⁽³⁹⁾, but, apart from the work of W. Pupp⁽⁷⁾ in the nineteen-thirties, no thorough experimental study of these oscillations and the moving striations by which they are accompanied, was made until that of Donahue & Dieke in 1951.⁽⁶⁾ These authors observed spontaneous striations in the inert gases and mercury vapour at pressures of a few torr. They established that (i) spontaneous striations are large amplitude phenomena (the modulation depth of the light output is sometimes as large as 100%) which give rise to a modulation of the discharge current and voltage by a few per cent; (ii) the striations travel towards the cathode with velocities $\sim 10^4$ cm/sec, except in the region near the cathode where both cathode-approaching and much faster anode-approaching waves ($\sim 10^5$ cm/sec) may be observed together, and (iii) several different modes of oscillation, with different frequencies, exist within certain ranges of discharge current. It appears that the anode-approaching striations had not previously been observed. The authors supposed these to be associated with a negative space charge, moving in the direction of the electron drift, and called

them "negative striations". Conversely, the cathode-approaching striations were thought to be linked with a positive space charge and were called "positive striations". The nature of Donahue & Dieke's "negative striations" is discussed briefly in Appendix E.

Ionization wave studies were carried out in Moscow in the early nineteen-fifties by A.A. Zaitsev and his co-workers⁽⁴⁰⁾ and by B. Klarfeld⁽⁴¹⁾. Amongst other topics, Zaitsev studied the positive column conditions under which moving striations occurred spontaneously or were absent, and found that in a stable regime artificial striations could be excited by modulating the voltage across the discharge or by applying an alternating voltage to a wire electrode placed near the cathode. One of Zaitsev's co-workers, L. Pekárek, investigated the transient disturbance in a stable or quasi-stable column, resulting from a voltage pulse applied between anode and cathode⁽⁴²⁾ (in later experiments he set up the disturbance by means of a ring electrode round the positive column). Since then, Pekárek has used this transient disturbance technique in a detailed and sustained research programme into the nature and mechanism of moving striations^{(4), (5), (43)}; his is probably the most important contribution to the present understanding of the phenomenon.

B. Klarfeld presented a long, detailed experimental report⁽⁴¹⁾ in 1952 on moving and stationary striations in the inert gases and some other gases and vapours. He found that there was no essential difference between moving and stationary striations, a conclusion which was confirmed by Pekárek who showed that standing striations are only a special case of moving striations^{(4), (43a)}. Klarfeld and later authors found that moving striations in hydrogen travel only towards the anode, ~~and Klarfeld also observed this effect in some other molecular gases.~~ This behaviour has been only partially explained.^{(46) (78) (79)}

Both theoretical and experimental studies have been made in more recent years by K. Wojacek⁽⁴⁷⁾, who has obtained a dispersion curve in reasonable agreement with ionization wave measurements at high current densities in the inert gases (he included the two-stage ionization

process via meta-stable states⁽⁴⁸⁾; H.S. Robertson⁽⁴⁹⁾, who claims that ionization waves occur spontaneously, only if metastable atoms are present and if the quantity $M(\partial F/\partial N)$ (where M = metastable concentration, F = total rate of ionization of the meta-stable atoms by electrons, and N = electron number density) is positive and large enough to offset the stabilizing effects of diffusion and wall losses; Kenjo & Hatta⁽⁵⁰⁾, who derive a dispersion equation and obtain experimentally and theoretically a relation between wavelength and tube radius; Alexeff & Jones⁽¹⁵⁾ who have observed and accounted for the variation of the speed of cathode-approaching and anode-approaching (probably electro-acoustic) waves as a function of pressure, and R.S. Cooper⁽¹⁰⁾, who, like most of the authors in earlier years and all of those mentioned in this paragraph, has produced a theory for small amplitude ionization waves and has also carried out an extensive experimental study of ionization waves in both unstable and quasi-stable regimes. Theories have also been presented by A.V. Nedospasov,⁽⁵¹⁾ Watanabe & Oleson,⁽⁵²⁾ I.M. Čapnik⁽⁵³⁾, H. Rother,⁽⁵⁴⁾ A.B. Stewart⁽⁵⁵⁾ and other authors.

Experimental studies of the microphysical processes in ionization waves have been carried out by a number of authors including Boyd and Twiddy⁽⁵⁶⁾ (probe measurements of the electron velocity distribution in stationary ionization waves), A.B. Stewart⁽⁵⁵⁾ and R.S. Cooper⁽¹⁰⁾ (probe measurements on moving ionization waves), and Paik, Shapiro & Gilbert⁽⁵⁷⁾ (microwave absorption and density variation in moving ionization waves). It was found in the latter three experiments that the variations in T_e were not in phase with the variations in n_e ; Stewart and Cooper state explicitly that the shift in the T_e wave, relative to the n_e wave, was towards the anode. Cooper measured a phase shift of about 10% of a wavelength and Paik et. al. found a shift of about 15% of a cycle. Pekárek & Krejčí^(43f) show theoretically that such a phase shift is required for the growth (and therefore spontaneous occurrence) of ionization waves. Paik et. al. also observed that the variations in light intensity were in phase with those in T_e , and Cooper found the variations in T_e and the electric field to be in phase.

(13) The mechanism of ionization waves

The predominant view of striations in the theories of the last decade is that they represent a perturbation of the local ionization rate, due to the space charge fields set up by any perturbation of the ion density, and that their propagation is controlled by diffusion processes.

Following on from the theory developed in references (43c), (43d) and (43e), Pekárek describes the mechanism of the propagation of ionization waves by means of the following three equations describing the interdependence of ion density, electric field and electron temperature perturbations (58):

$$\epsilon = -\frac{E_0}{n_0} n_i - \frac{T_e}{n_0} \frac{\partial n_i}{\partial z} \quad (13)$$

$$\frac{\partial n_i}{\partial t} = D_a \frac{\partial^2 n_i}{\partial z^2} + Z'_\theta n_0 \theta \quad (14)$$

$$\frac{\partial \theta}{\partial z} - a\theta = -b\epsilon \quad (15)$$

where $\epsilon = E - E_0$, n_i and $\theta = T_e - T_{e0}$ are the perturbations in the electric field, ion density and electron temperature, n_0 is the unperturbed ion density, D_a the ambi-polar diffusion coefficient, Z the ionization rate per electron and $Z'_\theta = (\partial Z / \partial \theta)_{\theta=0}$; a and b are constants which depend on T_{e0} , E_0 , the electron mean free path and the mean fraction of energy lost by an electron per collision. These three equations are combined to form the integro-differential equation

$$\frac{\partial n_i}{\partial t} = D_a \frac{\partial^2 n_i}{\partial z^2} + T_e Z'_\theta b n_i - T_e Z'_\theta b \left(a + \frac{E_0}{T_e} \right) \int_z^\infty e^{a(z-\xi)} n_i(\xi) d\xi \quad (16)$$

The solution of this equation for different values of the plasma parameters is obtained by numerical analysis and reveals the development in time and space of an initial perturbation $n_i(z, t=0)$ which occurs in the immediate vicinity of $z=0$. Fig. 3 (a) (58)(5) illustrates the

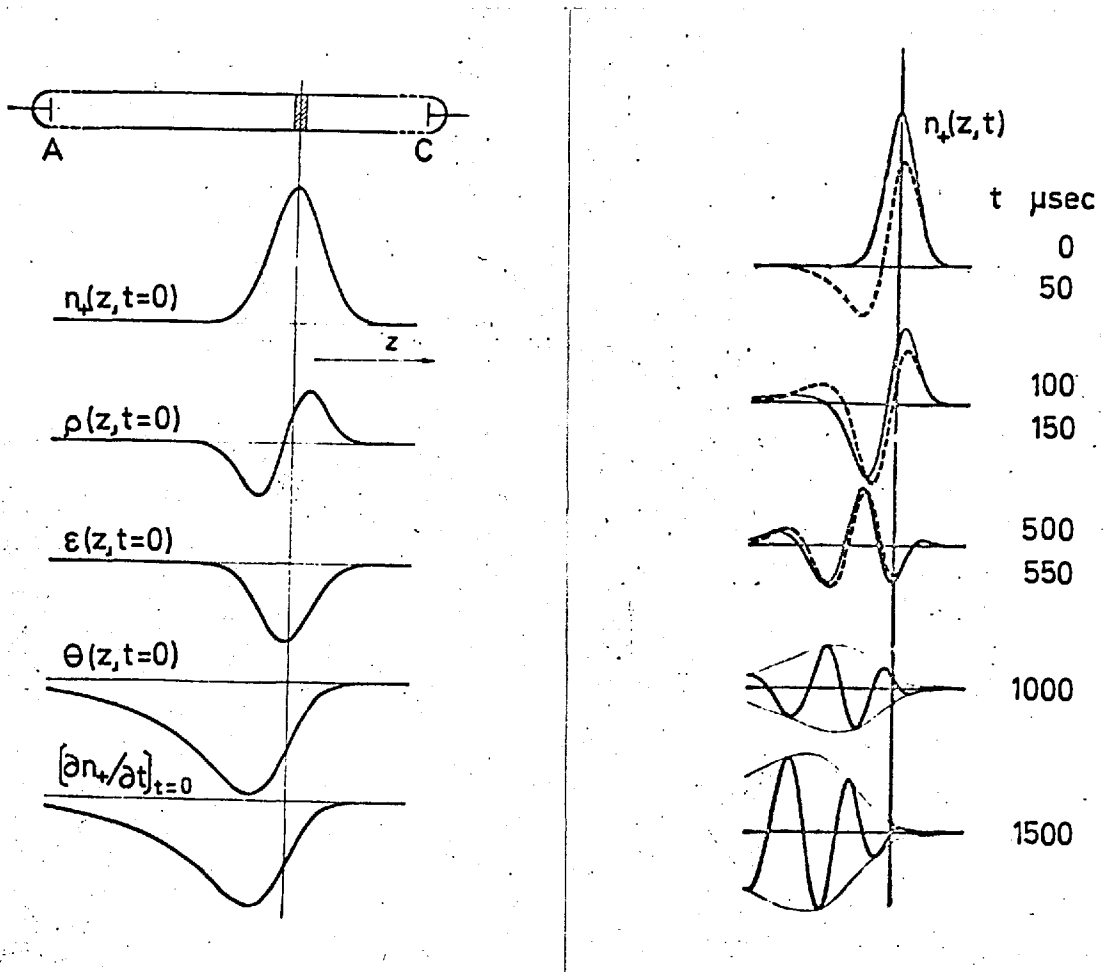


FIG 3 Propagation of striation wave packet. (a) Initial perturbations and (b) development of wave packet in time and space. From paper by L. Pekárek (refs. 5 and 58).

perturbations $\rho = n_+ - n_e$, ϵ , θ and $\partial n_+ / \partial t$ which accompany the initial perturbation.

The propagation mechanism is as follows. The increase in ion density, n_+ , is accompanied by an increase in electron density, n_e , where the maximum in n_e is slightly less than the maximum in n_+ , owing to the greater mobility of the electrons; n_e is also displaced towards the anode, effectively instantaneously, because of the electron drift. The resulting space charge ρ and space charge field ϵ are shown in the second and third curves of fig. 3(a). The field ϵ gives rise to the electron temperature perturbation θ which is also rapidly displaced towards the anode by the drift motion and which has the same sign as ϵ . This is accompanied by a decrease in $\partial n_+ / \partial t$ which is proportional to θ . The original increase in ion density at $z = 0$ has thus led to a decrease of ion density at a point nearer the anode, and the process is then repeated in reverse to produce an increase still nearer to the anode. A very similar diagram and description of the propagation mechanism are presented by Kenjo & Hatta⁽⁵⁰⁾.

The development of successive striations in time and space is shown in fig. 3(b)⁽⁵⁸⁾⁽⁵⁾. Each individual maximum in the ion density (i.e. each striation) decays with a time constant depending on the pressure and other plasma parameters. At the same time it is displaced in the direction of the cathode because the ionization rate is higher on that side of the maximum than at the maximum itself (see fig. 3(a)). The initial disturbance thus develops into a wave packet (named a "wave of stratification" by Pekárek) which propagates towards the anode; the centre of the wave packet moves at the group velocity v_g . The individual striations of the packet move backwards towards the position of the initial disturbance with the phase velocity v_p . Pekárek & Krejčí^(43e) have shown theoretically that for high current discharges, where ionization waves may only occur by artificial excitation, the group and phase velocities are approximately equal and opposite. This has been confirmed experimentally by Novák & Růžička⁽⁹⁾. In the case of spontaneous striations at lower values of the discharge current, v_p is usually an order of magnitude less than v_g ; it is not yet known

clearly why this happens although Pekárek & Krejčí⁽⁴⁾ have shown how the result $|v_p| < |v_g|$ may be obtained theoretically.

As observed in equations (13) to (15), the theory developed by Pekárek & Krejčí and Pekárek is one-dimensional; there are no terms containing $\partial/\partial r$ such as might be expected from the presence of a radial electric field and density gradient. The theory nevertheless accounts for the following observed features of moving ionization waves excited in a stable regime of the positive column:

- (i) a single pulse disturbance produces a packet of striations which travels away from the disturbance towards the anode with velocity v_g ; no striations appear on the cathode side of the disturbance;
- (ii) the individual striations travel towards the position of the disturbance with velocity v_p ;
- (iii) at high discharge currents (above the Pupp limit) $v_g \approx -v_p$ and the observed values of v_g and v_p are within an order of magnitude of the calculated values (on assuming reasonable values for one or two unmeasurable plasma parameters);
- (iv) with increasing distance towards the anode, the striation wavelength and the width of the wave packet increase slowly and the striation frequency decreases slowly.
- (v) there is an optimum wavelength which the striations assume.

The significance of each of the three terms on the right hand side of equation (16) is as follows. The first term describes the damping of the waves by the ambi-polar diffusion of ions in the z direction. The shorter the wavelength, the heavier is the damping, and so the diffusion sets an approximate lower limit on the wavelength. The third term is the only one which is oscillatory; this term contains the constant a which is the reciprocal of the characteristic distance over which the electron temperature perturbation (and therefore $\partial n_+/ \partial t$) is damped; it sets an upper limit on the striation wavelength. The second term describes the wave growth which occurs when ϵ has a positive value at the maximum in n_+ (or when the T_e wave is shifted towards the anode, relative to the ϵ wave).

In their theory of ionization waves at high currents (i.e. where the electron Debye length is much shorter than the wavelength), Pekárek & Krejčí^(43e) derive an expression for the ion density perturbation at (z, t) from which a dispersion equation is obtained. This is discussed in section IV (7) where a simplified form of this equation is shown to be in fairly good agreement with the dispersion curves for the backward waves observed in the present experiments.

CHAPTER II

APPARATUS

The apparatus for these experiments was previously used by Little & Jones for electro-acoustic wave studies and is described briefly in references (2) and (25). The main elements of the discharge apparatus are shown in fig. 4 and a block diagram of the apparatus for generating and detecting the waves is given in fig. 5.

(14) Discharge apparatus

A discharge of several amperes was obtained most conveniently by the use of a mercury pool cathode C. The positive column occupied almost the entire volume of the discharge and constituted a plasma of about 10^{11} ions or electrons per c.c. The number density of neutral atoms was in the range 10^{13} - 10^{15} cm^{-3} . The diameter of the main tube was 5 cm; a positive column of diameter 3 cm. was obtainable, when required, by the insertion of a 3 cm. tube inside the main tube. The length of the horizontal part of the column was 110 cm, most of which lay inside the magnetic field coils F. The hot spot on the mercury surface was kept stationary by the nickel cylinder N. A nickel umbrella U shielded the discharge from jets of mercury emanating from the cathode spot.⁽⁵⁹⁾ The electrode S was used for starting the discharge; it was covered with a glass sleeve over its lowest three centimetres in order to lengthen the ignition spark. The discharge was earthed at the anode A which was a plane water-cooled copper disc, nickel-plated to minimise the deposition of anode material on the tube wall. The auxiliary electrode D was similarly plated and could be water-cooled for use as a second anode; otherwise, when at floating potential, it helped to prevent the discharge from striking onto the nearby baffle valve and vacuum gauges. The discharge tube was joined to the remainder of the vacuum system by means of "Viton-A" O-rings which were capable of withstanding temperatures of the order of 200°C .

The discharge current was supplied by a 400V, 20A motor-generator set with a limiting resistor between generator and cathode. No smoothing

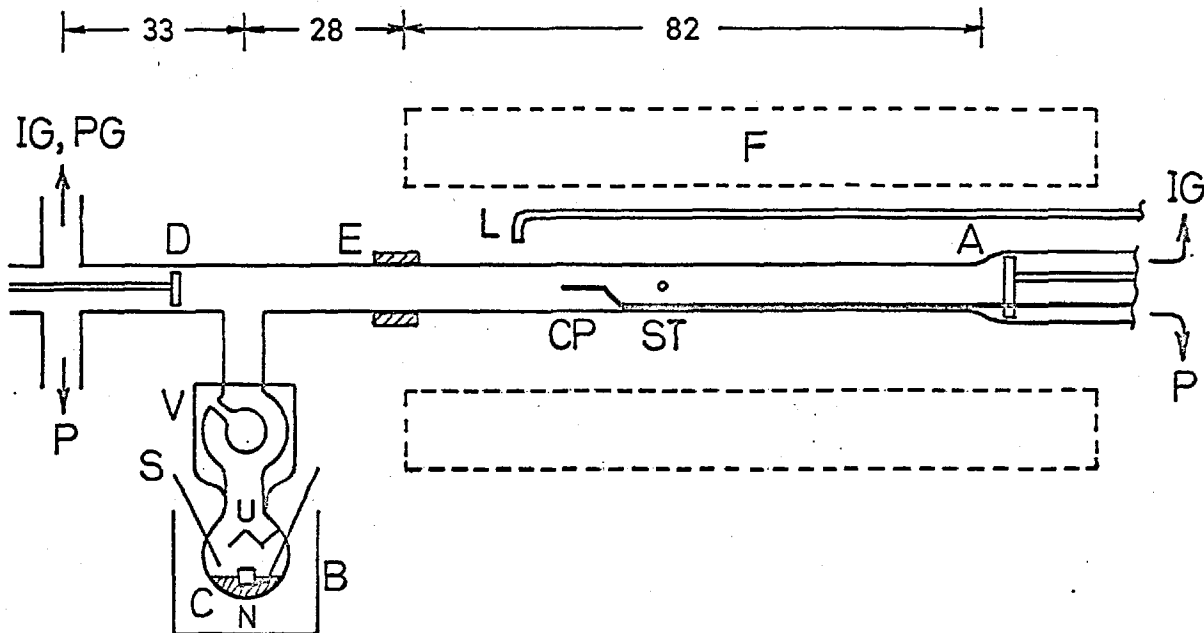


FIG 4 Discharge apparatus. A anode, B cooling bath, C mercury pool cathode, D floating disc or auxiliary anode, E exciter coil, F magnetic field coils, IG ionization gauge, PG Pirani gauge, L light guide, N nickel cylinder, P baffle valve and vacuum pumps, S starter electrode, CP cathode-facing probe, ST side tube for radial probe, U nickel umbrella, V cold trap. Dimensions in centimetres.

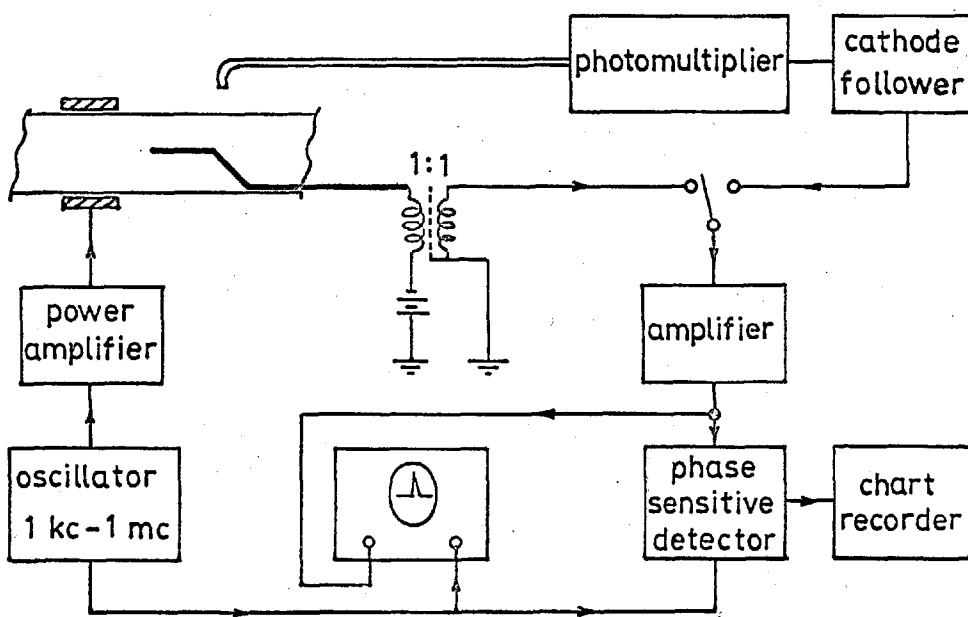


FIG 5 Apparatus for generating and detecting waves of plasma density.

circuit was included because the wave frequencies were all much higher than the ripple frequency of the voltage supply.

The pressure in the mercury discharges was measured by two ionization gauges, situated in large diameter side tubes at either end of the main tube. In the other gas discharges the pressure was much higher and could be measured only by the Pirani gauge, which was placed at the cathode end of the discharge.

The mercury vapour pressure in the plasma column was determined mainly by the temperature of the cooling bath surrounding the mercury pool and by the pumping speed at either end of the tube. A steady pressure was maintained by keeping the bath temperature constant to within 0.1°C ; this was found by Little & Jones to be essential for obtaining reproducible measurements of electro-acoustic waves. The pressure range over which the mercury discharge could be operated was 0.05 - 5 millitorr.

(15) The non-mercury plasma columns

When a non-mercury plasma column was required in the horizontal tube, the cold-trap above the cathode was filled with liquid nitrogen, which effectively prohibited the passage of mercury vapour into the tube. The latter was then provided with a steady stream of gas and an arc was established, with the mercury pool still acting as the cathode. This technique for obtaining continuous high current discharges in gases other than mercury vapour has been described by Allen & Magistrelli⁽⁵⁹⁾. It appears from their measurements that the mercury vapour on the anode side of their trap, which contained dry ice, constituted no more than about 0.01 of the gas number density. It may be shown that this degree of impurity would decrease the speed of electro-acoustic waves in the gas by a factor $(1 - 0.01)^{\frac{1}{2}}$.

The gases used were neon, argon and hydrogen, in the pressure range 10 - 30 millitorr. A needle valve was used to control the inflow of either neon or argon. In the case of hydrogen, the gas was allowed to leak into the discharge through the wall of a heated nickel tube; this provided a finer control of the flow rate and also purified the gas. The gases were let in at the cathode end of the discharge tube, so the baffle

valve at that end was closed and the other one slightly opened to allow the flow of a steady stream of gas along the main tube.

The strong disadvantage encountered with this experimental arrangement was that the discharge tube often cracked or imploded, usually at the cold-trap where the glass was under strain from the large temperature gradients. When the discharge was run in neon or argon, only a few hours of operation were obtained before tube failure occurred. The circumstances and the probable underlying cause of the cracking are described in Appendix F.

(16) Magnetic fields

The steady longitudinal magnetic field was provided by fifteen 8-turn coils, F, spaced so that the field was uniform to within 1% over most of the experimental region of the positive column. Two motor-generator sets were capable of supplying fields in the ranges 0 - 60 and 0-600 gauss respectively.

An alternating magnetic field in the range of a few milligauss to a few gauss was produced by the exciter coil E. This was used in the frequency range 4 - 160 kc/s. The coil consisted of 24 turns in a single layer of width 2 cm. The most effective generation of waves was obtained when E was situated in the region of non-uniform field at the end of the field coils. An explanation of this is given in Appendix G.

(17) Diagnostic apparatus

Langmuir probes. Most of the measurements on wakes and some measurements on waves were carried out by means of the cathode-facing Langmuir probe CP; the plasma parameters were in general obtained with the radial probe RP. Each of these presented to the plasma a plane 0.25 mm platinum wire tip. The details of construction of CP are given in fig. 6. This shows the final design used by Little & Jones to meet the requirements that the probe should be accurately positioned along 60 cm of the column and across the column, and that it should perturb the plasma as little as possible.

By using ceramic tubes (d, e and f) and ceramic cement (g), it was possible to construct a thin, fairly rigid probe, with a total length

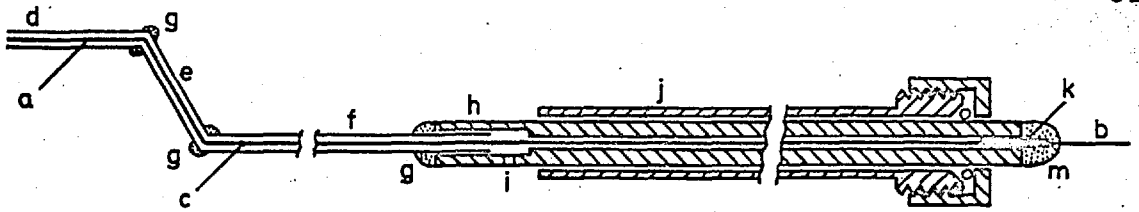


FIG 6 Details of Langmuir probe. a 0.25 mm platinum wire; b copper wire with glass fibre sleeve; c hard solder joint; d, e ceramic tubes 0.5 mm o.d.; f ceramic tube 2 mm o.d., 100 cm long; g Melbond ceramic cement; h thick-walled copper tube 4 mm o.d., 100 cm long; i hole for evacuation; j brass tube 6.5 mm o.d., with o-ring fitting; k ceramic sleeve; m araldite bond.

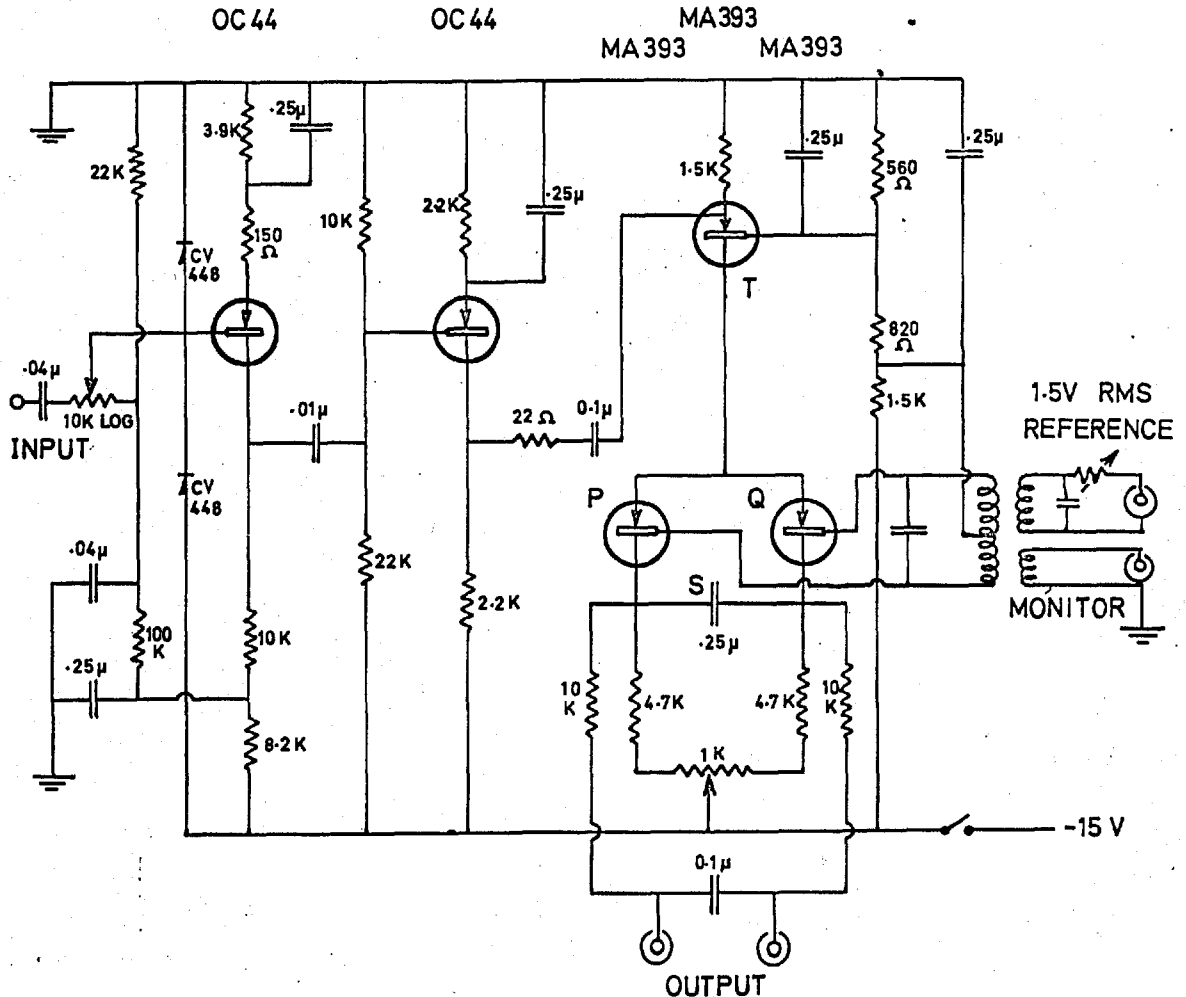


FIG 7 Circuit for phase sensitive detector. 5 - 100 kc/s. Frequency range 5 - 100 kc/s.

of almost 200 cm. Segment d was made sufficiently long for the perturbation of the plasma at the probe tip by the stem e to be negligible. (The problem of plasma perturbation by probes has been studied by Paulikas & Pyle⁽⁶⁰⁾).

The platinum wire tip was made flush with the end of the ceramic tube by cutting it as close to the tube end as possible, with a razor blade, and then grinding it with a flat piece of fine india stone. By sufficiently gentle grinding it was possible to avoid increasing the area of the tip appreciably and to leave an annular gap of about 0.02 mm between the tip and the ceramic. Such a gap was required to prohibit sputtering from the tip onto the ceramic, which would have altered the probe collecting area.

The ceramic tube f passed out of the plasma column through a narrow slit at the bottom of the anode and fitted tightly into the copper tube h. Further to the right (in fig. 4) the probe passed through a sliding vacuum seal (Wilson seal). It could be driven axially through the seal at a speed of 1.3 mm/sec by a synchronous motor (Drayton, Type RQ) and rotated at 40 degrees of arc per minute by a small synchronous motor.

The probe circuit for the wave experiments is shown in fig. 5. For the detection of plasma density waves the probe was held at a strongly negative potential (approximately - 50 volts) so that it measured fluctuations in the ion current. The purpose of the 1:1 transformer, containing an earthed screen between windings, was to eliminate the fluctuations in plasma potential picked up by the probe; only the fluctuations of ion current were transmitted to the phase sensitive detector.

Photomultiplier. Light from a narrow section of the positive column was transmitted to the photomultiplier outside the magnetic field, via a short collimator tube (0.5 mm diameter) and a 2-metre perspex rod with a right angle bend near the collimator; the rod lay inside an opaque tube and acted as a light guide. The acceptance angle of the collimator set a lower limit of about 1 cm to the wavelengths observable. Photomultiplier and light guide could be driven parallel to the discharge tube by a synchronous motor identical to that which moved the probe CP.

The photomultiplier signal passed through an emitter-follower transistor circuit to an amplifier and then to the phase sensitive detector.

Phase sensitive detector. A commutator type of phase sensitive detector⁽⁶¹⁾ was used to detect the wave signal against the background noise in the signal from either the probe or photomultiplier. The circuit diagram is given in fig. 7.

The essential mechanism of the circuit is as follows. The signal-plus-noise input is amplified by means of the two OC44 transistors and then modulates the current through the transistor T. This current passes through transistors P and Q which, because they operate close to cut-off, are alternately switched off by the reference signal for half a period at a time. The condenser S and its parallel resistance have a long time constant ($\tau = 0.002$ sec). The current I, through P and Q, which has the same frequency ω as the reference signal, is integrated to give condenser S a charge of the order of $(\pi + \alpha)/\omega$

$$(\omega\tau/2\pi) 2I \int_{\alpha/\omega}^{(\pi + \alpha)/\omega} \sin \omega t \, dt \approx \tau I \cos \alpha$$

where $\pm \alpha$ or $\pi \pm \alpha$ is the phase difference between the reference signal and the signal emerging from T. As the latter is proportional to the amplitude A of the signal from the probe or photomultiplier, the output voltage obtained from S is proportional to $A \cos \alpha$.

The random noise components in the current through P and Q contribute almost nothing to the voltage across S because (i) the integration over a period τ eliminates the components whose frequency differs from ω by more than π/τ , and (ii) the noise components are comprised of wave trains of duration $\ll \tau$ and of random phase, so that even those lying in the frequency range $\omega - \pi/\tau$ to $\omega + \pi/\tau$ are integrated to approximately zero.

It should be noted that as far as the wavelength of a wave in the plasma column is concerned, the phase sensitive detector makes no distinction between propagating waves (e.g. $\sin(\omega t - kz)$) and standing waves (e.g. $\sin \omega t \cos kz$). This distinction can only be made by

looking for a phase shift between the detected and reference signals on the oscilloscope (if the detected signal is observable and is not masked by a stronger constant-phase signal⁽²²⁾ which could be conducted along the column), or by consideration of the experimental conditions and of the damping shown by the chart recorder traces. The mechanism of the backward waves allows them to travel only in one direction, and forward waves towards the cathode are probably eliminated by heavy damping (section (6)); therefore no standing waves are considered to occur in the present experiments.

CHAPTER III

EXPERIMENTAL RESULTS

(18) All the dispersion curves were obtained with the exciter coil situated at the cathode end of the magnetic field coils, 26 cm from the right angle bend of the discharge. The amplitude of the exciter field was sometimes as large as 3 or 4 gauss, but more often less than 1 gauss. For the low frequency backward waves an exciter field of the order of 10^{-2} gauss was usually sufficient to produce clear waves in the output signal of the phase sensitive detector. Two dispersion curves were obtained from the mercury column without the steady longitudinal magnetic field B, but most of the waves were recorded with B = 10, 15 or 20 gauss (usually 15 gauss). A few isolated points were obtained at B = 0 in neon and hydrogen.

The dispersion curves were obtained with the photomultiplier acting as the detector; this integrates the wave signal from all parts of the plasma column lying within the narrow acceptance cone of the collimator. Almost as good a sensitivity was attainable with the moving cathode-facing probe as detector. A few wave traces were recorded with the latter in order to investigate the variation of the forward wave amplitude and phase with r, the distance from the axis.

At all the discharge conditions used in these experiments (p = 0.3 - 30 millitorr, $I_p = 2.5 - 8A$, B = 10-20 gauss) waves were readily observable in the output signal from the phase sensitive detector. They were also often observable on the double beam oscilloscope when the signal was obtained from a portion of the plasma column close to the exciter, but only in certain cases was the wave at larger distances from the exciter discernible on the oscilloscope. It was then occasionally possible to see a shift of the detected wave signal relative to the exciter signal. As mentioned at the end of section (17), the phase sensitive detector does not distinguish between propagating and standing waves but it is considered that none of the waves detected in these experiments were standing waves.

(19) The two groups of dispersion curves

The curves of ω against k obtained from the discharges in four different gases (neon, argon, hydrogen and mercury vapour) fall into two groups: those having negative slope (backward waves) and those having positive slope (forward waves). A negative slope means that the phase and group velocities are in opposite directions: the wave energy is propagated away from the exciter but each individual wave "crest" or "trough" moves towards the exciter, as described in section (13). A positive slope implies that both phase and group velocities are in a direction away from the exciter. The two groups will be referred to as backward and forward waves respectively. These curves are presented in fig. 8(a) and (b), together with curves obtained by other observers for backward waves in mercury⁽²²⁾ and helium⁽¹²⁾, and forward waves in argon⁽³⁾, hydrogen⁽⁴⁵⁾⁽⁶²⁾ and helium⁽¹²⁾; the discharge conditions for each curve are listed on the following page. The curves obtained in the present experiments are later shown separately on a larger scale and discussed in more detail. We shall here consider simply the empirical dispersion equations which best fit the curves of fig. 8.

Backward waves. The backward waves may be described to a rough approximation by the empirical relation

$$\omega k = \text{constant.} \quad (17)$$

The curves for the backward waves in mercury are fairly accurately represented by this relation. A marked reduction in ωk at the lower frequencies is observed in the neon and argon curves; the long wavelength dispersion curve in argon for example fits the equation $\omega/k = a(\omega + b)^2 - c$ where $a = 2.5 \times 10^{-5}$ cm sec, $b = 2\pi \times 10^4$ rad/sec and $c = 1.6 \times 10^5$ cm/sec. Some idea of the departure of each experimental curve from equation (17) is given by the following table in which X is the factor by which ω decreases from top to bottom of the curve and Y is the corresponding factor by which ωk decreases (ωk increases in the case of the mercury column with $B = 15$ gauss):

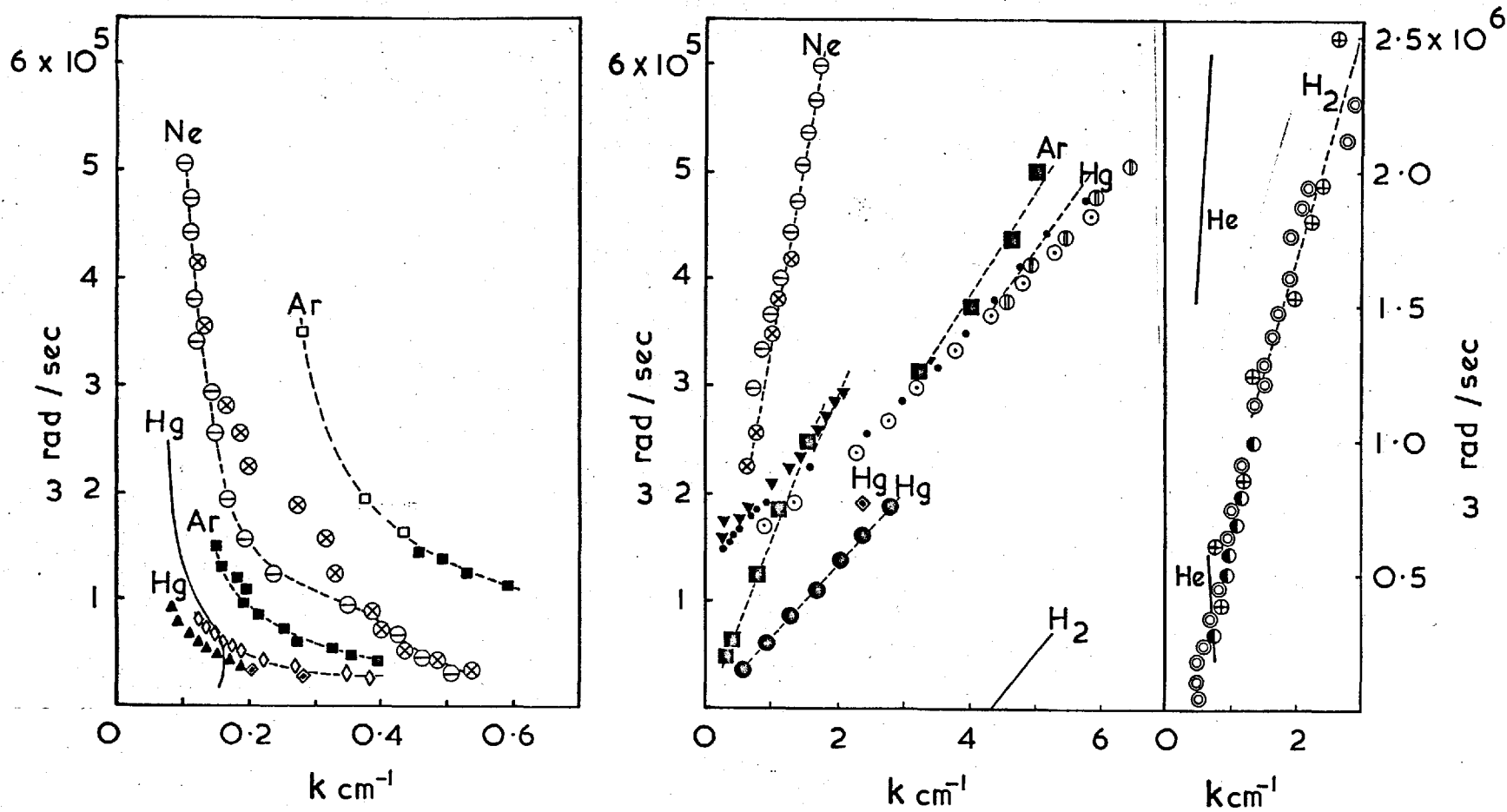


FIG 8 (a) Dispersion curves for backward waves. (b) Dispersion curves for forward waves.

Table I(a) Discharge parameters for backward waves

Symbol	Gas	T_e (eV)	p (m Torr)	B_z (gauss)	E_z (V/cm)	I_D (A)	N_e (cm^{-3})	Diam	Ref
⊖	Ne	7.0	26	15	0.7	6	0.6×10^{11}	5	
⊗	Ne	7.2	18	15	0.7	6	1	5	
□	Ar		30	15		5.5	5	5	
■	Ar	3.4	14	15	0.7	5	4	5	
◇	Hg	2.5	2-5	0	0.25- 0.35	7.5	5	5	
▲	Hg	1.5	2	15	0.25	7.5	5	5	
◊	Hg	2.5	0.6	15	0.1	7.5	2	5	
Solid curve	Hg	2.0	2	0		0.1		2.2	22

Table I(b) Discharge parameters for forward waves

Symbol	Gas	T_e (eV)	p (m Torr)	B_z (gauss)	E_z (V/cm)	I_D (A)	N_e (cm^{-3})	Diam	Ref
⊖	Ne	7.0	26	15	0.7	6	0.6×10^{11}	5	
⊗	Ne	7.2	18	15	0.7	6	1	5	
■	Ar	0.6	40	0	~0	0.01	0.025	~5	3
▼	Hg	5.2	0.4	45	0.1	9		5	2
⊖	Hg	2.2	0.4	0	0.1	9		5	35
•	Hg	3.5	0.4	15	0.1	8	2	5	
◊	Hg	2.5	0.6	15	0.1	7.5	2	5	
●	Hg	4.2	0.3	20	0.1	8	0.3	3	
○	Hg		0.4	0		8		5	
Solid curve	H ₂		10^3	0		0.13		2	45
⊙	H ₂	5.4	20	40		2.8		5	62
⊕	H ₂	5.4	20	10		4		5	62
●	H ₂	6.1	17	10	1.1	2.5	0.5	5	
Solid curve	He	18	10	0	2	0.03		3	12

Table 2.

Curve	X	Y
Neon	16	3
Argon (long λ)	7	1.6
Argon (short λ)	3	1.5
Mercury (B=15)	4	1.2 ⁻¹
Mercury (B=0)	3	1.2

Forward waves. The forward waves are mainly of the form

$$\omega/k = a(KT_e/m_i)^{1/2} = ac_s \quad (18)$$

where $0.4 < a < 1.4$, except at the lower frequencies where some of the curves approach a cut-off in frequency or wave number.

In the high frequency region, the curves for the non-mercury columns are all described by equation (18), but in the 5 cm diameter mercury column at 0.4 millitorr the curves are represented by $\omega = 0.6 c_s k + 2c_s/R$ at $B = 0$ and $\omega = 0.5 c_s k + 1.5 c_s/R$ at $B = 15$ gauss. These are of the same form as the high frequency portion of the (0,1) mode described by L.C. Woods (see section (8)): $\omega = 0.72 c_s k + 2.2 c_s/R$.

In the low frequency region, the curves for the 0.4 millitorr, 5 cm mercury column approach a cut-off frequency of about 1.5×10^5 rad/sec, and the curve obtained from the hydrogen column approaches a cut-off wave number of about 0.5 cm^{-1} . Both of these cut-off values were obtained by Little & Jones⁽²⁵⁾⁽⁶²⁾. The cut-off wave number is simply the wave number of stationary striations in the hydrogen column when no excitation is applied. The remaining curves conform to equation (18).

(20) Waves in mercury vapour

The dispersion curves for waves in mercury vapour were obtained under the eight different sets of experimental conditions listed in the following table (with $I_D \approx 8A$):

Table 3.

Symbol	p millitorr	B gauss	Diam. cm
●	0.4	15	5
⊙	0.4	0	5
◇	0.6 - 1	15, 22	5
●	0.3	15, 20	3
○	0.9	15	3
◇	2 - 5	0	5
▲	2	15	5
—	5	15	5

We shall consider the features of the waves corresponding to each set of conditions.

Curves ● and ⊙. These curves are drawn on a larger scale in fig. 9 together with eight points which appear scattered at random at low exciter signal frequencies. The true frequencies of these eight points are assumed to be higher harmonics of the exciter frequency (the order of the harmonic is marked alongside each point), in which case the eight points should all be shifted upwards onto the experimental curve marked ●. Such harmonics are generated at the larger values of the exciter signal and are sometimes observable on the oscilloscope.

Two theoretical curves representing L.C. Woods' (0, 2) mode at two different electron temperatures are also shown in fig. 9. These are in agreement with the experimental curves in two main respects: they approach a cut-off frequency as the wave number becomes small and they lie well below the $\omega = kc_s$ line at the higher frequencies.

The damping of the waves marked ● and ⊙ is represented in fig. 10 in which the imaginary part k_I of the wave number is plotted against the frequency. In the case of the waves obtained at $B = 15$ gauss (marked ●) there is a rise in k_I from 0.03 to 0.08 cm^{-1} as the frequency increases from 1.5×10^5 to 2.7×10^5 rad/sec. Over the same frequency range (at $p = 0.4$ millitorr, $B = 45$ gauss, $I_D = 9A$, $d = 5$ cm) Little & Jones⁽²⁵⁾ observed k_I to rise from 0.04 to 0.20 cm^{-1} . At

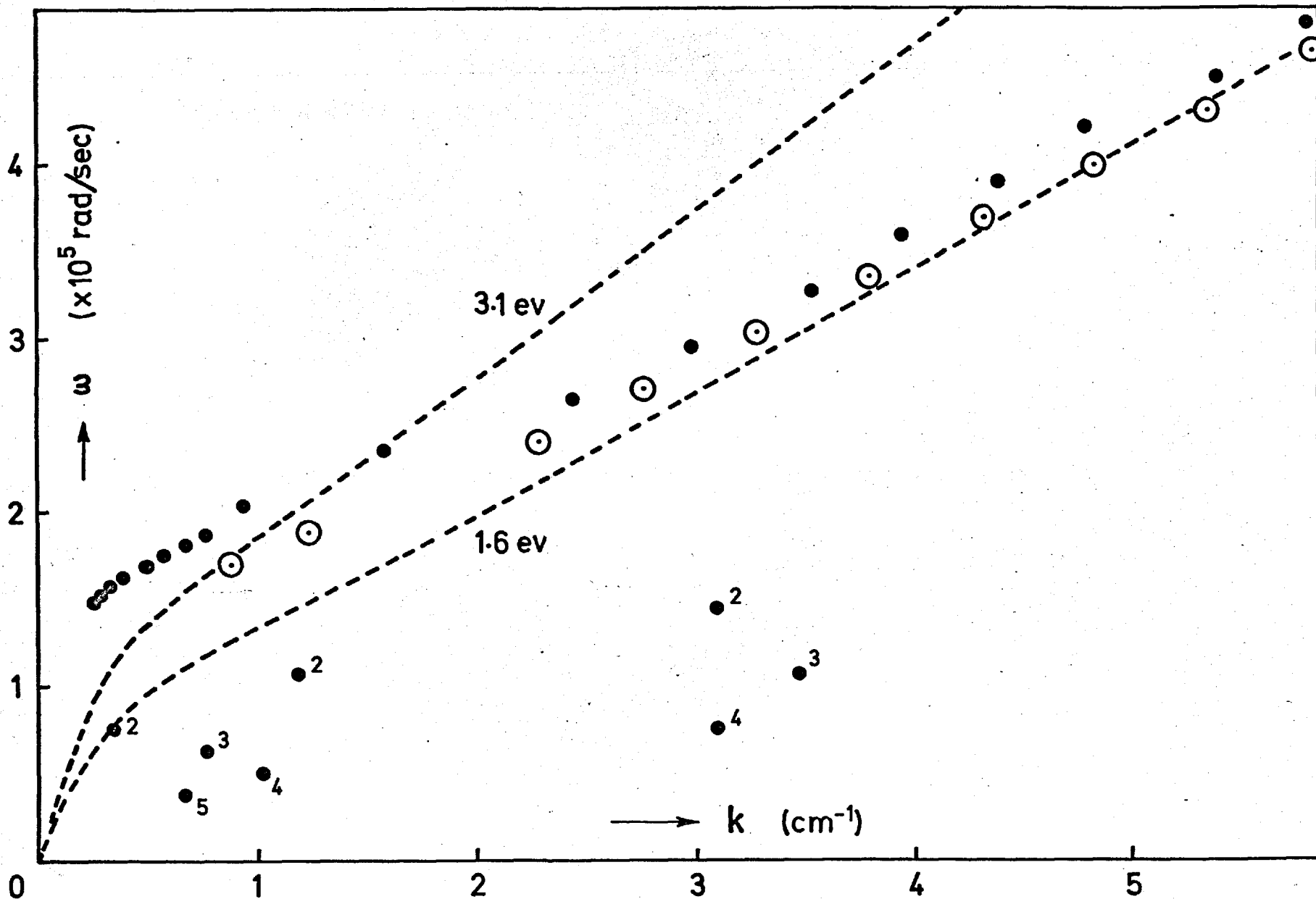


FIG 9 Dispersion curves for forward waves in mercury. $p = 0.4$ mtorr, $d = 5$ cm.
 ● $B = 15$ gauss, ○ $B = 0$. Numbered points represent higher harmonics,
 plotted at exciter frequency. ---- (0,1) mode from theory of L.C.Woods.
 at two values of T_e .

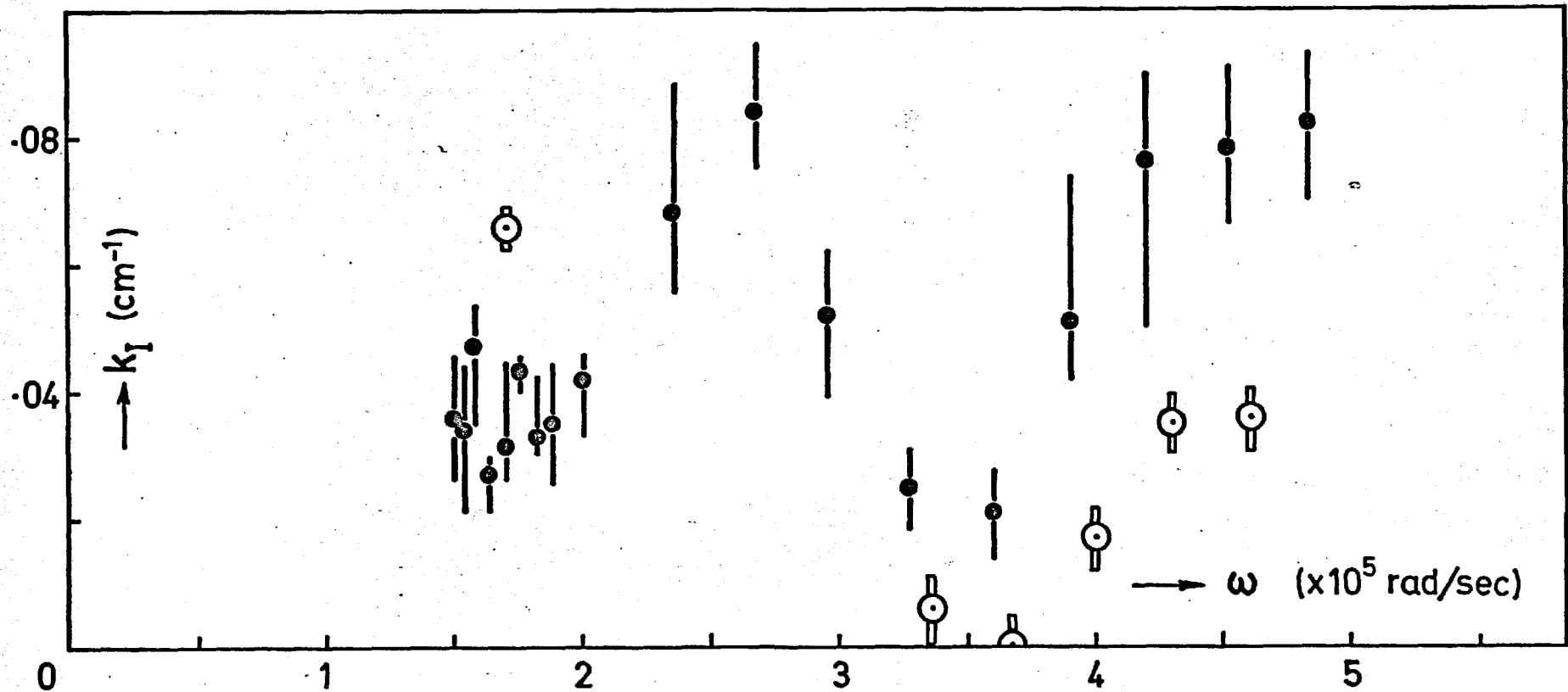


FIG 10 Damping of forward waves in mercury. $p = 0.4$ mtorr, $d = 5$ cm.
 ● $B = 15$ gauss, ○ $B = 0$. Error bars represent variation in k_I along wave train.

slightly higher frequencies there is a sharp decrease in k_{\perp} to about 0.02 cm^{-1} where particularly long wave trains of high signal-to-noise ratio are obtained; thereafter the damping again increases with ω . Similar behaviour in k_{\perp} was observed at $\omega > 3 \times 10^5 \text{ rad/sec}$ under the zero-field condition (waves marked \odot). The values of k_{\perp} at the lower frequencies are not included because of the poor quality of the wave trains in this region; at the lowest frequencies, however, k_{\perp} at $B = 0$ was roughly double the values obtained at $B = 15 \text{ gauss}$. The error bars in the values of k_{\perp} represent the extremes in the estimated average value of k_{\perp} from the wave traces, taken over the main region where the wave amplitude changes; the first few wavelengths from the exciter position, where k_{\perp} is often negative (representing wave growth), or zero, are ignored.

Examples of the wave traces obtained under the conditions \bullet and \odot are given in figs. 11(a) and (b) and fig. 12.

Curves \diamond . At slightly higher pressures, 0.6 - 1 millitorr, both backward and forward waves were obtained. The backward wave traces were of poor quality and so the value of k_{\perp} for these waves (of the order of 0.03 cm^{-1}) was difficult to estimate. These waves were observable only at frequencies $\lesssim 0.5 \times 10^5 \text{ rad/sec}$, down to $0.25 \times 10^5 \text{ rad/sec}$ which is the lower frequency limit of the phase sensitive detector. They are represented in fig. 8(a) and again in fig. 16.

The higher frequency waves in the same pressure region were forward waves, some of which are represented in fig. 8(b). A more detailed graph, fig. 13, contains three groups of points marked \diamond : a low frequency group lying on a line at a slope of $0.5 c_s$; a higher frequency group at a slope of $0.75 c_s$, and another higher frequency group lying on the theoretical (0,1) mode curve for $T_e = 2.5 \text{ eV}$. It was noted that the two lowest points of the second group (A' and B') were produced by a fairly large exciter signal; at smaller exciter signals the waves at these two frequencies are represented by the two uppermost points (A and B) of the third group.

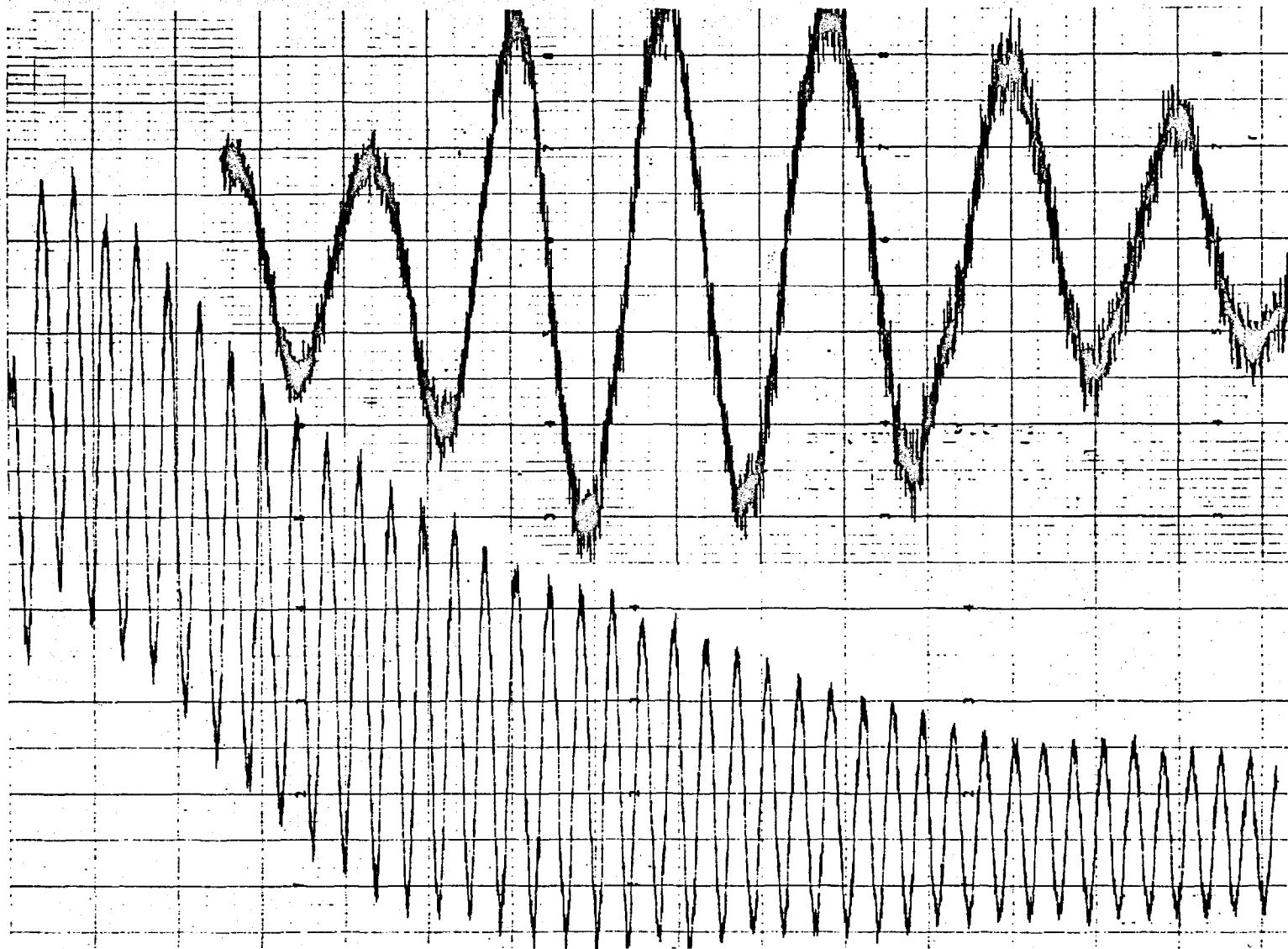


FIG 11 (a) Wave traces at 1.9 and 3.6×10^5 rad/sec from mercury discharge.
 $p = 0.4$ mtorr, $B = 15$ gauss, $d = 5$ cm. Forward waves.

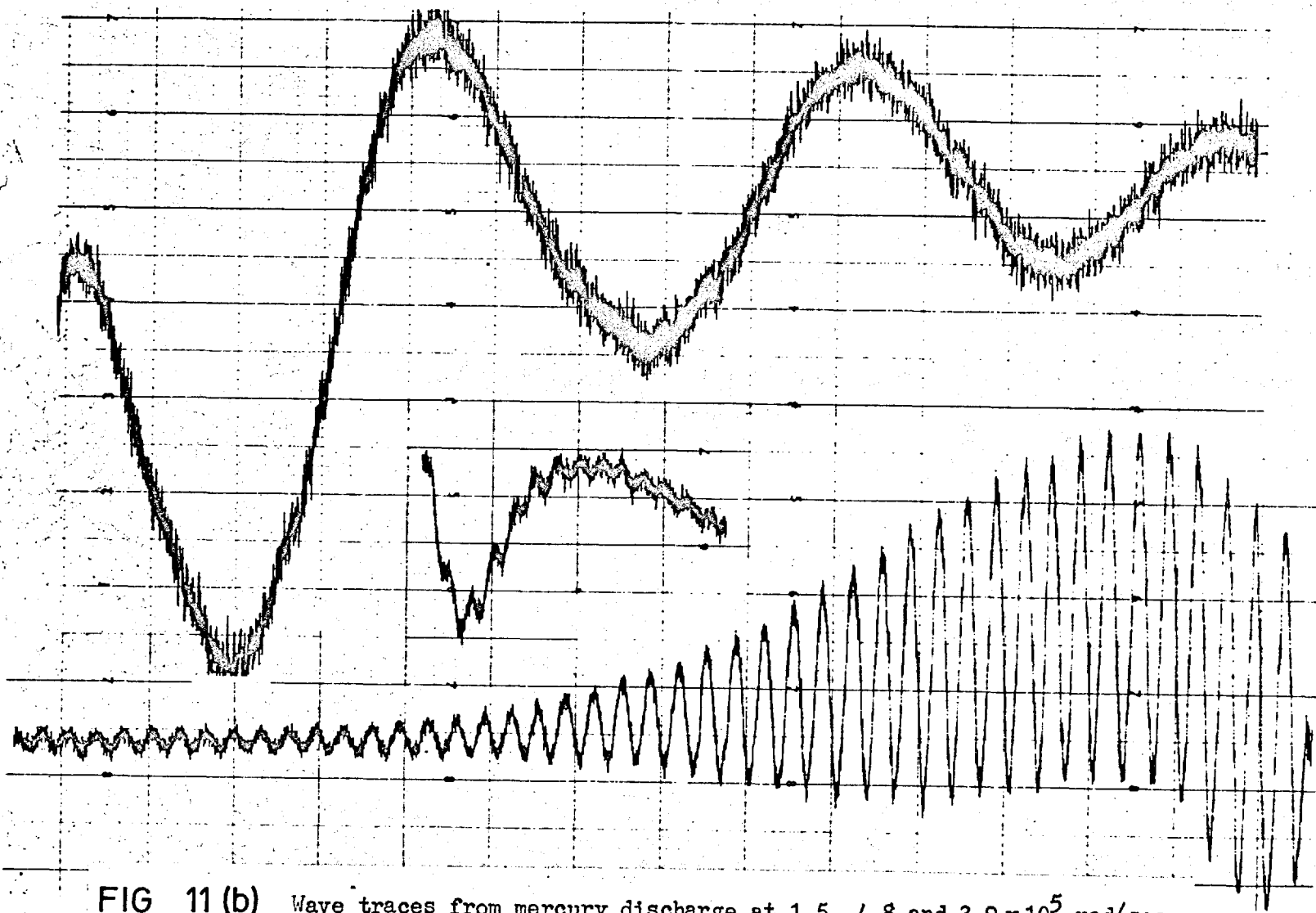


FIG 11 (b) Wave traces from mercury discharge at $1.5, 4.8$ and 3.9×10^5 rad/sec.
 $p = 0.4$ mtorr, $B = 15$ gauss, $d = 5$ cm. Forward waves.

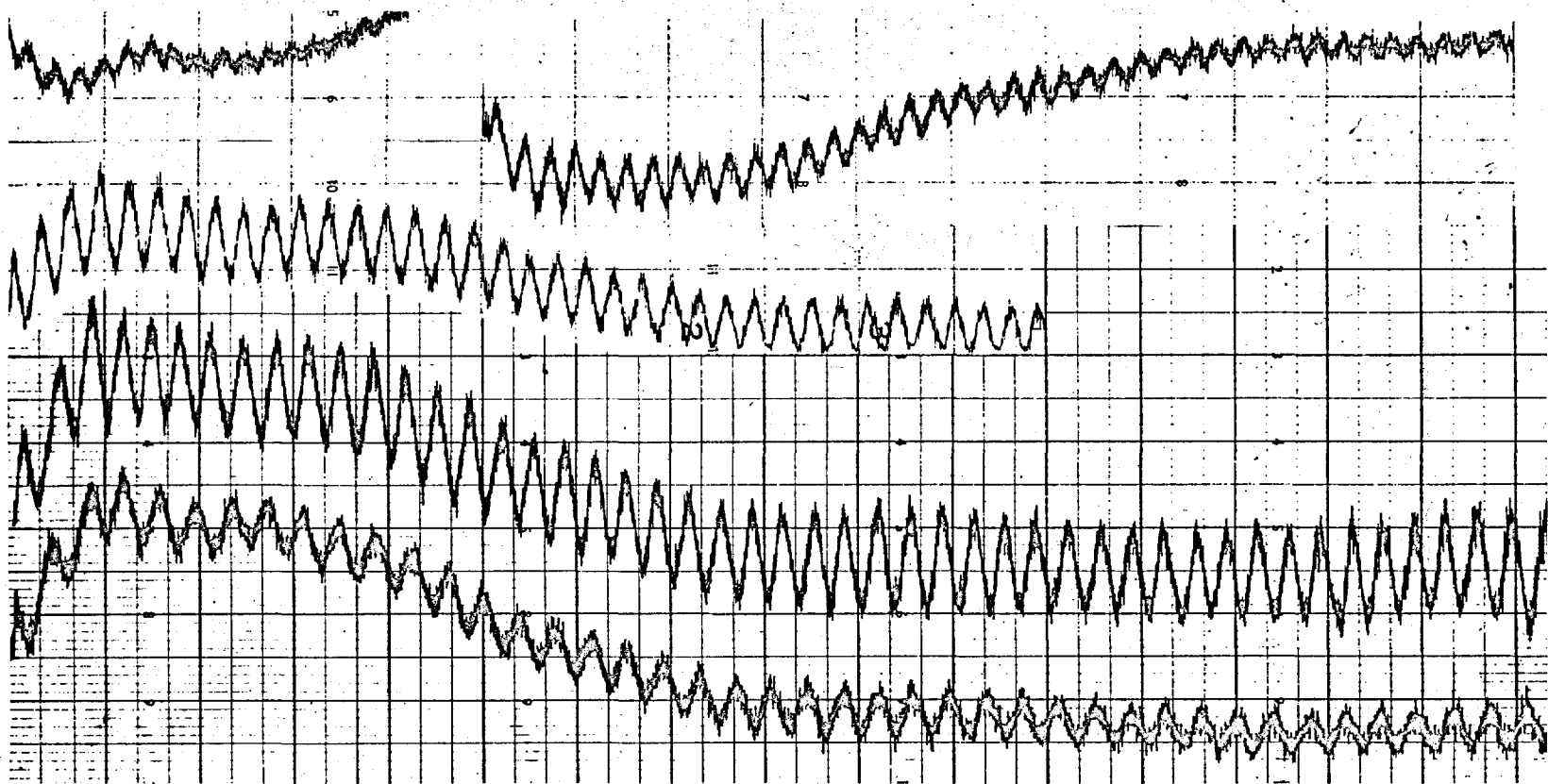


FIG 12 Wave traces from mercury discharge at $4.6, 4.3, 4.0, 3.6$ and 3.3×10^5 rad/sec.
 $p = 0.4$ mtorr, $B = 0$, $d = 5$ cm. Forward waves.

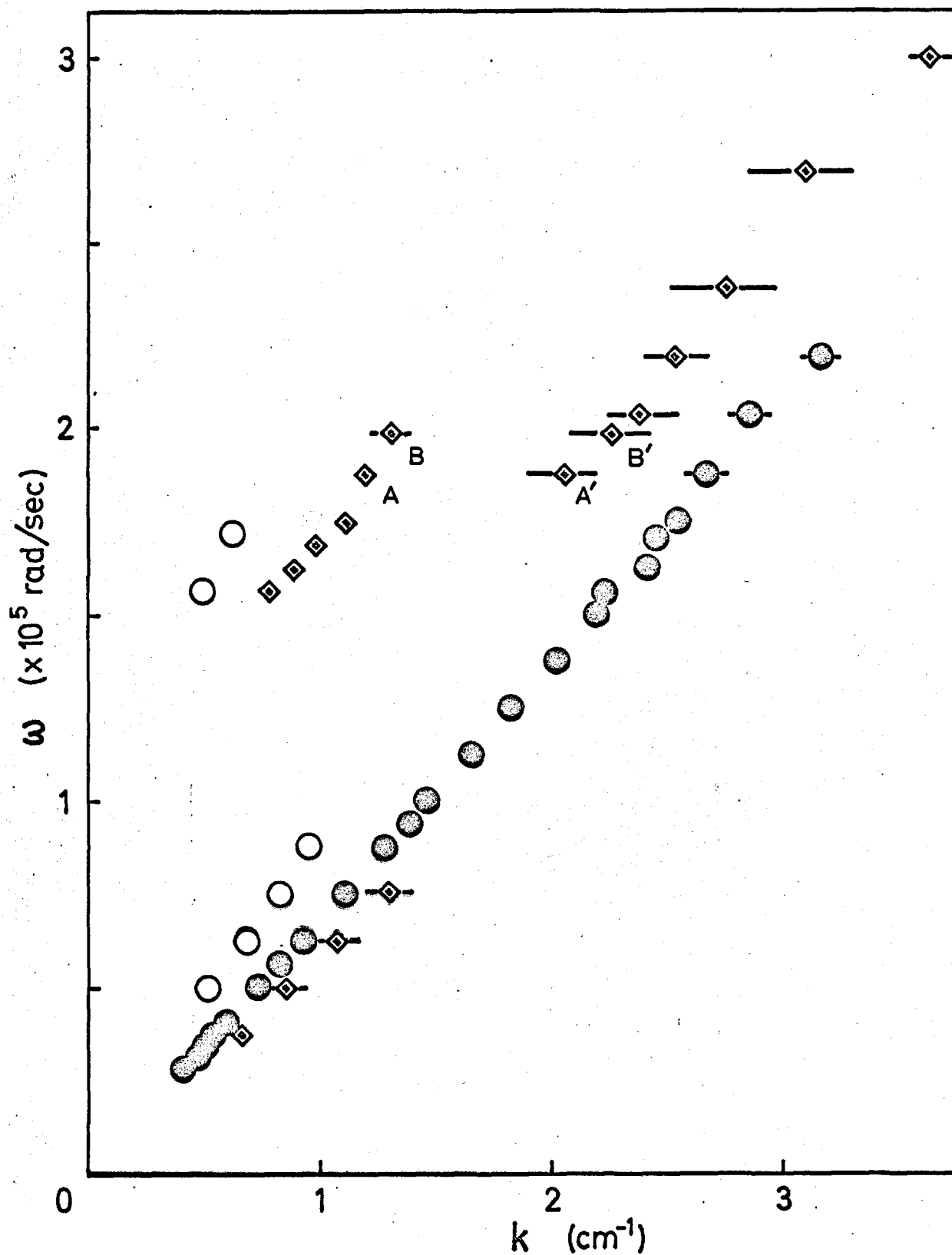


FIG 13 Dispersion curves for forward waves in mercury. \bullet $d = 3$ cm, $p = 0.3$ mtorr; \circ $d = 3$ cm, $p = 0.9$ mtorr; \diamond $d = 5$ cm, $p = .6-1$ mtorr.

Curves \odot and \circ . Fig. (13) also contains experimental points obtained from a 3 cm. mercury column with $B = 15$ and 20 gauss. An unsuccessful attempt was made to detect waves with $B = 0$.

The main series of points marked \odot lie at a slope of $0.5 c_s$ (where $T_e = 4.2$ eV). Examples of the corresponding wave traces are presented in fig. 14 and the damping is plotted in fig. 15. The fourth trace in fig. 14 ($\omega = 1.4 \times 10^5$ rad/sec) shows damping over the first half followed by growth over most of the second half; therefore both a positive and a negative value of k_{\perp} are given in fig. 15 at this frequency. Growth was predominant at lower frequencies, and damping at higher frequencies.

The low frequency wave traces in fig. 14 exhibit an unusual feature, viz. the fairly sudden cessation of the waves at a distance of about 50 cm from the exciter coil. There was no obvious change in the positive column at this point.

The waves represented by \circ were of small amplitude. The electron temperature was not measured in this case but we shall assume that it is equal to the value measured in the 5 cm column at 0.6 millitorr, i.e. 2.5 eV. Two of them lie on the theoretical (0,1) curve for $T_e = 4.2$ eV, and the four low frequency points lie along a slope of $0.8 c_s$ (where $T_e = 2.5$ eV).

Curves \diamond , \blacktriangle and \equiv . At the higher mercury vapour pressures, 2-5 millitorr, only backward waves were observed; the dispersion curves are shown in fig. 16. These were all very heavily damped, as illustrated in the wave traces of fig. 17. Those observed at zero magnetic field (marked \diamond) had $k_{\perp}\lambda \gtrsim 2.3$ and $k_{\perp} \sim 0.1$ cm⁻¹, whilst those obtained in the presence of the magnetic field (marked \blacktriangle and \equiv) had $k_{\perp}\lambda$ almost as great. At the highest frequencies ($\sim 1 \times 10^5$ rad/sec) the

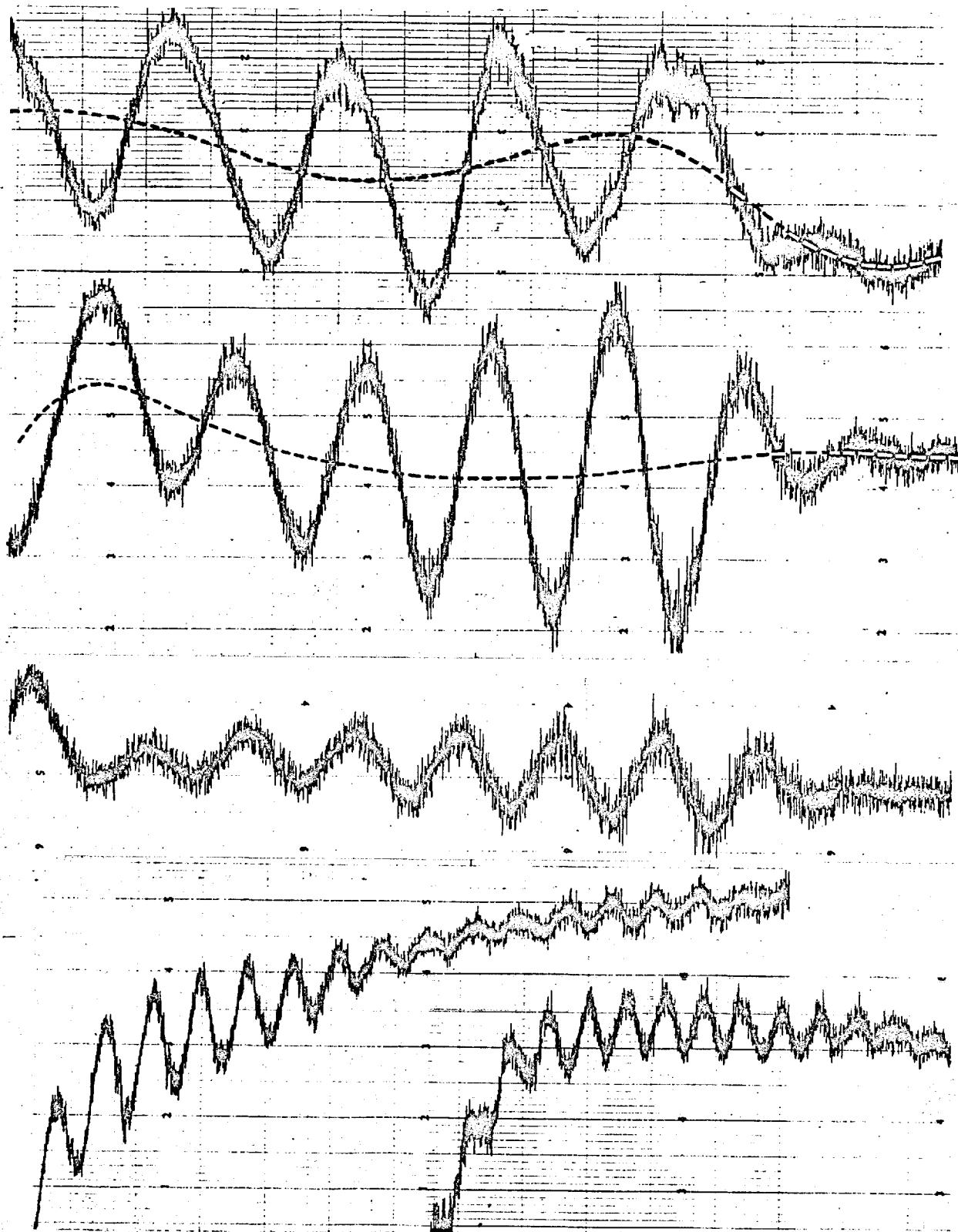


FIG 14 Wave traces from mercury discharge at $0.38, 0.50, 0.63, 1.38$ and 1.69×10^5 rad/sec. $p = 0.3$ mtorr; $B = 15, 20$ gauss; $d = 3$ cm. Forward waves.

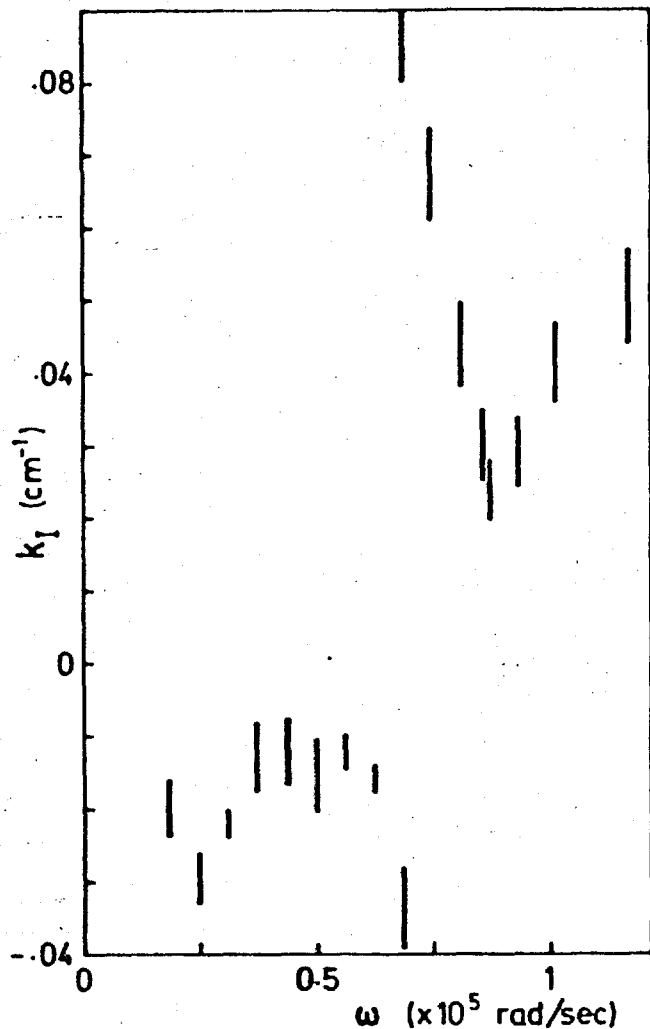


FIG 15 Damping and growth of forward waves in mercury, measured over middle portion of each wave trace. $d = 3$ cm, $p = 0.3$ mtorr, $B = 15, 20$ gauss

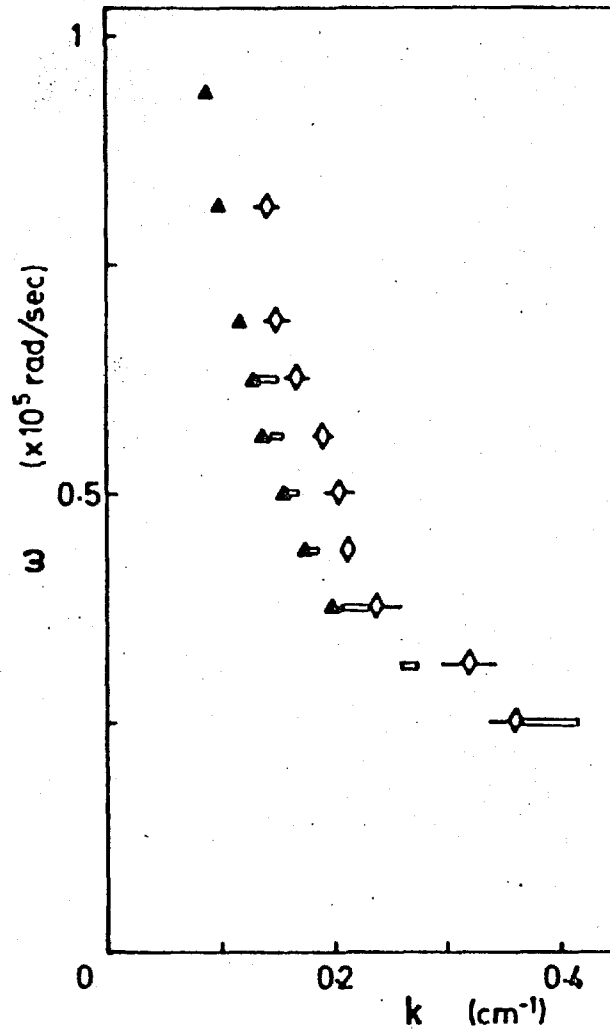


FIG 16 Dispersion curves for backward waves in mercury. $d = 5$ cm. \blacktriangle $p = 2$ mtorr, $B = 15$ gauss; \square $p = 5$ mtorr, $B = 15$ gauss; \diamond $p = 2-5$ mtorr, $B = 0$.

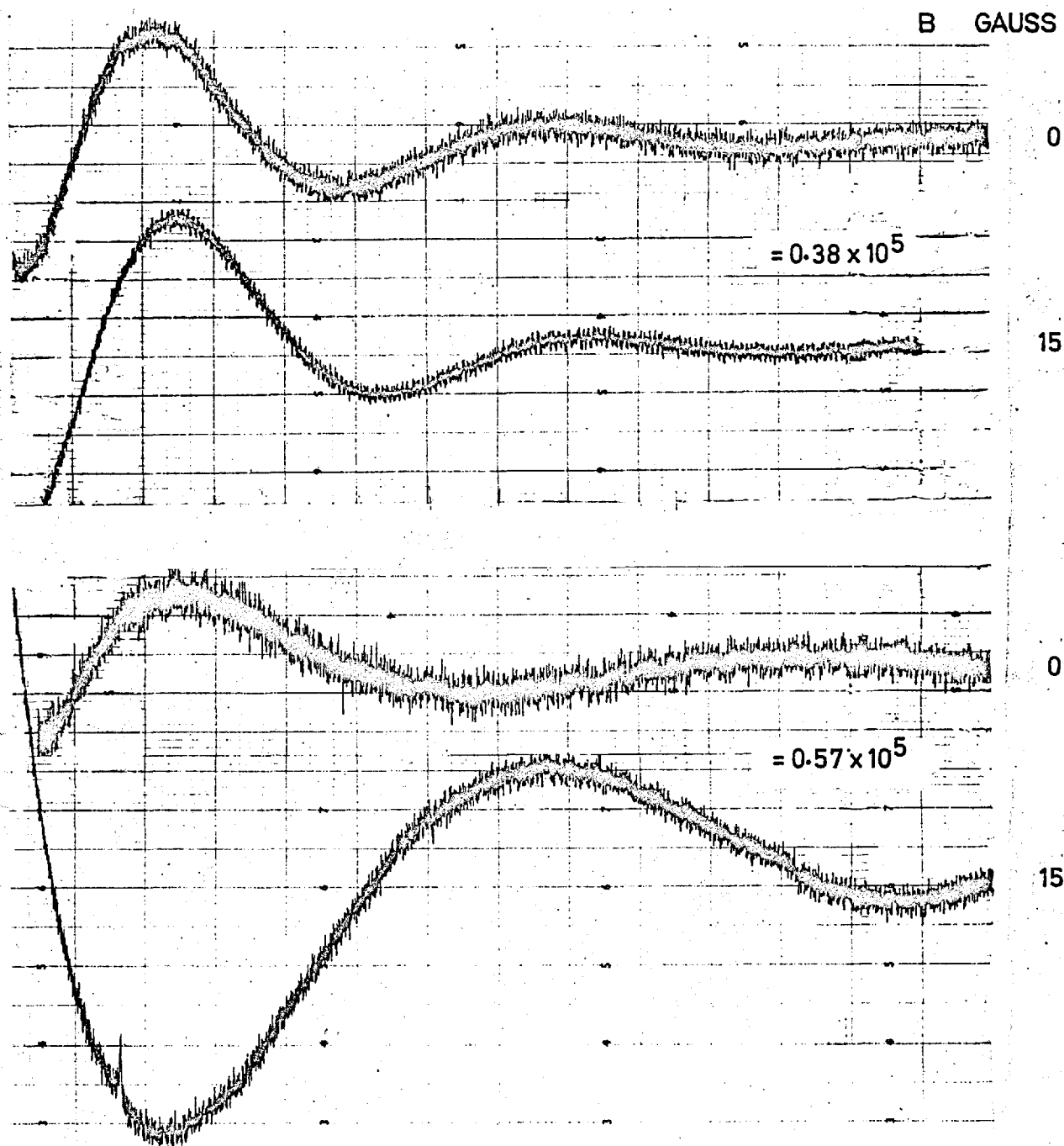


FIG 17 Wave traces from mercury discharge at 0.38×10^5 rad/sec ($B=0$ and 15 gauss) and 0.57×10^5 rad/sec ($B=0$ and 15 gauss).
 $p = 2-5$ mtorr, $d = 5$ cm. Backward waves.

wavelength was longer than the region of the column under observation and only one half-wavelength could be measured.

Increase of wavelength of backward waves with distance. A feature of many of the backward waves, especially those in which the damping is not very heavy (e.g. in argon), is the increase of the wavelength λ with increasing distance z from the exciter. This is demonstrated clearly in the top trace of fig. 17 in which the successive half-wavelengths are 8, 12 and 15 cm. In such cases, the wave number plotted on the dispersion diagrams is calculated from the average of the half-wavelengths, omitting the first half-wavelength.

(21) Waves in neon

The dispersion curves for waves in a 5 cm neon column were obtained under the four sets of experimental conditions given in the following table:

Table 4.

Symbol	p millitorr	B gauss	I_D A
⊖	26	15	6
⊗	18	15	6
○	13	9	8
⊙	26	0	6

Both forward and backward waves were observed under each of these sets of conditions. At $\omega > 1.5 \times 10^5$ rad/sec the two types of wave were observed concurrently (see fig. 18(a) and (b)).

The backward waves are widely scattered in the region 1×10^5 to 2×10^5 rad/sec; the series of points marked ⊖ and ⊗ both form a bulge away from the dashed curve at such frequencies. It is noted that the phase and group velocities of the backward waves in this frequency range are of the order of c_s , and so the scatter may represent some interaction between backward and forward waves.

At the point marked P on both fig. 18(a) and (b), the wave trace is irregular: the successive spacings of the forward wave peaks are 10.1, 12.5, 19.0, 19.6 and 13.4 cm. and the wavelength of the concurrent back-

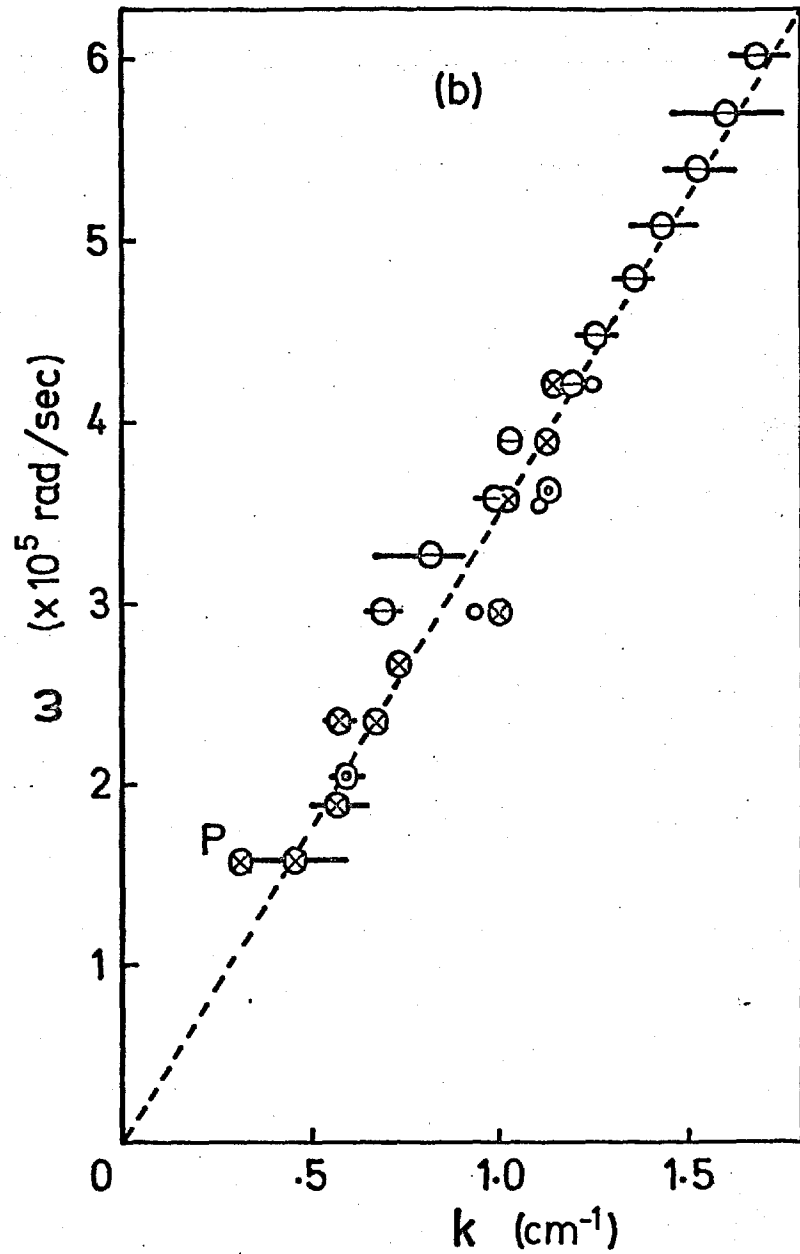
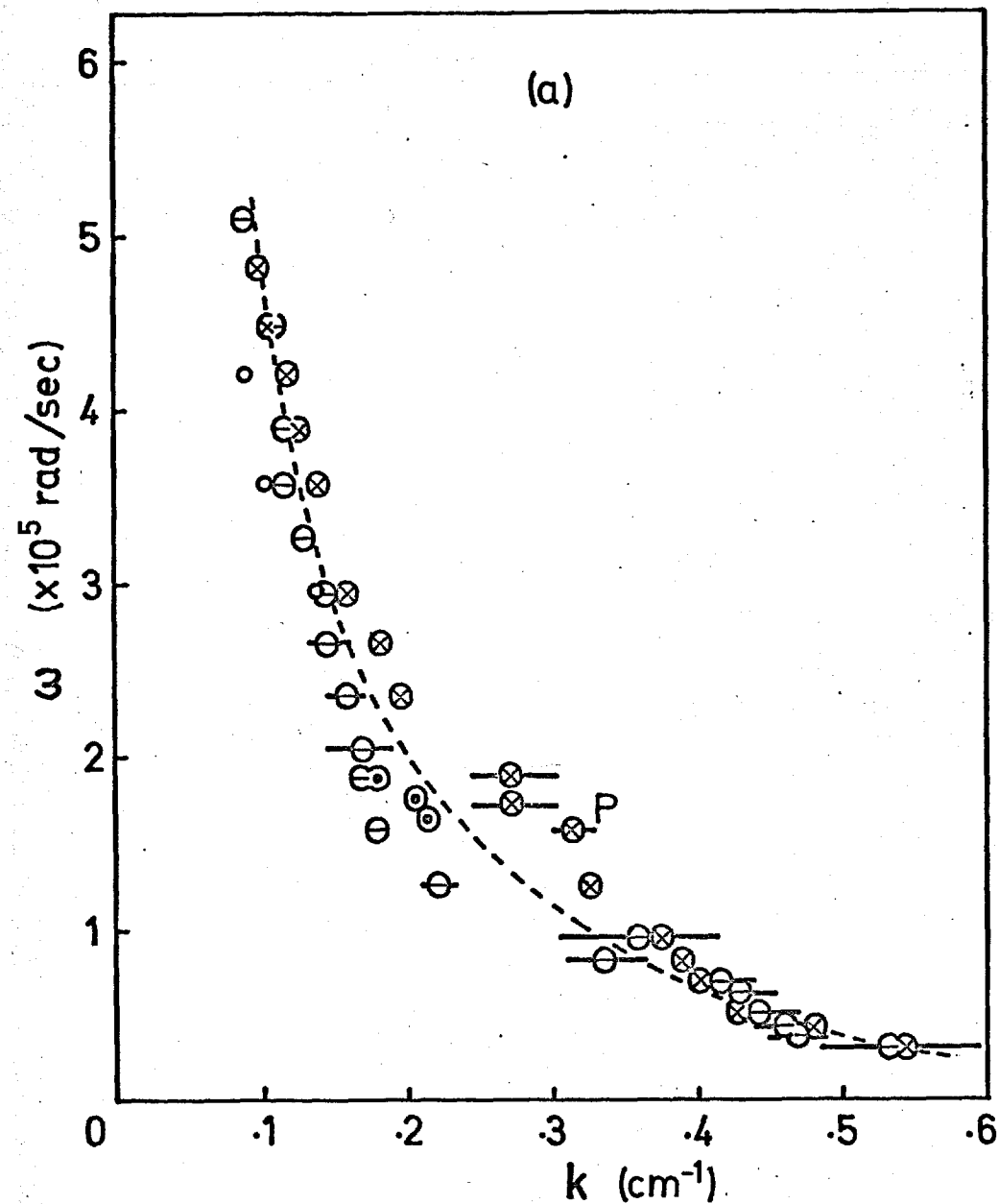


FIG 18 Dispersion curves for (a) backward and (b) forward waves in neon. \ominus $p=26$ mtorr, $B=15$ gauss; \otimes $p=18$ mtorr, $B=15$ gauss; \odot $p=26$ mtorr, $B=0$; \circ $p=13$ mtorr, $B=9$ gauss.

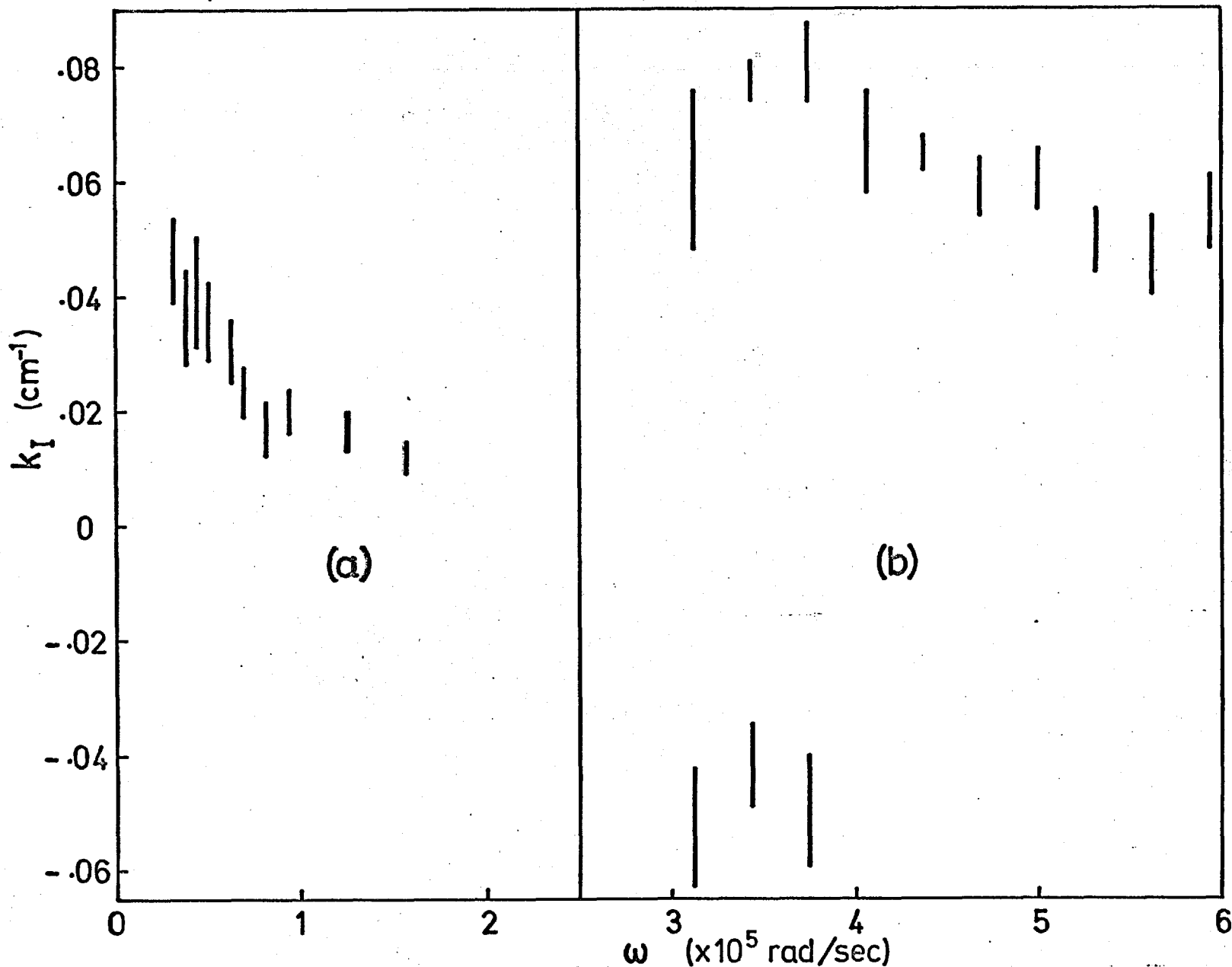


FIG 19 Damping of (a) backward and (b) forward waves in neon. $p=26$ mtorr, $B=15$ gauss. The negative values of k represent growth over second half of wave trace.

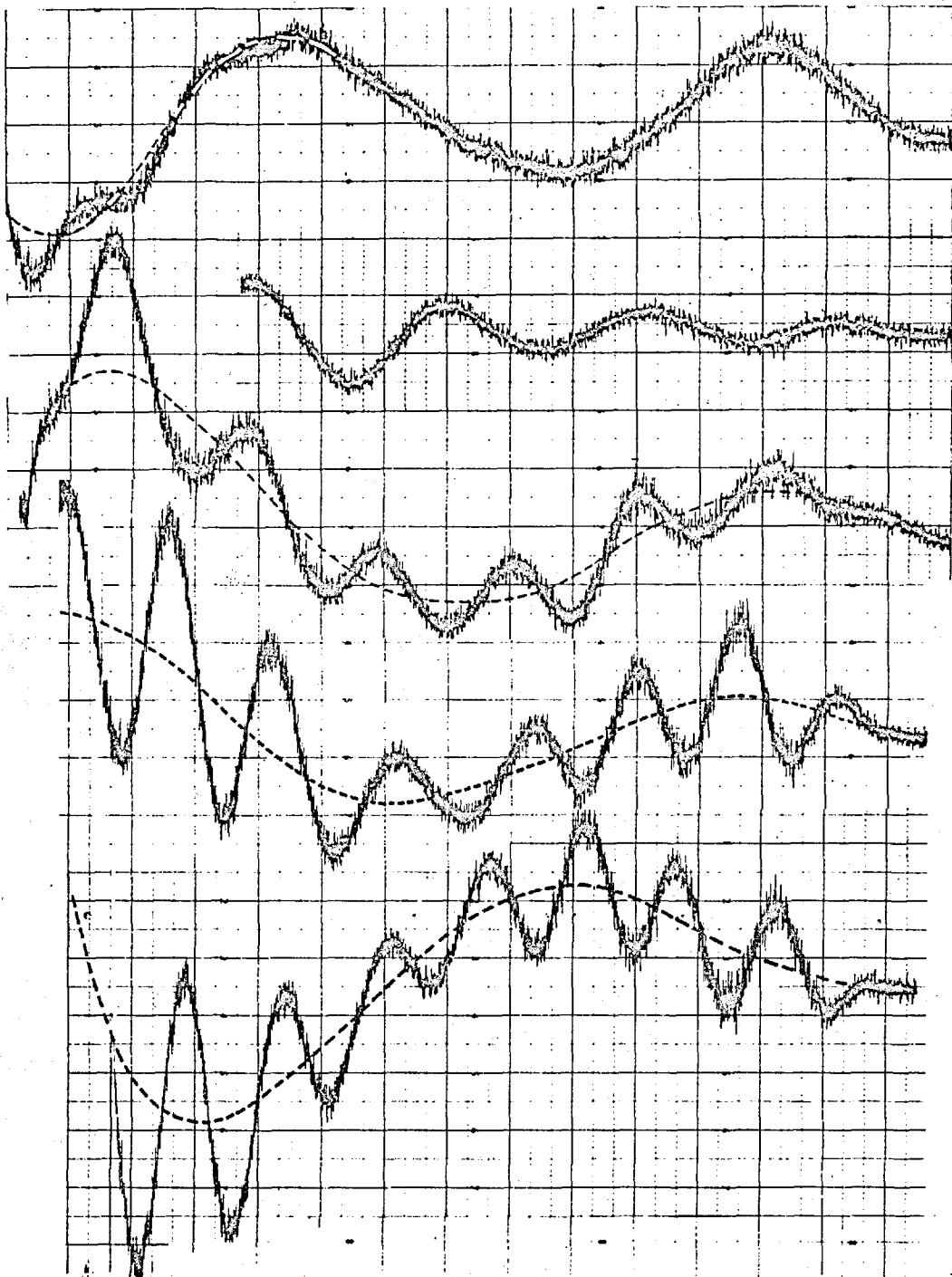


FIG 20 Wave traces from neon discharge at 1.6, .44, 3.0, 3.3 and 3.6×10^5 rad/sec. $p = 26$ mtorr, $B = 15$ gauss. Backward and forward waves.

ward wave is 20 cm. The irregularity of the wave pattern is a consequence of the superposition of backward and forward waves of comparable wavelength.

The experimental points in fig. 18(b) are somewhat scattered in the region of $\omega = 3 \times 10^5$ rad/sec but otherwise lie close to the straight line $\omega/k = 0.6 c_s$.

The damping of the backward and forward waves for the first set of discharge conditions (marked \ominus) is represented in fig. 19(a) and (b). The value of $k_{\perp} \lambda$ is fairly constant for the backward waves. The forward waves in the range $3 \times 10^5 - 3.6 \times 10^5$ cm/sec are damped over the first half of each wave trace and then grow over a distance of two or three wavelengths; both positive and negative values are assigned to k_{\perp} in this range. At higher frequencies there is damping over the entire wave trace, with k_{\perp} decreasing slightly as ω rises, as in the theoretical curves in fig. 1(b) at $a \gg 0.5$.

Wave traces obtained at five different frequencies are shown in fig. 20. It is noticeable in the traces at $\omega = 3 \times 10^5$, 3.3×10^5 and 3.6×10^5 rad/sec that the wavelength and damping of the short wavelength forward waves vary with distance z along the column. The wavelength, amplitude and the median line (i.e. the profile of the backward wave) obtained from these three traces are plotted in fig. 21. The wavelength and amplitude variations are, on the whole, out of phase with one another; there is also a slight correlation between the amplitude variations and the backward wave profiles.

(22) Waves in argon

The waves observed in argon, in the pressure range 10 - 30 millitorr, were all backward waves. They were observed mainly under the first set of conditions listed below, and three experimental points were obtained under each of the second and third conditions:

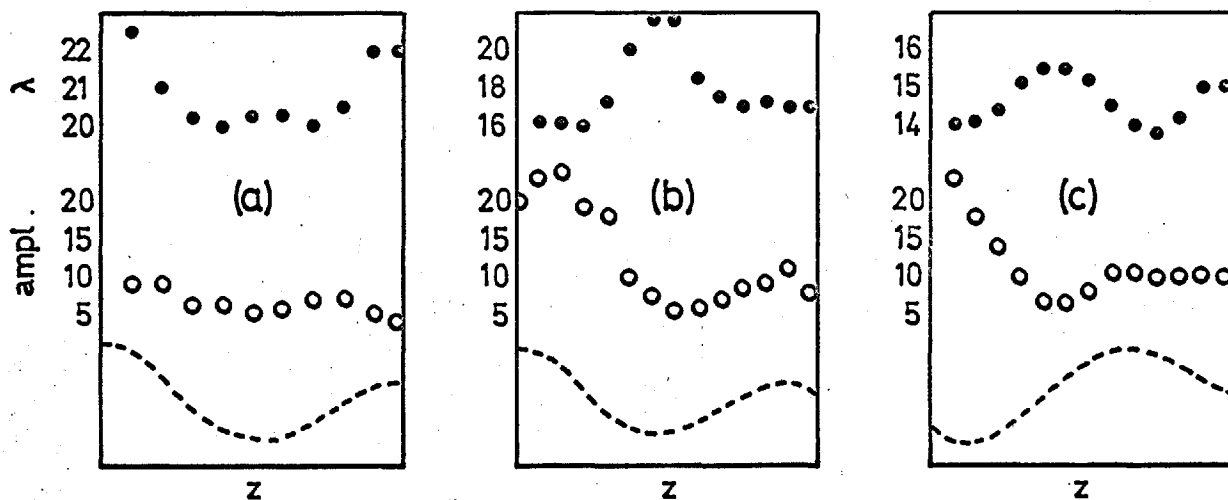


FIG 21 Wavelength and amplitude (in arbitrary units) versus axial distance in neon. Obtained from wave traces in fig. 20 at (a) 3.0×10^5 , (b) 3.3×10^5 and (c) 3.6×10^5 rad/sec.

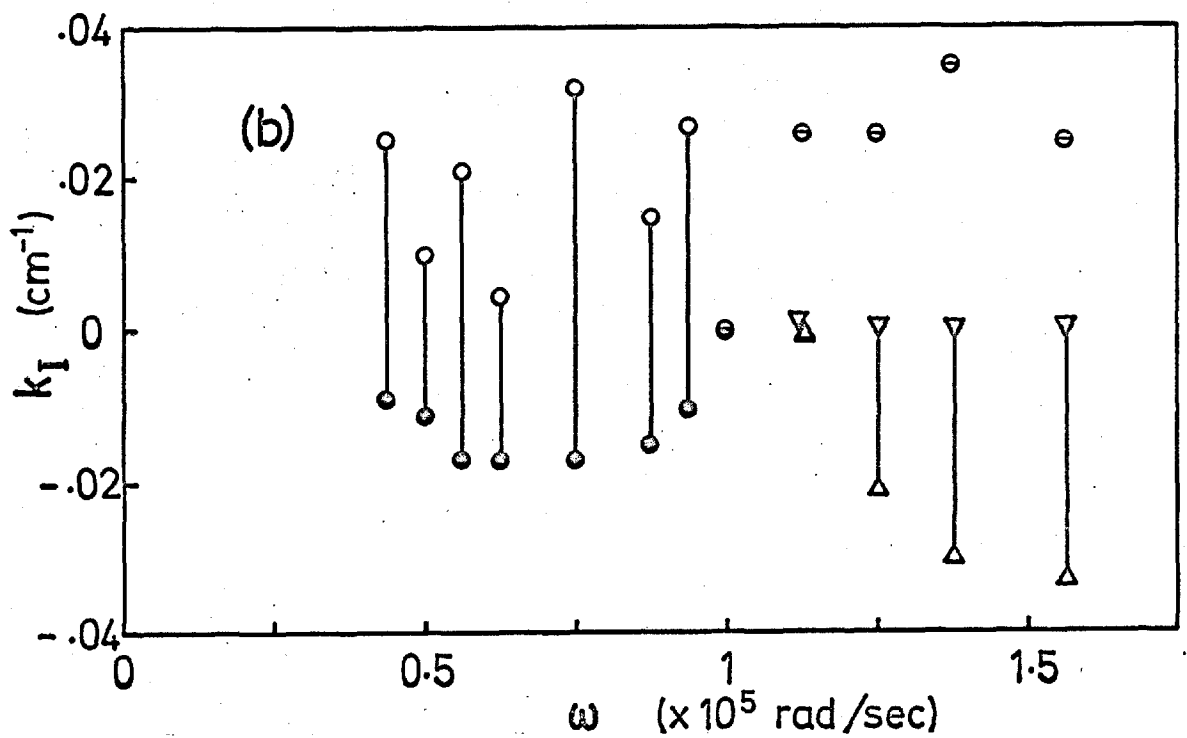
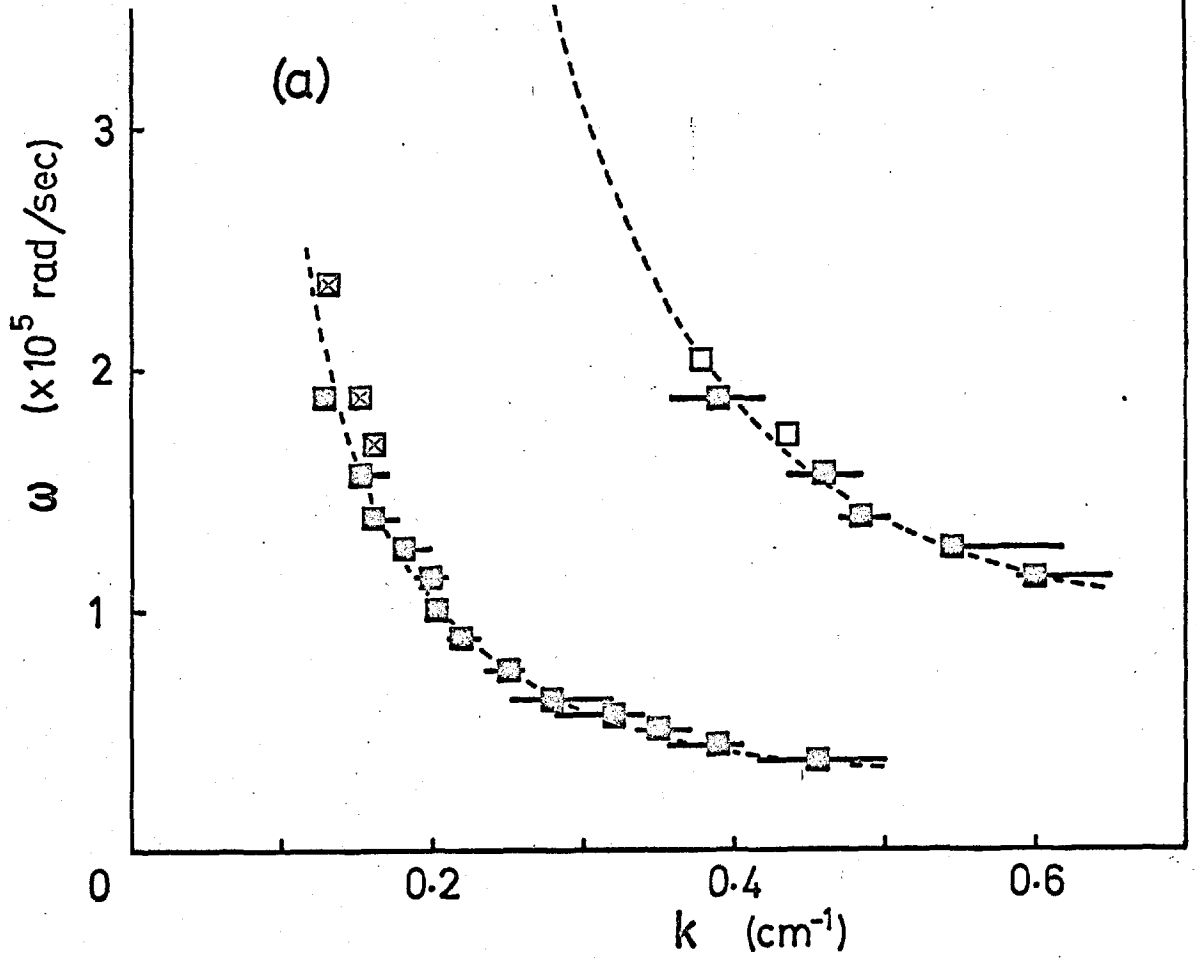


FIG 22 (a) Dispersion curves for backward waves in argon. \blacksquare $p = 14$ mtorr, \square $p = 30$ mtorr, \boxtimes $p = 10$ mtorr. $B = 15$ gauss.
 (b) Damping of backward waves in argon at $p = 14$ mtorr. \odot $z < 30$ cm, \circ $z > 30$ cm, \odot all z , long λ component. Δ $z < 30$ cm, ∇ $z > 30$ cm, short λ .

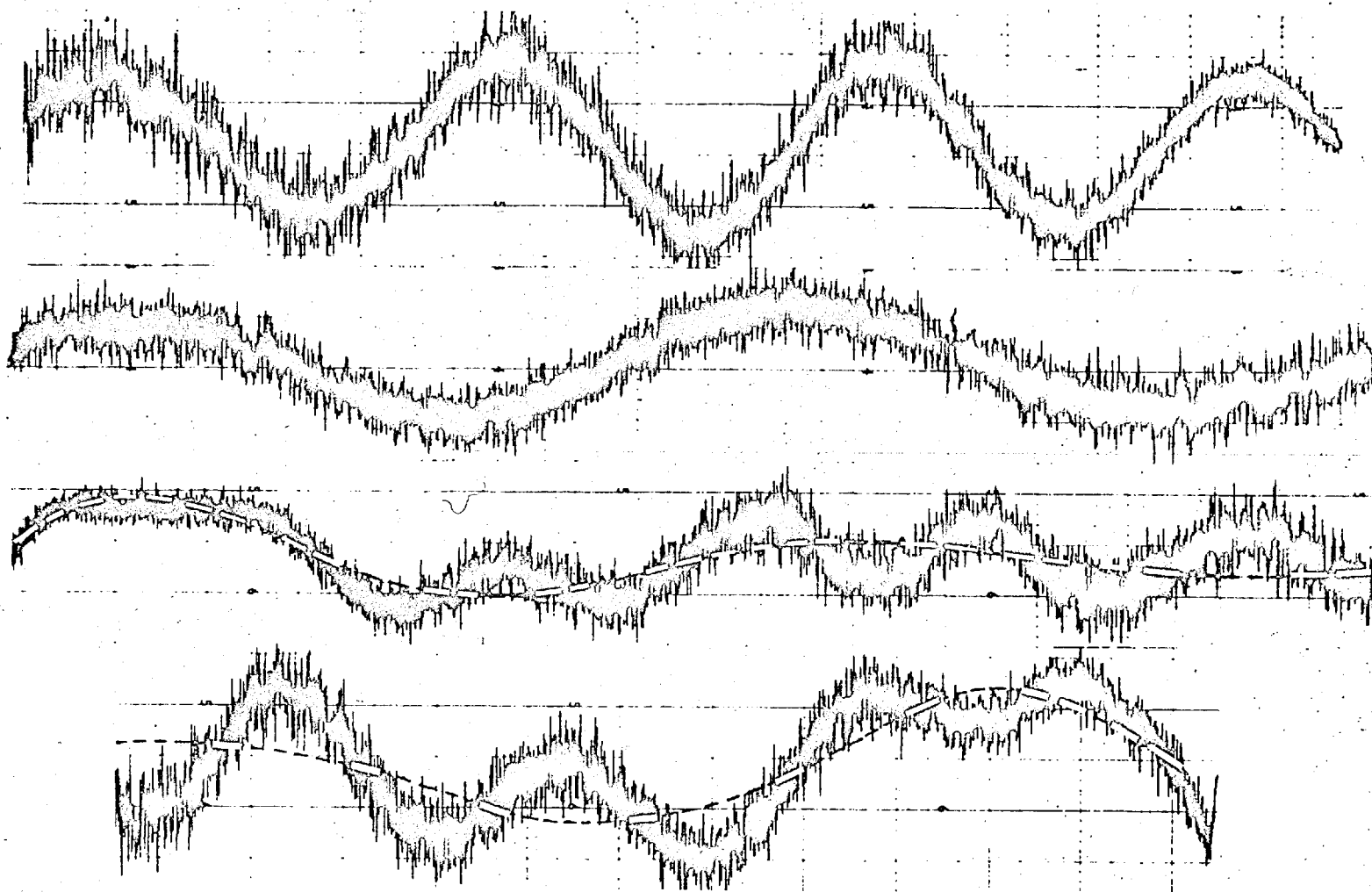


FIG 23 Wave traces from argon discharge at $.50, .95, 1.25$ and 1.57×10^5 rad/sec.
 $p = 14$ mtorr, $B = 15$ gauss.

Table 5.

Symbol	p millitorr	B gauss	I_D A
☐	14	15	5
□	30	15	5.5
☒	10	15	5.5

As shown in fig. 22(a), the experimental points form two distinct dispersion curves. Under the first set of conditions, waves were not observable at $\omega \geq 2 \times 10^5$ rad/sec. Between 1.9×10^5 and 1.1×10^5 rad/sec, each wave trace was made up of two distinct wave components with a wavelength ratio of 3 to 1. This effect is illustrated in the two lowest wave traces in fig. 23 where the long wavelength component is represented by the dotted line. The long λ component shows continuous damping along the column, whereas the short λ component grows over the range 20 - 40 cm from the exciter and remains fairly constant in amplitude at greater distances. It appears from this behaviour that there is a transfer of energy from the long wavelength to the short wavelength mode. The occurrence of more than one backward wave mode has been observed in argon at much higher pressures (~ 12 torr) by Donahue & Dieke⁽⁶⁾.

The values of k_I are plotted in fig. 22(b). Where the damping of either mode in the region near the exciter ($z < \text{about } 30$ cm) is different from that in the region further away ($z > \text{about } 30$ cm), two values of k_I are shown for that mode. The long wavelength mode shows a tendency towards greater damping at higher frequencies, especially in the region near the exciter.

As mentioned earlier in this section, the waves in argon consistently grow in wavelength as z increases.

(23) Waves in hydrogen

A dispersion curve of positive slope, shown in fig. 24, was obtained for waves in the frequency range $0 - 1.1 \times 10^6$ rad/sec at one set of discharge conditions ($p = 17$ millitorr, $B = 10$ gauss, $I_D = 2.5A$); the experimental points are marked \odot . Waves were also observed at

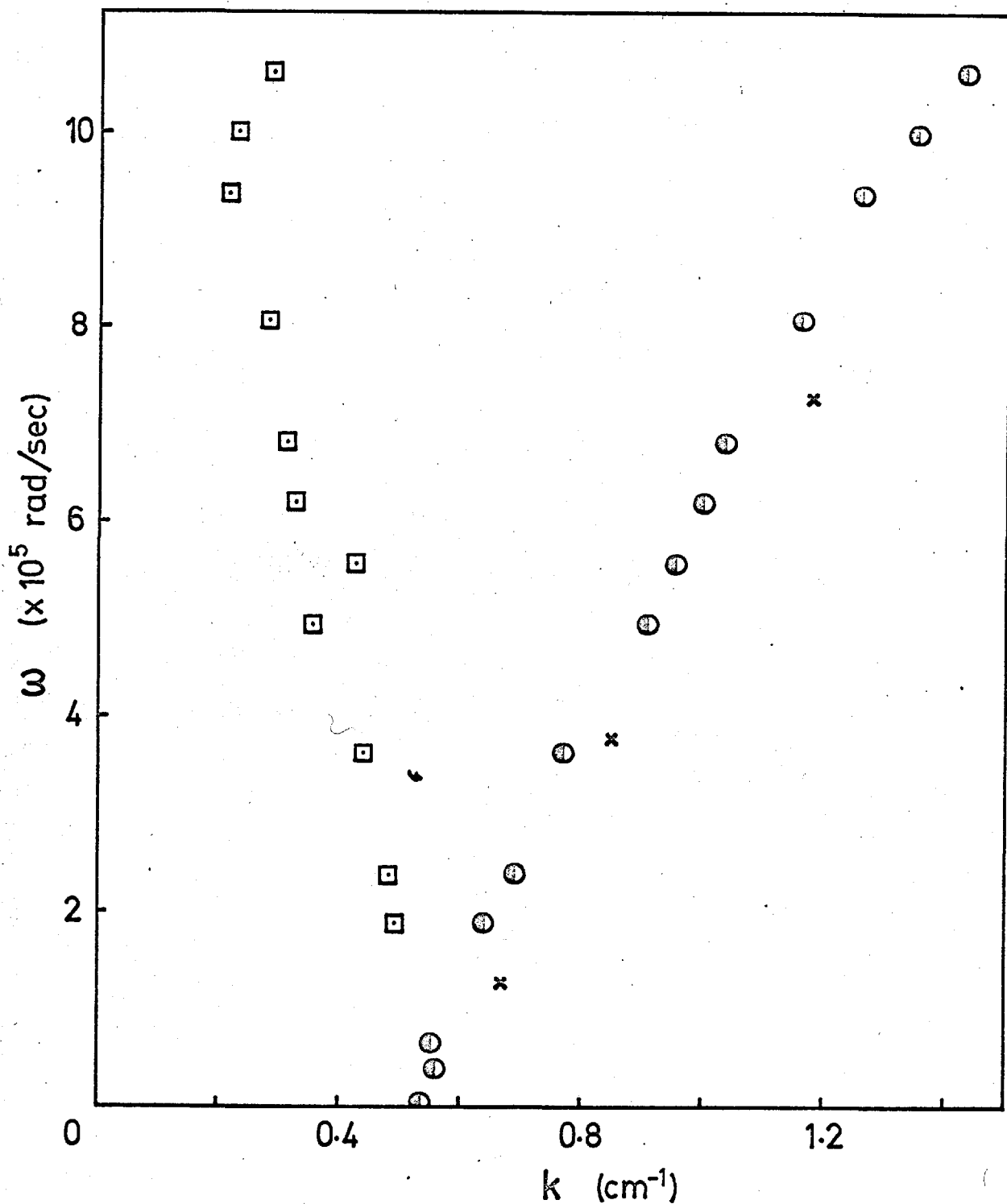


FIG 24 Dispersion curves for waves in hydrogen discharge at $p = 17$ mtorr.
 x $B = 0$; \odot $B = 10$ gauss; \square waves represented by median lines of
 wave traces for the points \odot (dashed lines in fig. 25).

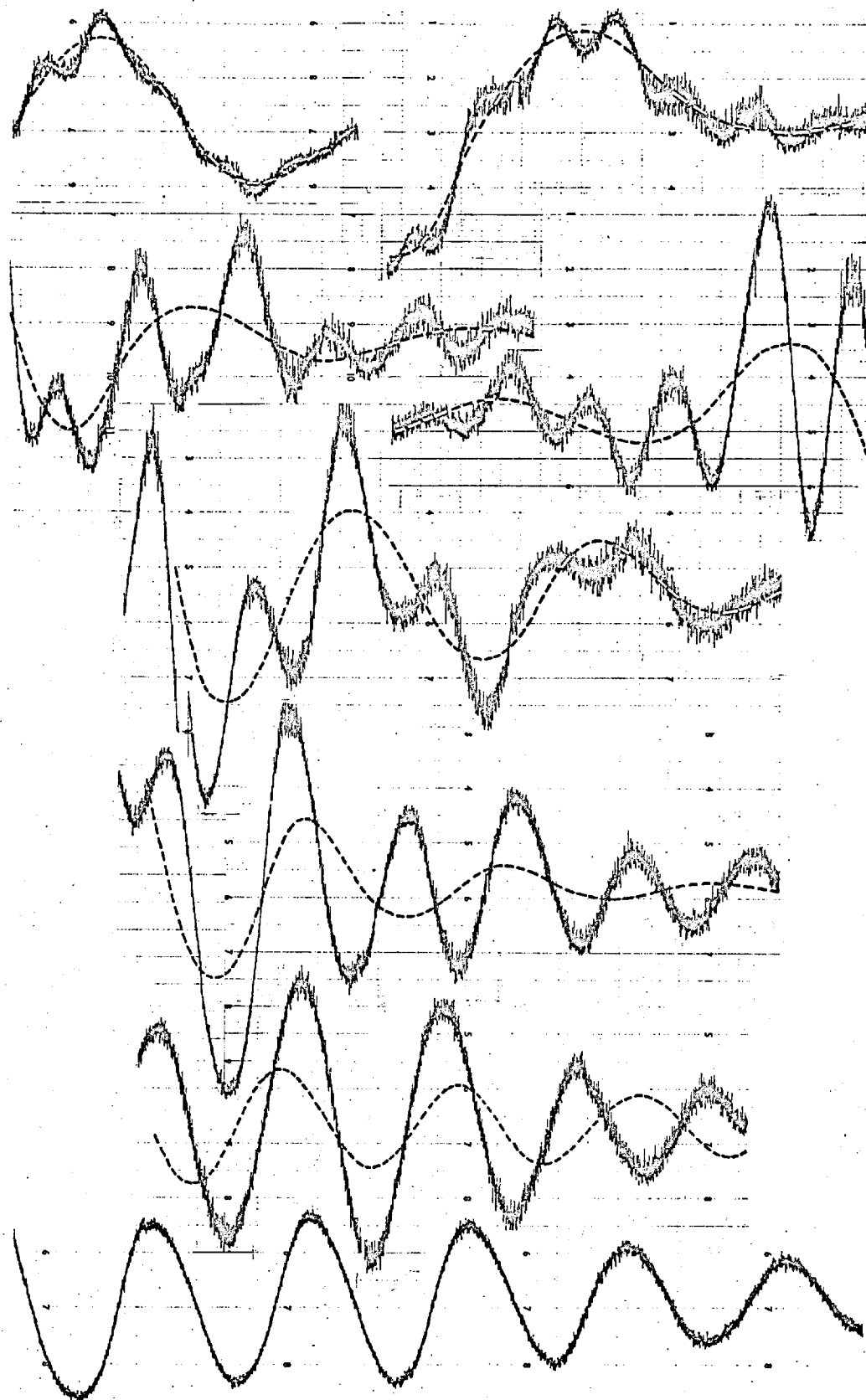


FIG 25 Wave traces from hydrogen discharge at 10.7, 9.4, 6.8, 6.2, 5.0 and 3.6×10^5 rad/sec. $p=17$ mtorr, $B=10$ gauss. 1.9 and 0.6×10^5

three widely scattered frequencies during a brief search for waves at zero magnetic field (at $p = 13$ millitorr, $I_D = 3A$); these points are marked \times . All the points are in good agreement with those obtained by Little & Jones⁽⁶²⁾, as shown in fig. 8(b). The curve drawn through the points \odot meets the k -axis at $k = 0.54 \text{ cm}^{-1}$ which is the wave number of the stationary striations visible in the column.

Examples of the irregular wave traces obtained for the hydrogen column are given in fig. 25, in descending order of exciter frequency. The apparently irregular variation of the amplitude with distance can be explained by assuming the waves to be super imposed on a wave pattern such as that represented by the dashed line in each trace. If the wave number of each of these dashed curves is plotted against the corresponding exciter frequency, the curve of negative slope in fig. 24 is obtained.

The dashed curves have been drawn in such a manner that (i) their wavelength remains constant, (ii) their amplitude decreases fairly uniformly with z , and (iii) the amplitude of the recorded waves (measured to the dashed curve) changes fairly smoothly with z . Under these constraints there is little latitude in the positions at which the maxima and minima of the dashed curves may be drawn.

Despite the irregularity of the wave traces, it appears that the damping of both the recorded waves and the dashed curves increases with frequency.

Two features of the forward wave dispersion curve are noted. Firstly, the curve approaches the straight line $\omega/k = 0.85 \times 10^6 \text{ cm/sec}$ (see fig. 8(b)). In this case the value of c_s depends not only on T_e but also on the relative abundance of H^+ and H_2^+ ions. With an electron temperature of 6.1 eV, c_s lies between 1.75×10^6 and $2.5 \times 10^6 \text{ cm/sec}$. This means that the velocity of the high frequency waves ($\omega > 10^6 \text{ rad/sec}$) lies between $0.35 c_s$ and $0.5 c_s$.

The second feature is the absence of any disturbance in the region of the ion cyclotron frequency ($\omega_{ci} = 0.5 \times 10^5 - 1 \times 10^5 \text{ rad/sec}$).

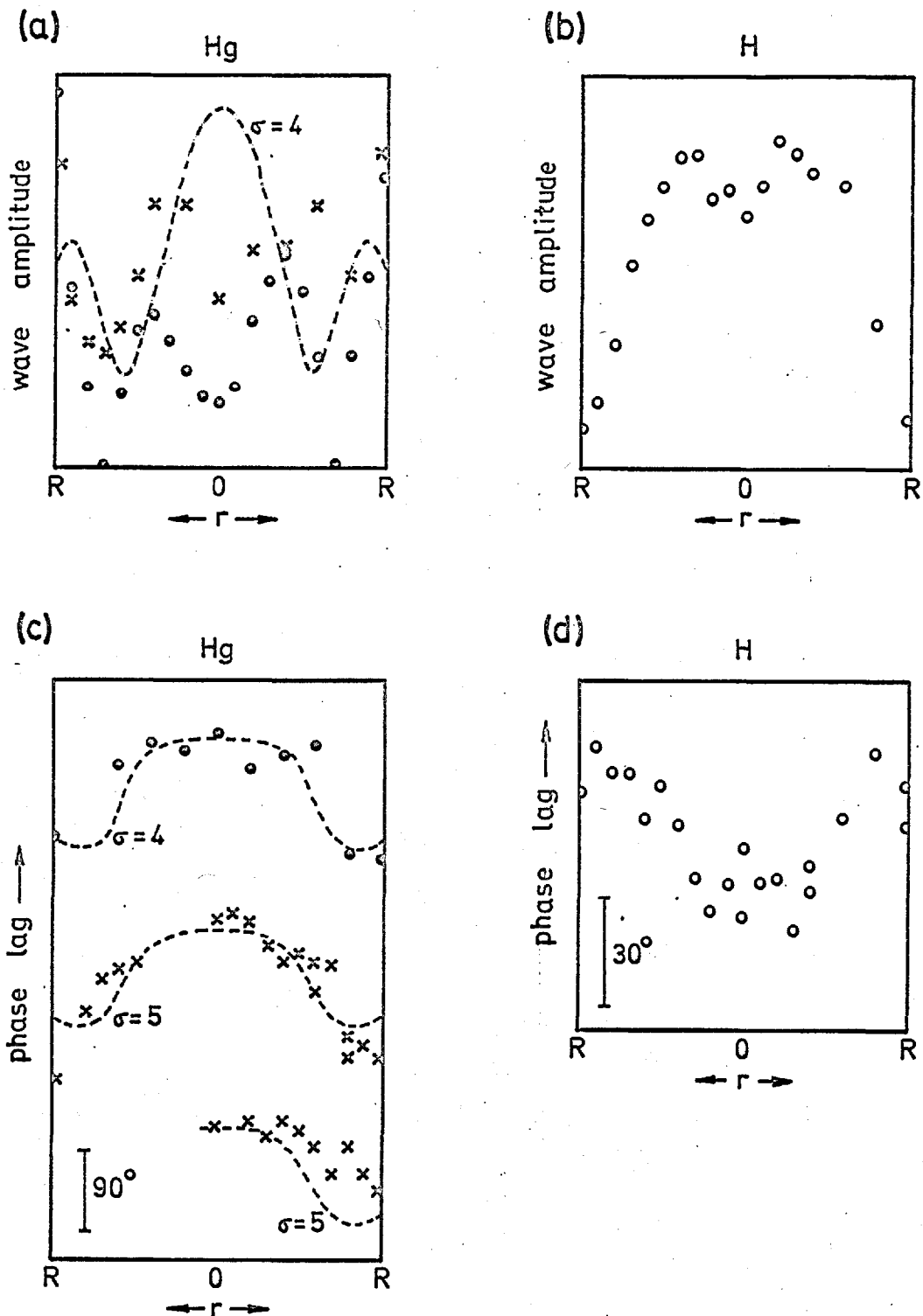


FIG 26 Radial variation of amplitude and phase of forward waves in mercury ($p = 0.4$ mtorr, $B = 15$ gauss) and hydrogen ($p = 17$ mtorr, $B = 10$ gauss). \circ $\omega = 1.9 \times 10^5$ rad/sec ($\sigma = 3.6$); \times $\omega = 2.4 \times 10^5$ rad/sec ($\sigma = 4.5$); \circ $\omega = 0.63 \times 10^5$ rad/sec. Dashed curves taken from the theory of L.C.Woods (ref. 18) where $\sigma = \omega R / c_s$.

This is to be expected from the fact that any interaction between an ion cyclotron wave and the forward wave would be largely destroyed by ion-neutral collisions ($\nu_{in} \gg \omega_{ci}$).

(24) Radial variation of amplitude and phase of forward waves.

Good quality wave traces were obtained with the cathode-facing probe when it was biased to draw several microamperes of ion current from the plasma. Waves traces were obtained at several radial distances from the axis in both mercury and hydrogen discharges. Measurements were made at three different frequencies and the results are plotted in fig. 26 (a),(b),(c) and (d). The dashed curves in (a) and (c) represent the (0,1) mode taken from L.C. Woods' theory.

There are obvious differences between the waves in mercury and those in hydrogen. The former reach their largest amplitude near the wall where there is a phase lead of 120° on the perturbation at the axis. The latter have their largest amplitude near the axis where there is a phase lead of roughly 40° on the perturbation at the wall.

Woods' theory shows that the radial profile of the amplitude of the (0,1) mode varies with frequency. Only the profile for $\omega = 2 \times 10^5$ rad/sec is drawn in fig. 26(a). At frequencies up to 4×10^5 rad/sec the theoretical (0,1) mode has an amplitude minimum at $r \approx \frac{1}{2}R$, whereas the experimental curve shows two minima, at $r = 0$ and $r = 0.85R$.

In fig. 26(c) there is agreement at 1.9×10^5 rad/sec between the theoretical and observed values of the phase change between wall and axis. At 2.4×10^5 rad/sec two different sets of results were obtained with different exciter currents and the agreement in both cases is not as good as at the lower frequency.

The radial profile of the density perturbation n_1 in hydrogen obtained at $\omega = 0.65 \times 10^5$ rad/sec, is approximately the same as that of the steady state ion (or electron) density n_0 . In both the n_1 and n_0 profiles, the value at the wall is about 0.1 of the value at the axis.

CHAPTER IV
DISCUSSION

Two types of dispersion curve have been described which represent forward and backward waves respectively. Both types consist of variations of the plasma density, and the mechanisms by which such variations may be produced are described below.

(25) Excitation of the waves

The question of wave modes was considered in Chapter I in the case of electro-acoustic waves. It is possible that more than one radial or azimuthal mode may occur in the case of ionization waves, but no investigation of this problem has been carried out (either here or, it seems, elsewhere).

It is obvious that the waves produced by means of an azimuthally symmetric exciter coil, such as that used in the present experiments, occur in the $m = 0$ azimuthal mode. This is supported by the approximate symmetry of the curves in fig. 26. Which radial mode, or mixture of radial modes, is observed depends on the excitation mechanism and on the relative damping of the modes. It is probable that any modes of high order that may be generated by the exciter coil, are damped out within a short distance of the exciter⁽²⁵⁾. A recent attempt has been made by Crawford and Kuhler⁽⁶³⁾ to excite electro-acoustic waves in an $m = 1$ mode. Using two exciter coils, one on either side of the tube, they found the excitation in this mode to be very weak: the $m = 1$ waves were observed only in the region near the exciter, and further away the waves corresponded to the $m = 0$ mode.

Excitation mechanisms. We shall consider briefly three possible ways in which the density waves are generated by the alternating magnetic field of the exciter coil. These are discussed in more detail in Appendix G.

(1) Squeezing of the plasma by the field. This is the mechanism suggested in an early paper by P.F. Little⁽²⁾ and by Crawford and Self⁽²²⁾, but it is inapplicable both in their experiments and in the present experiments where the plasma resistivity is high. The lines of magnetic field diffuse

through the column in a time $\sim 10^{-6}$ sec, which is much less than the wave period. (2) Modulation of the ion loss rate. This is described by Little and Jones⁽²⁵⁾ who show that the perturbation of the ion density is proportional to $B_0^2 (1 + 2\tilde{B}_1/B_0)$, where \tilde{B}_1 and B_0 are the a.c. and d.c. magnetic field components in the z direction. (3) Production of alternating drift motion of the ions and electrons together by the crossed electric and magnetic fields. The drift velocity has (a) a radial component $(\tilde{E}_\theta \times B_z/B_0^2)$ and (b) a longitudinal component $(\tilde{E}_\theta \times B_r/B_0^2)$, where \tilde{E}_θ is the a.c. electric field, and B_r and B_z are the radial and longitudinal components of the total magnetic field B_0 at the exciter.

The combined effect of mechanisms (2) and (3)(a) may be compared experimentally with that of (3)(b) by measuring the wave amplitude when the exciter is situated well inside the d.c. field coils (position A) where $B_r = 0$, and when it is placed just outside the coils (position B). Little change would be expected in the effect of (2) and (3)(a) in moving the exciter from position A to position B, but mechanism (3)(b) would be ineffective at A. It is found in a 9A, 0.4 millitorr mercury discharge with $B_z = 45$ gauss that the amplitude increases by almost an order of magnitude when the exciter is moved from A to B (see diagram on p. 174). As the dispersion curves were obtained with the exciter coil situated at the end of the d.c. field coils where B_r is appreciable, the waves in this discharge must have been generated mainly by the $\tilde{E}_\theta \times B_r/B_0^2$ drift.

Both \tilde{E}_θ and B_r are zero at $r = 0$ and increase with r , whilst the plasma density decreases with r to a low value at the edge of the column. The corresponding density perturbation must therefore increase from zero at $r = 0$ and possibly pass through a maximum as r increases. The perturbation of the ion loss rate is also zero at $r = 0$ where the radial electric field is zero. This perturbation is proportional to the longitudinal a.c. magnetic field \tilde{B}_1 and is therefore 90° out of phase with the $\tilde{E}_\theta \times B_r/B_0^2$ drift. It thus appears that the waves generated by the exciter coil may occur only in those modes in which the amplitude is zero at the axis. The perturbation would, however, diffuse to the axis, thereby allowing the possibility that the principal radial mode be excited.

FORWARD WAVES

(26) Waves in the (0,1) mode. It was noted earlier that the dispersion curves for a 5 cm diameter mercury discharge at 0.4 millitorr (marked \odot and \ominus) approach a cut-off on the ω -axis. These are compared in fig. 9 with the curves representing the (0,1) mode in L.C. Wood's theory⁽¹⁸⁾; there is only qualitative agreement here between experiment and theory. The main discrepancy occurs at the higher frequencies where the experimental phase velocities are 20 to 30% less than the theoretical values. Woods, Little and Jones⁽⁶⁴⁾ have recently reported a similar discrepancy. However, since these authors find that the qualitative agreement extends not only to the shape of the dispersion curve but also to the radial variation of amplitude and phase at different frequencies, there is little doubt that these waves propagate in the (0,1) mode.

The frequency dependence of the damping of these waves is not readily explicable. L.C. Woods has given a semi-quantitative account of the effect of the electron drift on the damping coefficient (see section (9)). The electron drift is considered to be responsible for the fact that the observed values of k_{\perp} are less than the calculated values by an order of magnitude. As shown in section (9), Woods obtains an expression for a critical frequency above which the waves should grow: this has the value 70 kc/s in the 0.4 millitorr mercury discharge. In contrast, k_{\perp} is found experimentally to approach zero at about 55 kc/s and to rise to larger positive values at higher frequencies.

(27) The dispersion curves $\omega/k = a c_s$. Most of the points plotted in fig. 13, from mercury discharges, and those in fig. 18(b), from neon discharges, lie along straight lines of the form $\omega/k = a c_s$. The dispersion curve for hydrogen in fig. 8(b) approaches this form at the higher frequencies. Values of the parameter a obtained from the dispersion curves are listed in the final column of the table on page 131. These lie in the range 0.5 to 0.8. The value 0.5 in the case of hydrogen is obtained on the assumption that the ions are all diatomic (H_2^+).

If it is considered that these curves represent the principal or (0,0) mode of propagation, some explanation is required for the fact that \underline{a} is appreciably less than unity. This parameter would be affected by each of the following factors: (a) the longitudinal drift velocities of ions and electrons, (b) errors in the measurement of T_e , (c) the presence of diatomic ions (or, in the case of the hydrogen discharge, the presence of monatomic ions).

(a) The effect of the drifts on the phase velocity is described by equation (8) (section (6)):

$$\begin{aligned} \omega/k &= c_s - \left[\frac{m_e v_{de}^2}{2m_i c_s} + v_{di} \right] \\ &= c_s - \Delta c_s \end{aligned}$$

This equation applies to an unbounded plasma in which collisions are neglected and in which the wave vector is parallel to the electron drift (or antiparallel to the ion drift). Table 6 shows values of $\Delta c_s/c_s$ calculated from this equation, using the drift velocities included in the table. The quantity $(v_{di})_c$ is the axial ion drift velocity obtained from experimental data applicable to a collision-dominated positive column. At the much lower pressures encountered in the mercury columns a more appropriate value of this drift may be calculated from the expression $\frac{1}{2}(eE_z/m_i)(R/c_s)$ where (R/c_s) represents approximately the mean life time of an ion before it reaches the tube wall. The value of $\Delta c_s/c_s$ is comparatively small in the mercury and neon columns, but in the case of the hydrogen column it is almost sufficient to account for the value of \underline{a} .

(b) The measurements of T_e are considered to have errors of less than 20%. In the case of the neon column the temperature measurements were made with a cathode-facing probe, whilst those in the other columns were made with a radial probe. The cathode-facing probe produces an

Table 6

Dispersion curve	c_s cm/sec	$(v_{di})_c$ cm/sec	$eE_z R/2m_i c_s$ cm/sec	v_{de} cm/sec	λ_{en} cm	λ_{in} cm	$\frac{\Delta c_s}{c_s}$	$a = \frac{\omega}{kc_s}$
Hg ●	1.3×10^5	4.5×10^4 *	0.5×10^4	2×10^7 Δ	12 ▲	13 ++		
Hg ⊙ †	1.1×10^5 †	4.5×10^4 *	0.6×10^4	2×10^7 Δ				
Hg ◆	1.1×10^5	3×10^4 *	0.6×10^4	2×10^7 Δ			0.1	0.5, 0.75
Hg ●	1.4×10^5	5×10^4 *	0.4×10^4	2×10^7 Δ			0.05	0.5
Hg ○ ‡	1.1×10^5 ‡	3.5×10^4 *		2×10^7 Δ				0.8
Ne ⊖	6×10^5	8×10^4 *	7.5×10^4	2×10^7 *	3 ▲	0.5 ▲	0.15	0.6
H ₂ ⊙	18×10^5	65×10^4 *	55×10^4	2×10^7 ▲	1.5 ▲	1 ▲	0.45	0.5

Notes

- † T_e assumed equal to the value for the ⊙ curve in fig. 8(b) (see Table 1)
- ‡ T_e assumed equal to the value for the ◆ curves.
- * A. von Engel ⁽⁶⁵⁾ pp. 41, 114, 119, 121, 124.
- Δ Allen and Magistrelli ⁽⁶⁶⁾.
- ▲ S.C. Brown ⁽⁶⁷⁾.
- ++ Little and Jones ⁽²⁵⁾.

exaggerated value of T_e because of the electron drift velocity; the error calculated from the theory of Allen & Magistrelli⁽⁶⁶⁾ is about 10%. If the total error in T_e for the mercury and neon discharges were +20%, we should still be left with appreciable discrepancies between the values of \underline{a} and $(1 - \Delta c_s/c_s)$ (see Table 6).

(c) The presence of diatomic ions in the neon and mercury discharges would help to account for these discrepancies further. Such ions do occur in neon⁽⁶⁸⁾ but their relative concentration in the present discharges is not known. It may be noted that in the case of electro-acoustic waves in an r.f. discharge in nitrogen, G.M. Sessler⁽⁶⁹⁾ found that an increase in n_e from 0.3×10^9 to $1.0 \times 10^9 \text{ cm}^{-3}$ was accompanied by a decrease of nearly 25% in the phase velocity. He explains that this is due to an increase in the density of N_3^+ ions relative to the densities of N^+ and N_2^+ ions.

It is perhaps significant in this context that the values of ω/k in other experiments on electro-acoustic waves in mercury or inert gas discharges, are mainly less than the theoretical values. Such a discrepancy is found in the measurements of Alexeff & Jones⁽¹⁵⁾ on "negative striations" (apparently electro-acoustic waves) in the inert gases; in one of the electro-acoustic modes observed by Crawford & Kuhler⁽⁶³⁾ in a 0.4 millitorr mercury discharge (Branch III, fig. 9(b)), and in the (0,1) mode observed by Woods, Little & Jones in a similar discharge. Crawford & Kuhler's Branch I, which has the form of Woods' (0,1) curve, is an exception: the observed phase velocities are slightly higher than those of the theoretical (0,1) curve. In the case of electro-acoustic waves in an r.f. discharge, G.M. Sessler^(38a) has found good agreement between experimental and theoretical phase velocities.

It may be noted that the two values of \underline{a} corresponding to the points marked \diamond are approximately in the ratio $\sqrt{2} : 1$. It is therefore possible that these values are associated with Hg^+ and Hg_2^+ ions respectively.

(28) Mode of the waves corresponding to $\omega/k = ac_s$. As shown by L.C. Woods⁽¹⁸⁾ and Bertotti, Cavaliere & Giupponi⁽¹⁹⁾, the principal mode of electro-acoustic waves in a bounded plasma is given almost exactly by the relation $\omega/k = c_s$ and the higher modes follow less simple dispersion relations. The principal mode is that in which $m = 0$ (i.e. no azimuthal variation) and in which both the ratio of the ion density perturbation to the steady state ion density and the phase of the wave are independent of radial position. Although the low values of a have not been accounted for completely, it seems probable that the waves represented by $\omega/k = ac_s$ correspond to the principal mode.

The waves corresponding to the points marked \odot (obtained from the 3 cm mercury discharge) show growth at low frequencies and damping at higher frequencies. This behaviour is roughly similar to that of L.C. Woods' (0,0) mode⁽¹⁸⁾ in which there is a change from low values of k_{\perp} at low frequencies to a larger constant value of k_{\perp} at $\omega \gtrsim c_s/R$. The reverse behaviour occurs in the (0,1) mode: k_{\perp} decreases as ω increases (see fig. 2(b)).

(29) Comments by Bertotti et. al. concerning the effect of the electron drift velocity on the principal mode. It should be noted that Bertotti et. al.^(19a) predict that any wave mode described by a dispersion relation of the form

$$\omega = a_1 k + a_2 k^2 + a_3 k^3 + \dots \quad (19)$$

(the a 's being complex constants), is eliminated by the longitudinal electron drift velocity. As this point has been quoted elsewhere⁽⁷⁰⁾ and is in contradiction to some of the results of the present experiments, it is necessary that we should examine the mathematical argument behind it.

Bertotti et. al. obtain the relation

$$\frac{d^2 \varepsilon_1}{du_0^2} - (2i\omega + \beta) u_0 \frac{d\varepsilon_1}{du_0} + (1-u_0^2)(\omega^2 - k^2 - i\omega\beta)\varepsilon_1 = 0 \quad (20)$$

where ε_1 is the energy perturbation in the wave, u_0 is the unperturbed average radial ion velocity in units of c_s and is a function of r , $\beta = v_{oz} \partial Z / \partial v_z$ and v_{oz} is the unperturbed longitudinal electron drift velocity. The energy perturbation may be expressed as an expansion in terms of k :

$$\varepsilon_1 = b_0(u_0) + b_1(u_0)k + b_2(u_0)k^2 + \dots \quad (21)$$

If the dispersion curve assumes the form $\omega = a_1 k + a_2 k^2 + a_3 k^3 + \dots$, as does the principal mode dispersion curve, it may readily be shown that at the lowest order in k equation (20) reduces to $db_0/du_0 = C \exp(\frac{1}{2}\beta u_0^2)$. Now at small values of k we may write $d\varepsilon_1/du_0 = db_0/du_0 = C \exp(\frac{1}{2}\beta u_0^2)$, and, because of the boundary conditions ($d\varepsilon_1/du_0 = 0$ at $u_0 = 0$ and $u_0 = 1$), the constant C must be zero. This means that $b_0(u_0)$ is a constant with respect to u_0 , i.e. it is a constant over a cross-section of the column. The authors do not appear to have shown that the assumption of equation (19) is tantamount to eliminating ε_1 : the principal mode still exists.

(30) Absence of forward waves in the argon discharge. It is noted that no forward waves are observed in argon at the three pressures used here: 10, 14 and 30 millitorr. Alexeff & Jones⁽¹⁵⁾ report a transition in argon from backward to forward waves at about 10 millitorr, and Vasil'eva et. al.⁽¹²⁾ find the same transition at about 4 millitorr. It is likely that forward waves would have been observed in the present experiments if lower pressures had been used.

BACKWARD WAVES

The dispersion curves for the backward waves were shown in fig. 8(a). These are described approximately by the empirical relation

$$\omega k = \text{constant} \quad (17)$$

The curves obtained from the three different gases Hg, A and Ne, lie at distinctly different values of the product ωk and we shall compare these with the values obtained from the dispersion equation of Pekárek & Krejčí^(43e).

(31) Dispersion equation according to Pekárek & Krejčí.

These authors have produced a one-dimensional theory for the propagation of ionization waves in a high current discharge^(43e), i.e. a discharge in which the Debye length is much smaller than the wavelength. They start with the following four equations: the continuity equations for ions and electrons, the Poisson equation and a heat flow equation (described in the appendix of ref. (43f)). They derive the following expression for the ion density perturbation at (z, t) following a perturbation in the form of a Dirac delta function at $(z = 0, t = 0)$:

$$n_+(z, t) = \frac{n_0}{2\pi} \int_{-\infty}^{+\infty} \exp \left[i(kz - \frac{Ak}{k^2 + a_1^2} t) + \phi(k)t \right] dk \quad (22)$$

where

$$n_0 = n_+(z, t = 0)$$

$$A = \left(\frac{3}{2} + \frac{16}{3\pi} \frac{T_{eo}}{E_0 \lambda_e} k \right) (E_0 + a_1 \frac{D_e}{\mu_e}) z'$$

$$a_1 = \frac{16}{3\pi} \frac{T_{e0}}{E_0 \lambda_e^2} \left(2\kappa + T_{e0} \frac{\partial \kappa}{\partial T_e} \right)$$

$T_e - T_{e0}$ = electron temperature perturbation

E_{e0} = unperturbed longitudinal electric field

λ_e = electron mean free path

D_e = electron diffusion coefficient

μ_e = electron mobility

Z' = $(\partial Z / \partial T_e)$ at $T_e = T_{e0}$

Z = ionization rate per electron

κ = average fraction of energy lost by an electron on colliding with a neutral atom

z = axial distance in the laboratory frame of reference, measured in the direction from anode to cathode.

Any component of the disturbance which has a wavelength k is of the form of the exponential term in equation (22). This term represents a propagating wave of frequency

$$\omega = \frac{Ak}{k^2 + a_1^2} \quad (23)$$

This is the dispersion relation in the laboratory frame of reference. It may be written as

$$\omega k = \frac{1}{1 + (a_1/k)^2} \left(\frac{3}{2} + \frac{16}{3\pi} \frac{T_{e0}}{E_0 \lambda_e} \kappa \right) \left(E_0 + a_1 \frac{D_e}{\mu_e} \right) Z' \quad (24)$$

In the present experiments, $T_{e0}/E_0 \lambda_e$ and $T_{e0}/E_0 \lambda_e^2$ are $\lesssim 1$, and κ and $T_{e0} \partial \kappa / \partial T_e$ are $\lesssim 10^{-2}$ (65), and so the terms in equation (24) containing κ or $T_{e0} \partial \kappa / \partial T_e$ may be omitted.

The equation then reduces to

$$\omega k = \frac{3}{2} E_0 Z' \quad (25)$$

which is of the form of equation (17).

If we consider the extreme case where k becomes $\ll a_1$, we find from equation (24) that the waves become forward waves with a phase velocity $\omega/k \approx (\frac{3}{2} E_0 Z'/a_1^2)$.

(32) Dispersion equation in the ion drift frame of reference.

If we replace z by $(x + v_{di} t)$ in equation (22), n_+ is transformed into the frame of reference moving with the ion drift velocity. The dispersion relation then becomes

$$\omega = \frac{Ak}{k^2 + a_1^2} - k v_{di} \quad (26)$$

which reduces to

$$\left(\frac{\omega}{k} + v_{di}\right) k^2 = \frac{3}{2} E_0 Z' \quad (27)$$

By linearising Pekárek & Krejčí's four basic equations, Righetti, Magistrelli, Enriques & Boschi⁽⁷⁰⁾ produce essentially the same dispersion equation in the ion drift frame of reference. Theirs may be written as

$$\omega k = \left(\frac{3}{2} + \frac{16}{3\pi} \frac{T_{eo}}{E_0 \lambda_e} \kappa\right) E_0 Z' (1 + H/k^2) - H\omega/k - G(k^2 + H) \quad (28)$$

where

$$H = -\frac{1}{2} a_1 \left(\frac{D_e}{v_{de}} + \frac{E_0}{4\pi n_e}\right)^{-1} \approx -a_1 v_{de}/2D_e$$

and $G = v_{di} + E_0 Z'/4\pi n_e \approx v_{di}$.

If $T_{eo}\kappa/E_0\lambda_e \ll 1$, equation (28) becomes

$$\left[\left(\frac{\omega}{k} + G \right) k^2 - \frac{3}{2} E_0 Z' \right] (k^2 + H) = 0 \quad (29)$$

This equation contains the dispersion relation mentioned above (equation (27)) and the independent relation

$$k^2 = -H \approx a_1 v_{de} / 2D_e \quad (30)$$

Righetti et. al. obtained dispersion curves for backward waves in a nitrogen discharge at 21, 27 and 31 millitorr. They evaluated the quantities H , G , $HG - b_1 E_0 Z'$ and $Hb_1 E_0 Z'$ (where $b_1 = \frac{3}{2} + \frac{16}{3\pi} \frac{T_{eo}}{E_0 \lambda_e} \kappa$) by fitting equation (28) to each experimental curve. They found the values of G to be in reasonable agreement with the ion drift velocities corresponding to E/p . It is not clear why there should be such agreement since equation (28) is applicable in the ion drift frame of reference, where as the experimental curves are obviously obtained in the laboratory frame.

(33) Determination of Z'

We shall compare the experimental curves with equation (25) which contains the measured parameter E_0 and the quantity Z' . The latter may be expressed as

$$Z' = \frac{\partial}{\partial T_e} (\sum_s Z_s) \quad \text{at } T_e = T_{eo} \quad (31)$$

where $\sum_s Z_s$ is the total ionization rate, per electron, from the ground and metastable states of the atoms. If the electron energy distribution is assumed to be Maxwellian, and the ionization cross-section of an atom in the state s is assumed to be $A_s (\epsilon - V_s)$, then

$$\begin{aligned} Z_s &= \int_{V_s}^{\infty} n_s A_s (\epsilon - V_s) v_r(\epsilon) \frac{2}{\sqrt{\pi}} \left(\frac{\epsilon}{T_e} \right)^{\frac{1}{2}} \exp \left(-\frac{\epsilon}{T_e} \right) d\left(\frac{\epsilon}{T_e} \right) \\ &= 6.7 \times 10^7 n_s A_s T_e^{3/2} \left(\frac{V_s}{T_e} + 2 \right) \exp \left(-\frac{V_s}{T_e} \right) \end{aligned} \quad (32)$$

V_s is the energy in electron-volts required to ionize an atom in the state s , A_s the initial slope of the curve of cross-section versus electron energy ϵ ; and $v_r(\epsilon)$ the random electron velocity. Essentially the same equation is given in Appendix 3 of the book by A. von Engel⁽⁶⁵⁾. On differentiating equation (32) with respect to T_e we obtain

$$Z'_s = 6.7 \times 10^7 n_s A_s T_e^{-\frac{1}{2}} \left[-\frac{v_s^2}{T_e^2} + 2.5 \frac{v_s}{T_e} + 3 \right] \exp(-V_s/T_e) \quad (33)$$

Curves of excitation or ionization cross-sections $\sigma(\epsilon)$ generally rise fairly steeply to a maximum value and then decrease more slowly as ϵ increases. Where $\sigma(\epsilon)$ falls much below the value $A_s(\epsilon - V_s)$ or reaches its maximum within a few electron-volts of V_s , Z_s and Z'_s are appreciably less than the values calculated from equations (32) and (33). The $\sigma(\epsilon)$ curve may usually be expressed reasonably well by two straight lines on the $\sigma(\epsilon)$ - ϵ plane, and the integration to obtain Z_s or Z'_s is then easily carried out. This has been done where necessary in calculating the values of Z_s and Z'_s presented below.

We shall use the suffixes g and $*$ to denote the ground and metastable states respectively. The density of metastable atoms n_* may be estimated roughly from the continuity equation,

$$n_e Z_{ex} = D_* \nabla_r^2 n_* + n_e Z_* \quad (34)$$

where Z_{ex} is the rate of excitation per electron from the ground to metastable states, ∇_r^2 is the operator $\frac{1}{r} \frac{\partial}{\partial r} (r \frac{\partial}{\partial r})$ and $D_* = \bar{v} \lambda_g / 3$ is the diffusion coefficient (\bar{v} and λ_g are respectively the mean random velocity and mean free path of the atoms). The radial variation of n_* is here assumed to be of the form $\cos(\pi r / 2R)$. It is also assumed that no metastable atoms are reflected back into the discharge by the tube wall. Such an atom is subjected to many collisions on reaching the layer of gas atoms at the wall and is likely to be transferred into a different excited state; it would then decay to the ground state. In the case of the mercury discharge, where the mean free path of the atoms

(ref. (65) p. 31) is of the same order of magnitude as the tube radius, $D_* \bar{v}_r^2 n_*$ is approximately equal to $n_* \bar{v}_* / R$ where \bar{v}_* is the mean random velocity of the metastable (or ground state) atoms.

Data on the cross-sections $\sigma(\epsilon)$ has been obtained from several sources. M.A. Cayless⁽⁷¹⁾ has presented curves for both $\sigma(\epsilon)$ and the excitation and ionization rates in mercury discharges. Little information about $\sigma(\epsilon)$ for the transitions from ground to metastable states in neon and argon is available: a small diagram is given by Massey & Burhop⁽⁷²⁾ in the case of neon, and we shall assume that the $\sigma(\epsilon)$ curve for argon is similar in shape and has a maximum value 1.5 times the maximum for neon. $\sigma(\epsilon)$ curves for ionization of neon, argon and mercury atoms in both the ground and metastable states have been calculated by L. Vriens⁽⁷³⁾. Values of A_g (for equation (33)) may be obtained from ref. (65) p. 63.

Values of most of the quantities which appear in equations (33) and (34) are listed in Table 7. The ionization rates and their derivatives and n_* were calculated on the assumption that the total number density of atoms n (which is approximately the same as n_g) is equal to $3.5 \times 10^{13} p$ where p is the observed pressure in millitorr. The factor 3.5×10^{13} is appropriate at a gas temperature of 273°K , whereas the gas temperature in all the discharges is considerably higher than room temperature. The temperature of the outer surface of the tube wall is of the order of 100°C and it is estimated that the gas temperature is 10 or 20 degrees higher. (Kagan & Lyagushchenko⁽⁷⁴⁾ estimate the wall temperature to be $\geq 400^\circ\text{K}$ in the case of 0.4 A discharges at 1 torr in neon and argon). At a gas temperature of say 410°K , n is equal to two-thirds of $3.5 \times 10^{13} p$ and the figures in the last six columns of Table 7 need to be reduced by a factor of 1.5. This correction has been included in the values of W in Table 8 and the values of $\frac{3}{2} E_g Z'$ in Table 9.

There is evidently a large proportion of metastable atoms in the mercury discharge. It is calculated that these account for about 70% of the total ionization rate. According to B. Klarfeld⁽⁷⁵⁾, stepwise ionization is significant in mercury discharges at pressures ≥ 1 millitorr: R.M. Howe⁽⁷⁶⁾ for example estimates that half the ions in his 4 A mercury discharge at 1.75 millitorr are produced via the metastable states.

Table 7. Quantities in equations (33) and (34)⁺

Gas	p m Torr	T _e eV	E ₀ V cm ⁻¹	B gauss	A _* 10 ⁻¹⁶ cm ² V ⁻¹	A _g 10 ⁻¹⁷ cm ² V ⁻¹	D _* 10 ⁴ cm ² sec ⁻¹	n _* 10 ¹² cm ⁻³	Z _{ex} 10 ⁵ sec ⁻¹	Z _g 10 ⁵ sec ⁻¹	Z _* 10 ⁵ sec ⁻¹	Z' _g 10 ⁵ sec ⁻¹ eV ⁻¹	Z' _* 10 ⁵ sec ⁻¹ eV ⁻¹
Ne	26	7.0	.7	15	1.2 a	.16 b	1	1	2 c	4.2	.8 a	2.1 a	.1 a
A	14	3.4	.7	15	2.5 a	2 b	.7	2	1 e	2.7	.8 a	4.3 a	.4 a
Hg	2	1.5	.25	15	1.2 a	10 d	1	10	2 d	.15 d	.3 a	.28 d	.7 a
	2(-5)	2.5	.25	0				20	6 d	1.0 d	3 a	1.4 d	3 a

a L. Vriens⁽⁷³⁾ b A. von Engel⁽⁶⁵⁾ c Massey & Burhop⁽⁷²⁾ d M.A. Cayless⁽⁷¹⁾

e assumed that max $\sigma_{ex} = 1.5 \times \max \sigma_{ex}$ for neon

+ gas temperature assumed to be 273^oK.

(34) Accuracy of calculated values of Z'

It is clear from equations (33) and (34) that Z' is directly proportional to n_g (or n) and therefore to p , and that it is a sensitive function of T_e . Through the term Z'_* , Z' is also dependent on the electron density, although to a much smaller extent. We shall consider the question of errors in p and T_e .

(a) Errors in p . It is likely that there are pressure gradients between the vacuum gauges at the ends of the discharge tube (fig. (4)) and the region of wave propagation.

In the mercury discharge the pressure is measured at each end by means of an ionization gauge. Nominal pressures of 2 millitorr or more are achieved by removing the cooling bath from the mercury pool cathode and keeping the baffle valves closed (or closed at the anode end and open at the cathode end). As the anode is cooled with water at about 10°C , the vapour pressure in that region is limited to just less than 1 millitorr, even though the pressure reading in the tube above the baffle valve at that end may be higher. Furthermore there is a transfer of mercury vapour from the hot cathode pool to the cool ($\sim 20^\circ\text{C}$) portion of the tube wall beneath the ionization gauge at the cathode end; the saturated vapour pressure in this region must be approximately 2 millitorr. Under these circumstances the pressure in the region of wave propagation must be somewhat less than the recorded values of p .

The higher pressures used in the neon and argon discharges could be read only on the Pirani gauge, situated at the cathode end of the discharge tube. The gas was introduced into the short half-inch tube connecting the gauge to the discharge tube and the latter was pumped from the anode end at slow speed. Under these conditions it is possible that the pressure in the region of wave propagation was again somewhat less than the measured value.

Some uncertainty in the value of p also arises from the gradients introduced by the pumping action of the longitudinal drifts of the charged particles. It is commonly observed that this effect increases

the pressure at the anode end of the discharge and is greatest when the tube radius is small (ref. (65) p. 256). H.G. Jones* finds that in a hydrogen discharge of a few amperes, with a mercury pool cathode, pressure gradients can exist in either direction, depending on the discharge parameters.

(b) Errors in T_e . The values of the electron temperature listed in Table 7 were obtained from the slope of the upper part of the probe characteristic. This part was usually linear over at least one decade in $\log I_e$, but at voltages more negative than $\sim(V_p - 3T_e)$ the curve often changed to a larger slope. This effect has been studied by R.M. Howe⁽⁷⁶⁾ who explains that it is due to the flux of energetic electrons to the tube wall where recombination with ions takes place. Only the more energetic electrons, those which are responsible for much of the ionization, can cross the ion sheath at the wall; there is consequently a depletion of such electrons in the energy distribution in the plasma. The effect disappears at several electron mean free paths from the wall. As $\lambda_{en} \gtrsim 3$ cm in the present discharges, the depletion of energetic electrons should occur throughout the cross-section of the tube. We should then expect the effective value of T_e in equation (33) to be less than the temperature of the bulk of slower electrons.

We may check the recorded values of T_e by comparing the power input and power dissipation in a 1 cm length of the plasma column. The power input from the electric field is $E_0 I_D$. This should be at least as great as the power W lost by the electrons in the ionization and excitation of atoms:

$$\begin{aligned}
 W &= W_g + W_* + \sum W_{ex} \\
 &= \pi R^2 \bar{n}_e (Z_g V_g + Z_* V_* + \sum Z_{ex} V_{ex}) \quad (35)
 \end{aligned}$$

where the average electron density \bar{n}_e is assumed to be equal to $2/3$ of the density at the axis and $\sum Z_{ex} V_{ex}$ represents the summation of the

* private communication

excitation energy over all the excited states. The power lost through elastic collisions with atoms is comparatively small.

Corresponding values of $E_0 I_D$ and W are presented in Table 8. The values of W in brackets correspond to electron temperatures 20% less than those given in the table. The last three columns show the relative values of the power losses due to ionization from ground and metastable states and to excitation.

Table 8. Power input and dissipation per cm of column

Gas	p m Torr	T_e eV	E_0 V cm ⁻¹	B gauss	$E_0 I_D$ watt cm ⁻¹	W watt cm ⁻¹	W_g/W %	W_{*}/W %	$\Sigma W_{ex}/W$ %
Ne	26	7.0	.7	15	4	2 (1)	37	3	60
A	14	3.4	.7	15	3.5	5 (2)	48	5	47
Hg	2	1.5	.25	15	2	2 (1)	2	5	93
	2-5	2.5	.25	0	2	11 (6)	7	10	83

The comparatively low value of W in the neon discharge indicates that the value of either n_e or T_e has been underestimated. It should be noted that the value of n_e for neon in Table 1(a) is less than the value for the present argon or mercury discharges by a factor of about 7. Since the currents are roughly equal in the neon and mercury discharges, and the electron drift velocities estimated from the extrapolation of the neon curve in fig. 61 of ref. (65) and the mercury curve in ref. (66) are of the same order of magnitude, we should expect the electron densities in these discharges to differ by a factor of no more than 2 or 3. It seems likely that the value of n_e for the neon discharge has been underestimated by a factor of more than 2 and that T_e has been slightly overestimated. With the probe facing against the electron drift velocity in this discharge, it may

be shown from the theory of Allen & Magistrelli⁽⁶⁶⁾ that the value of T_e obtained from the slope of the probe characteristic is too large by 10%.

The values of W for the argon and zero-field mercury discharges suggest that the effective values of T_e are less than the recorded values by about 10% in the former and 40% in the latter. The figure of 40% appears to be unreasonably large, but the absence of the magnetic field probably allows a comparatively greater loss of energetic electrons to the wall.

If we reduce T_e in equation (33) by the percentages suggested above, the values of Z' in the neon, argon and zero-field mercury discharges would be reduced by factors of 1.4, 1.7 and 4 respectively.

(35) Experimental and theoretical values of ωk

The following table shows the average value of ωk for each experimental dispersion curve and the corresponding value of $\frac{3}{2} E_0 Z'$ (see equation (25)). The figures in brackets represent the value of $\frac{3}{2} E_0 Z'$ when stepwise ionization is ignored.

Table 9. Values of ωk and $\frac{3}{2} E_0 Z'$

Gas	p m Torr	T_e eV	E_0 V cm ⁻¹	B gauss	ωk	$\frac{3}{2} E_0 Z'$
					$10^4 \times \text{sec}^{-1} \text{cm}^{-1}$	$10^4 \times \text{sec}^{-1} \text{cm}^{-1}$
Ne	(18-)26	7.0	.7	15	4	15 (15)
A	14	3.4	.7	15	$\frac{7}{2}$	33 (30)
Hg	2	1.5	.25	15	.8	2.5 (.7)
	2(-5)	2.5	.25	0	1	10 (3.5)

We see that $\frac{3}{2} E_0 Z'$ is greater than ωk by factors ranging from 3 to 15. The latter figure applies to the long wavelength branch of the dispersion curve in argon, which we shall regard as a special case (see section (37) below). The remaining four curves have $\frac{3}{2} E_0 Z'$ greater than

ωk by factors of 4, 5, 3 and 10 respectively. If T_e is reduced by the percentages suggested in the previous section, $\frac{3}{2} E_0 Z'$ would exceed the value of ωk for each of these four curves by a factor of about 3.

The main uncertainty in the theoretical value of ωk lies in the determination of Z' . After corrections have been made for the likely errors in p and T_e , the calculated values of Z' could still be in error by factors of 3 or more. Measurements of p in or near the region of wave propagation and more exact information about the energy distribution of the fast electrons are required in order to reduce this uncertainty. Furthermore, little attention has been given to the effect of the finite size of the plasma column on the wave propagation, although preliminary measurements by H.G. Jones (private communication) indicate that the waves are axially symmetric and the wave fronts convex when observed in the anode to cathode direction. (At 4 kc/s in a 2 millitorr mercury discharge the phase shift between axis and wall is $\sim 20^\circ$). It is reasonable to assume, however, from the above experimental results and discussion that the theory of Pekárek & Krějci describes the main features of backward waves at low pressures, viz. the shape and position of the dispersion curve on the ω - k diagram. We therefore identify these backward waves as ionization waves.

(36) Minimum value of the wave number

The experimental dispersion curves approach a low wave number limit k_{\min} when ω is made large. This is especially noticeable in the dispersion curve from the neon discharge and to a lesser extent in the curves for the present mercury discharge and the nitrogen discharge of Righetti et al. (70). Such behaviour can be explained to some extent by means of equation (29).

In the laboratory frame of reference equation (29) would be written as

$$(\omega k - \frac{3}{2} E_0 Z') (k^2 - k_0^2) = 0 \quad (35)$$

where $k_0^2 = a_1 v_{de} / 2D_e$ and $a_1 = (16/3\pi) (T_{e0} / E_0 \lambda_j^2) (2\kappa + T_{e0} \partial \kappa / \partial T_e)$. This

represents two independent dispersion relations which appear above as equations (25) and (30). Values of a_1 may be obtained roughly from curves of κ and T_e versus E/p (ref. (65) pp. 126, 248). These are listed in Table 10, together with the values of k_c .

Table 10. The parameters a_1 and k_c

Discharge	a_1 cm ⁻¹	$k_c = \sqrt{a_1 v_{de} / 2D_e}$ cm ⁻¹
Ne, 26 m Torr	.03	.03
A, 14 m Torr	.001	.005
Hg, 2 m Torr	.002	.01

The electron diffusion coefficient D_e has been put equal to $\frac{1}{3} \bar{c}_e \lambda_e$ where \bar{c}_e is the mean random velocity and λ_e the mean free path. The actual values of D_e are likely to be much smaller because the mean free path of the electrons is reduced by their interaction with induced dipoles in the gas atoms (ref. (65) p. 141). This would make k_c larger than a_1 in all the discharges and of the same order of magnitude as k_{\min} in the neon and mercury discharges.

As the frequency is increased it appears that k decreases according to equation (25) and then approaches the limit k_c well before reaching values of the order of a_1 at which equation (25) is invalid. There is a large discrepancy, however, between the values of k_{\min} from either of the two argon curves (fig. 22(a)) and the value of k_c . It is therefore uncertain whether or not the expression $(a_1 v_{de} / 2D_e)^{\frac{1}{2}}$ should be identified with the minimum value of k .

(37) Long wavelength branch of the dispersion curve in the argon discharge

The two branches of the dispersion curve in argon occur at $\omega k \approx 2 \times 10^4$ and $\omega k \approx 7 \times 10^4$. In the frequency range where the waves of the two branches coexist, 18-30 kc/s, they have wavelengths in the ratio of 3 to 1 and appear to be coupled: the short wavelength component

grows over several wavelengths at the expense of the long wavelength component which is damped.

The comparison of the values of ωk and $\frac{3}{2} E_0 Z'$ suggests that the short wavelength branch is the normal curve for the argon plasma. The most clearly defined of the waves observed in argon are those at a pressure of 30 millitorr, which lie on this branch (fig. 22(a)).

The coexistence of two or more modes of moving striations has been observed in neon⁽⁷⁷⁾ and argon⁽⁶⁾ at much lower currents and much higher pressures than those in the present discharges.

L. Pekarek* finds that when the current in a neon discharge is raised to about 1 A or more, the striations propagate in only one mode (and also fit the relation " $\omega k = \text{constant}$ " much more closely). It is not expected that there should be more than one mode in a pure, high current argon discharge either, although this possibility should not be rejected. There is the alternative possibility that the long wavelength mode is sustained by impurity mercury ions in the discharge. In order to make $\omega k = 2 \times 10^4 \text{ sec}^{-1} \text{ cm}^{-1}$ at an electron temperature of 3.4eV and electric field of 0.7 volt/cm, a density of about 4×10^{12} mercury atoms per cm^3 would be necessary. This would require that there be droplets of mercury, on the tube wall just above the cold trap say, at a temperature of about 0°C .

(38) The two dispersion curves in hydrogen

Density waves in hydrogen discharges have commonly been observed as forward waves, with group and phase velocities towards the anode. Fig. 24 however contains both a forward and a backward dispersion curve from the hydrogen discharge at 2.5A and 17 millitorr. These meet together on the k-axis at the wave number of the standing striations in the discharge. The two types of wave co-exist, producing wave-forms such as those in fig. 25. Similar wave forms were observed by Righetti et. al.⁽⁷⁰⁾ in a 12 millitorr hot-cathode discharge in hydrogen, from which they plotted the points shown in fig. 27. The points for the short wavelength component are rather widely scattered but those

* private communication.

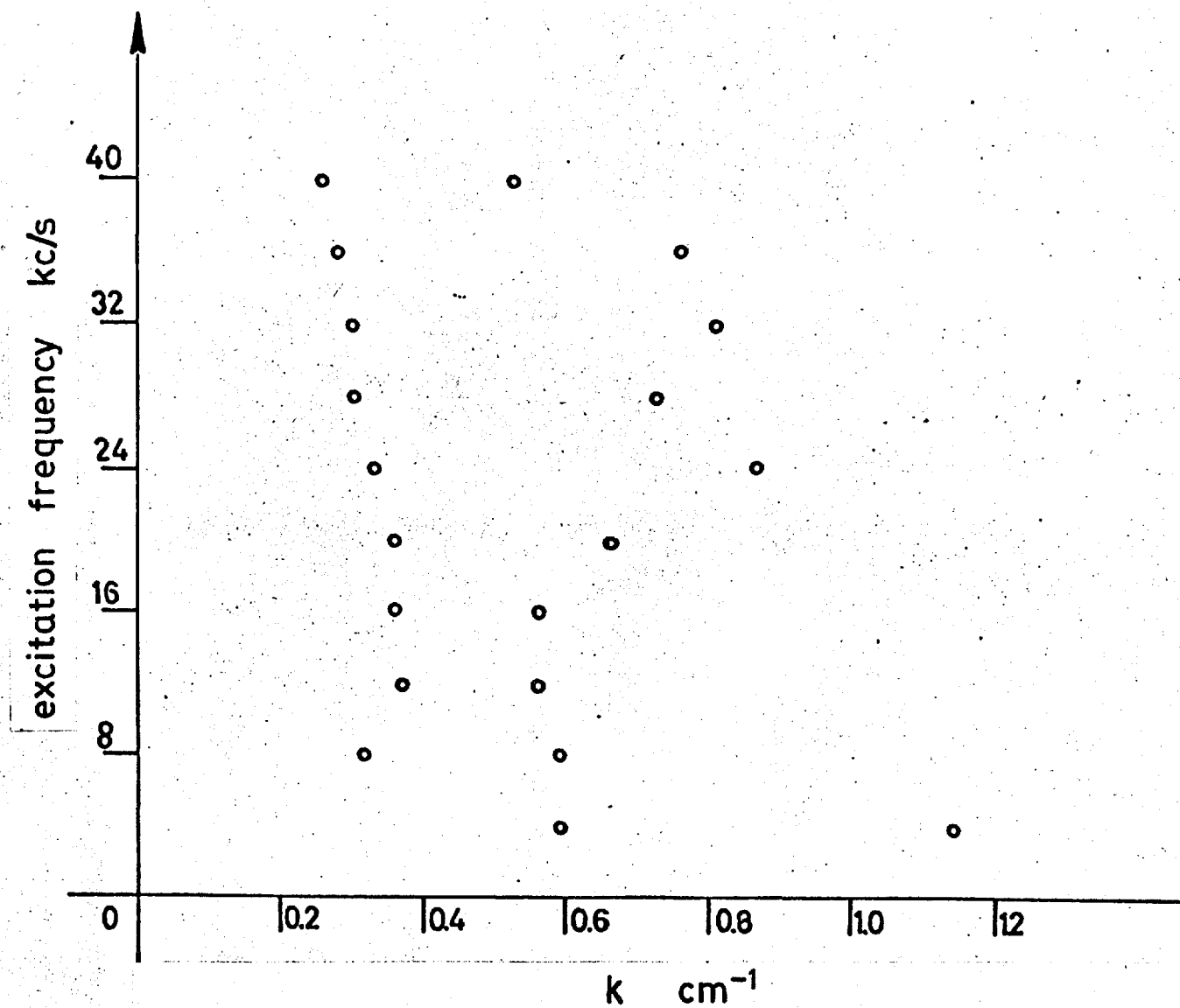


FIG 27 Waves in hydrogen discharge of Righetti et al. $p=12$ mtorr, $B=0$, $T_e=43,000$ °K, $n_e=1.2 \times 10^9 \text{ cm}^{-3}$.

for the long wavelength component form a clear dispersion curve of negative slope.

A similar pair of dispersion curves has been obtained by L. Pekárek⁽⁷⁸⁾ and Pekárek et. al.⁽⁷⁹⁾ from a discharge in a mixture of 46% hydrogen and 54% neon. When the mixture is richer in hydrogen, only forward waves are observed and when it is richer in neon, only backward waves are observed. (see Appendix E(2)).

Since no backward waves have previously been observed in hydrogen it is possible as in the argon discharge, that the backward waves are due to the presence of impurity ions in the discharge.

(39) Damping of the backward waves

The frequency dependence of the damping coefficient k_I , i.e. the imaginary part of the wave number, is best illustrated in fig. 19(a) which applies to the neon discharge. k_I was not clearly defined in either the argon discharge, where the waves were of small amplitude, or the mercury discharge, where the waves were of very long wavelength and were heavily damped. The relation between k_I and ω in fig. 19(a) is roughly of the form $\omega k_I = \text{constant}$.

An expression for k_I may be obtained from the term $\phi(k)$ in equation (22). This term represents the reciprocal of the growth time of a density perturbation and is expressed by Pekárek & Krejčí as

$$\phi(k) = b_1 E_0 Z' \frac{D_e}{v_{de}} - b_1 E_0 Z' \frac{a_1}{k^2 + a_1^2} - k^2 D_a \quad (36)$$

where $b_1 = \frac{3}{2} + \frac{16}{3\pi} (\tau_{e0}/E_0 \lambda_e) k \approx \frac{3}{2}$. The first term on the right hand side of the equation is a growth term and the other two are damping terms.

Consider the variation of the amplitude of waves in a wave packet as the packet moves towards the anode with the group velocity $|\omega/k|$. The spatial growth rate is given by

$$k_I = -\frac{k}{\omega} \phi(k) \quad (37)$$

(We choose the sign of k_I to be positive when there is damping). If we

replace $b_1 E_0 Z'$ by ωk and assume that $a_1^2 \ll k^2$, then

$$k_I = -(k^2 D_e / v_{de}) + a_1 + k^3 D_e / \omega \quad (38)$$

Similarly, the expression for k_I derived by Righetti et. al. (70) may be reduced to the form

$$k_I = -(k^2 D_e / v_{de}) + a_1 \quad (39)$$

Let us apply equation (38) to the neon discharge. If D_e is assumed to be equal to $\bar{c}_e \lambda_e / 3$, the growth term is larger than the sum of the damping terms by an order of magnitude in the observed frequency range. This expression for D_e is, however, larger than the actual value (see section (36) above) and so it is uncertain whether growth or damping is predicted by equation (38). It is noted that the growth term and the sum of the damping terms each increase as the frequency decreases.

(40) Effect of magnetic field on wave propagation

In the absence of the longitudinal magnetic field the wave traces on the chart recorder are often irregular and show a poor signal-to-noise ratio. The only clearly defined series of waves at zero field are those in the 5 cm mercury column. A few wave traces have also been obtained from the neon and hydrogen discharges. A comparison of the waves in the mercury discharge at $B=0$ and at $B=15$ gauss shows that the magnetic field (i) increases the signal-to-noise ratio, and the signal amplitude per unit of exciter current, and (ii) decreases the product ωk for the backward waves. The first effect is illustrated in figs. 11, 12 and 17 and the second effect in fig. 16.

The reduction of ωk by a magnetic field is reported by Zaitsev & Vasil'eva⁽⁸⁰⁾. They observe that in an argon-mercury discharge ($p \sim 1$ torr, $I_D = 100-200$ mA, diameter = 2 cm), ωk decreases by 30% when B is raised from 0 to 1000 gauss.

The application of the magnetic field reduces the rate of loss of the charged particles to the wall and so the electron temperature falls. This reduces the term Z' and therefore the term ωk . There is also less discharge noise at lower electron temperatures. The effect of the magnetic field on the signal amplitude is discussed in Appendix G.

CHAPTER V
CONCLUSIONS

(41) Summary

Experimental curves have been obtained for the dispersion and damping of both forward and backward waves in low pressure d.c. discharges. Some of the forward waves have phase velocities less than those expected from the measured values of the electron temperature, even after allowance is made for longitudinal drifts of the charged particles. The backward waves have values of ωk which are also less than the calculated values. There is, however, sufficient agreement between the experimental and theoretical dispersion curves for the forward waves to be identified as electro-acoustic waves in one or other of the two lowest radial modes, and the backward waves as ionization waves. There is little correlation between the theoretical and observed values of the damping coefficient for either type of wave.

(42) Significance of results

These experiments supplement earlier work on forward and backward waves in d.c. discharges. The dispersion curves obtained by Little & Jones approached a cut-off frequency (in mercury) or a cut-off wavelength (in hydrogen), whereas some of the present curves are of the more simple form $\omega/k = ac_s$. Hatta & Sato had previously found such a dispersion relation for waves in argon, but under somewhat different conditions. Earlier authors had demonstrated that either forward or backward waves may occur in a positive column, depending on the value of the pressure. It has been shown here in the neon discharge that forward and backward waves may co-exist. This fact is relevant to any theory of the transition between forward and backward waves. Most experiments on ionization waves have been carried out at pressures in the range 0.1-10 torr and few of these have been concerned with dispersion curves. Crawford & Self obtained a backward wave dispersion curve at a much lower pressure in mercury vapour, 2 millitorr, but this was not at the time thought to be associated with ionization waves. The present experiments and those

of Righetti et. al. have since linked the backward waves at low pressures with the ionization wave theory of Pekárek & Krejčí.

(43) Suggestions for further investigation of forward and backward waves

As far as future work on forward and backward waves is concerned, certain theoretical and experimental investigations would be of interest. The theory of ionization waves needs to be extended to bounded plasmas. In principle this could be done by including perturbations of the electron temperature and ionization rate in the theory of electro-acoustic waves in a collision-dominated positive column. Apart from providing more appropriate dispersion curves for ionization waves, this procedure might clarify the transition between forward and backward waves. It would also be desirable to include the electron drift velocity in such a theory to see how this affects (i) the propagation of forward waves in the principal mode and (ii) the damping of the forward waves.

On the experimental side, further measurements on backward waves are required in order to test more thoroughly the validity of Pekárek & Krejčí's dispersion equation. It is desirable to have dispersion curves at several different pressures in a particular gas, together with accurate measurements of p and T_e (or, better still, the electron energy distribution), and also some information on the shape of the wave fronts. The discrepancies between the experimental and theoretical phase velocities of the forward waves and the effect of the tube diameter on both types of wave also require further investigation.

EXTERNALLY EXCITED WAVES IN LOW-PRESSURE PLASMA COLUMNS

P. J. Barrett* and P. F. Little

United Kingdom Atomic Energy Authority, Research Group, Culham Laboratory, Berkshire, England

(Received 21 January 1965)

This Letter reports measurements on low-frequency waves in hydrogen, neon, argon, and mercury arcs ($f = 4\text{-}400$ kc/sec, $p = 0.3\text{-}30$ mTorr, longitudinal magnetic field = 0 or 10-45 gauss, column diameter = 5 or 3 cm). Currents of several amperes were obtained in these gases with a mercury-pool cathode, using a liquid-nitrogen trap in the discharge path.¹ Waves were excited in the positive column by a coil placed 80 cm from the anode and detected by a photomultiplier on the anode side of the coil, as in earlier experiments here on compression-al waves in a low-pressure mercury arc.²⁻⁴

The dispersion curves obtained fall into two groups, those having negative slope (backward waves, Fig. 1) and those having positive slope (forward waves, Fig. 2). Curves obtained by other observers for backward waves in mercury⁵ and forward waves in argon⁶ and hydrogen⁷ are included, together with some of the measurements in mercury reported previously². The symbols specifying the various conditions are explained in Tables I and II.

The backward waves may be described approximately by the empirical relation

$$\omega k = \text{constant.} \quad (1)$$

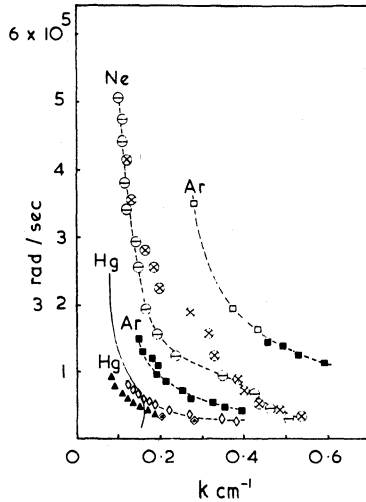


FIG. 1. Backward waves. The symbols represent results in different discharges (see Table I).

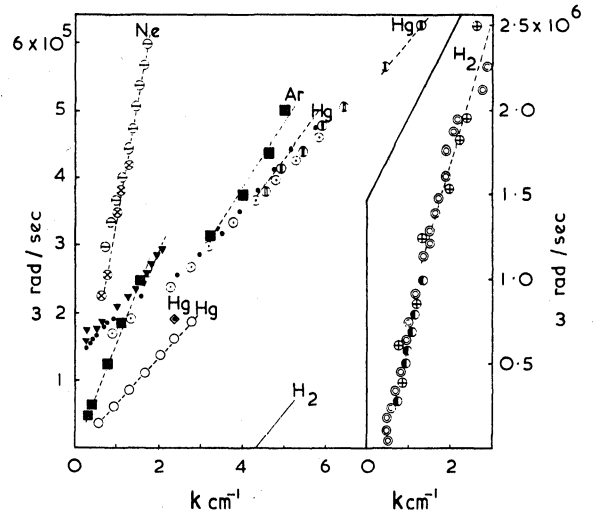


FIG. 2. Forward waves. The meaning of the symbols is given in Table II.

The forward waves are of the form

$$\omega/k = \alpha c_s$$

where $c_s = (kT_e/m_i)^{1/2}$, and $0.4 < \alpha < 1.4$ (see Table II). At low frequencies some of the forward waves exhibit a cutoff in frequency or in wave number. In weak magnetic fields the waves are usually more easily excited: The dispersion curves are not altered by more than 20%, so magnetic fields do not affect the wave propagation critically.

In mercury, at 0.6 mTorr only, both backward and forward waves can be detected. The latter have very small amplitude and appear in a narrow frequency range near $\omega \approx 2 \times 10^5$ rad/sec. At higher pressures, only backward waves are observed and at lower pressures, only forward waves. In neon, at 26 and 18 mTorr,

we observe both types of wave simultaneously over a wide frequency range at $\omega > 2.5 \times 10^5$ rad/sec. The phase and group velocities of the backward waves are much larger than those of the forward waves in this range. There is no evidence of strong coupling (i.e., no observable energy transfer) between these two types of wave. In argon, however, the two backward wave modes are coupled: The short-wavelength mode grows at the expense of the long-wavelength mode at large distances from the exciter.

The attenuation observed varies greatly and in some instances the wave amplitude grows over part of the plasma column. Backward waves in mercury are strongly attenuated; the damping length $\delta \sim 0.5\lambda$. For backward waves in argon and neon the damping is less, $1.5\lambda < \delta < 10\lambda$. Forward waves in neon show alternate regions

Table I. Discharge parameters for backward waves.

Symbol	Gas	T_e (eV)	p (mTorr)	B_z (gauss)	E_z (V/cm)	I_D (A)	N_e (cm^{-3})	Diam	Ref
⊖	Ne	7.0	26	15	0.7	6	0.6×10^{11}	5	
⊗	Ne	7.2	18	15	0.7	6	1	5	
□	Ar		30	15		5.5	5	5	
■	Ar	3.4	14	15	0.7	5	4	5	
◇	Hg	2.5	2-5	0	0.25-0.35	7.5	5	5	
▲	Hg	1.5	2	15	0.25	7.5	5	5	
◆	Hg	2.5	0.6	15	0.1	7.5	2	5	
Solid curve	Hg	2.0	2	0		0.1		2.2	a

^aSee reference 4

Table II. Discharge parameters for forward waves.

Symbol	Gas	T_e (eV)	p (mTorr)	B_z (gauss)	E_z (V/cm)	I_D (A)	N_e (cm^{-3})	Diam	$\alpha = \omega/kc_s$	Ref
⊖	Ne	7.0	26	15	0.7	6	0.6×10^{11}	5	0.6	
⊗	Ne	7.2	18	15	0.7	6	1	5	0.6	
■	Ar	0.6	40	0	~0	0.01	0.025	~5	0.85(1.4)	b
▼	Hg	5.2	0.4	45	0.1	9		5	0.9	c
⊕	Hg	2.2	0.4	0	0.1	9		5	0.75	d
●	Hg	3.5	0.4	15	0.1	8	2	5	0.65	
◆	Hg	2.5	0.6	15	0.1	7.5	2	5	0.75	
○	Hg	4.2	0.3	20	0.1	8	0.3	3	0.45	
⊙	Hg		0.4	0		8		5		
Solid curve	H ₂		10^3	0		0.13		2		e
○	H ₂	5.4	20	40		2.8		5	0.45	
⊕	H ₂	5.4	20	10		4		5	0.45	a
⊖	H ₂	6.1	17	10	1.1	2.5	0.5	5		

^aSpontaneously generated waves from noise analysis.⁴

^bSee reference 6.

^cSee reference 2.

^dSee reference 3.

^eSee reference 7.

of growth and damping, but on the average, $\delta \sim 3\lambda$. In mercury, in the 5-cm tube, the same value of δ applies for forward waves when $\omega < 3 \times 10^5$, but at higher frequencies regions of growth appear and $\delta \sim 10\lambda$ overall. In the 3-cm tube $\delta \sim 3\lambda$ for these forward waves at $\omega > 1.4 \times 10^5$, and it is the lower frequencies that grow slowly over most of the length observed. Waves in hydrogen show $\delta \sim \lambda$ at the lowest frequencies, and $\delta \sim 3\lambda$ when ω is increased to 3×10^5 . At $\omega > 3 \times 10^5$, regions of growth and damping again appear and the damping length increases to $\delta \sim 10\lambda$ average.

To some extent these waves behave like moving striations. In rare gases a transition from forward to backward waves is seen to occur as the pressure is increased.⁸ Measurements on backward waves in argon⁹ at high pressure ($p = 1$ Torr, $f = 650$ -1100 cps) are well described by Eq. (1), and the existence of two modes in the argon curves marked  may be related to the multiple modes seen at 12 Torr in this gas.¹⁰ We find no backward waves at all in hydrogen; this is consistent with the fact that striations in hydrogen and some other molecular gases are forward waves.¹¹

At higher pressures these moving striations which are backward waves have been interpreted as ionization waves.¹² Observations on backward waves at low pressures, near 1 mTorr, have not been explained.^{5,13} It is probable that

the waves of Fig. 1 are ionization waves, but they are externally excited small-amplitude waves in a stable regime of the discharge, in contrast to the naturally occurring large-amplitude waves arising in oscillatory regimes. (Small pulsed perturbations have been studied in a stable regime by Pekárek¹⁴ and, recently, in a quasistable regime by Cooper.¹⁵)

The forward waves of Fig. 2 have velocities near the Tonks-Langmuir electroacoustic wave velocity c_S ¹⁶; with one exception their velocity is below c_S . The ion-neutral collision frequency is greater than the wave frequency in most instances, so $\omega/k < c_S$ is to be expected.⁸ The waves are probably electroacoustic in nature, though modified by ionization processes and ion-neutral collisions. The exceptionally high wave velocity in argon at low frequencies⁶ may be partly accounted for if $\gamma > 1$ should be included in c_S .

Our thanks are due to Mr. H. G. Jones and Mr. C. R. Middleton for their assistance with the hydrogen measurements.

*On attachment from Department of Physics, Imperial College, London.

¹J. E. Allen and F. Magistrelli, *Nature* **194**, 1167 (1962).

²P. F. Little, *Proceedings of the Fifth International Conference on Ionization Phenomena in Gases, Munich, 1961* (North-Holland Publishing Company, Am-

sterdam, 1962), p. 1440.

³P. F. Little, *Nature* 194, 1137 (1962).

⁴P. F. Little and H. G. Jones, to be published.

⁵F. W. Crawford and S. A. Self, Proceedings of the Sixth International Conference on Ionization Phenomena in Gases, Paris, 1963, edited by P. Hubert (S.E.R.M.A., Paris, 1964), Vol. 3, p. 129.

⁶Y. Hatta and N. Sato, Proceedings of the Fifth International Conference on Ionization Phenomena in Gases, Munich, 1961 (North-Holland Publishing Company, Amsterdam, 1962), Vol. 1, p. ~~475~~ 478.

⁷S. Pfau and A. Rutscher, *Ann. Physik* 6, 244 (1960).

⁸M. Y. Vasil'eva, A. A. Zaitsev, and E. D. Zndryukhina, *Izv. Nauk, SSSR, Ser. Fiz.* 23, 995 (1959) [translation: *Bull. Acad. Sci. USSR, Phys. Ser.* 23, 982 (1959)]; I. Alexeff and W. D. Jones, Oak Ridge National Laboratory Report No. ORNL-3652, April 1964 (un-

published), p. 56.

⁹K. Wojaczek, *Ann. Physik* 2, 68 (1958).

¹⁰T. Donahue and G. H. Dieke, *Phys. Rev.* 81, 248 (1951).

¹¹L. Pekárek, *Czech. J. Phys.* 8, 699 (1958).

¹²L. Pekárek, Proceedings of the Sixth International Conference on Ionization Phenomena in Gases, Paris, 1963, edited by P. Hubert (S.E.R.M.A., Paris, 1964), Vol. 2, p. 133.

¹³K. H. W. Foulds, *J. Electron. and Control* 2, 270 (1956).

¹⁴L. Pekárek, *Czech. J. Phys.* 9, 67 (1959); *Phys. Rev.* 108, 1371 (1957).

¹⁵R. S. Cooper, Massachusetts Institute of Technology Report No. MIT-424, September 1964 (unpublished).

¹⁶L. Tonks and I. Langmuir, *Phys. Rev.* 33, 195 (1929).

APPENDICES

FOR PART A

APPENDIX A

Relationships between $\frac{\partial V_p}{\partial z}$, $\frac{\partial n_e}{\partial z}$ and $\frac{\partial T_S}{\partial z}$.

The variations of V_p , n_e and T_S with z have been shown in fig. 12 to be closely linked. It is observed that at any value of z greater than 3 mm the algebraic signs of $\partial V_p/\partial z$ and $\partial T_S/\partial z$ are the same while those of $\partial T_S/\partial z$ and $\partial n_e/\partial z$ are opposite. These two results may be obtained from the equation of motion and the continuity equation for the electrons:

$$n_e m_e \left(\frac{\partial \bar{v}_{ez}}{\partial t} + \bar{v}_{ez} \frac{\partial \bar{v}_{ez}}{\partial z} + \bar{v}_{e1} \nabla_{\perp} \bar{v}_{ez} \right) = -n_e e E_z - (\nabla \cdot \underline{\underline{P}}_e)_z \quad (1)$$

$$\frac{\partial n_e}{\partial t} + \nabla \cdot (n_e \underline{\underline{v}}_e) = 0 \quad (2)$$

where the bar over a symbol shows that it is a macroscopic quantity and where

$$\underline{\underline{P}}_e = m_e \sum (\underline{v}_e - \underline{\bar{v}}_e)(\underline{v}_e - \underline{\bar{v}}_e)$$

is the stress tensor⁽²⁵⁾ in the electron gas. The summation extends over unit volume.

The tensor term in (1) may be expanded thus:

$$\begin{aligned} (\nabla \cdot \underline{\underline{P}}_e)_z &= n_e m_e \frac{\partial}{\partial z} \overline{(v_{ez} - \bar{v}_{ez})^2} + m_e \overline{(v_{ez} - \bar{v}_{ez})^2} \frac{\partial n_e}{\partial z} \\ &+ n_e m_e \nabla_{\perp} \overline{(v_{e1} - \bar{v}_{e1})(v_{ez} - \bar{v}_{ez})} + m_e \overline{(v_{e1} - \bar{v}_{e1})(v_{ez} - \bar{v}_{ez})} \nabla_{\perp} n_e \end{aligned} \quad (3)$$

All the variables are functions of position only and so the operator $\partial/\partial t$ is zero. Equation (1) may be further simplified by omitting the ∇_{\perp} terms. This is not unreasonable since we should expect the average of the random velocity product, $\overline{(v_{ez} - \bar{v}_{ez})(v_{e1} - \bar{v}_{e1})}$, to be comparatively small, and $\nabla_{\perp} \bar{v}_{ez}$ is likely to be appreciably less than $\partial \bar{v}_{ez}/\partial z$ near

the axis of the wake (as in the case of the fig. 12 measurements). Equation (1) then becomes

$$n_e \frac{\partial}{\partial z} \left(\frac{1}{2} m_e \bar{v}_{ez}^2 + m_e \overline{(v_{ez} - \bar{v}_{ez})^2} \right) + m_e \overline{(v_{ez} - \bar{v}_{ez})^2} \frac{\partial n_e}{\partial z} = n_e \frac{\partial V_p}{\partial z}$$

where the kinetic energies are expressed in electron-volts. For a Maxwellian distribution $\bar{v}_{ez}^2 = 0.85 \bar{v}_{ez}^2$ and $\overline{(v_{ez} - \bar{v}_{ez})^2} \approx 0.3 \bar{v}_{ez}^2$, and, since $T_S = \frac{1}{2} m_e \bar{v}_{ez}^2$, the equation may be written as

$$1.5 n_e \frac{\partial T_S}{\partial z} + 0.6 T_S \frac{\partial n_e}{\partial z} = n_e \frac{\partial V_p}{\partial z} \quad (4)$$

It may be shown from the curves in fig. 12 that the first term in (4) is at least three times larger than the second term over much of the observed region, but that this inequality is reversed in the range $z < 3$ mm (where n_e decreases rapidly towards the obstacle) and in the range $12 < z < 15$ mm. The discrepancy in the latter range is due perhaps to errors in the slopes of the curves; the T_S curve has been drawn here with a very small slope. It is to be expected that $\left| \frac{\partial n_e}{\partial z} \right|$ is in general somewhat less than $\left| \frac{\partial T_S}{T_S} \right|$, because of the comparatively large mean value of n_e , which is probably the result of the streaming of electrons into the dark region from the plasma at the anode end of the wake. It then follows from (4) that

$$\frac{\partial T_S}{\partial z} \sim \frac{\partial V_p}{\partial z} \quad (5)$$

which is in agreement with the curves in fig. 12.

The continuity equation, (2), may be written in the form

$$\nabla_z (n_e \bar{v}_{ez}) = f(z) = -\nabla_{\perp} (n_e \bar{v}_{e\perp})$$

It is not permissible to put $f(z) = 0$; because of the helical nature of the macroscopic electron motion there is everywhere some interchange of perpendicular and axial electron flux. It is necessary, however, to make the assumption that the gradients of n_e and \bar{v}_{ez} in the dark region are sufficiently large to make $|n_e \partial \bar{v}_{ez} / \partial z|$ and

$|\bar{v}_{ez} \frac{\partial n_e}{\partial z}|$ appreciably larger than $f(z)$, the spatial rate of this interchange of flux. Then

$$n_e \frac{\partial \bar{v}_{ez}}{\partial z} \sim - \bar{v}_{ez} \frac{\partial n_e}{\partial z}$$

or

$$n_e \frac{\partial}{\partial z} \left(\frac{1}{2} m_e \bar{v}_{ez}^2 \right) \sim - m_e \bar{v}_{ez}^2 \frac{\partial n_e}{\partial z}$$

or

$$n_e \frac{\partial T_S}{\partial z} \sim - 2T_S \frac{\partial n_e}{\partial z} \quad (6)$$

which is again in agreement with the curves in fig. 12.

APPENDIX BElectron Cyclotron Wave

Dispersion relation. The dispersion equation for the electron cyclotron wave may be derived from the three equations

$$\frac{\partial \underline{v}_e}{\partial t} = \frac{e}{m} (\underline{E} + \frac{1}{c} \underline{v}_e \times \underline{B}) \quad (1)$$

$$\underline{E} = -\nabla V \quad (2)$$

$$\nabla \cdot \underline{v}_e = 0 \quad (3)$$

where \underline{v}_e is the macroscopic electron velocity, \underline{E} the electric vector of the wave and V the electrostatic potential. The ion motion is negligible in the frequency range of interest here ($\omega \gg \omega_{ci}$) and we shall assume that n_i is constant in space and time. Since $n_e \approx n_i$ equation (3) follows from the steady state equation of continuity, $\nabla \cdot (n_e \underline{v}_e) = 0$.

The axes of the cartesian co-ordinate system may be chosen so that the z axis is parallel to \underline{B} and the xz plane contains the wave vector \underline{k} . It is assumed that the variables in the three equations above are each proportional to $\exp i(\omega t + k_x x + k_z z)$. From the x , y and z components of equation (1) it may be shown that

$$\omega = \omega_{ce} \left(\frac{k_z^2}{k_z^2 + k_x^2} \right)^{\frac{1}{2}} = \omega_{ce} \cos \theta \quad (4)$$

where θ is the angle between \underline{k} and \underline{B} . This is the dispersion relation for an electron cyclotron wave of small amplitude.

Effect of transverse density gradient. If there is a density gradient $\nabla_x n_e$ in the x direction, the equation of continuity may be written as

$$n_e (ik_z v_{1z} + ik_x v_{1x}) + v_{ex} \nabla_{\perp} n_e = 0 \quad (5)$$

where \underline{v}_1 is the perturbation component of \underline{v}_e . If equation (3) is replaced by equation (5), the following dispersion relation is obtained:

$$\omega^2 = \omega_{ce}^2 \frac{k_z^2}{k_z^2 + k_x^2 - ik_x \Delta_{\perp} n_e / n_e} \quad (6)$$

It is evident that either or both of the frequency ω and the wave number k are complex quantities. In the present experiment it is assumed that in the drift frame $\omega = a + ib$ and $k = k_R + k_I = (a + ib)/v_d \cos \theta$. Writing $\Delta_{\perp} n_e / n_e$ as k_g we may derive the following equation from equation (6):

$$\left(\frac{k_I}{k_R} \right)^2 = \frac{[1 + (k_x^2 k_g^2 / k^4)]^{\frac{1}{2}} - 1}{[1 + (k_x^2 k_g^2 / k^4)]^{\frac{1}{2}} + 1} \quad (7)$$

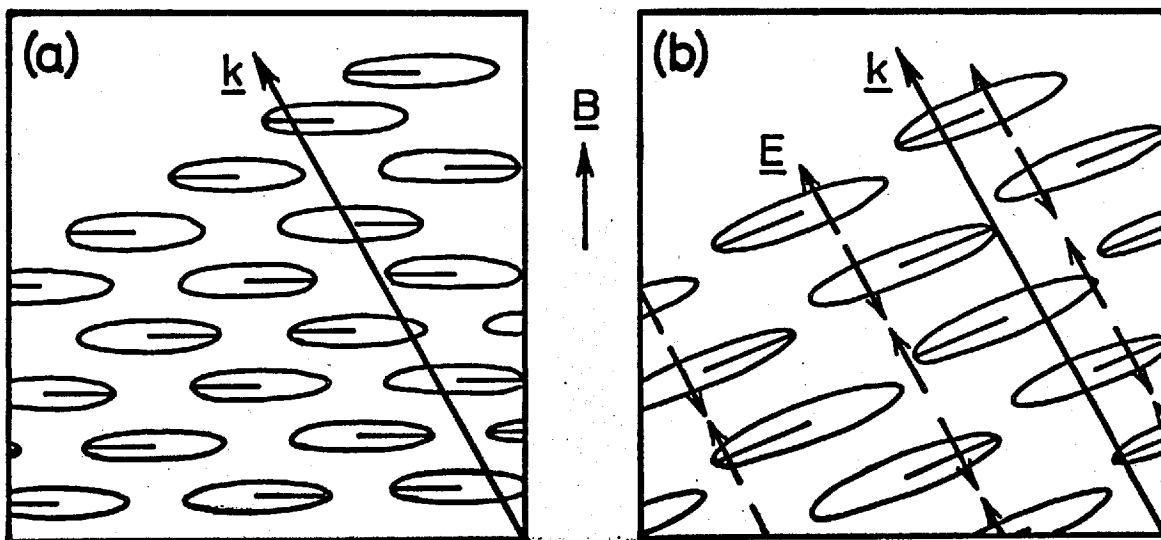
Let us assume that $k_{\perp} = 5.2 \text{ cm}^{-1}$, $k_z = 4.2 \text{ cm}^{-1}$ and $k_g \approx 2 \text{ cm}^{-1}$ in the wakes represented in figs. 12 and 14. Then from equation (7) $k_I/k_R \approx 0.1$. This is somewhat less than the observed value from fig. 12, $k_I/k_R = 0.3 \pm 0.1$.

Physical description. We consider what happens when a wave is excited, at an angle θ to the magnetic field, at a frequency ω which may be increased towards ω_{ce} . As ω approaches ω_{ce} ($\omega < \omega_{ce} \cos \theta$), the motion of the electrons perpendicular to the field increases sharply. Stringer⁽²²⁾ explains that the quasi-neutrality condition of the plasma then "requires a corresponding increase in the neutralising flow of electrons along the field lines. However, motion along field lines is limited by electron inertia, which imposes a limit on the growth of the perpendicular motion and hence on the approach to ω_{ce} . As

the limit is approached, the longitudinal electric field ($\underline{E} // \underline{k}$) resulting from the small residual space charge dominates over the transverse component".

The nature of the wave is illustrated below. In (a) the electron velocity vectors rotate about the direction of \underline{B} . The successive wave fronts encountered by an observer on moving along \underline{k} have different phases of rotation which clearly tends to produce successive increases and decreases of electron density. The tendency is counteracted by the periodic movement of the electron guiding centres up and down along the lines of magnetic field. As $\omega \rightarrow \omega_{ce} \cos \theta$ and the velocity and radius vectors increase, it is obvious that more rapid motion along the field lines is required. The stage is finally reached when quasi-neutrality is maintained only by the bending over of the orbits almost into the plane of the wave front, as in (b).

In the limiting condition shown in (b) the velocity vector \underline{v}_e is approximately perpendicular to \underline{k} . Stringer shows that the dispersion relation $\omega = \omega_{ce} \cos \theta$ may be derived from the condition $\underline{k} \cdot \underline{v}_e = 0$. In this condition the electrons are rotating about the magnetic field component $B \cos \theta$ with a frequency $\omega_{ce} \cos \theta$, and the electrostatic field \underline{E} is approximately parallel to \underline{k} as shown in (b).



APPENDICES

FOR PART B

APPENDIX CBasic dispersion equation for electro-acoustic waves

The dispersion equation is derived from the following seven equations concerning the perturbation of the ion and electron density.

Equations of state:

$$p_i = c_i^2 n_i m_i \quad (\text{where } c_i^2 = \gamma_i KT_i/m_i) \quad (1)$$

$$p_e = c_e^2 n_e m_e \quad (\text{where } c_e^2 = \gamma_e KT_e/m_e) \quad (2)$$

Equations of continuity:

$$\frac{\partial n_i}{\partial t} + n_o \nabla \cdot \underline{v}_i = 0 \quad (3)$$

$$\frac{\partial n_e}{\partial t} + n_o \nabla \cdot \underline{v}_e = 0 \quad (4)$$

Equations of motion:

$$\frac{\partial \underline{v}_i}{\partial t} = \frac{e}{m_i} \underline{E} - \frac{\nabla p_i}{n_o m_i} \quad (5)$$

$$\frac{\partial \underline{v}_e}{\partial t} = -\frac{e}{m_e} \underline{E} - \frac{\nabla p_e}{n_o m_e} \quad (6)$$

Poisson equation:

$$\nabla \cdot \underline{E} = 4\pi e (n_i - n_e) \quad (7)$$

The quantities n_i and n_e are the perturbation components of the total ion and electron densities, $(n_i + n_o)$ and $(n_e + n_o)$.

It is assumed that the propagation is in the z direction and that each of the variables in these equations is proportional to $\exp i(\omega t - kz)$. Equations (3) to (7) may then be written in the linearized form as follows:

$$\omega n_i - n_0 k v_{iz} = 0 \quad (3a)$$

$$\omega n_e - n_0 k v_{ez} = 0 \quad (4a)$$

$$i\omega v_{iz} = eE_z/m_i + ikc_i^2 n_i/n_0 \quad (5a)$$

$$i\omega v_{ez} = -eE_z/m_e + ikc_e^2 n_e/n_0 \quad (6a)$$

$$E_z = -4\pi e(n_i - n_e)/ik. \quad (7a)$$

The variables v_{iz} , v_{ez} and E_z may be eliminated from equations (5a) and (6a), leaving two equations in n_i and n_e , from which we eliminate these two variables to obtain the dispersion equation

$$(\omega^2 - \omega_{pe}^2 - k^2 c_e^2)(\omega^2 - \omega_{pi}^2 - k^2 c_i^2) = \omega_{pe}^2 \omega_{pi}^2 \quad (8)$$

Under the condition that ω^2 and $c_i^2 k^2$ are much less than ω_{pe}^2 , equation (8) assumes the form of equation (1) in section (4):

$$\left(\frac{\omega}{k}\right)^2 = \frac{(c_e^2 m_e/m_i) + c_i^2(1 + c_e^2 k^2/\omega_{pe}^2)}{1 + c_e^2 k^2/\omega_{pe}^2} \quad (9)$$

The dispersion equation for electron plasma waves, $\omega^2 = \omega_{pe}^2 + k^2 c_e^2$, may also be obtained from equation (8).

APPENDIX D

Dispersion equation for electro-acoustic waves in a plasma column with ion collisions.

The dispersion equation, (8), in Appendix C is modified by the radial dimension of the plasma and by the ion collisions. If the collision term $\underline{v}_i \nu$, where ν is the ion collision frequency (with neutrals and ions), is added to the right hand side of equation (5) in Appendix C, this has the effect of adding $i\omega\nu$ to the expression in the second pair of brackets in equation (8). If we now assume that the variables in equations (1) to (7) are of the form $A(r) \exp i(\omega t - kz - m\theta)$ and replace $-k^2$ by α , where α is given by $\nabla^2 q = \alpha q$ and q represents any of the variables⁽⁸¹⁾, equation (8) becomes

$$(\omega^2 - \omega_{pe}^2 + c_e^2 \alpha)(\omega^2 + i\omega\nu - \omega_{pi}^2 + c_i^2 \alpha) = \omega_{pe}^2 \omega_{pi}^2 \quad (10)$$

Now the equation in q may be expanded to

$$\frac{1}{r} \frac{\partial}{\partial r} \left(r \frac{\partial q}{\partial r} \right) + \frac{1}{r^2} \frac{\partial^2 q}{\partial \theta^2} + \frac{\partial^2 q}{\partial z^2} - \alpha q = 0$$

$$\text{or } \frac{1}{r} \frac{\partial}{\partial r} \left(r \frac{\partial q}{\partial r} \right) + \left(-k^2 - \alpha - \frac{m^2}{r^2} \right) q = 0 \quad (11)$$

If we put $k^2 + \alpha = -k_c^2$, equation (11) takes the form of Bessel's equation

$$\frac{1}{r} \frac{\partial}{\partial r} \left(r \frac{\partial q}{\partial r} \right) + \left(k_c^2 - \frac{m^2}{r^2} \right) q = 0$$

which has the solution

$$q = A J_m (k_c r) \quad (12)$$

Under the condition that ω^2 and $\omega\nu$ are much less than ω_{pi}^2 , equation (10) takes the more simple form

$$\omega^2 + i\omega\nu + c_s^2 \alpha = 0$$

or

$$\omega^2 + i\omega\nu = c_s^2 (k^2 + k_c^2) \quad (13)$$

APPENDIX E

Three types of anode-approaching striation.

(1) "Negative" striations of Donahue & Dieke

Fast anode-approaching striations may sometimes be observed near the cathode of a low current discharge in the presence of the usual cathode-approaching striations. These were first observed by Donahue & Dieke⁽⁶⁾ and have also been studied by J.R.M. Coulter⁽⁸²⁾. Their occurrence is explained by L. Pekárek* as follows. When the positive column conditions are suitable for the growth of ionization waves, the packet of striations produced by any small disturbance (see section (13)) reaches the anode and the individual striations cause oscillations in the discharge voltage. The voltage oscillations generate further striations at the cathode end of the discharge. Any given wave packet thus gives rise to a new wave packet. The process continues until there are no gaps between wave packets and the entire column is filled with moving striations. It may happen that the oscillations fed back from anode to cathode produce new striations which fail to synchronize with the existing striations. The consequent mismatch is observed as a disturbance or "negative" striation in the otherwise uniform striation pattern, travelling towards the anode at the group velocity of the ordinary striations.

(2) Striations in hydrogen

Striations in hydrogen discharges have commonly been observed to propagate towards the anode (see section (12)). In searching for an explanation of this phenomenon, L. Pekárek⁽⁷⁸⁾ and Pekárek et. al⁽⁷⁹⁾ have studied the change of direction that occurs in a hydrogen-neon mixture as the proportion of hydrogen is changed. When the proportion of hydrogen is less than 46% the striations travel towards the cathode, and when it exceeds 46% they travel towards the anode.

The following explanation of this observation is suggested by Pekárek. A perturbation in n_1 is accompanied by perturbations in n_e , T_e and Z (section (13)). Suppose the perturbation n_{11} is positive: n_{e1} then has a maximum just to the anode side of the maximum in n_{11} and, by

*private communication

enhancing the ionization rate at that point, tends to produce a drift of the perturbation Z_1 towards the anode. The perturbation T_{e1} , on the other hand, has a maximum just to the cathode side of the maximum in n_{i1} and tends to make Z_1 drift towards the cathode. The direction in which Z_1 drifts, i.e. the direction of the striation, depends upon which of these two opposing effects is the stronger. If this hypothesis is correct, the T_{e1} perturbation obviously exerts the stronger effect on the drift of Z_1 in the neon-rich mixture and the n_{e1} perturbation is the predominant one in the hydrogen-rich mixture. It is not known, however, what criteria determine which effect is the stronger.

(3) Striations at low pressure

It has been observed in inert gas discharges that a decrease in pressure from several tens of millitorr to several millitorr results in a change of direction of the striations: at the lower pressures they travel towards the anode. This phenomenon was mentioned in section (11). The phase velocities of the anode-approaching waves, both artificially excited⁽¹²⁾ and spontaneously occurring⁽¹⁵⁾, are consistent with the assumption that these are electro-acoustic waves.

APPENDIX FFailure of cold trap

When the discharge was run in neon or argon, only a few hours of operation were obtained before the tube either cracked or imploded. The failure usually occurred at the cold trap where the glass was under strain from the large temperature gradients. It is thought that the greatest strain occurred in the lower rim of the outer sphere of the trap, where the glass has the sharpest curvature and where the discharge is constrained to change direction.

Such failure occurred in one of several different circumstances: (i) initial evacuation of a new tube; (ii) introduction of liquid nitrogen in the trap; (iii) starting of the discharge at an unduly high voltage; (iv) at discharge conditions where the column is unstable (in neon at 4 millitorr, for example, where the discharge is close to extinction and has large drift velocities), and (v) after running the discharge for a few hours (spontaneous cracking).

No failure occurred with a hydrogen discharge, either during a three day run by the author or during many weeks of operation by Little & Jones. A feature of the hydrogen discharge which seems significant is that it removed the very thin metallic-looking film that developed on the tube wall and on the wall near the top of the trap during the operation of the discharge in neon or argon. The film was probably a deposit of metal particles from the electrodes.

Electrode materials have been shown in the case of fractured glass from mercury clamp switches to produce "a mosaic craze cracking to a depth of the order of one thousandth of an inch" on the internal surface of the glass (from a report by the General Electric Company, London). It was concluded that the final complete fracture of the glass was due to very high local stresses caused by differential expansion of the embedded metallic particles and the glass. A similar process may render the cold trap less able to withstand strains or shocks.

APPENDIX G

Mechanism of wave excitation

Three possible ways in which density waves may be generated by means of an exciter coil were mentioned in section (25). We now consider each of these in more detail.

(i) Compression of plasma by alternating magnetic field. The local magnetic field can be regarded as squeezing the plasma (radially at the plane of the exciter coil) with a pressure $p \propto (B_0 + B_1 \sin \omega t)^2$ or $p \propto B_0^2 + 2B_0 B_1 \sin \omega t$ where $B_1 \ll B_0$. In the absence of the steady field, B_0 , the alternating component of the pressure p is proportional to $(B_1 \sin \omega t)^2$, which has an a.c. component $\frac{1}{2} B_1 \cos 2\omega t$. This is the mechanism suggested in two previous papers concerning low frequency waves in a positive column (2), (22). It is evident, however, that the mechanism is inapplicable if the field lines diffuse across the plasma column in a time much shorter than the wave period.

The rate of change of magnetic flux due to decay of the flux by ohmic losses is obtained from the equation

$$\frac{\partial \phi}{\partial t} = \frac{\eta}{4\pi} \int \nabla^2 \underline{B} \cdot \underline{dS} \quad (1)$$

where ϕ is the flux and η the resistivity⁽⁸³⁾. For a plasma with a characteristic dimension L (e.g. the column radius), this equation defines a decay time for the field lines, τ , given by

$$\frac{\phi}{\tau} = \frac{\eta}{4\pi} \frac{\underline{B} \cdot \underline{S}}{L^2} \quad (2)$$

or

$$\tau = 4\pi L^2 / \eta \quad (3)$$

τ represents the time for field lines to diffuse through a plasma of dimension L or, conversely, the time taken for plasma, compressed momentarily

by the magnetic field, to diffuse across the field.

In the present experiments $\eta_{||} = E_z/j_z \approx 3 \times 10^7$ e.m.u. It may be shown, furthermore, that $\eta_{\perp}/\eta_{||} = 3.4$ for a Lorentz gas in a strong magnetic field⁽⁸⁴⁾ (a fully ionized gas in which the electrons do not interact with each other and the ions are at rest. Assuming that this ratio is applicable to the present arc discharges, we obtain $\eta_{\perp} \approx 10^8$ e.m.u. The decay time τ is then approximately 10^{-6} sec, which is shorter than the wave period by at least an order of magnitude. The squeezing mechanism is therefore ineffective in the present experiments.

(ii) Modulation of the ion loss rate. This is the mechanism suggested by Little and Jones⁽²⁵⁾. Since $\omega \gg \omega_{ci}$ it is only the electrons that are influenced directly by the magnetic field. This influence extends to the ions through the ambipolar diffusion at right angles to the field. Little and Jones have mistakenly supposed n_i to be proportional to $D_{e\perp}^{-1}$, where $D_{e\perp}$ is the perpendicular diffusion coefficient for electrons, and thence to B^2 . ($D_{e\perp} = D_e/(1 + \omega_{ce}^2 \tau_e^2) \approx D_e/\omega_{ce}^2 \tau_e^2$ where D_e is the electron diffusion coefficient in the absence of a magnetic field, ω_{ce} is the electron cyclotron frequency and τ_e the electron-neutral collision period).

It is evident that insofar as the rate of ion loss in such low pressure discharges is controlled by ambipolar diffusion to the wall, the loss rate is modulated through the ω_{ce}^2 term in

$$D_{a\perp} = D_a / (1 + \omega_{ce}^2 \tau_e^2 \mu_i / \mu_e) \quad (4)$$

where D_a , μ_i and μ_e are respectively the ambipolar diffusion coefficient, ion mobility and electron mobility in the absence of a magnetic field. This equation may be obtained from the expressions for $D_{a\perp}$, $D_{i\perp}$, $\mu_{i\perp}$ and $\mu_{e\perp}$ given in the book by A. Simon⁽⁸⁵⁾.

In a 0.4 millitorr mercury discharge with $B_0 = 45$ gauss (as in the experiments of Little and Jones), $\omega_{ce}^2 \tau_e^2 \mu_i / \mu_e \sim 10$ and

$$D_{a\perp} \propto B^{-2} \propto (1 - 2B_1 \sin \omega t / B_0) . \quad (5)$$

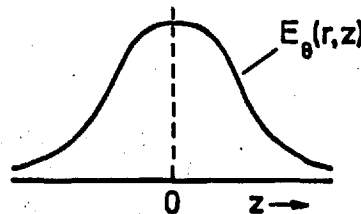
If, in the same discharge, $B_0 = 0$ and $B_1 = 2$ gauss, then

$$\omega_{ce}^2 \tau_e^2 \mu_1 / \mu_e \ll 1 \text{ and}$$

$$D_{a\perp} \propto (1 + a B_1^2 \sin^2 \omega t)^{-1} \propto (1 + \frac{1}{2} a B_1^2 \cos 2 \omega t) \quad (6)$$

where a is a constant and $aB_1^2 \ll 1$. In either case $D_{a\perp}$ is slightly modulated by the alternating magnetic field. The consequent modulation of the radial density profile gives rise to a small alternating density gradient $\partial n_1 / \partial z$ which is propagated electro-acoustically. This gradient obviously varies with r .

(iii) Production of alternating drift of plasma by crossed electric and magnetic fields. The alternating magnetic field \tilde{B}_1 gives rise to an alternating electric field \tilde{E}_θ in the azimuthal direction, whose amplitude $E_\theta(r, z)$ is a function of r and z . $E_\theta(r, z)$ increases with r and has a dependence on z shown qualitatively in the sketch.



The combination of \tilde{E}_θ and the radial longitudinal components of the magnetic field at the exciter produce

an alternating drift \underline{v}_D of ions and electrons together:

$$\underline{v}_D = \frac{\tilde{E}_\theta \times (\underline{B}_{oz} + \underline{B}_{or} + \tilde{B}_{1z} + \tilde{B}_{1r})}{(\underline{B}_0 + \tilde{B}_1)^2} \quad (7)$$

$$\approx \frac{\tilde{E}_\theta \times \underline{B}_{oz}}{B_0^2} + \frac{\tilde{E}_\theta \times \underline{B}_{or}}{B_0^2} \quad (\text{since } \tilde{B}_1 \ll B_0) \quad (8)$$

$$= \underline{v}_{Dr} + \underline{v}_{Dz}$$

The crossed fields $\underline{E}_{or} \times \underline{\tilde{B}}_{1z}$ and $\underline{E}_{oz} \times \underline{\tilde{B}}_{1r}$ would also produce an alternating drift of the plasma, but this would be in the azimuthal direction and does not concern us here.

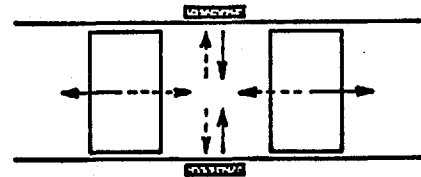
The variation of \underline{v}_D with r and z is shown at the bottom of the page. The short lines at right angles to the diverging magnetic field lines (\underline{B}_0) represent both the magnitude and direction of \underline{v}_D . The a.c. field is assumed to be so small that the lines of \underline{B}_0 are not distorted by it.

When $B_0 = 0$ equation (8) becomes

$$\underline{v}_D = \frac{\underline{\tilde{E}}_\theta \times \underline{\tilde{B}}_{1z}}{B_1^2} + \frac{\underline{\tilde{E}}_\theta \times \underline{\tilde{B}}_{1r}}{B_1^2} \quad (9)$$

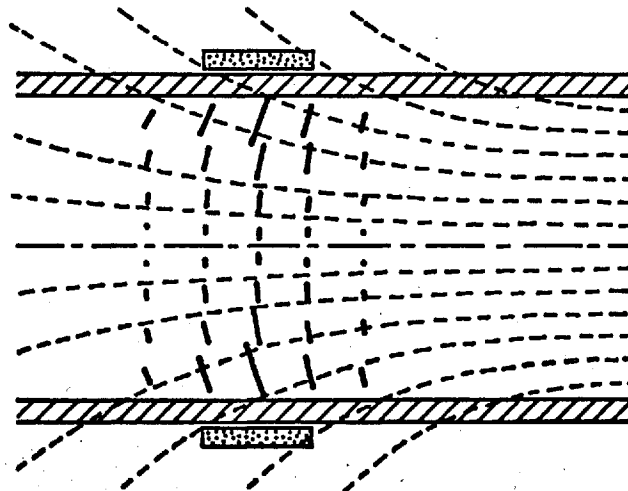
which fluctuates at twice the frequency of the exciter signal. The z component, $(\underline{\tilde{E}}_\theta \times \underline{\tilde{B}}_{1r})/B_1^2$, is zero in the plane of the exciter coil and rises to a maximum at a short distance from this plane on either side.

The effect of the z component is represented by the motion of two slabs of plasma in opposite directions, as shown in the sketch. The radial motion is



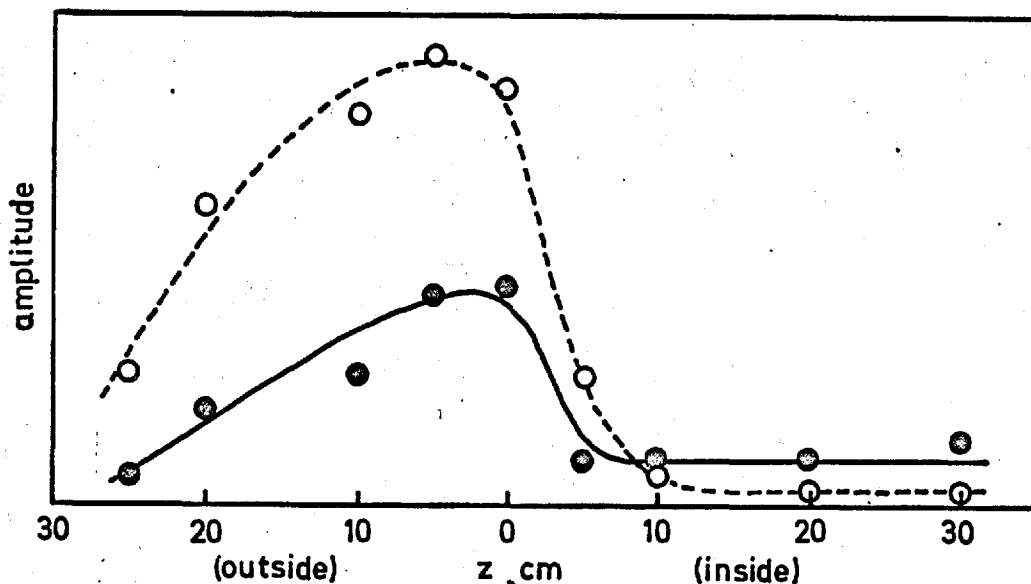
v_{Dz} and v_{Dr}

also included. The dotted and solid arrows differ in time by a quarter of a period of the exciter signal.



v_D and B_0 near exciter

Variation of wave amplitude with exciter position. It was mentioned in section (25) that the wave amplitude is observed to increase considerably when the exciter is moved from a position well inside the field coils (where $B_{or} = 0$) to a position just outside. The variation of amplitude with distance z of the exciter coil from the end of the field coils is shown in the following figure.



These measurements were made on a mercury vapour column under the conditions $p = 0.4$ millitorr, $I_D = 9A$, $B = 45$ gauss and $\omega = 2.2 \times 10^5$ rad/sec. The solid curve represents the amplitude measured at a distance of one wavelength from the exciter coil whilst the dashed curve corresponds to the amplitude at about three wavelengths from the exciter coil.

These curves are of the form expected from the assumption that the radial field B_{or} plays an important part in the wave generation. It is clear that under the set of conditions mentioned above, the $\underline{E}_\theta \times \underline{B}_{or}$ mechanism is far more effective than the $\underline{E}_\theta \times \underline{B}_{oz}$ and ion loss rate mechanisms in the generation of waves at $z = 0$.

REFERENCES

Part A (including General Introduction)

1. P.F. Little & H.G. Jones, Proc. Phys. Soc. (GB), 85, p.979 (1965).
2. P.F. Little & H.G. Jones, Culham Lab. Prog. Rep. CIM-PR6 p.21 (1963).
3. K. Nobata, Jap. J. Appl. Phys., 2, 719 (1963).
4. A.V. Gurevich, Geomagnetizm i aeronomiya, 4, p.1, p.192 (1964).
5. A.V. Gurevich & L.P. Pitaevskii, ibid., 5, 637 (1965).
6. Ya. L. Al'pert, A.V. Gurevich & L.P. Pitaevskii, Soviet Phys. - USP., 6, 13 (1963); "Artificial Satellites in Rarefied Plasmas" (Published in Moscow 1964, translation published in New York, 1965).
7. A.H. Davies & I. Harris, Rarefied Gas Dynamics 3rd Int. Symp., III, 661 (1963) (Academic Press, New York).
8. J.C. Taylor, Ph.D. thesis, University College, London, 1964.
9. U. Samir & A.P. Willmore, Planet.Space Science, 13, 285 (1965).
10. D.F. Hall, R.F. Kemp & J.M. Sellen, AIAAJ 2, 1032 (1964); "Generation and Characteristics of Plasma Wind Tunnel Streams", TRW Space Technology Labs., Redondo Beach, California (July 1963).
11. W.A. Clayden, Rarefied Gas Dynamics 3rd Int. Symp., II 435 (1963).
12. N. Kawashima, Memo No. 1827, Japan Atomic Energy Res. Inst., Dec.1964.
13. H. Alfvén & C.-G. Fälthammar, "Cosmical Electrodynamics" (2nd ed. Oxford University, 1963) p. 46.
14. P.J. Barrett, Phys. Rev. Letters, 13, 742 (1964).
15. J.E. Allen & F. Magistrelli, report published by Comitato Nazionale Energia Nucleare, Rome, December 1962.
16. P.F. Little, Proc. 5th Int. Conf. Ioniz. Phen. Gases, Munich, 1961, p. 1440.
17. C.B. Wharton, Risö Rep.No. 18, Internat. Summer Course 1960, Denmark.
18. H.S. Robertson, Phys. Fluids, 7, 1093 (1964).
19. N.D. Twiddy, Proc. Roy. Soc., A 275, 338 (1963).
20. N.A. Vorob'eva, Yu. M. Kagan & V.M. Milenin, Soviet Phys. - Tech. Phys., 8, 423 (1963).
21. L. Tonks & I. Langmuir, Phys. Rev., 34, 876 (1929).
22. T.E. Stringer, J. Nucl. Energy Part C, 5, 89 (1963).
23. G.A. Paulikas & R.V. Pyle, Univ. California Rad. Lab. Rep. UCRL-10379, July 1962.

24. A. Boschi & F. Magistrelli, *Nuovo Cimento*, 29, 487 (1963).
25. L. Spitzer, "Physics of Fully Ionized Gases". (Interscience Publishers, New York, 1962), p. 24.

Part B

1. L. Tonks & I. Langmuir, *Phys. Rev.*, 33, 195 (1929).
2. P.F. Little, Proc. 5th Int. Conf. Ioniz. Phen., Munich, 1961, p. 1440.
3. Y. Hatta & N. Sato, *ibid.*, p. 478.
4. L. Pekárek & V. Krejčí, *ibid.*, p. 573.
5. L. Pekárek, Proc. 6th Int. Conf. Ioniz. Phen., Paris, 1963, Vol. 2, p.133.
6. T. Donahue & G.H. Dieke, *Phys. Rev.*, 81, 248 (1951).
7. K. Wojaczek & A. Rutscher, *Beiträge aus der Plasmaphysik*, 3 217 (1963), 4 41 (1964).
- 7(a) R.S. Palmer & A. Garscadden, Aerospace Research Lab. Rep. ARL 65-120 June 1965 (United States Air Force).
8. A.W. Cooper & N.L. Oleson, Proc. 5th Int. Conf. Ioniz. Phen., Munich, 1961, p. 566.
9. M. Novák & T. Růžička, *Czek. J. Phys.*, 11, 878 (1961).
10. R.S. Cooper, Massachusetts Instit. Tech. R.L.E. Tech. Rep. 424, September 1964.
11. T.E. Stringer, *J. Nucl. Energy, Part C*, 5, 89 (1963).
12. M.Y. Vasil'eva, A.A. Zaitsev & E.D. Zndryukhina, *Bull. Acad. Sci. USSR, Phys. Ser.* 23, 982 (1959).
13. L. Spitzer, "Physics of Fully Ionized Gases" (Interscience Publishers, New York, 1962), p. 58.
14. J.V. Parker, California Instit. Technology, Rep. No.19, December 1962.
15. I. Alexeff & W.D. Jones, Oak Ridge Nat. Lab. Rep., ORNL-3652, April 1964, p. 56.
16. V.A. Liperovski, *Soviet Phys.-JETP*, 12, 951 (1961).
17. D.R. Davies, D.Phil. thesis (in preparation), Oxford University.
18. L.C. Woods, *J. Fluid Mech.*, 23, 315 (1965).
- 19(a) B. Bertotti, A. Cavaliere & P. Giupponi, Laboratorio Gas Ionizzati Rep. LGI 64/25, Frascati, 1964.
- (b) B. Bertotti & A. Cavaliere, *Nuovo Cimento*, 35, 1244 (1965).

20. L. Tonks & I. Langmuir, Phys. Rev. 34, 876 (1929).
21. T.E. Stringer, J. Nucl. Energy, Part C, 6 267 (1964).
22. F.W. Crawford & S.A. Self, Proc. 6th Int. Conf. Ioniz. Phen., Paris, 1963, Vol. 3, p. 129.
23. I. Alexeff & R.V. Neidigh, Phys. Rev., 129 516 (1963).
24. I. Alexeff & W.D. Jones, Oak Ridge Nat. Lab. Rep., ORNL-3564, p.55, p.59.
25. P.F. Little & H.G. Jones, Proc. Phys. Soc., 85, 979 (1965).
26. D. Montgomery, I. Alexeff & R.V. Neidigh, Bull. Am. Phys. Soc., Ser. II, 9 325 (1964); M.J. Haggerty, Canadian J. Phys., 43 1750 (1965).
27. I. Alexeff & W.D. Jones, Proc. 7th Int. Conf. Phen. Ioniz. Gases, Belgrade, 1965.
28. T.C. Chow, Phys. Rev., 37, 574 (1931).
29. R.W. Revans, Phys. Rev. 44 798 (1933).
30. E.B. Armstrong, K.G. Emeleus & T.R. Neill, Proc. Roy. Irish Acad., 54 A 291 (1951).
31. F.W. Crawford & G.S. Kino, Proc. I.R.E. (U.S.A.) 49, 1767 (1961).
32. F.W. Crawford, Phys. Rev. Letters, 6 663 (1961).
33. M. Geller & M. Luceraine, Compt. Rend., 253 1542 (1961).
34. J.A. Decker, J. Appl. Phys., 35 497 (1964).
35. P.F. Little, Nature, 194 1137 (1962).
36. A. Wong, N. D'Angelo & R.W. Motley, Phys. Rev. Letters, 9 415 (1962); Phys. Rev., 133 A436 (1964).
37. J.L. Shohet, Phys. Rev., 136A 125 (1964).
38. G.M. Sessler, Phys. Letters, 16 277 (1965); 5^e Congres Int. D'Acoustique, Liege, 1965; Proc. 7th Int. Conf. Phen. Ionized Gases, Belgrade, 1965.
39. E.V. Appleton & A.G.D. West, Phil. Mag., 45, 879 (1923).
40. A.A. Zaitsev, Vestnik Moskovskogo univ., Ser. fiz-mat. nauk, 6 No.10 41 (1951); Doklady AN SSSR, 84 41 (1952).
41. B. Klarfeld, ŽETP 22 66 (1952).
42. L. Pekárek, Vestnik Moskovskogo univ., Serija fiz-mat nauk 9 No. 3 73 (1954).
- 43(a) L. Pekárek, Czek. J. Phys., 4 295 (1954).
- (b) L. Pekárek, Czek. J. Phys., 7 533 (1957).

- (c) L. Pekárek & V. Krejčí, *Czek. J. Phys.* 11 729 (1961).
- (d) L. Pekárek & V. Krejčí, *Czek. J. Phys.*, 12 450 (1962).
- (e) L. Pekárek & V. Krejčí, *Czek. J. Phys.*, 13 881 (1963).
- (f) L. Pekárek & V. Krejčí, *Czek. J. Phys.*, 12 296 (1962).
44. L. Pekarek, *Czek. J. Phys.*, 8 699 (1958), 11 849 (1961).
45. S. Pfau & A. Rutscher, *Ann. Physik*, 6 244 (1960).
46. L. Pekárek, V. Krejčí & O. Štirand, *Czek. J. Phys.*, 13, 243 (1963).
47. K. Wojaczek, *Beitr. Plasmaphys.* 1 30 (1961), 2 13 (1962); *Ann. Phys.* 3 37 (1959).
48. A.V. Nedospasov & Yu. B. Ponomarenko, *Proc. 6th Int. Conf. Ioniz. Phen.*, Paris, 1963, Vol. 2 223; *Soviet Phys. - JETP* 19 631 (1964).
49. H.S. Robertson, *Phys. Rev.*, 105, 368 (1957); *Proc. 5th Int. Conf. Ioniz. Phen.*, Munich, 1961, p. 550.
50. T. Kenjo & Y. Hatta, *J. Phys. Soc. Japan*, 19 2313 (1964).
51. A.V. Nedospasov, *Soviet Phys. - Tech. Phys.*, 3 153 (1958).
52. S. Watanabe & N. Oleson, *Phys. Rev.*, 99 646 (1955).
53. I.M. Čapnik, *Soviet Phys. - JETP*, 7 1033 (1958).
54. H. Rother, *Ann. Physik, Ser. 7*, 4 373 (1959); 5 252 (1960).
55. A.B. Stewart, *J. Appl. Phys.* 27 911 (1956).
56. R.F. Boyd & N.D. Twiddy, *Proc. Roy. Soc., A*, 259 145 (1960).
57. S.F. Paik, J.N. Shapiro & K.D. Gilbert, *J. Appl. Phys. (USA)*, 35 2573 (1964).
58. L. Pekárek, Culham Laboratory Study Group on Plasma Waves, September 1964.
59. J.E. Allen & F. Magistrelli, *Nature*, 194 1167 (1962).
60. G.A. Paulikas & R.V. Pyle, *Univ. of California Rad. Lab. Rep. UCRL-10379*, July 1962.
61. R.A. Smith, *IEE (GB), Radio Section Memo No. 6*, 1951.
62. P.F. Little & H.G. Jones, *Culham Lab. Prog. Rep. CLM-PR6 p. 21* (1963).
63. F.W. Crawford & R.J. Kuhler, *Proc. 7th Int. Conf. Phen. Ionized Gases, Belgrade, 1965*.
64. L.C. Woods, P.F. Little & H.G. Jones, *ibid.*
65. A. von Engel, *"Ionized Gases"* (2nd ed., Oxford University, 1965).
66. J.E. Allen & F. Magistrelli, report published by Comitato Nazionale Energia Nucleare, Rome, December 1962.

67. S.C. Brown, "Basic Data of Plasma Physics" (Massachusetts Instit. Tech., 1959).
68. A. von Engel, "Ionized Gases" (2nd ed., Oxford Univ., 1965) p. 114.
69. G.M. Sessler, Proc. 7th Int. Conf. Phen. Ionized Gases, Belgrade, 1965
70. G.B. Righetti, F. Magistrelli, L. Enriques & A. Boschi, *ibid.*
71. M.A. Cayless, Brit. J. Appl. Phys., 10 186 (1959).
72. H.S.W. Massey & E.H.S. Burhop, "Electronic and Ionic Impact Phenomena" (Oxford University 1952), p. 77.
73. L. Vriens, Phys. Letters, 8 260 (1964).
74. Yu. M. Kagan & R.I. Lyagushchenko, Optics and Spectrosc. (USA), 17 90 (August 1964).
75. B. Klarfeld, J. Tech. Phys. USSR, 5 924 (1938).
76. R.M. Howe, J. Appl. Phys., 24, 881 (1953).
77. L. Pekárek & M. Novák, Czek. J. Phys.,
78. L. Pekárek, Proc. 7th Int. Conf. Phen. Ionized Gases, Belgrade, 1965.
79. L. Pekárek, V. Krejci, O. Stirand & L. Laska, Phys. Rev. Letters, 15 721 (1965).
80. A.A. Zaitsev & M.Ya. Vasil'eva, Radiotekhnika i Elektronika, 7 557 (1962).
81. L.C. Woods, J. Fluid. Mech., 13 570 (1962).
82. J.R.M. Coulter, Physica, 26 949 (1960).
83. L. Spitzer, "Physics of Fully Ionized Gases" (Interscience Publishers, New York, 1962), p. 42.
84. L. Spitzer, *ibid.*, p. 143.
85. A. Simon, "An Introduction to Thermonuclear Research" (Pergamon Press, 1959), p. 160.

ACKNOWLEDGEMENTS

These experiments were carried out in the Culham Laboratory of the United Kingdom Atomic Energy Authority Research Group. The author is much indebted to the Director of Culham Laboratory for the use of experimental facilities. He is deeply grateful to Dr. R. Latham for the supervision and continual encouragement of this work. He also owes a great deal to Drs. R.J. Bickerton and A. von Engel for advice on parts of the work, and especially to Dr. P.F. Little for providing the apparatus and much inspiration and helpful comment. Thanks are due to Mr. H.G. Jones for performing the wave amplitude measurements presented on page 174.